Exploring metallo-supramolecular architectures: towards recognition of functional nucleic acid structures for fighting disease



By

James Samuel Craig

A thesis submitted to the University of Birmingham for the degree of

DOCTOR OF PHILOSOPHY

School of Chemistry

College of Engineering and Physical Sciences

University of Birmingham

10/09/2023

UNIVERSITY OF
BIRMINGHAM

University of Birmingham Research Archive

e-theses repository

This unpublished thesis/dissertation is copyright of the author and/or third parties. The intellectual property rights of the author or third parties in respect of this work are as defined by The Copyright Designs and Patents Act 1988 or as modified by any successor legislation.

Any use made of information contained in this thesis/dissertation must be in accordance with that legislation and must be properly acknowledged. Further distribution or reproduction in any format is prohibited without the permission of the copyright holder.

Abstract

The work in this thesis investigates the non-canonical DNA binding and *in vitro* blood stability of modified metallo-supramolecular cylinders, their CB[10] rotaxanes, and metallo-supramolecular pillarplexes. These investigations looked at the rotaxane formed by the metallo-supramolecular cylinder and CB[10], revealing inhibition of their exceptional DNA binding, where their *pseudo*-rotaxane showed minor change. This set the precedent for unparalleled control of their DNA binding, pushing development of a modified rotaxane system allowing for their controlled biological release. Towards this, a rotaxane of the metallo-supramolecular cylinder was designed with a capping group which cleaved in the presence of glutathione, allowing glutathione dependant release of cylinder and restoration of its unprecedented DNA binding. Due to the functional success of these systems *in vitro, in vivo* studies have entered an initial planning stage. Towards this, a method for the separation and detection of metallo-supramolecular cylinders and their rotaxanes from rats whole blood was developed, allowing quantitative detection of metal ion concentration and intact structure determination. Finally, we report the first studies into the DNA binding of new metallo-supramolecular pillarplexes. This revealed potent DNA binding and an affinity for DNA 4WJ's and forks. We also observe a difference in DNA binding which is dependent on the metal in the pillarplex, either gold or silver, suggesting both may have different modes of action in biological systems, and potential for different theragnostic applications.

Acknowledgements

I would first like to thank my supervisor, Professor Michael Hannon, for his support and time throughout this PhD and allowing me to follow my research interests. He has played an instrumental role in my progress, sharing insight and knowledge which has been invaluable for this research. I would also like to thank Dr Nikolas Hodges for sharing his knowledge of biological studies and for the supportive learning environment he has provided. Next, I would like to thank the Physical Sciences for Health program for providing a solid knowledge basis for my research and professional growth. Lastly, I would like to thank the EPSRC for the funding to conduct this research and PhD.

To all the friends I have made along the way during this exceptional journey. Your help and support, taking many forms, has given comfort and motivation through the most challenging of times. Whilst there are too many names to thank everyone individually, I would like to convey special thanks to a few. To Callum, for his willingness to share his experience and for bringing me into the group with open arms. To Katie, for sharing innumerable highs and lows and always being up for a laugh. To Ross, Hugo, and Cat for always helping me with my research and for shared conversations, hobbies, assorted confectionary, and coffee, I couldn't have wished for better fellow group members.

I would like to thank everyone who has supported me in learning new science and techniques throughout my research. To Doug, for teaching me how to handle radioactive isotopes and perform polyacrylamide gel electrophoresis. To Christopher, for teaching me how to use a mass spectrometer, and for all the associated helpful conversions, from which I have learnt so much.

I would also like to thank my family, for pushing me to achieve my best, and always encouraging me to follow my love of science. Finally, I would like to thank my partner Emma, who has supported and encouraged me through every high and low, always helping me to keep my goals in sight, and for being the most supportive and amazing person to share this journey with.

For these reasons, and so many more, I would like to dedicate this thesis to all of you.

Publications

1. Ana B. Caballero, Lucia Cardo, Sunil Claire, James S. Craig, Nikolas J. Hodges, Anton Vladyka, Tim Albrecht, Luke A. Rochford, Zoe Pikramenou, and Michael J. Hannon. “Assisted delivery of anti-tumour platinum drugs using DNA-coiling gold nanoparticles bearing lumophores and intercalators: towards a new generation of multimodal nanocarriers with enhanced action”. Chem. Sci., 2019, 10, 9244–9256, DOI: 10.1039/C9SC02640A.
2. Catherine A. J. Hooper, Lucia Cardo, James S. Craig, Lazaros Melidis, Aditya Garai, Ross T. Egan, Viktoriia Sadovnikova, Florian Burkert, Louise Male, Nikolas J. Hodges, Douglas F. Browning, Roselyne Rosas, Fengbo Liu, Fillipe V. Rocha, Mauro A. Lima, Simin Liu, David Bardelang, and Michael J. Hannon. “Rotaxanating Metallo-supramolecular Nano-cylinder Helicates to Switch DNA Junction Binding”. J. Am. Chem. Soc. 2020, 142, 49, 20651−20660, DOI: 10.1021/jacs.0c07750.
3. Lazaros Melidis, Harriet J. Hill, Nicholas J. Coltman, Dr. Scott P. Davies, Dr. Kinga Winczura, Tasha Chauhan, James S. Craig, Dr. Aditya Garai, Catherine A. J. Hooper, Ross T. Egan, Jane A. McKeating, Nikolas J. Hodges, Zania Stamataki, Pawel Grzechnik, Michael J. Hannon. “Supramolecular Cylinders Target Bulge Structures in the 5′ UTR of the RNA Genome of SARS-CoV-2 and Inhibit Viral Replication”. Angew. Chem. Int. Ed. 2021, 60, 18144. DOI: 10.1002/anie.202104179.
4. James S. Craig, Larry Melidis, Hugo Williams, Samuel Dettmer, Alexandra A. Heidecker, Callum Campbell, Douglas F. Browning, Roland Sigel, Silke Johannsen, Ross Egan, Brech Aikman, Angela Casini, Alexander Pöthig, Michael J. Hannon. “Organometallic Pillarplexes that bind DNA 4-way Holliday Junctions and Forks”. *J. Am. Chem. Soc.* 2023, 145, 25, 13570–13580. DOI: 10.1021/jacs.3c00118
5. Aditya Garai, Ross T. Egan, James S. Craig, Lazaros Melidis, Hugo Williams, Christopher M. Williams, Fengbo Liu, Simin Liu, Neil Champness, Sarah Griffin, Alex Pöthig, Nikolas J. Hodges, and Michael J. Hannon. “Thiol triggered uncaging of DNA 3-way junction binding nano cylinder from rotaxane”. (Manuscript to be submitted)

Table of contents

Abstract 2

Acknowledgments 3

Publications 4

Abbreviations 8

Chapter 1: Introduction 11

1.1: Background 11

1.2: DNA history, structures, and binders 13

1.2.1: Intro to DNA – From discovery to the modern day 13

1.2.2: DNA structure 14

1.2.3: Different nucleic acid structures and binding them 17

1.2.3.1: Covalent nucleic acid binding and cisplatin 18

1.2.3.2: DNA minor and major grooves and binding 21

1.2.3.3: Intercalation in nucleic acids 25

1.2.3.4: Binding nucleic acid junctions and bulges 28

1.2.3.5: Binding nucleic acid G-quadruplexes 38

1.2.3.6: Binding nucleic acid i-motifs 42

1.2.4: Summary of nucleic acid structures 46

1.3: Metallo-supramolecular complexes: towards nucleic acid recognition 48

1.3.1: Metallo-supramolecular cylinders 48

1.3.2: Metallo-organic supramolecular Pillarplexes 54

1.3.3: Metallo-supramolecular tetrahedra 56

1.3.4: Other supramolecular helical nucleic acid binders 58

1.3.5: Rotaxane caged Pt G-quadruplex binder 59

1.4: Thesis overview 61

1.5: References 63

Chapter 2: Rotaxanating metallo-supramolecular cylinders – towards controlled release 73

2.1: Introduction 73

2.2: Effects of full and *pseudo*-rotaxanation on DNA interactions of metallo-supramolecular cylinders 76

2.3: An alternative method for cylinder·CB[10] based rotaxane formation 91

2.4: De-capping di-nitrobenzene capped cylinder rotaxanes - towards controlled release 95

2.5: Nucleic acid interactions of cylinders with modified structures 107

2.6: Investigation of crude CB[n] reaction mixture 117

2.7: Conclusion 122

2.8: Experimental 124

2.8.1: Synthesis and characterization of complexes 124

2.8.2: Experiments 143

2.9: References 148

Chapter 3: Stability in and extraction of cylinders and rotaxanes from Rats whole blood, *in vitro* 152

3.1: Introduction 146

3.2: Using ICP-MS for quantitative detection of nickel ions from rats' whole blood 155

3.3: Separation and detection of supramolecular cylinders and rotaxanes from rats' whole blood and their stability 157

3.3.1: Developing a separation and detection method 157

3.3.2: Stability of supramolecular cylinders in rats' whole blood 163

3.3.3: *Pseudo*-rotaxanation effect on the stability of cylinders in rats' whole blood 174

3.4: Conclusion 180

3.5: Experimental 184

3.5.1: ICP-MS of rat's whole blood: 184

3.5.2: Blood Incubation and MS detection experiment 184

3.5.3: Synthesis and characterization of cylinders 185

3.6: References 187

Chapter 4: Metallo-supramolecular pillarplexes as DNA Junction and Fork binders 189

4.1: Introduction 189

4.2: Nucleic acid interactions of supramolecular pillarplexes 192

4.2.1: Electrophoresis studies 192

4.2.2: Spectroscopic studies 203

4.2.3: Atomic force microscopy 206

4.3: Rotaxanation of Pillarplexes: Towards a 3-tiered Russian doll system 209

4.4: Conclusion 215

4.5: Experimental 217

4.5.1: Synthetic experimental 217

4.5.2: Experiments 218

4.6: References 223

Chapter 5: Summary, conclusions, and further work 225

5.1: Summary 225

5.2: Conclusions 227

5.3: Further work 228

Chapter 6: Appendix 231

6.1: Agarose gel electrophoresis of circular supercoiled and linearized pBR-322 plasmid DNA with pillarplex ligand 231

6.2: CD spectra of both M and P enantiomers of $[Fe_2(L)_3]^{4+}$ 232

6.3: ESI+ MS spectra of $[Fe_2(L)_3 \cdot (CB10)]^{4+}$ alone after blood purification process at starting and finishing time points 233

6.4: CT-DNA binding curve for $[Ni_2(L')_3]$ from CD values at 250 nm 234

6.5: CT-DNA binding curve for gold Pillarplex from CD values at 250 nm 235

Abbreviations

µL	Microlitre
µM	Micromolar
ε	Molar extinction coefficient
2D	Two dimensional
3WJ	Three-way junction
4WJ	Four-way junction
AFM	Atomic force microscopy
bp	Base pair
CB[10]	Cucurbit-10-uril
CD	Circular dichroism
CT	Calf thymus
DMSO	Di-methyl sulfoxide
DNA	Deoxyribonucleic acid
DNB	Di-nitro benzene
DOSY	Diffusion-ordered NMR spectroscopy
DS-21	Double stranded 21 mer
DS-DNA	Double stranded DNA
EDTA	Ethylenediaminetetraacetic acid
EMSA	Electrophoretic mobility shift assay
ESI-MS	Electrospray ionisation mass spectrometry
ESI+	Electrospray ionisation positive mode
eq	Equivalents
FRET	Förster resonance energy transfer

g	Grams
GSH	Glutathione
HIV-1	Human immunodeficiency virus – 1
HJ	Holliday junction
HPLC	High-performance liquid chromatography
IC50	Half-maximal inhibitory concentration
ICD	Induced circular dichroism
ICP-MS	Inductively coupled plasma mass spectrometry
ILD	Induced linear dichroism
kDa	Kilo Daltons
L	Original imine ligand
L’	2-imidazole ligand
L’’	Picolyl capped 2-imidazole ligand
L^{*}	Azo ligand
L'^{4}	4-imidazole ligand
L^{DNB}	Di-nitrobenzene capped 2-imidazole ligand
L^{Q}	Isoquinoline ligand
LD	Liner dichroism
mg	Milligrams
ml	Millilitre
MLCT	Metal to ligand charge transfer
mm-3WJ	Mismatched three-way junction
MS	Mass spectrometry
MTT	(3-(4,5-Dimethylthiazol-2-yl)-2,5-Diphenyltetrazolium Bromide)
MV^{2+}	Methyl viologen

MWCO	molecular weight cut off
m/z	Mass to charge ratio
nm	Nanometre
NMR	Nuclear magnetic resonance
Oligo	Oligonucleotide
PAGE	Polyacrylamide gel electrophoresis
PAL24	Palindromic 24 mer
PES	Poly ether sulphone
ppb	Parts per billion
ppt	Parts per trillion
RNA	Ribonucleic acid
RF	Retention factor
SARS-CoV-2	Severe acute respiratory system coronavirus 2
SNAr	Nucleophilic aromatic substitution
SS	Single strand
SS-DNA	Single stranded DNA
TAR	Trans activator response region
TAT	Trans activator protein
TB buffer	Tris boric acid buffer
TBN buffer	Tris boric acid sodium chloride buffer
TEMED	Tetramethyl ethylenediamine
TLC	Thin layer chromatography
TOF	Time of flight
UV-Vis	Ultraviolet-visible spectroscopy
Y	Y shaped junction

Chapter 1: Introduction

1.1: Background

The average life expectancy for the population has been a rising figure in recent times and continues to grow, resulting in an increase in the total elderly population.[1,2] With this increasing demographic comes weaker immune systems and therefore a greater susceptibility to viral infection and age associated disease such as cancer, which has led to increased hospitalisations and medical costs.[3–5] On top of this, the recent SARS-CoV-2 pandemic (UK only 10/03/2022 - 159,295 Lives and hundreds of billions in medical costs and lost business) has highlighted the immense need for new therapeutics which can treat such diseases. [6,7] With hospitalisations and deaths associated directly from viral infection as well as from the inability to access necessary treatment through closures and restricted access.[6,7] The development of a broad-spectrum anti-proliferative drug would offer an immediate treatment to reduce hospitalisations and mortality rates. Functional nucleic acid structures are attractive targets to achieve this due to their importance in the pathogenesis of viral infections and cancer. This, however, has substantial hurdles to overcome, most notably genetic mutations which affect targeted structures, causing binding site changes and resulting in resistance.[8–10]

To develop new broad spectrum anti-viral/bacterial/cancer drugs, new biological targets are required which circumvent resistances and utilize key biological processes.[11–13] Nucleic acid structures offer themselves as attractive therapeutic targets, being involved in crucial biological processes and containing essential genetic information.[14] In particular, higher order nucleic acid structures such as junctions and

bulges present unique targets associated with key biological processes such as replication. Interfering with these key nucleic acid structures and associated functions could have potent biological effects.[15–18]

Supramolecular metal complexes have been developed which can interact with these higher order nucleic acid structures.[19] Which have yielded potent cytostatic and apoptotic biological effects with subsequent developments allowing for control of their activity to increase specificity and efficacy.[20,21] Other metallo-supramolecular complexes have since been developed which share similar properties with hopes of achieving similar potent biological activity.[22] Continued development and investigation of these complexes holds promise for the discovery of potent therapeutic candidates.

In this thesis I will investigate how metallo-supramolecular cylinders and pillarplexes interact with important nucleic acid structures. I explore the use of rotaxanation as a method for controlling the nucleic acid binding of these complexes, and how this may lead to controlled/targeted release. We also explore the stability of cylinders and their associated full and *pseudo*-rotaxanes in rats whole blood, to gain insight into their biological modes of action and discuss how this can be used to improve future designs. Lastly, we investigate the nucleic acid binding of metallo-supramolecular pillarplexes, which present new metals and supramolecular architecture with which unique DNA junction and fork binding is observed. To place this in context the project background and the state of the art is described in this chapter.

1.2: DNA History, structures, and binders

1.2.1: Intro to DNA – From discovery to the modern day

The presence of DNA was first discovered by Friedrich Miescher in 1868 where they reported the finding of a precipitate from the cell's nucleus.[23] This precipitate (which would later be identified as DNA) was indigestible with protease, immediately eliminating the possibility of it being a protein. Elemental analysis also indicated that it contained an abundance of phosphorus and a lack of sulphur, highlighting it as a novel biomolecular discovery.

Many years later in 1953, Rosalind franklin and Raymond Gosling produced an x-ray structure of calf thymus DNA (Figure 1.01) which revealed several properties of its structure.[24] This showed that the structure was very likely helical in nature, there were approximately 10 residues per full helical turn and that the phosphate backbone lay on the outside of the structure.

Shortly after this, Watson and Crick suggested the structure for DNA which we use today. They highlighted the right-handed anti-parallel double helical structure around a central axis with an external phosphate backbone perpendicular to the specific A-T and G-C base pairs in the hydrophobic central cavity.[25]

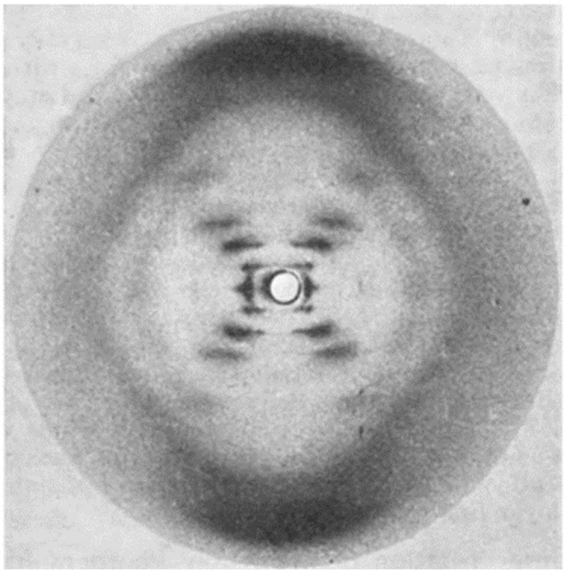


Figure 1.01: Shows the x-ray structure acquired by Rosalind Franklin and Raymond Gosling which was used to deduce structural characteristics of DNA. Adapted from the referenced publication with permission.[24]

These are some of the key discoveries which have resulted in the understanding of genetic information and how it is stored. This has led to the sequencing of the entire human genome which has deepened our understanding of biological mechanisms and disease alike.[26]

Our knowledge of DNA has expanded further, yielding different nucleic acid structures and associated biological functions.[27] Applications of DNA have expanded outside of biological systems with applications even in electronics due to structure and information storage capacity.[28] As our understanding of DNA continues to deepen, so too will its applications and potential.

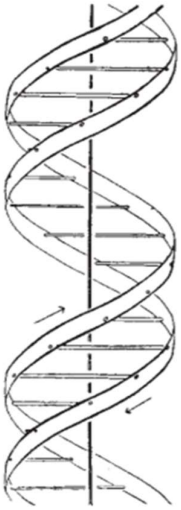


Figure 1.02: Shows the DNA structure proposed by Watson and Crick. Adapted from the referenced publication with permission.[25]

1.2.2: DNA structure

Deoxyribonucleic acid (DNA) is a polyanionic molecule comprised of monomer nucleobases containing a deoxyribose sugar, a phosphate anion, and an aromatic nitrogenous base. The nitrogenous bases can be of four distinct types, Adenine (A), Thymine (T), Guanine (G) and Cytosine (C) which exhibit hydrogen bonding between one another in the pairs of A-T and G-C which can be seen in Figure 1.03.[29,30]

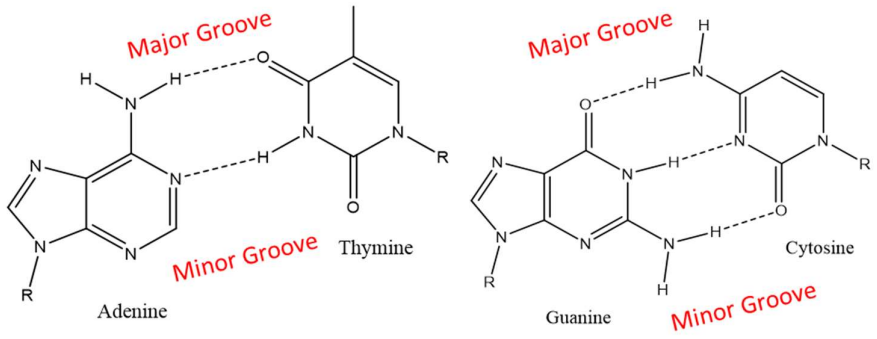


Figure 1.03: Shows the structure of A,T,G and C, the hydrogen bonding in their respective pairs and locations relative to the grooves of the DNA structure.

These nucleobases combine to form a DNA molecule running from a 5' to a 3' position. Two of these molecules form hydrogen bonds between the aromatic nitrogenous bases of the complementary strand whilst optimising stacking interaction on top of one another's aromatic ring systems. This produces the B-form of DNA which is a right-handed anti-parallel double helix structure with around 10 base pairs per turn. We associate this structure with genetic information storage and represents most of the DNA in the body at any single point in time (Figure 1.04).[31] The DNA structure has several different regions which can interact with external molecules. There is a negatively charged phosphate backbone which is responsible for the polyanionic nature of the molecule. The π-stacked bases offer a hydrophobic environment which is capable of being occupied by other planar aromatic species. Finally, the double helical nature results in the formation of a minor (1.2 nm wide) and major groove (2.2 nm wide) which can be seen in Figure 1.04.[32] The differing sizes and functional groups of these grooves give them differing interactions with biomolecules and chemotherapeutics alike. [33–35]

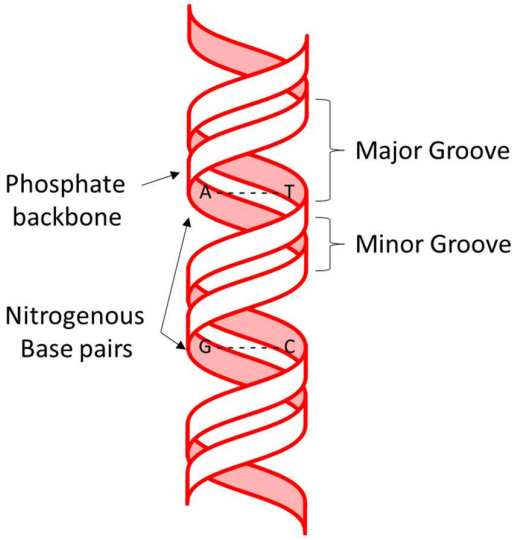


Figure 1.04: Shows the double helical structure of B-- DNA and it's different structural components and environments.

Other forms of DNA also exist which bear resemblance to the B-DNA structure. A-DNA occurs in dehydrated environments and purine rich DNA sequences. It is a right-handed helix with a wider structure (2.3 nm) where the base pairs are stacked at an angle with a reduced distance between one another (0.26 nm).[36] A-DNA is found in

DNA-RNA hybrid structures during transcription and has been shown to be used by bacteria to prevent DNA damage in desiccated states.[37,38]

Z-DNA also exists which is a left-handed helix and a narrower diameter than B-DNA of 1.8 nm.[36] This structure is higher in energy that its other counterparts as is defined by its zigzag backbone arrangement which gives it its name. The structure occurs transiently in most cases and is composed of alternating purine/pyridine bases where the purines are flipped to maintain hydrogen bonding. Z-DNA is much rarer than its counterparts but has shown to occur during negative supercoiling to reduce torsional strain as well as in unique situations such as fear and extinction learning in mouse models.[39,40]

Alternative, more dynamic, DNA structures exist which present themselves as attractive theragnostic targets for disease diagnosis and treatment due to their links with important biological processes.[41]

1.2.3: Different nucleic acid structures and binding them

The importance of DNA in biology cannot be understated, it contains all the information required for a living organism which is reflected in its considerable size. Within this, the nucleic acids code for genes which represent proteins with numerous applications across the living organisms body. Faults in this sequence or interfering with transcription can lead to the formation of disease.[42] Cancer is a primary example of a disease that can form in this case, which is where cell proliferation is uncontrolled, and the cancerous cells cause damage to the rest of the body. Targeting the genes responsible for this uncontrolled replication or interfering with DNA replication itself can prove to be an effective cancer treatment.[43,44] Targeting the replication process offers increased selectivity for cells undergoing greater levels of DNA replication. Replication targeting represents a biologically active DNA structure, the replication fork, where therapeutics can be tailored to target and interact with it.[45] Interacting with a replication fork and associated machinery as well as RNA bulges has also proved to be an effective anti-viral strategy.[46–48] Targeting a structure associated with a key biological process such as this also aids in avoiding drug resistance pathways which normally develop through a change in sequence as opposed to change in secondary structure.[9] These nucleic acid structures, among others, offer themselves as attractive therapeutic

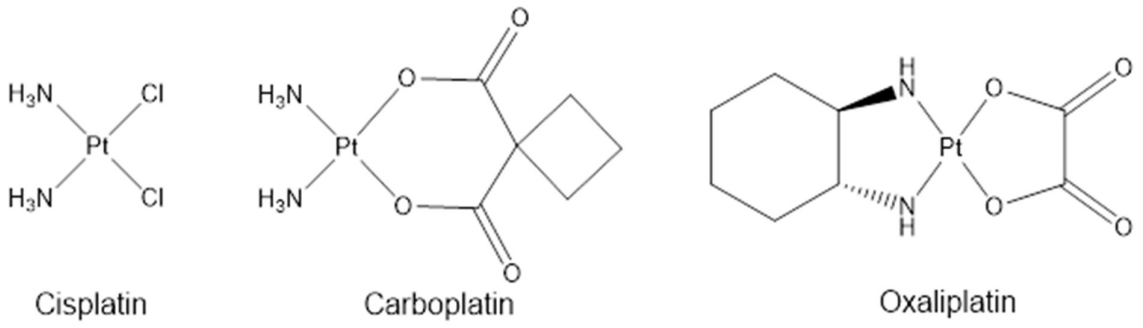


Figure 1.05: Chemical structures of cisplatin, carboplatin and oxaliplatin.

targets due to their involvement in biological processes and the selectivity that this offers. [49]

1.2.3.1: Covalent nucleic acid binding and Cisplatin

Cisplatin was first reported in 1845 with its anti-proliferative effects being revealed by Barnett Rosenburg during an investigation of the effects of electrolysis on bacteria growth using platinum electrodes.[50,51] This led to the testing of Cisplatin as an anti-cancer drug in 1974 and subsequent approval in 1978.[52] Cisplatin is a square planar complex with two chlorine ligands and two ammonia ligands in a cis arrangement (Figure 1.05). Cisplatin behaves in several different ways upon entering the body, binding to many different biological structures including proteins, collagen and DNA.[53–55] However it is thought that its apoptotic effects are achieved by covalently crosslinking at the N7 site in purine residues, resulting in a kinked DNA structure which prevents replication.[56] This occurs due to displacement of the chlorine ligands in the cytoplasm by water molecules. The result is a potent electrophile which can attack

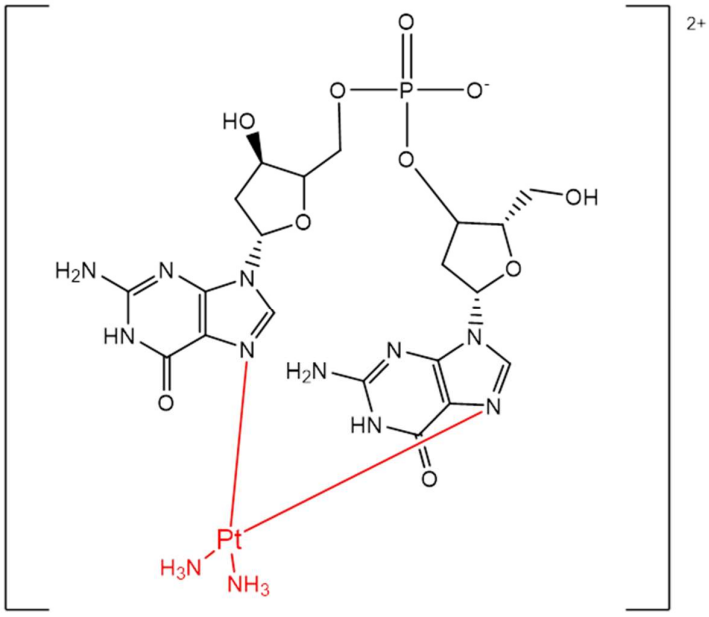


Figure 1.06: Shows the structure of cisplatin covalently bounds to the N7 side on two adjacent guanine bases as an illustration of one of cisplatin's DNA binding modes.

nucleophilic sites such as the S-H groups on proteins and nitrogen donor atoms on nucleic acids. Cisplatin will bind the N7 centre on purine residues (Figure 1.06), resulting in DNA damage and apoptotic cell death. This has been used to treat numerous types of cancer with remarkable success including leukaemia, lymphomas, breast, testicular, ovarian, head, neck, cervical cancer, and sarcomas.[57]

Some cancer types are resistant to Cisplatin, and most can develop resistance to the drug after it has been used.[58] This occurs for several reasons including reduced accumulation and retention of Cisplatin through the degradation or lack of expression of membrane transport proteins which are responsible for its uptake, as well as reduced endocytosis.[58] Alongside this, upregulation of different genes, gene silencing, epigenetic changes, and histone acetylation all impact resistance. The variety of resistance mechanisms further reflects the numerous different modes of action of cisplatin *in vivo*, highlighting one of the drugs key issues, lack of specificity.[59]

The lack of a specific binding target means cisplatin binds many different targets in healthy and cancer cells alike, resulting in a wide range of biological effects, including its anti-cancer properties. However, this also leads to numerous unintended toxicities and side effects including ototoxicity, nephrotoxicity, neurotoxicity, haematological toxicity, hepatotoxicity, nausea, vomiting, mutagenicity, and carcinogenicity.[60,61] These can leave patients with chronic, life long, side effects and additional complications later in life including additional cancers caused by the treatment for the first.

The need to reduce side effects, increase efficacy and avoid resistance has led to the development of new platinum anti-cancer drugs alongside novel covalently binding drugs. The first of a new generation was carboplatin (Figure 1.05), which replaced the

chloride leaving groups with a bis-carboxylate ligand which reduced the aquation rate.[61] Carboplatin showed reduced side effects and toxicities compared to cisplatin with comparable effects and the same mechanism of action via covalent DNA binding.[62,63] However, with this comparable mode of action and efficacy comes comparable resistance, meaning alternatives were still required.[64] Towards this, Oxaliplatin (Figure 1.05) was developed which in some cancers is not cross-resistant with cisplatin and is currently widely used as a colorectal cancer treatment.[65] Despite this, it also has negative side effects, most prominently neurotoxicity which is its dose limiting factor.[66]

The clinical success of these platinum agents has led to the development of many more complexes. This includes trans-platinum-based agents, which offer different binding modes which avoid the resistances of cisplatin.[67] Polynuclear platinum agents have also been developed which exhibit potent DNA binding, condensation, and structural changes.[68–70] Drugs with differing structural geometries have also been developed with tetrahedral and octahedral arrangements as well as piano stool structures. Tetrahedral titanocene complexes offers comparable or improved toxicity over cisplatin via a different mode of action, thought to be anti-proliferative effects via cysteine protease targeting, yet they also lack specificity.[71] Octahedral ruthenium complexes have also showed activity against cancer cell lines as well metastasised cancers whilst offering low collateral toxicity.[72] Piano stool structures offer diverse and interchangeable structural characteristics, but involve a hydrophobic arene which promotes non-covalent interactions, water substitutable groups and biologically active groups.[73] Due to their versatility and varied design, different variations have shown

activity against cancer cell lines through differing modes of action including through covalent DNA adduct formation.

1.2.3.2: DNA minor and major grooves and binding

With the successes and failures of cisplatin and other covalent DNA binding agents there has been attempted to recognise and selectively interact with DNA structures through other means. This has given rise to non-covalent DNA binding agents which recognise intermolecular interactions and environments selectively to achieve targeting and biological effects. One classification targets the minor or major grooves of DNA, both of which possess their own characteristics and biological relevancies.

The DNA minor groove is 6 Å wide and 8.2 Å deep making it the narrower of the 2 with a deep cavity.[32,74] Presented in this groove are the functional groups of the DNA bases

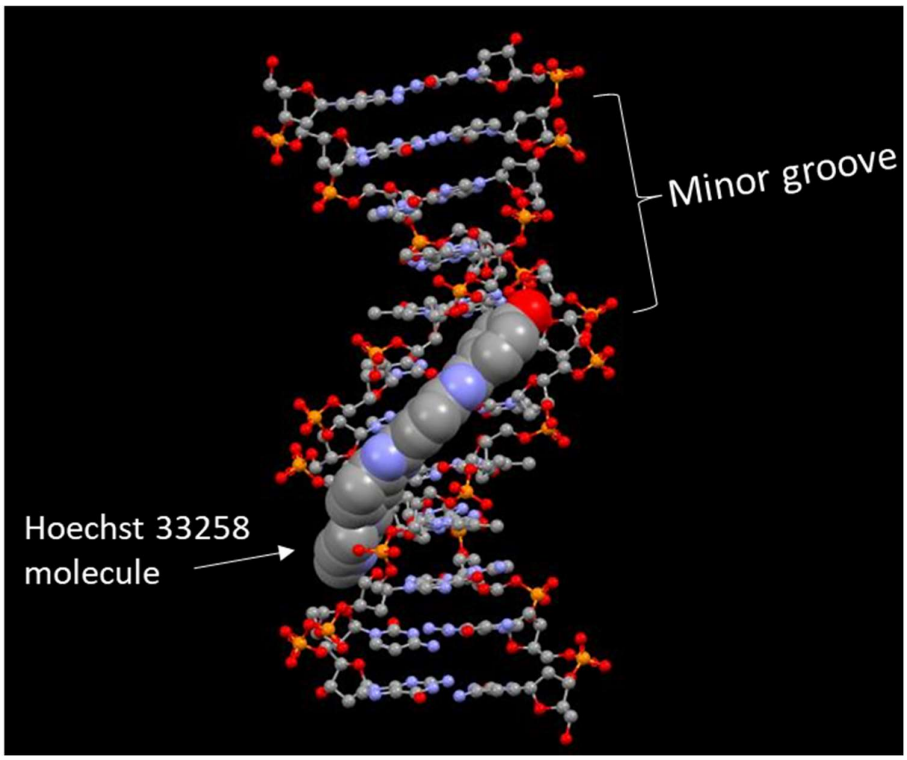


Figure 1.07: RCSB PDB 264D, the three-dimensional crystal structure of the minor groove a-tract DNA dodecamer d(CGCAAATTTGCG) complexed with Hoechst 33258 as an example of bound minor groove binding molecule. The image was generated using Mercury from the PDB file from the referenced publication.[211]

which reside within the central part of the DNA structure. From the grooves, external molecules can detect sequence from the arrangement of these groups, as well as interact with them, and are linked to the DNA's overall structure.[75] Proteins, peptides and drugs interact with the minor groove using these properties (Figure 1.07) and are involved in the key process such as DNA replication and transcription.[76–79]

Many molecules have shown binding to the minor groove, but several main characteristics are prominent amongst these. These are poly-aromatic systems with a degree of curvature in their structure, matching that of the minor groove, and possess one or more positive charges.[80] This cationic charge attracts the agents to A-T rich sequences which expose electronegative functional groups into the minor groove.[74] Hydrophobic and van der Waals also play a significant impact in the binding of these agents to the minor groove. Distamycin (Figure 1.08) is an example of a minor-groove binding polyamide which exhibits antibiotic and antiviral activity. This activity is linked to its ability to compete with proteins binding the minor groove and inhibit transcriptions

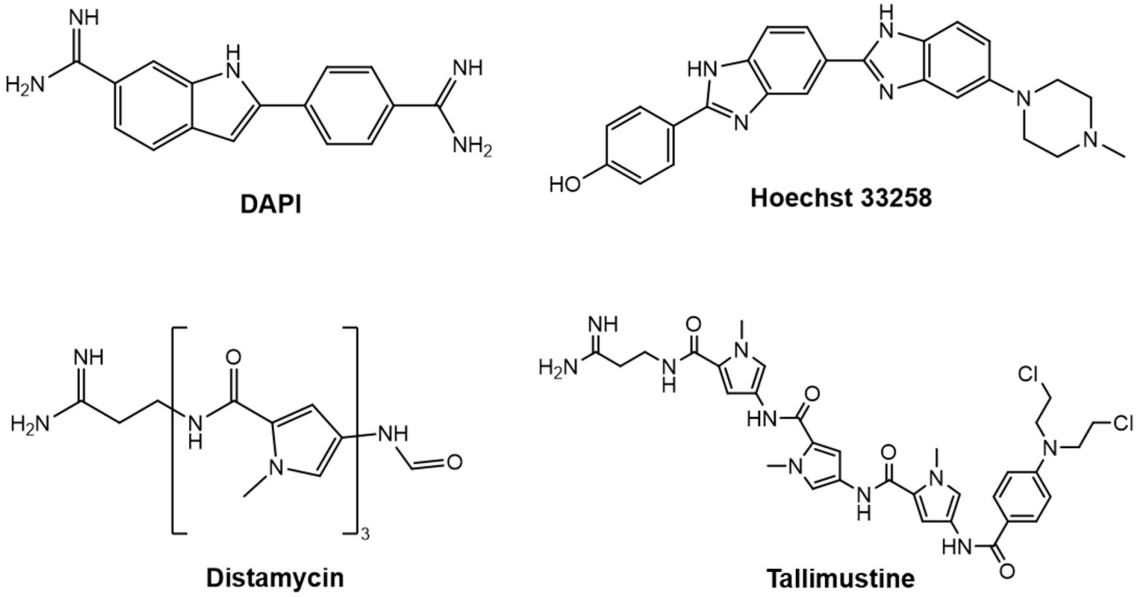


Figure 1.08: Shows the structures of the four minor groove binding agents DAPI (top left), Hoechst 33258 (top right), Distamycin (bottom left) and Tallimustine (bottom right).

factors which are vital for replications.[81] The inherent DNA binding properties of distamycin and ability to easily modify it have led to applications in cancer therapy despite showing no activity without modification.[82] Tallimustine (Figure 1.08) was a benzoyl mustard derivative of distamycin designed for anticancer activity, it is an alkylating agent which causes DNA damage with antineoplastic effects.[83] Other minor groove binding agents exist with applications outside of therapeutics. Hoechst 33258 and DAPI (Figure 1.08) are two DNA minor groove binding agents which serve as fluorescent dyes due to their ability to fluoresce upon binding to DNA.[84] These differ slightly to other minor groove binding drugs by containing an aryl group along its polyamide chain. These have applications in spectroscopic and microscopy studies of nucleic acid interactions and cellular imaging.[74,84,85]

The major groove is the larger of the two grooves with a width of 11.6 Å and a depth of 8.5 Å. It also presents a prominent binding site for proteins, peptides, and drug molecules due to the range of functional groups it offers, and greater room compared to that of the minor groove.[74] The functional groups exposed by the DNA bases allow different proteins to interact with the major groove at different [86–88] locations depending on the sequence, to perform different tasks (example Figure 1.09). Examples include proteins responsible for DNA replications and transcription, as well as proteins with zinc finger binding domains. Zinc fingers have been shown to interact specifically with the major groove through binding domains on the α-helix interacting with the functional groups in the major groove.[89]

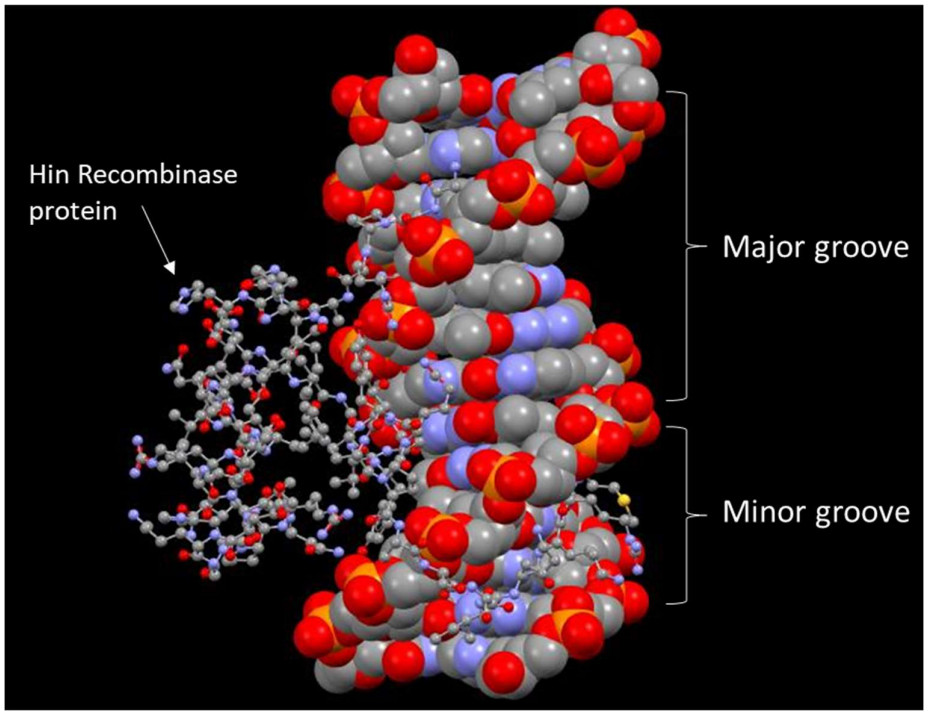


Figure 1.09: Shows RCSB PDB 1HCR Hin Recombinase protein Bound to the major groove of DNA through 3 α-helix groups, and the minor groove through two polypeptide chains an example of a bound major groove binding molecule. The image was generated using Mercury using the PDB file from the referenced publication.[212]

Some drugs function by interacting with the major groove of DNA (Figure 1.10). Pluramycins are a class of natural product derivative which bind the major groove of DNA with a modifiable structure to tailor its targeting and effects.[90] Pluramycins are biologically active through alkylating the N7 site on guanine bases with very high specificity and have shown activity against tumours and bacteria. Methyl green is also a major groove binding small molecule which, has been shown to inhibit the binding of RecA (a protein involved in DNA repair) to DNA by blocking of the major groove.[91] Methyl green has been a useful diagnostic tool to monitor triplex DNA formation by a decrease in fluorescence due to its exclusion from DNA.[92] Helical metallo-supramolecular cylinders have also demonstrated potent binding to the DNA major groove due to their cationic charge and π-stacking interactions.[93] This has resulted in

strong intramolecular DNA condensation which may be one mode of action for their potent biological effects.[20]

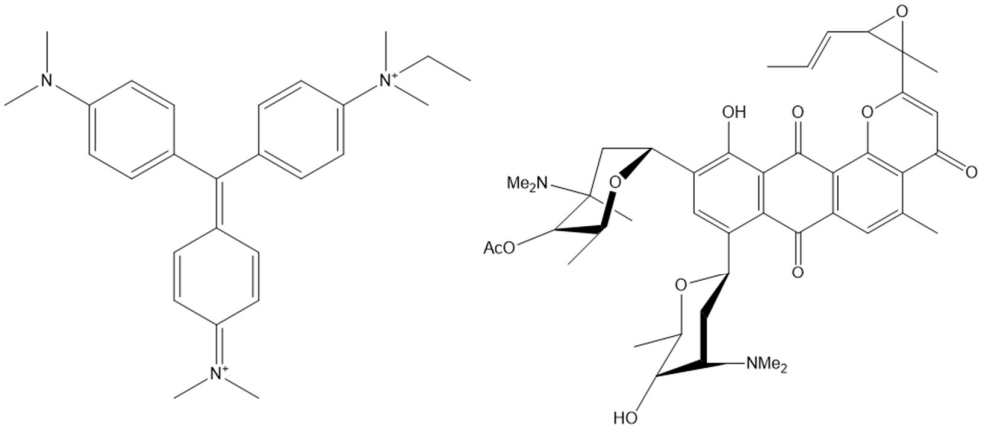


Figure 1.10: Shows the structure of Methyl green (left) and an example of the pluramycin derivative, Pluramycin A (right).

1.2.3.3: Intercalation in nucleic acids

Intercalation is a non-covalent interaction where a planar aromatic group of a molecule is inserted parallel between two adjacent base pairs in the DNA's central helix.[31] This occurs due to electrostatic attraction between the usually cationic molecule and the anionic phosphate backbone, hydrophobic interactions and π-stacking between the bases and the planar aromatic group (Figure 1.11). [31,94] When intercalation occurs, the bases must separate to create room for the intercalating group, this separation is of 3.4 Å and results in the overall lengthening and rigidifying of the DNA structure to an extent which is dependent on the intercalating molecule.[31] This increase in separation also gives rise to the neighbouring exclusion principle which states that the maximum number of intercalation sites is one per two base pairs. This is thought to be due to structural or conformational changes which occur due to an intercalated group which alters the adjacent site making it sterically unavailable.[95] DNA intercalators may have

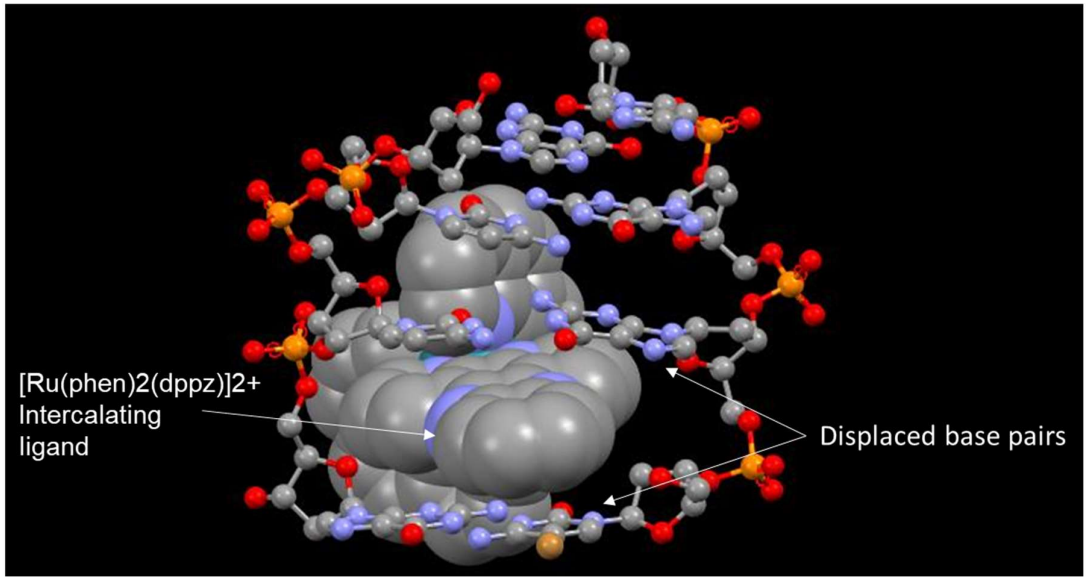


Figure 1.11: The RCSB PDB 5LFW of Lambda-[Ru(phen)$_2$(dppz)]$^{2+}$ bound to a short, substituted DNA sequence an example of a bound DNA intercalator. The image was generated using Mercury using the PDB file from the referenced publication.[213]

many different therapeutic modes of actions or diagnostic functions, however classical intercalators are thought to function via impairing DNA/RNA synthesis, topoisomerases 1 and 2 function, and by extension DNA damage.[96,97]

Daunorubicin (Figure 1.12) is an example of an intercalating therapeutic drug which is a toxic anthracycline aminoglycoside which is used to treat leukaemia.[98,99] Daunorubicin functions similarly to doxorubicin in that it intercalates between base pairs, inhibiting topoisomerase and polymerase activity and by extension causing single/double strand breaks and gene expression, resulting in cell wide damage and apoptosis.[31] Another common intercalator is ethidium bromide (Figure 1.12) which is commonly used in gel electrophoresis experiments as a DNA stain due to its fluorescent nature once intercalated.[100] It has also previously been used to treat parasitic infections in cattle which has been in contrast to its feared mutagenicity due to its intercalative nature.[101]

DNA Intercalators can also be attached to metal complexes which can confer additional functionality through enantiomeric binding, increased cationic charge, metal to ligand charge transfer spectroscopy and more.[102] With this in mind, $[Ru(bpy)_2(dppz)]^{2+}$, a diatonic mono-nuclear ruthenium complex was developed utilizing two bi-pyridine ancillary ligands and an intercalating phenazine group (Figure 1.12).[103] This complex shows no emissions whilst alone in solution, due to quenching of the fluorescence by water molecules in the solvation shell. However, upon

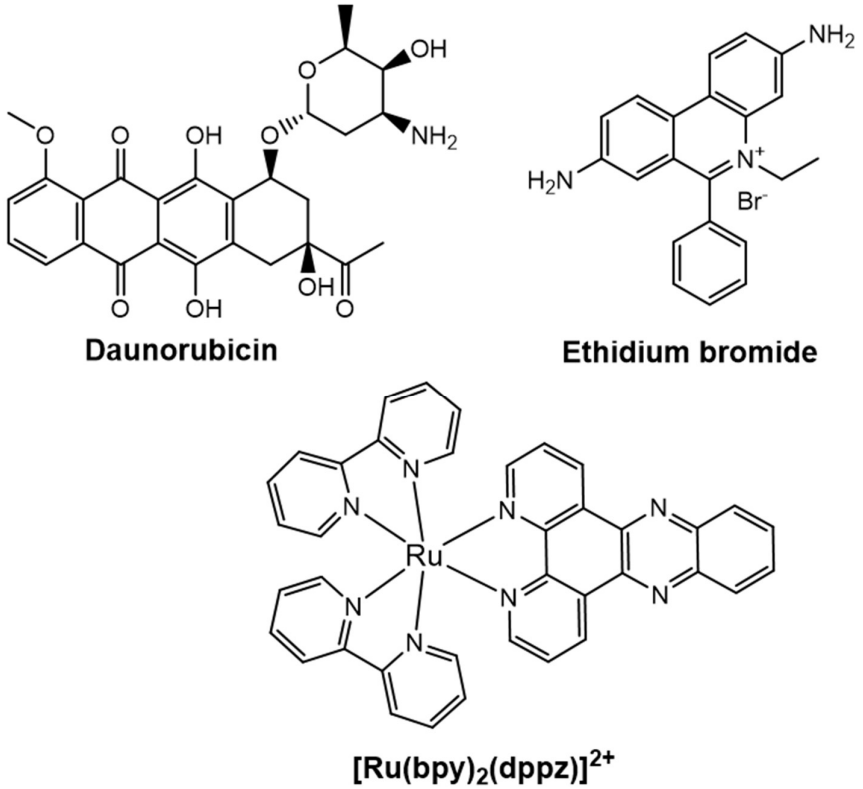


Figure 1.12: The structures of Daunorubicin (top left), Ethidium bromide (top right) and $[Ru(bpy)_2(dppz)]^{2+}$(bottom).

intercalation with DNA and exclusion of water due to the hydrophobic environment, emission dramatically increases, creating a light switch effect. This potent effect has led to the development of more polypyridyl metal complexes with varying metals and ligand structure with the hope of utilising and tailoring these photophysical properties for theragnostic applications.[104–106]

1.2.3.4: Binding nucleic acid junctions and bulges

DNA three-way junctions (3WJ's) are where three DNA molecules connect around a single branch point (Figure 1.13).[107] A related structure is formed transiently during replication as part of the replication fork where the junction adopts a Y-shaped structure.[108,109] 3WJ's are also important intermediate structures during mutagenesis, the Cre-Lox recombination pathway associated with genome editing, and in trinucleotide repeat expansions which are associated with degenerative neurological disease.[110–112] The biological importance of this secondary DNA structure highlights it as an attractive therapeutic target for the treatment of disease. The stabilising and halting of replication forks is associated with DNA damage and genomic instability due to the exposure of vulnerable SS's of DNA during the replication process and replication fork collapse with a resulting DS break.[113–115] Using replication as a therapeutic target allows for enhanced targeting and impact towards certain disease.



Figure 1.13: Crystal structure of a DNA three-way junction taken from the PDB 1EKW. Adapted from the referenced publication with permission.[124]

For instance, cancerous cells replicate at faster rates than healthy cells, and replication plays a crucial role during viral infection.[116–121]

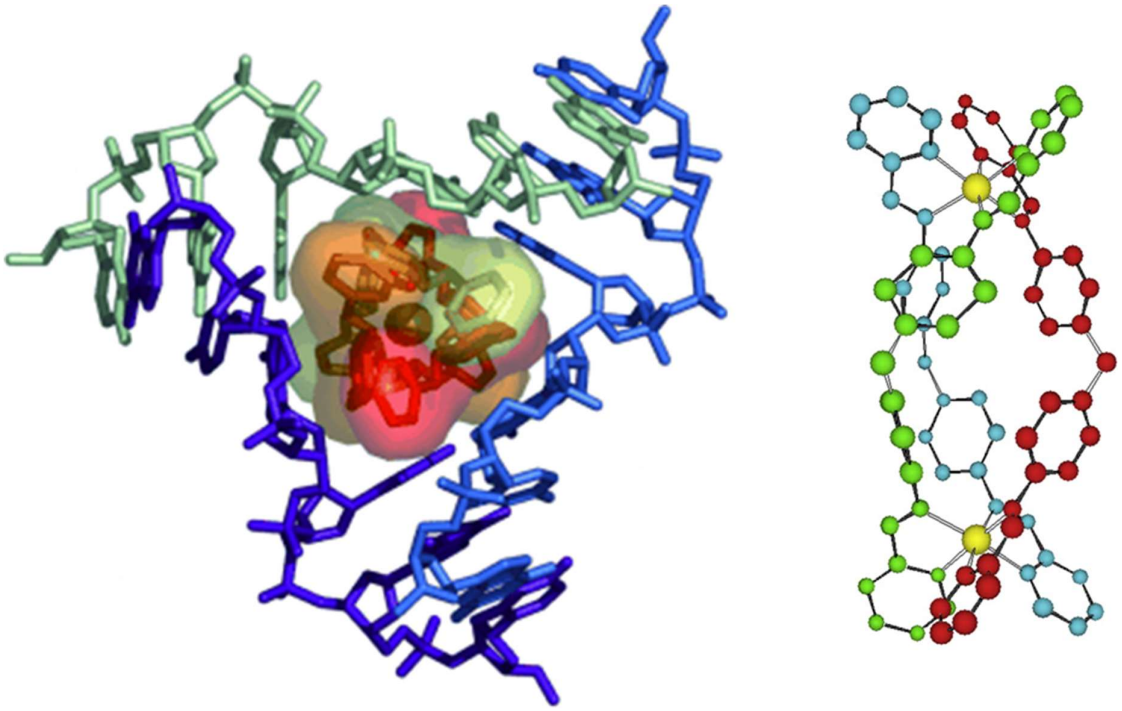


Figure 1.14: Shows the structure of the $[Fe_2(L)_3]^{4+}$cylinder in the branch point of the DNA three-way junction formed by the palindromic hexanucleotide 5'-d-(CGTACG)-3' (left) adapted from reference with permission.[19] And the structure of the metallo-supramolecular cylinder with ligands L as green, blue and red, and the metal centres as yellow, adapted from reference with permission.[20]

Several drug compounds have been developed which have shown binding, selectivity, and specificity for 3WJ's.[16] The first was the metallo-supramolecular cylinder (Figure 1.14).[19] This is a structure containing two metal centres linked by three organic tetradentate ligands in a helical arrangement with a tetra-cationic charge.[122] These cylinders have been crystalised with a DNA hexamer palindrome which formed a 3WJ with the cylinder at the central branch point where the bases were stacked onto the cylinders central di-aniline unit for favourable π-stacking interactions (Figure 1.14).[19,123] Since their initial development, new iterations of these metallo-supramolecular cylinders have been created with the aim of controlling this 3WJ binding for enhanced biological effect.[21]

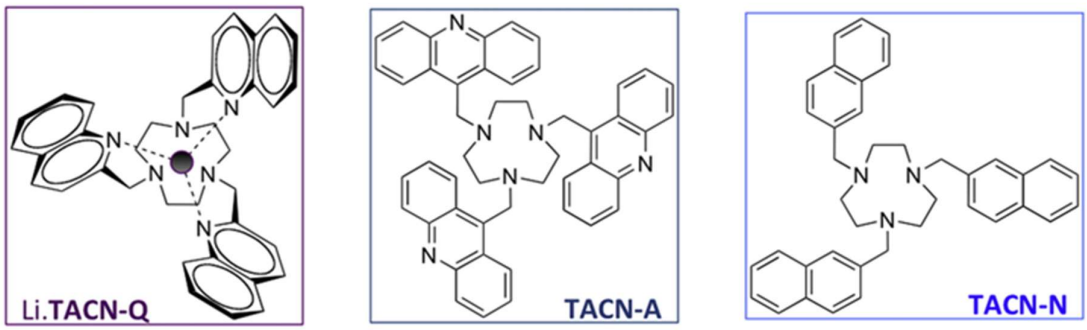


Figure 1.15: Shows the structures of the different TACN complexes used, TACN-Q containing a Li metal centre (left), TACN-A (middle), and TACN-N (right). This image was adapted from the referenced publication with permission.[124]

Triazacyclononane (TACN) complexes (Figure 1.15) have also been shown to bind to 3WJs, with the greatest selectivity achieved by functionalisation with quinoline ligands (TACN-Q).[124] TACN-Q demonstrated little interaction with double stranded (DS) DNA through the lack of a melting temperature shift or displacement and inability to displace a competitor from a DS structure. TACN-Q did however show a marked increase in 3WJ melting temperature of 4.9 °C as well as demonstrating displacement of a 3WJ binding competitor at 8 eq. This indicated remarkable binding and selectivity for DNA 3WJ's whilst showing reduced affinity for DS structures. This binding was attributed to the π-stacking of the quinoline groups to the bases in the junction cavity, combined with the helical conformation that it adopts, further enhancing this binding. The authors also remark on the potential for this complex to be a diagnostic agent for binding assays due to its tailorable fluorescence due to containing a modifiable metal centre, as well as its specificity for 3WJ's.

Cationic azacryptands (Figure 1.16) have also been developed with similar structural characteristics to the previously reported supramolecular azacryptands by Lehn et al. and the metallo-supramolecular cylinders.[122,125] They have shown potent 3WJ binding which has been attributed to their cationic charge, and flexible aromatic ligands in their

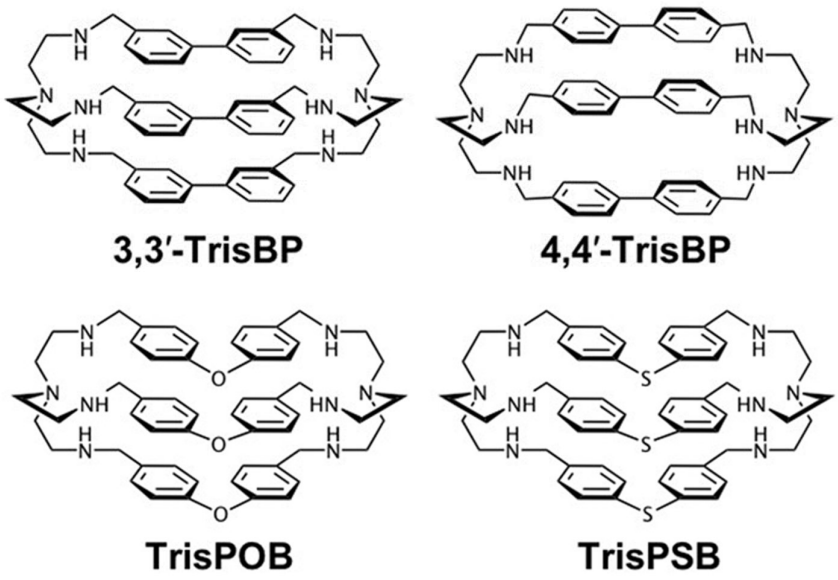


Figure 1.16: Shows the chemical structures of the four different cationic azacryptands which were studied with respect to their three-way junction binding. Adapted from reference with permission.[128]

core structure which allows them to optimise their π-stacking interactions.[126] Four azacryptand structures were investigated, revealing that those with two central aromatic rings were the most effective 3WJ binders and stabilisers, linking again to the metallo-supramolecular cylinders central di-aniline unit. This same class of azacryptands has also demonstrated G-quadruplex binding (which will be discussed further in the next section) and potent toxicity in cancer cell lines.[127,128] Their activity was linked to DNA damage in the form of DS breaks which is notably different to other quadruplex and junction binders.

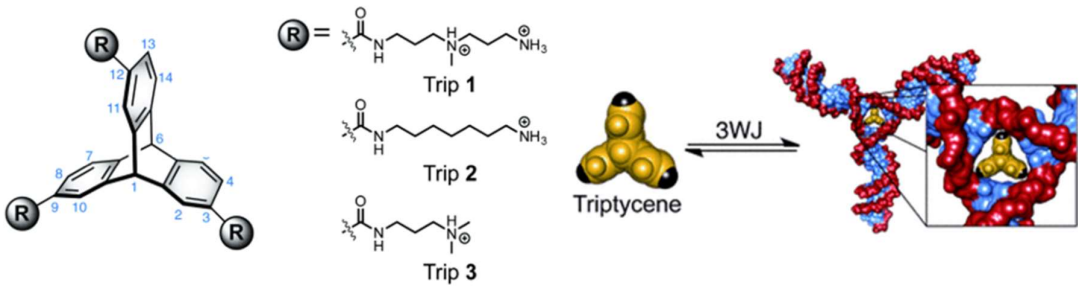


Figure 1.17: Shows the structure of the triptycene molecule (left) and the different R groups as well as its binding to the branch point of a DNA three-way junction (right). Modified from reference with permission.[129]

Another class of 3WJ binders was also developed, based on the small organic molecule triptycene with varying R group lengths (Figure 1.17) which impact on steric effects and charge.[129] These compounds demonstrated strong 3WJ binding and specificity, owing to their three-point symmetry and aromatic planar surfaces. Their specificity for 3WJ's over DS DNA was shown through little to no change in melting temperatures for DS DNA, while 3WJ's showed an increase of 18.5-28.5 °C depending on the R group. They also demonstrated toxicity against cisplatin resistant A2780 cells at 50 μM concentrations and above. These same structures have also shown binding to trinucleotide repeats associated with degenerative disease.[130] The authors suggest that this triptycene molecule may improve repair processes *in vivo* for a therapeutic effect or allow detailed study of the disease due to their fluorescent properties and selective binding.

DNA four-way junctions (4WJ's) are also known as Holliday junctions after their discoverer Robin Holliday in 1964 who proposed their existence in fungi for gene

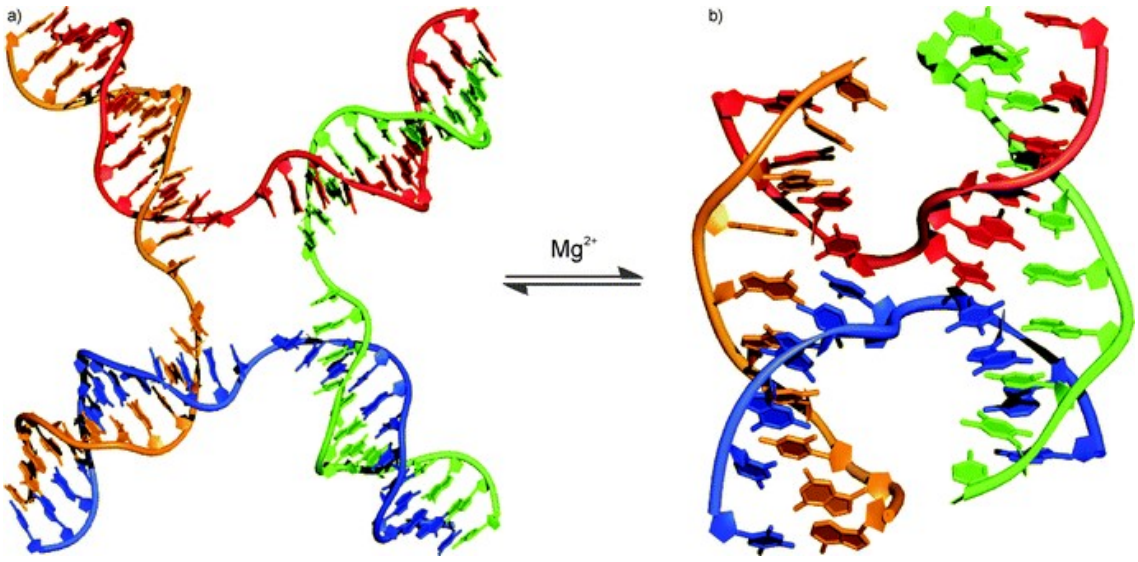


Figure 1.18: Shows the structure of the open form four-way junction (a) and stacked X conformation (b). Transition between these structures is caused by shielding of the anionic backbone by cations (Mg^{2+}). Taken from reference with permission.[214]

interconversion between homologous chromosomes.[131] They are now most known for their role in homologous recombination pathways which include genetic recombination during meiosis and DNA damage repair when double strand (DS) breaks have been detected.[132] Holliday junctions occur in one of two states: an open square planar conformation in the shape of a cross, (figure 1.18) which occurs when interacting with proteins,[133] as well as a closed X-stacked arrangement where the helix arms sit on top of one another, that usually occurs in high salt conditions when unbound. Due to the vital role 4WJ structures play in DNA repair and how this links into cell survival and avoidance of apoptosis, they have been suggested as therapeutic targets for cells where replication occurs quickly or with poor regulation.[134] Holliday junctions have also been shown to form in the telomeric region of human DNA where they are required for the alternative lengthening of telomeres (ALT) pathways.[135] A variety of structures have been made which have shown binding to DNA 4WJ's, including cyclic peptides with aromatic chain groups, mononuclear metal complexes and derivatives of acridine.[16] As well as this, peptides have also been shown to bind which inhibit distinct junction processing enzymes such as helicases and resolvases.[136]

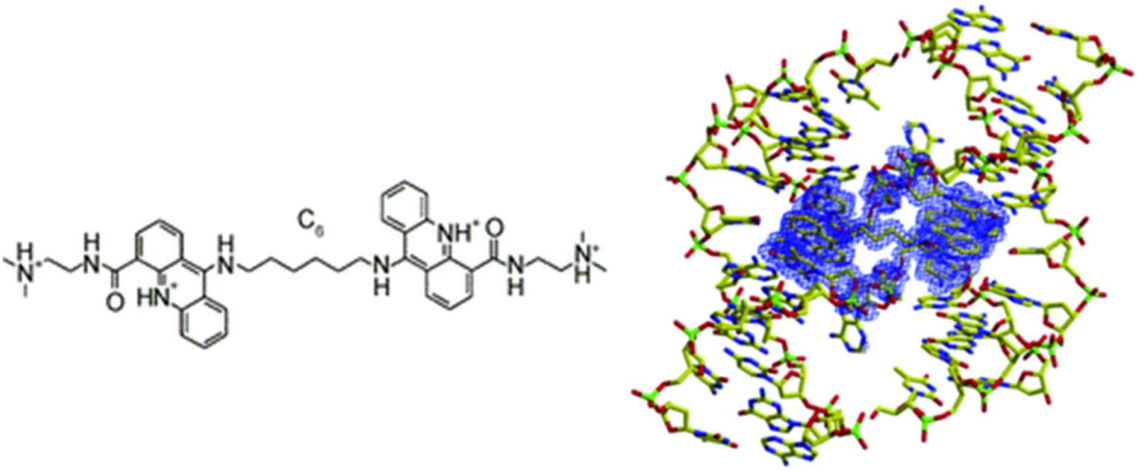


Figure 1.19: Shows the bis-acridine molecule C6 (left) and the electron density of the bis-acridine molecule bound to the junction crossover region. Adapted from reference with permission.[137]

A Bis-acridine C6 (C6 referring to carbons in the linker chain) has been shown to bridge across the branch point of an X-stacked confirmation 4WJ (Figure 1.19).[137] The binding was shown via a crystal structure with the crystalised bis-acridine lying across the branch point where the acridine moieties replace adenines of either side with the C6 chain lying in the minor groove. This binding was attributed to a cationic charge helping to overcome the anionic charges in the X-stacked arrangement as well as acridine stacking with the pyrimidine bases.

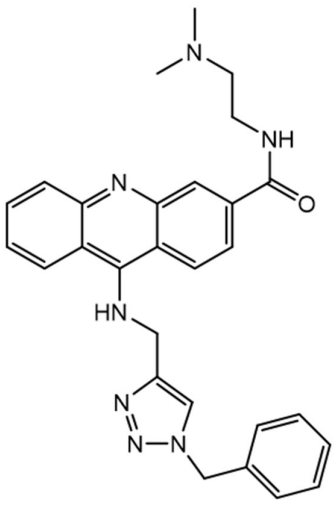


Figure 1.20: Shows the structure of the acridine molecule capable of forming 4WJ at low temperature.

A similar structure using just one acridine unit has been found to induce a 4WJ structure at low temperatures (Figure 1.20).[138] By "low temperatures" the authors make the point that annealing is not required for 4WJ formation, and instead, this molecule is able to promote 4WJ at room temperature, highlighting its applicability for living systems over previous candidate molecules. These acridines were also found modest preference for 4WJ structures over DS DNA and highlight the molecules potent 9.1 μM toxicity in cancer cell lines, highlighting it as a suitable candidate for further work. A mononuclear platinum complex $[Pt(H_2bapbpy)]^{2+}$ has been reported to form a 4WJ like arrangement from the palindromic hexanucleotide 5'-d(CGTACG)-3' in a crystal structure with (Figure 1.21).[139] This square planar platinum molecule forms a distorted arrangement due to steric clash of the hydrogens on the ligand structure, resulting in a somewhat helical geometry. The binding of this complex to a 4WJ is assigned to its cationic charge, helical structure, and π-stacking interactions. This compound showed nuclear localisation and strong anti-proliferative properties in

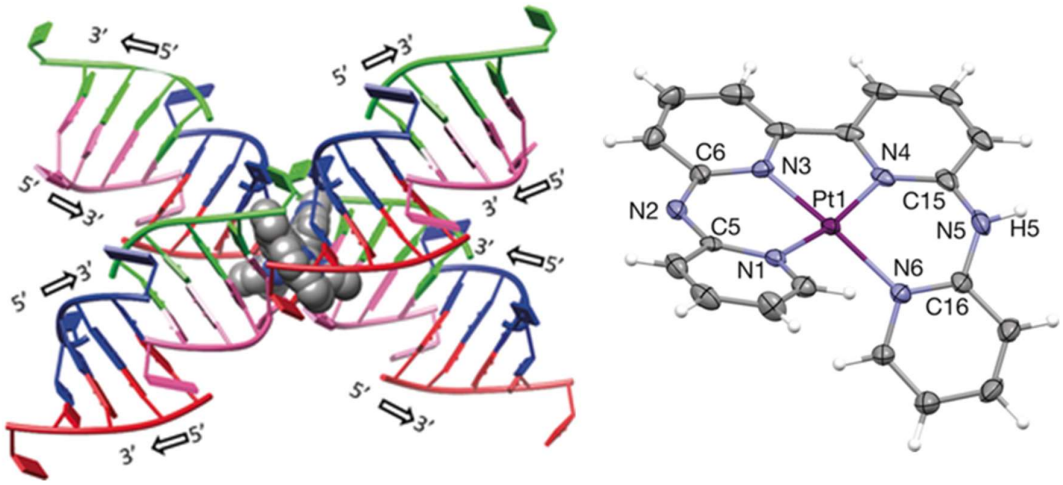


Figure 1.21: Shows the two of mono-nuclear platinum complex $[Pt(H_2bapbpy)]^{2+}$ forming an X stacked 4WJ structure with the hexanucleotide 5'-d(CGTACG)-3' (left). And the structure of the helical mono-nuclear platinum complex $[Pt(H_2bapbpy)]^{2+}$ (right). Adapted from reference with permission.[137]

cancer cell lines both resistant and non-resistant to cisplatin, suggesting a differing mode of action which could be linked to the structures 4WJ binding. However, insufficient studies have been carried out to confirm 4WJ binding in solution either *in vitro* or *in vivo*, leaving further work to assess 4WJ binding in solution.

Bulge structures in DNA and RNA (Figure 1.22) represent unique structural binding environments capable of being targeted which are involved with key biological processes. Bulges occur where unpaired nucleotides loop out from a double stranded region of DNA or RNA and can result in a bend or kink in the overall structure at that location.[140] These bulges are involved in protein recognition such as that of the Tat

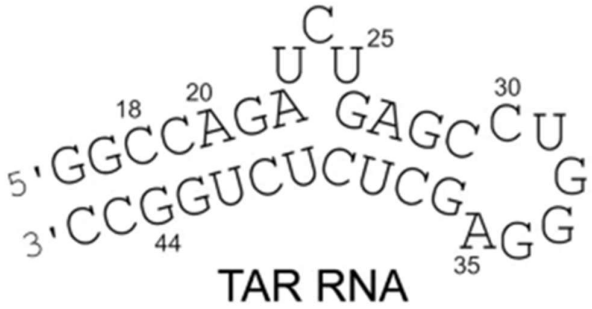


Figure 1.22: Shows the UCU bulge of the TAR RNA sequence as an example of a nucleic acid structure with a bulge. Adapted from the referenced publication with permission.[46]

protein binding to a three base bulge structure in the HIV-1 TAR RNA which is crucial for replication.[141] These bulges affect the structure of the surrounding DNA/RNA through the conformation they adopt, either external or intercalated. External results in exposed nucleic acids and a primarily conserved structure (unfavourable due to hydrophobic interactions) or an intercalated base and a kinked structure with increased major groove size.[142,143] This increased major groove size has a knock-on effect on protein recognition due to increased exposure of the bases which is vital for protein binding.[144] Metal ions and cationic small molecules have been shown to stabilise bulge sites by providing cationic charge to shield anionic phosphate charges under their sterically and electrostatically strained conditions.[144] This precedent, and their significance in diseases (viral infection, cancer, trinucleotide repeat expansion) make them a suitable and attractive therapeutic target.[141,145,146]

A helical spirocyclic complex (Figure 1.23) with a sugar residue and a wedge shape have been synthesised1 which demonstrate selective affinity for 2 base bulges.[147]

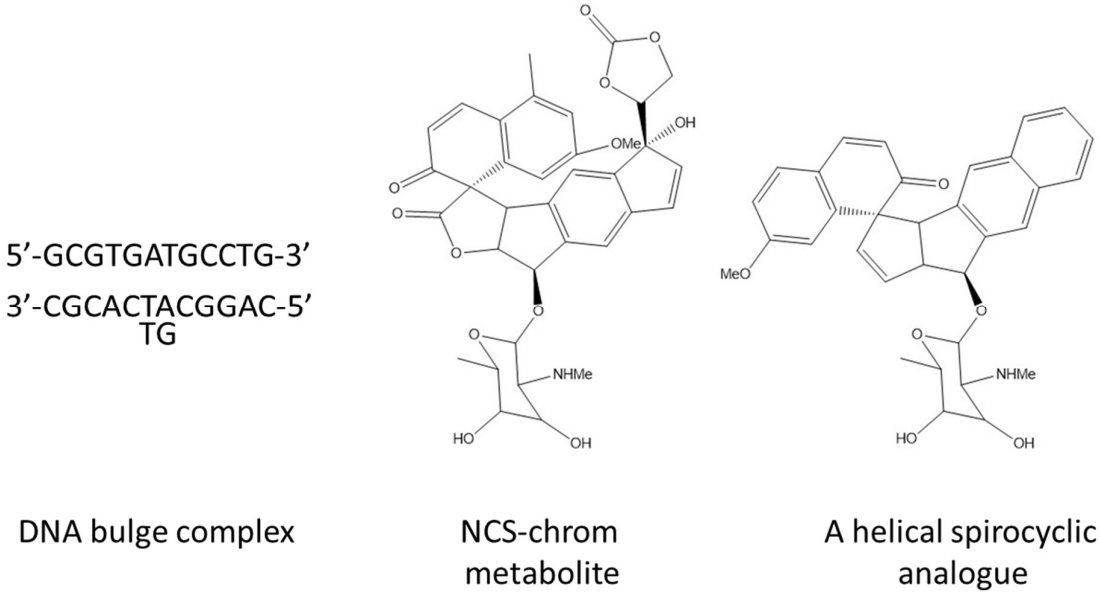


Figure 1.23: Shows the helical spirocyclic complex (right) its synthetic starting point (centre) and the DNA with a bulge with which it was evaluated. Taken from reference with permission.[147]

They have bound to the 2-base bulges, distorting the shape of the DNA in that region which has resulted in the inability for DNA polymerase to progress past that region. This slows down DNA synthesis and prevents other interactions at the bulge site due to its competitive occupancy.

The cationic nature of metallo-organic structures, combined with modifiable organic frameworks makes them ideal therapeutic candidates for the targeting of bulges. A tri-cationic rhodium complex $[Rh(bpy)_2(chrysi)]^{3+}$ (Figure 1.24) has been shown to selectively bind at locations with base mismatches and only a single base by extrusion of the mismatched base and insertion at that location.[148] This complex also exhibits photoactive properties where upon irradiation when bound to DNA, it induces a DS break at that location, causing severe DNA damage. The interaction of this complex with single base bulges was also investigated, yielding a similar binding affinity (T_m within 2 °C) for bulges as with mismatched base pairs, with a photocleavage effect only occurring at the bulge location. This selective affinity for unusual nucleic acid structures, coupled with the added functionality conveyed by the metallo-organic framework, presents strong therapeutic potential.

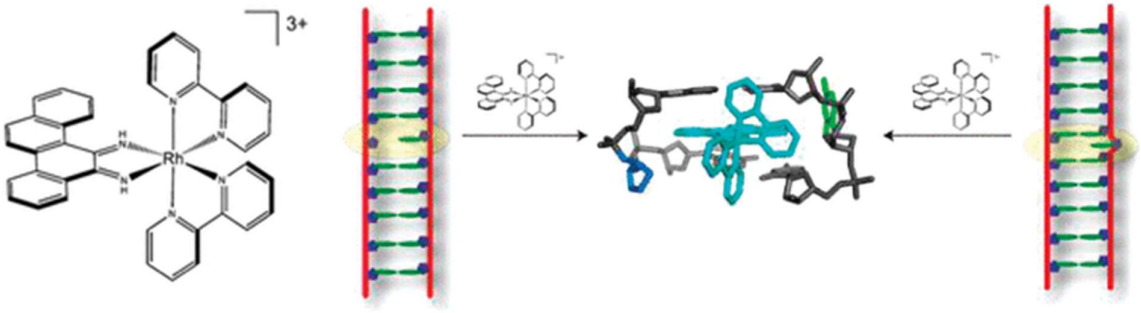


Figure 1.24: Shows the structure of $[Rh(bpy)_2(chrysi)]^{3+}$ (left) and its interactions between a-basic sites and bulges (right). Adapted from reference with permission.[148]

Metallo-supramolecular cylinders have also demonstrated binding to RNA bulge structures (Figure 1.25) and interference with viral replication and will be discussed

further in chapter 1.3.1. Briefly, they have been shown to bind the bulge associated with the binding of the TAT protein in the HIV-1 TAR RNA sequence and have consequently shown reduced viral replication.[46,80] Similarly, they have shown the ability to bind bulges in the 5' untranslated region of the SARS-CoV-2 genome and demonstrated inhibition of viral replication.[48]

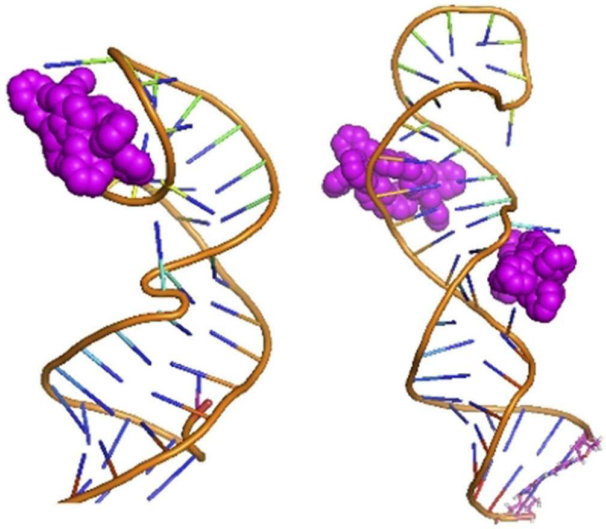


Figure 1.25: Shows binding of the cylinder structure to the stem loop and stem of SL3 RNA. Adapted from reference with permission.[48]

1.2.3.5: Binding nucleic acid G-quadruplexes

G-quadruplexes are nucleic acid structures comprised of two or more tetrads of guanine molecules bonding to one another through Hoogsteen base pairing (Figure 1.26).[149,150] The guanine tetrad structures are stabilised through π-stacking interactions with the tetrads above/below, through coordination to a central monovalent cation, usually K^+, but can also be Na^+ or Li^+. Molecular crowding conditions also stabilise G-quadruplex structures.[151] These structures can be comprised of 1-4 DNA molecules forming an intra or intermolecular G-quadruplex and in doing so, can form one of many topologies.

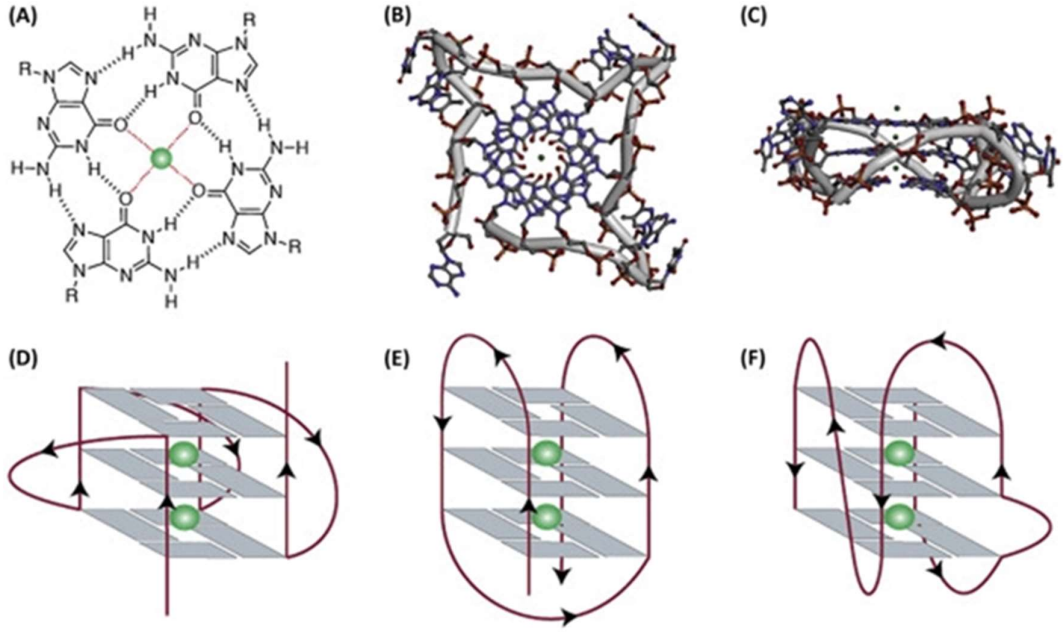


Figure 1.26: Schematic of G-quadruplex Hoogsteen base pairing (A). H-Telo sequence top down (B) and side view (C). Diagrams of unimolecular G-quadruplexes, parallel (D) anti-parallel (E) and hybrid bulge (F). Taken from reference with permission.[149]

G-quadruplexes appear to adopt several functions in living systems, highlighting their importance in several key biological processes. They have been found to be prevalent in the telomeric regions of DNA which are associated with ageing, lifespan, and controlled cell death. Telomeres also play a key role in cancer, where telomerase extends the telomeres, effectively immortalising cancer cells.[152] For this reason, G quadruplexes have become a target in cancer therapy, where complexes have been made which interact with the telomeres through G4 binding, with the aim of interfering with telomere maintenance. This results in increased telomere damage and dysregulation, changes in oncogene expression and increased genomic instability, resulting in anti-cancer properties.[152,153] G-quadruplexes are also associated with regulating transcription, with a link between their presence and reduced mRNA levels, linking them to an ability to control transcription machinery.[154] G-quadruplexes have also been found to promote certain epigenetic changes in DNA as well as have their

stability impacted by specific methylation positions, indicating a deep and complex relationship with important biological functions such as gene expression.[155,156]

Due to the increasingly better understood biological significance of G-quadruplexes, several molecules have been developed which specifically recognise them. Typically, these compounds are large and planar to span the G-tetrad size, aromatic to engage in π-stacking interaction, and have a cationic charge for electrostatic attraction to the dense anionic charge on the quadruplexes exterior.[149,157]

Pyridostatin (Figure 1.27) is an example of an organic complex which exhibits strong selective binding for G-quadruplexes.[158] The binding of these complexes to G-quadruplexes has been ascribed to its rigid aromatics linked by flexible amide bonds allows for adaptive binding of aliphatic amine side chains exhibiting hydrogen bonding and electrostatic interactions, acting like grippers to the G-quadruplexes grooves. The authors noted the cationic groups should be specifically located to optimise G-

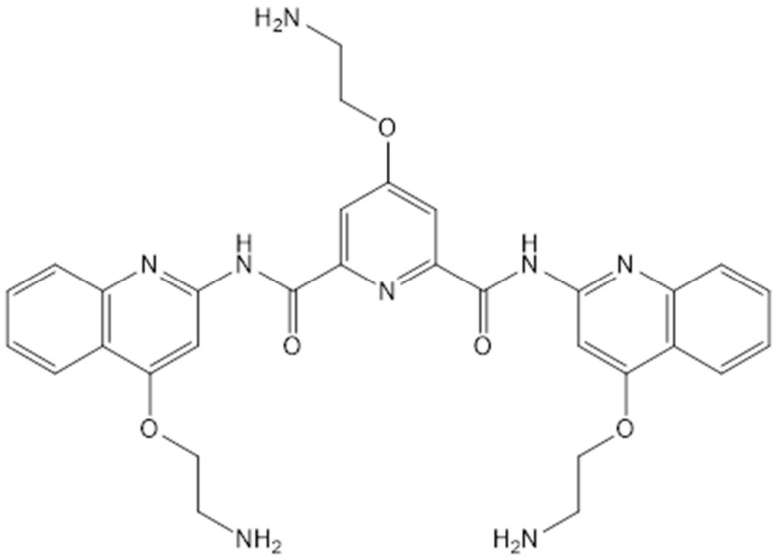


Figure 1.27: The chemical structure of pyridostatin.

quadruplex binding over alternative structures. This ligand has shown activity against tumours with deficient DNA repair systems through inducing DS breaks which the cell

is unable to repair due to the lack of BRCA1/2 or PARP proteins whilst being considerably less damaging to healthy cell that maintain these.[159]

Metal complexes with G-quadruplex targeting specificity have also been developed which are composed of a similar organic framework to pyridostatin which chelates a central metal atom.[160] These are called salphen complexes (Figure 1.28) and have been shown to chelate platinum, copper, vanadium, and nickel with varying biological/biophysical effects. The best binding was seen from the square planar salphen complexes with Ni, Pt and Cu due to their planar arrangements. However, the square pyramidal V salphen complex showed poorer G-quadruplex binding, but

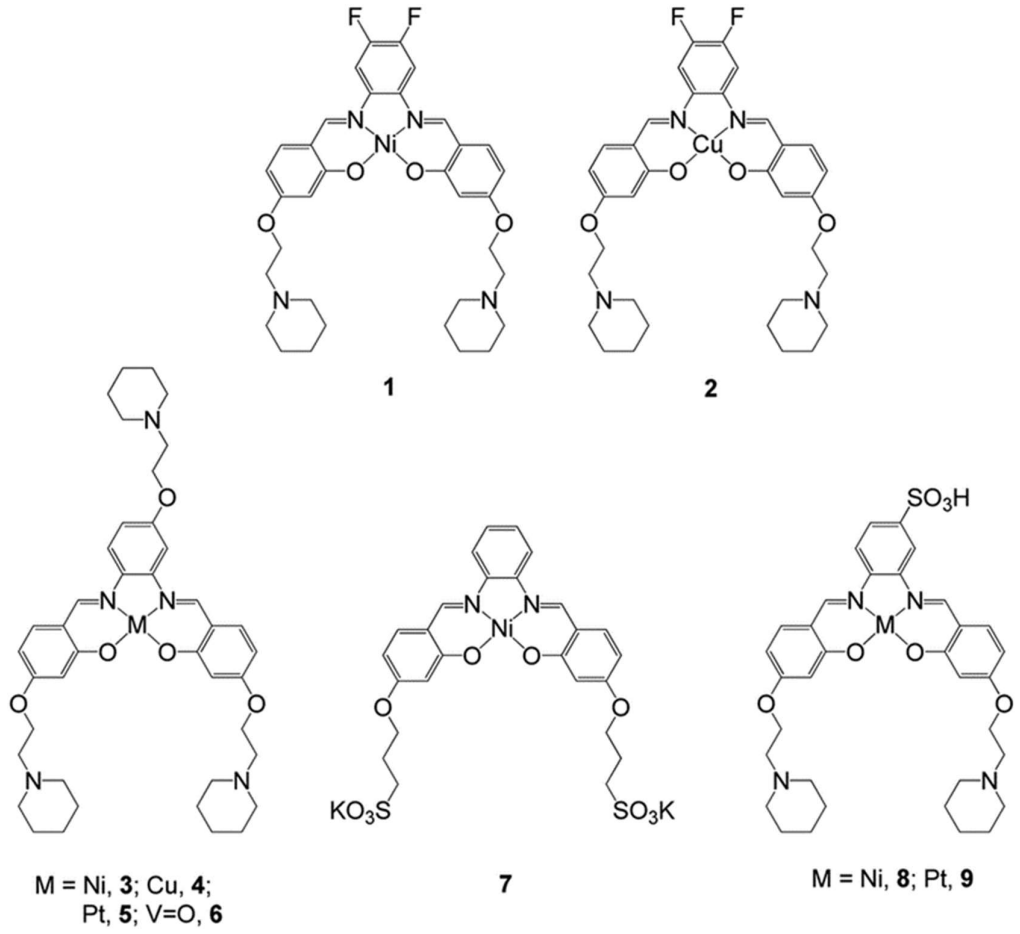


Figure 1.28: Shows the different structures of the G-quadruplex binding metal-salphen complexes. Taken from reference with permission.[160]

greater specificity for it over DS DNA, which the authors ascribed to the axial ligand preventing DS DNA intercalation. It was also noted that the Pt complex was emissive and showed nuclear uptake, emphasising its relevance for further investigation and further design.

1.2.3.6: Binding i-motifs

The intercalated-motif (i-motif) is a four stranded DNA structure where cytosine to cytosine Hoogsteen base pairs, in which one C is protonated at the N3 site, form a helical structure (Figure 1.29).[161] The bases are uniquely intercalated between one another with 1, 3 or 4 parallel strands, spaced in an anti-parallel manner.[162] These structures are stabilised by π-stacking interactions between the cytosine base pairs and hydrogen bonding between the sugars of antiparallel strands. This produces two large major grooves and two very narrow minor grooves on the exterior of the structure. Because i-motifs need a protonated cytosine residue to form, it was thought these structures need acidic conditions and as such their biological relevancy was questioned. However, they have since been detected in the nuclei of human cells and

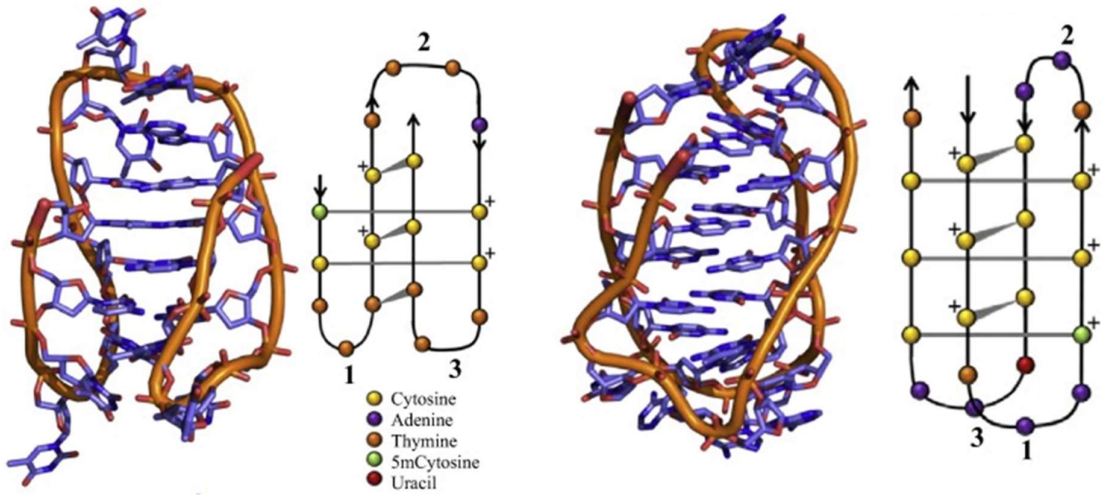


Figure 1.29: Shows the NMR structures and schematic structures of two different unimolecular i-motifs DNA's. Adapted from reference with permission.[166]

at neutral pH, resulting in increased biological interest in this structure.[163–167] Given their cytosine rich sequences, their complementary strand must be guanine rich, which is associated with forming G-quadruplexes, indicating the two may be interlinked. It has been shown that both i-motifs and G-quadruplexes do not exist simultaneously at the same location, and that the induction and stabilisation of one, destabilises the other.[168,169] it was proposed that this is due to steric hinderance and that it allows added control and functionality in biological processes. i-Motif function is becoming better understood due to studies into their locations in genomes and their spaciotemporal mapping. They occur prominently in the G1 phase of the cell cycle, associated with translation and replication, as well as at gene promoter regions and interact with poly-c binding proteins.[164,170,171]

Several structures have been found and developed which show affinity for and binding to i-motif DNA. iMab is an antibody fragment which has been identified and used in studies to assess the spatiotemporal distribution of i-motif structure *in vivo*.[164] This has led to greater understanding of where and when they occur during the cell life cycle by using immunofluorescent imaging. The sugar containing natural product baicalin (Figure 1.30) has also been identified as an i-motif binder through in-silico screening, FRET-melting and fluorescent intercalator displacement assays.[172] These molecules serve as synthetic precursors for future probes in the investigation of i-motif structures *in vivo*. An aminated derivative of the antibiotic heliomycin (Figure 1.30) has also been developed with selective affinity for i-motifs over DS DNA and G-quadruplexes, offering another potential scaffold for the development of i-motif binding complexes.[173] The cationic porphyrin TMPyP4 (Figure 1.30) was one of the first complexes which had shown binding to i-motifs.[174] NMR revealed that TMPyP4 bound externally at the top

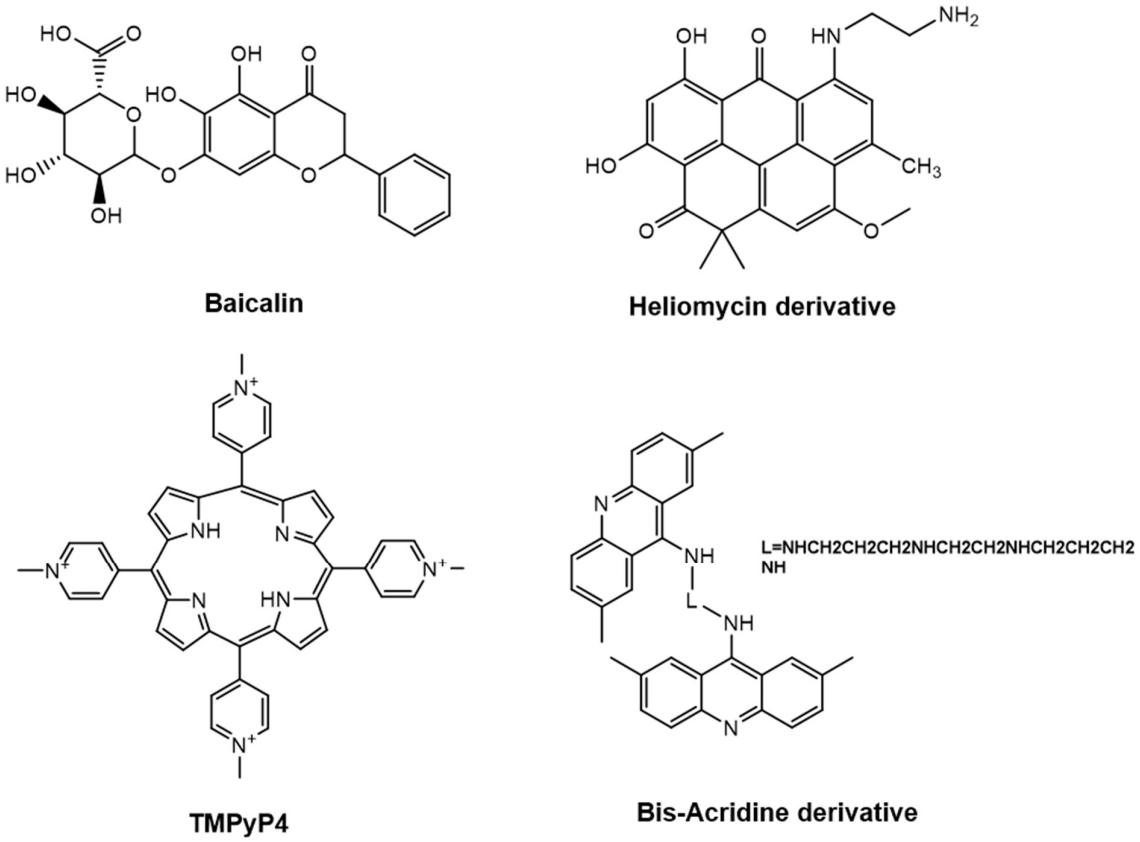


Figure 1.30: Shows the structures of the i-motif binding ligand Baicalin (top left), a heliomycin derivative (top right), TMPyP4 (bottom left) and a bis-acridine derivative (bottom right).

and bottom of the i-motif structure, however this only had a minor impact on the melting temperature of the structure (<20 °C). Alongside this, TMPyP4 also showed considerably more affinity for DS and G-quadruplex DNA, highlighting it's lack of specificity and comparably poor i-motif binding. A bis-acridine derivative (Figure 1.30) with dual targeting for both G-quadruplex and i-motif DNA has shown potent activity against cancer cells.[175] It demonstrates a poorer affinity for DS DNA and strong anti-proliferative effects, reduction in transcription and gene expression, and eventual apoptosis. Two more i-motif interacting compounds were identified from the NCI diversity library, IMC-48 and IMC-76 (Figure 1.31), the former an i-motif stabilising ligand and the later a destabilising ligand through stabilising of a corresponding

hairpin.[176] The presence of these molecules was shown to impact the stability of the corresponding BCL2 i-motif and hairpin structures, consequently regulating gene expression from this region. This demonstrates the power of such structures *in vivo*, and their therapeutic potential.

Comparable to previously discussed non-canonical DNA structures, few metal

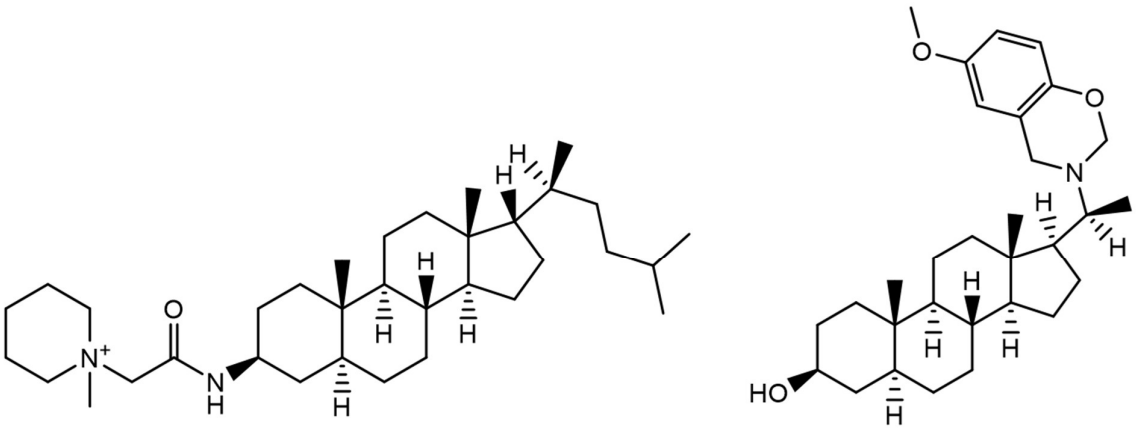
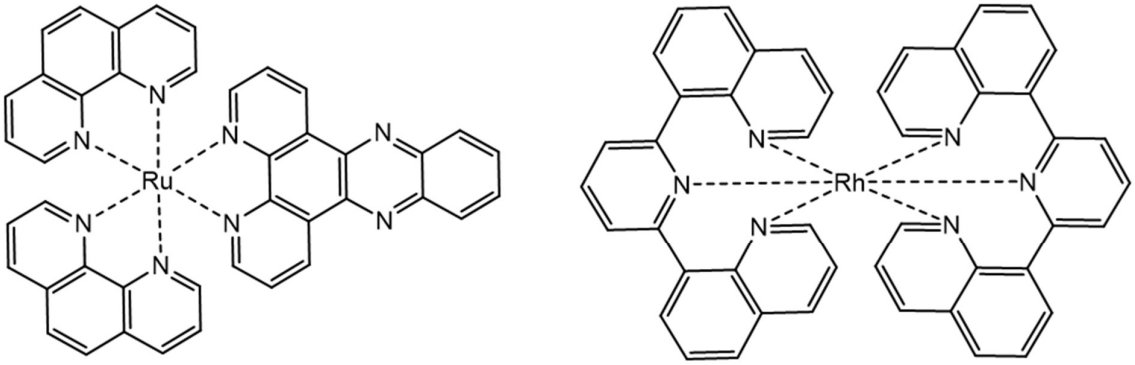


Figure 1.31: Shows the chemical structures of IMC-48 (left) and IMC-76 (right).

complexes have been identified which demonstrate affinity and binding for i-motifs. The DS DNA intercalator $[Ru(phen)_2(dppz)]^{2+}$ (Figure 1.32) has been identified as a metal complex that can bind to i-motif loops.[177] It was noted that the size of the loop was important for the i-motifs binding by $[Ru(phen)_2(dppz)]^{2+}$, with smaller loop lengths not resulting in stabilization. $[Ru(bqp)_2]^{2+}$ (Figure 1.32) is a complex which has been developed as a molecular probs for the detection of i-motifs in complex samples.[178] The authors note there are several isomers of this complex, all of which possess differing photophysical properties and sensitivities towards DNA. The Λ-cis enantiomer shows selective fluorescence in the present of i-motif DNA, and through lifetime studies can reveal i-motif presence from a solution of different DNA structures. They also

highlight that the fluorescence of this complex is associated with DNA binding rather than solvent exclusion. This suggests previously non-emissive complexes could in fact hold DNA structure dependant fluorescence, enabling them to act as fluorescent probes for certain DNA structures.



$[Ru(phen)_2(dppz)]^{2+}$ $[Ru(bqp)_2]^{2+}$

Figure 1.32: Shows the structures of $[Ru(phen)_2(dppz)]^{2+}$(left) and $[Ru(bqp)_2]^{2+}$(right).

1.2.4: Summary of nucleic acid structures

In 1.2.3 I have summarised the broader field of nucleic acid structures and their links to biological functions. Their individual associations with disease have also been noted, highlighting their potential as a therapeutic or diagnostic drug target. Compounds that have shown selective binding to these structures have been discussed to highlight a link between what allows them to exhibit their selective binding, and their structure. These insights lay the groundwork for understanding how to develop new complexes

that share this selective targeting but can also be modified to have additional therapeutic or diagnostic effects.

A concurrent theme is that of avoiding covalent adducts between therapeutics and their biological targets. Instead, supramolecular interactions are favoured because of the variety of intermolecular interactions they possess allowing increased specificity and reduced peripheral binding. Supramolecular metal complexes that bind DNA structures have also been highlighted as they offer unique benefits over their purely organic counterparts. This comes in the form of adopting unique geometries, required for interacting with specific structures, along with an increased size, cationic charge and desirable photophysical properties. Non-canonical DNA structures such as those discussed in section 1.2, offer unique potential as therapeutic targets as they could offer increased resistance to mutation as they are the primary component of a biological process.

From here I will discuss properties of the supramolecular metal complexes I will be using in this thesis. I will also discuss the broader field of metallo-supramolecular complexes to highlight links between their structures and function, as well as the additional methods they use to achieve increased functionality. This will provide a background to this thesis' work, and a scaffold from which to build from.

1.3: Metallo-supramolecular complexes: towards nucleic acid recognition

Supramolecular interactions are vital for biological interactions, allowing for varied and specific reversible binding of molecules to one another for important biological processes.[34] These interactions include π-stacking interactions, van der Waals, hydrophobicity, electrostatics, hydrogen bonding, host guest interactions, and metal-ligand coordination.[31] Combining organic structures with metal centres provides additional characteristics which are otherwise difficult or impossible to obtain, such as helicity.[122] Metal centres allow for unique photophysical properties, enhanced electrostatics, redox reactions, and unique structural geometries dictated by the metal centre.[102] These additional structural properties allow for strong and specific binding to occur such as that between zinc finger motifs and B-DNA.[89,179,180] Zn^{2+} ions are incorporated in a tetrahedral arrangement inside this protein motif, holding the secondary structure of the cysteine and histidine amino acids together.[89,179,180] This enables strong and specific recognition of DNA structures at key locations such as gene promoter regions, key for transcription and replication.[180] Many metallo-supramolecular complexes have been developed with the aim of exploiting the same metal and supramolecular interactions to achieve therapeutic and diagnostic function, some of which have been discussed in section 1.2 and more will be discussed in section 1.3.

1.3.1: Metallo-supramolecular cylinders

Metallo-supramolecular cylinders are complexes typically composed of three ligands and two metal centres with a helical structure and a tetra-cationic charge as previously

mentioned in section 1.2.3.4 (Figure 1.14).[122] The cylinders are approximately 2 nm is length, 1 nm in width and are synthesised in a one pot synthesis by mixing 2 eq of the metal salt and 3 eq of the ligand, followed by counterion conversion, filtration, and precipitation for purification. $[Fe_2(L)_3]^{4+}\bullet 4X^-$ (X=anion) was the first cylinder synthesised,[122] where the chloride as counterion (X) could be one of several others to affect solubility in different solvents - chloride is generally chosen as it affords the complex solubility in aqueous solutions.[122] Modified ligands and different metal centres can also be used, allowing for more complex organic architectures or different properties such as stability, metallo-ligand charge transfer absorption, and fluorescence.[104] Nickel centres offer increased stability over iron; however, their paramagnetic nature makes NMR studies more challenging.[122] All these cylinder complexes also adopt either a P or M helical configuration and he two enantiomers can be separated from one another using the chiral stationary phase cellulose and a sodium chloride solution.[181,182]

The $[Fe_2(L)_3]^{4+}$ cylinder demonstrated binding to the major groove of B-DNA (Figure 1.33).[93] Circular dichroism (CD) revealed an induced CD signal and maintenance of the DNA's signal, indicating binding and a binding site size of around 1:5 base pairs.[93] Linear dichroism (LD) revealed and induced CD signal, implying a consistent binding mode and condensation of the DNA.[93] Additionally, atomic force microscopy (AFM) revealed condensation of and kinks in the DNA structure. NMR and molecular dynamics studies also supported the binding of the cylinder to the major groove.[183] The different enantiomers, P and M (determined by the winding of the organic ligand around the 2 metal centres), also demonstrated different binding, with the M enantiomer preferring the major groove and the P enantiomer preferring the minor groove.[184,185]

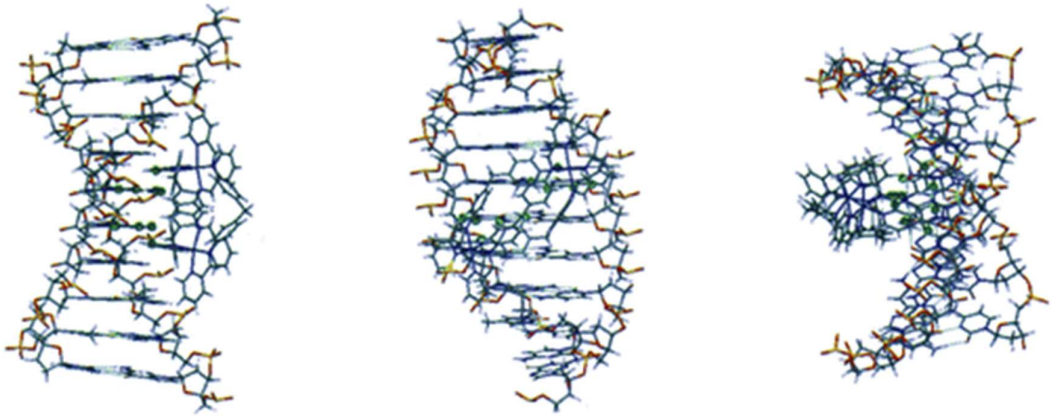


Figure 1.33: Shows the structure of $[Fe_2L_3]^{4+}$ docked into the major groove of $[5'\text{-}d(GACGGCCGTC)]_2$ as shown by NMR experiments. Taken from reference with permission.[93]

A metallo-supramolecular cylinder was also crystalised in the central branch point of a DNA 3WJ (Figure 1.14), presenting a near perfect fit in the structures central cavity, supported by π-stacking interactions between the ligands central aromatic rings and the DNA bases.[19] Electrophoretic and NMR studies confirmed this mode of action in solution, supporting this unprecedented DNA binding.[123,186] Since then, a cylinder has also been crystalised in the branchpoint of an RNA junction, further expanding the biological possibilities of this complexes mode of action *in vivo*.[187] This could mean the cylinder has alternative modes of action *in vivo*, associated with impaired replication and prevention of DNA transaction, as already shown by $[Ru_2(L)_3]^{4+}$.[188] Ruthenium cylinders offer the greatest stability along with luminescence allowing for photophysical applications, however, yields of the Ru complexes are low, affecting the extent of studies that can be performed.[189]

As mentioned previously, metallo-supramolecular cylinders have also shown binding to nucleic acid bulges and loops which share features reminiscent of DNA junctions.[47] An example is the cylinder binding the three-base bulge in TAR RNA, preventing the binding of the viral trans activator protein which is essential for viral replication (Figure

1.22).[46] This was shown via gel shift assays, revealing a decreasing proportion of Tat/TAR complex on additions of cylinder, as well as footprinting gels revealing reduced cleavage at the bulge site due to protection by the bound cylinder. This effect was then explored by an investigation of HIV-1 viral replication *in cellulo*.[80] This showed nickel and ruthenium cylinders were effective at inhibiting HIV-1 viral replication *in cellulo* at concentrations where cell viability was not significantly impacted. Activity against SARS-CoV-2 was also established by binding of the cylinder to bulge structure in the 5' untranslated region of its genome.[48] Binding targets were established by SHAPE analysis and molecular dynamics, revealing bulge and junction binding (Figure 1.25). inhibition of viral replication was determined by the percentage of cells expressing spike proteins, with Ru and Ni cylinders showing anti proliferative effects at concentrations which had minimal effect on host cell viability. Studies of cylinders against cancer cell lines have also been carried out, revealing toxicities around 2-5 times lower than cisplatin and potent cytostatic effects.[20,189] Most importantly, this toxicity was not associated with genotoxicity like that of cisplatin, meaning an alternative, non-covalent, mechanism of action is achieved, avoiding the adverse effects associated with non-specific covalent binding.

The unprecedented nucleic acid binding and structural modifiability of these cylinder has led to the development of many different variations on this cylinder structure to achieve functions *in vivo*.[20,21,46,122] One mechanism to exploit is the ability for certain cylinders to cleave DNA under specific conditions. $[Ru_2(L)_3]^{4+}$ has demonstrated photocleavage of DNA upon irradiation with wavelengths of light of around 400-700 nm (580 maxima).[190] This may provide an excellent scaffold for the development of a photosensitising agent, allowing control of the cylinders biological activity through the

application of an external light source, permitting incredible specificity. A copper (I) cylinder comprising of two ligands with two ethyl groups on each of the ligands central phenyl units and two Cu(I) metal centres (Figure 1.34 top) have also shown DNA binding and cleavage.[191] The cylinder has weaker DNA binding compared to other tetra-cationic cylinders, highlighting the importance of electrostatics in DNA binding. DNA cleavage was shown to be because of exposure to reactive oxygen species, in this case, H_2O_2, resulting in double strand breaks as shown by AFM.[191]

The effects of changing the central bridging ligand atom have also been investigated. Replacing CH_2 with S or O (Figure 1.34 middle and bottom) revealed little to no change on the DNA binding of the cylinder, further highlighting the important of supramolecular interactions such as π-stacking and electrostatics.[192] This modification did, however, affect thermal stability, noting O reduced this and S increased this. Aside from this, this

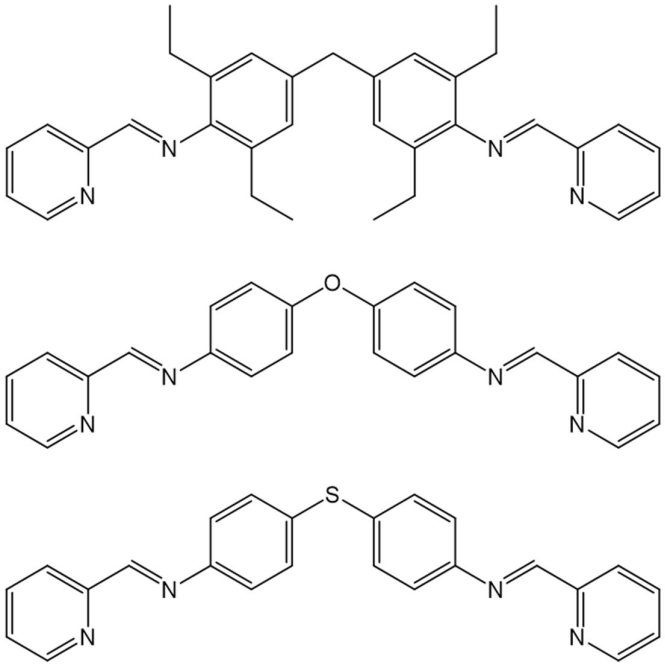


Figure 1.34: Shows the different ligand structures synthesised and investigated. The top ligand is used in the di-nuclear Cu(I) cylinder with 2 ligands. The middle ligand is the structure of the ligand where the central CH_2 is replaced with O. The bottom ligand is the structure of the ligand where the central CH_2 is replaced with S.

modification may allow for added functionality and new biological mechanisms of action.

Amino acids and peptides have also been attached to the ends of these cylinders with the aim of conferring addition properties. Attaching arginine residues to the ends of the cylinder has been shown to confer near complete control over the synthesis of specific enantiomers depending on the use of L or D arginine (Figure 1.35 bottom).[193] This also conferred increased charge located on the residues, improving DNA binding, as well as increasing the toxicity compared to cylinders with the original ligand L. The tripeptide glycine-glycine-serine has also been attached to the end of the cylinders (Figure 1.35 top and middle) ligand with the aim of conferring sequence specificity dependant on the peptide.[194] The tripeptide resulted in little change in the DNA binding and other

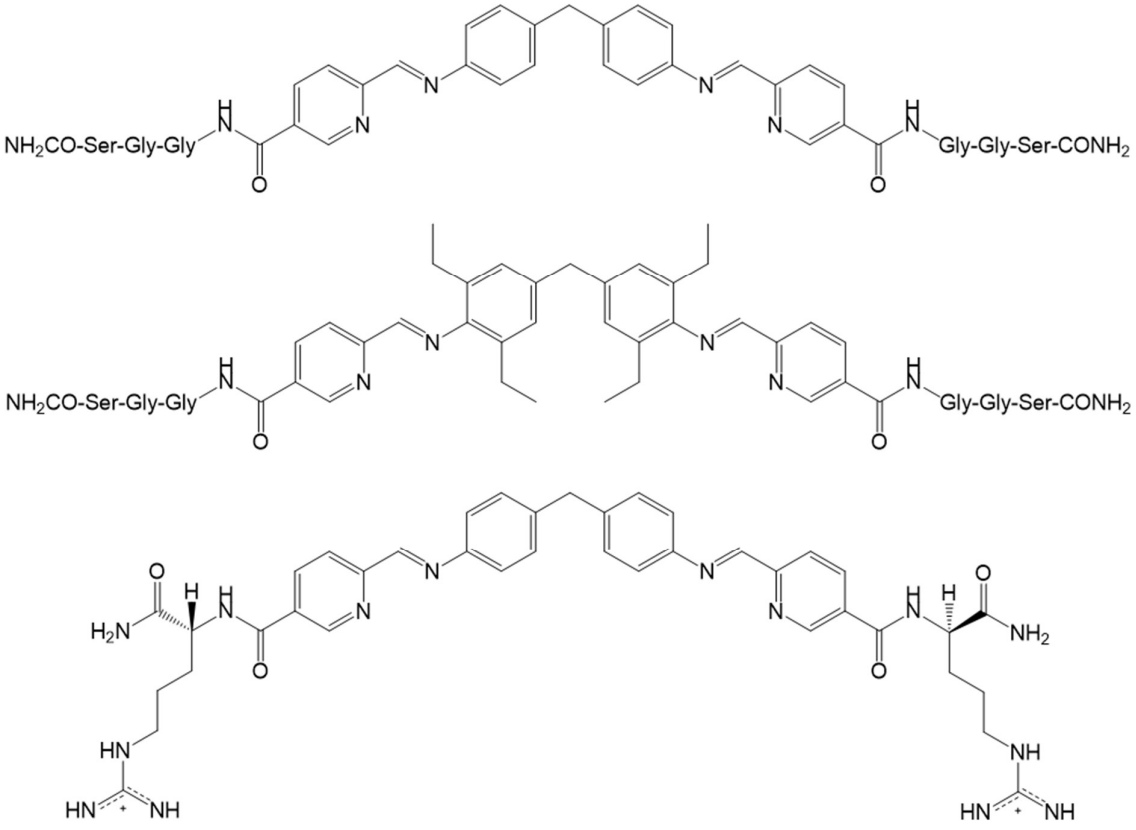


Figure 1.35: Shows the structure of the two different tripeptide ligands used (top and middle) and the structure of the ligand conjugated with D-arginine at each end (bottom).

properties of the cylinders, likely because the central ligand structure remains unaltered by the peptide.

1.3.2: Metallo-organic supramolecular Pillarplexes

Pillarplexes are a relatively new class or Metallo-supramolecular host-guest complex, first reported in 2016, comprising of two cyclophane ligands and eight metal centres either being gold(I) or silver(I) (Figure 1.36).[22,195] These pillarplexes have a tetra-cationic charge and possess many of the supramolecular interactions that other complexes owe their successes too. These complexes are also capable of host-guest relationships, having space for a linear guest molecule, such as the demonstrated 1,8-diaminooctane, allowing for rotaxanation and by extension added functionality. Modification of the ligand structure is also possible, replacing the pyrazolate moiety

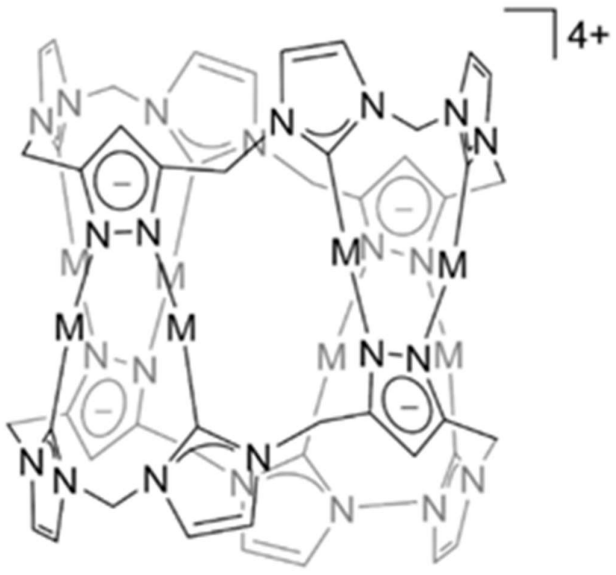


Figure 1.36: Shows the structure of a pillarplex where M may be Ag(I) or Au(I).

with a 1,2,4-triazolate group.[196] This conferred additional flexibility to the structure as well as allowing hydrogen bonding between other pillarplexes, enabling self-recognition between other cationic pillarplexes.

As a first investigation into biological activity, the stability and toxicity of both gold and silver Pillarplexes were explored against bacterial, fungal, and human cancer cells lines.[197] The silver pillarplex showed activity against bacterial and fungal cell lines as well a moderate toxicity against HepG2 liver cancer cell line. The gold pillarplex was close to inactive against bacterial and fungal cells with lower activity against the cancer cell line than the silver. The increased toxicity of the silver pillarplex was attributed to its instability resulting in the release of silver ions, whereas the low activity of the gold pillarplex was attributed to its greater stability and remaining intact. This suggests the gold pillarplex it a suitable host complex for further investigation into *in vivo* drug delivery and activity, due to its increased stability over its silver counterpart.

Rotaxanes have also been formed out of Pillarplexes by threading of a 1,12-diaminododecane molecule through the silver pillarplex and subsequent capping by di-tertbutyl benzoate group for the full [2]rotaxane.[198,199] The authors identified this silver pillarplex [2]rotaxane could be trans-metalated with high yield to the gold pillarplex [2]rotaxane through the addition of AuCl (Figure 1.37). They revealed that modification of the pH to acidic conditions transformed this silver rotaxane to a purely organic [3]rotaxane by demetallation of the silver ions. This [3]rotaxane could be subsequently restored to the silver pillarplex [2]rotaxane by addition of Ag(I) oxide, increase of pH and 16 hrs at 70 °C.

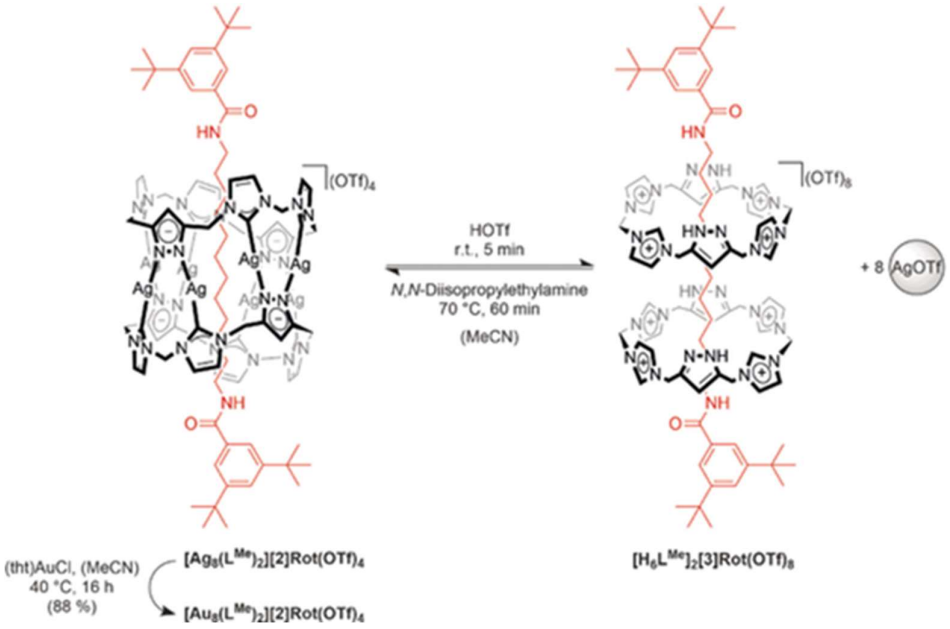


Figure 1.37: Shows the scheme for trans-metalation of the pillarplex [2]rotaxane between silver and gold. As well as the acid/base assisted interconversion between the pillarplex [2]rotaxane and organic [3]rotaxane. Taken from reference with permission.[198]

1.3.3: Metallo-supramolecular tetrahedra

A $[Fe^{II}_4L_4]^{8+}$ Tetrahedron structure (Figure 1.38) has been reported which demonstrates binding to single stranded DNA, unpaired nucleobases, 3WJ's and 4WJ's. This complex also quenches the emission of the fluorescent DNA tag FAM, which enables rapid detection of binding due to a decrease in detectable fluorescence. Additionally, the quenching has been shown to be dependent on the distance between

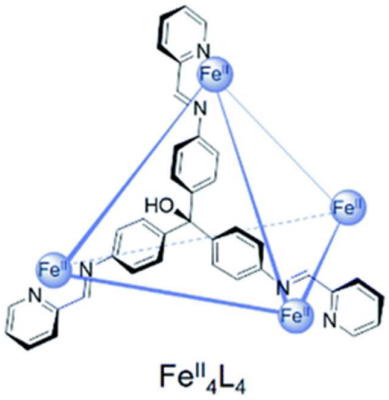


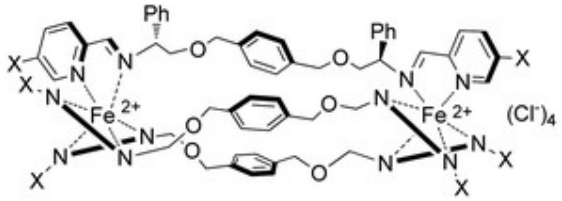
Figure 1.38: Shows the structure of the $Fe^{II}_4L_4$ tetrahedron.

FAM and the $Fe^{II}_4L_4$ Tetrahedron. This, coupled with controls, allows for special detection of the binding site on the DNA structure, dependant on the strength of the fluorescence quenching. This was shown by altering mismatch locations along DS DNA and observing changes in fluorescence based on number of mismatches and the location of the mismatch relative to FAM. Similarly, 3WJ arm length with FAM attached were altered showing a reducing in fluorescence quenching the further FAM was from the junctions branch point (which is the proposed binding location of the $Fe^{II}_4L_4$ Tetrahedron). This complex offers potential diagnostic applications in the development of assays to assess these structural features which can be associated with genetic disease.

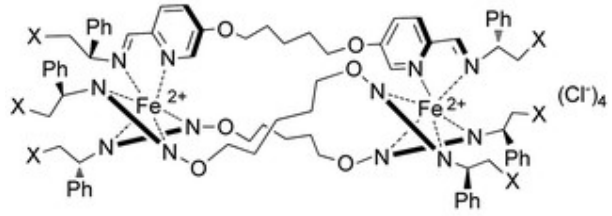
This same $Fe^{II}_4L_4$ Tetrahedron structure has also shown the ability to bind to and interact with G-quadruplex structures.[200] They are able to exhibit the same fluorescent quenching, which is seen with unpaired nucleotide and junction binding, provide information on binding topography to the G-quadruplex. What is more interesting, are the aggregates created when the tetrahedral bind to them resulting in a precipitation of the larger particles. This aggregation was shown by reduced absorption after filtering and mixing, circular dichroism, electrophoresis, and dynamic light scattering. The formation of aggregates also protected the G-quadruplex from digestion by S1 nuclease, highlighting the ability of the tetrahedra to interfere with biological processes associated with the quadruplex structure. The authors suggest further work and design could yield probes which can regulate gene expression and carry active therapeutic molecules.

1.3.4: Other supramolecular helical nucleic acid binders

A class of metallo-helices, also referred to as a flexicate, has been produced which share similar structural characteristics of the metallo-supramolecular cylinders (Figure 1.39). These optically active complexes are comprised of three organic ligands and two metal centres, a tetra-cationic charge, and an array of supramolecular interaction. These structures differ in their ligand structure and the metals they chelate, avoiding the di-aniline unit in favour of other varied structures containing oxygen, alkyl chains and phenyl rings.[201–203] These flexicates have shown binding to both canonical and non-canonical DNA structures and toxicity against cisplatin resistant cancer cell lines without exhibiting genotoxicity.[201] These complexes have also demonstrated binding to nucleic acid bulges and G-quadruplexes, potentially linking this to their undefined mode of biological activity.[204–206] Most recently, post assembly modification of the structure has been used to synthetically add functional moieties to the structure, which has yielded enhanced biological activity and targeting.[207]



Δ_{Fe},R_C-$[Fe_2\mathbf{L^{1a}}_3]Cl_4$ (X = H)
Δ_{Fe},R_C-$[Fe_2\mathbf{L^{1b}}_3]Cl_4$ (X = OH)



Δ_{Fe}-$[Fe_2\mathbf{L^{2a}}_3]Cl_4$ (X = H)
Δ_{Fe}-$[Fe_2\mathbf{L^{2b}}_3]Cl_4$ (X = OH)

Figure 1.39: Shows the different structures of the metallo-helices known as flexicates. Taken from reference with permission.[201]

Another chiral supramolecular metallo-helix was formed using two metal centres and a single multi(12)dentate pre-organized peptide ligand using solid phase peptide synthesis (Figure 1.40).[208] Helix enantiomers are synthesised by controlling the stereochemistry of the proline residues used in the synthesis of the ligand. These complexes show potent 3WJ binding, as shown through electrophoretic studies, as well as the ability to bind replication foci inside living cells through co-localisation of fluorescent signal *in cellulo*.[209]

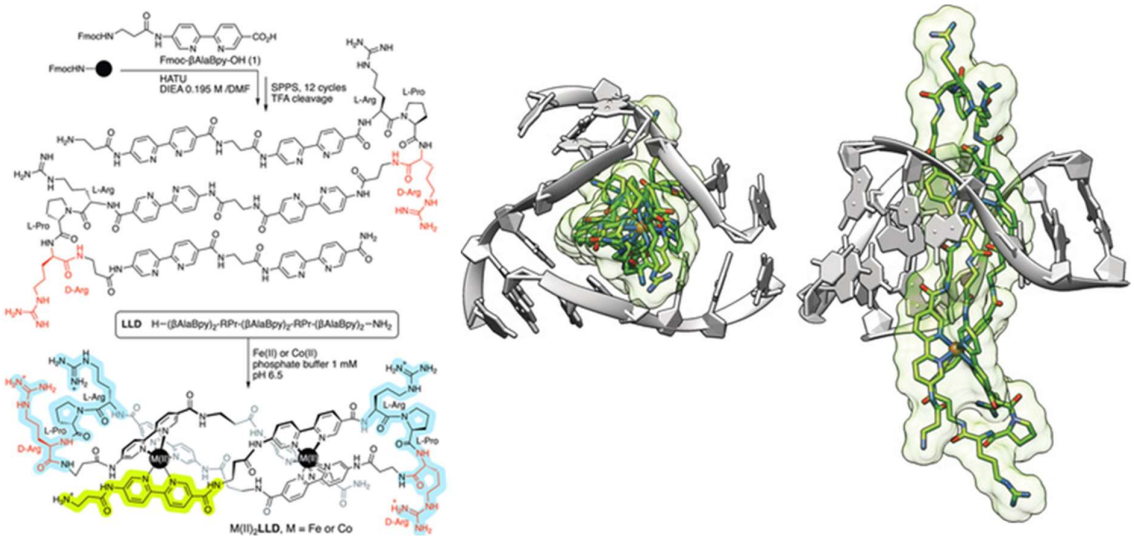


Figure 1.40: Shows the structure of the metallo-peptide helicate ligand and its formation into a helicate (left). A model of the metallo-peptide helicate binding a 3WJ can also be seen (right) as generated by the GaudiMM molecular modelling platform. Adapted from reference with permission.[209]

1.3.5: Rotaxane caged Pt G-quadruplex binder

Rotaxanation can convey additional functionality to a biologically active molecule by preventing its non-rotaxanated forms mode of action *in vivo*. This has been done with a Pt(II) salphen complex which has been mentioned previously (section 1.2.3.5 Figure 1.28) and exhibits G-quadruplex binding, has been rotaxanated by a macrocycle and one of two bulky stopper groups which are sensitive to either enzymatic cleavage or light (Figure 1.41).[210] They demonstrated complete inhibition of DNA binding whilst

rotaxanated, which was restored upon cleavage of either stopper, resulting in release of the DNA binding agent. Rotaxanation also demonstrated increased cellular uptake compared to the Pt(II) salphen complex alone. Both enzyme and photo cleavable rotaxanes showed activity *in cellulo* greater than that of the complex alone, once exposed to their respective stimuli, with the photo sensitive complex demonstrating the most profound increase in toxicity. These mechanically interlocked molecules showcase the staggering potential for therapeutic applications of the controllable mechanical bond.

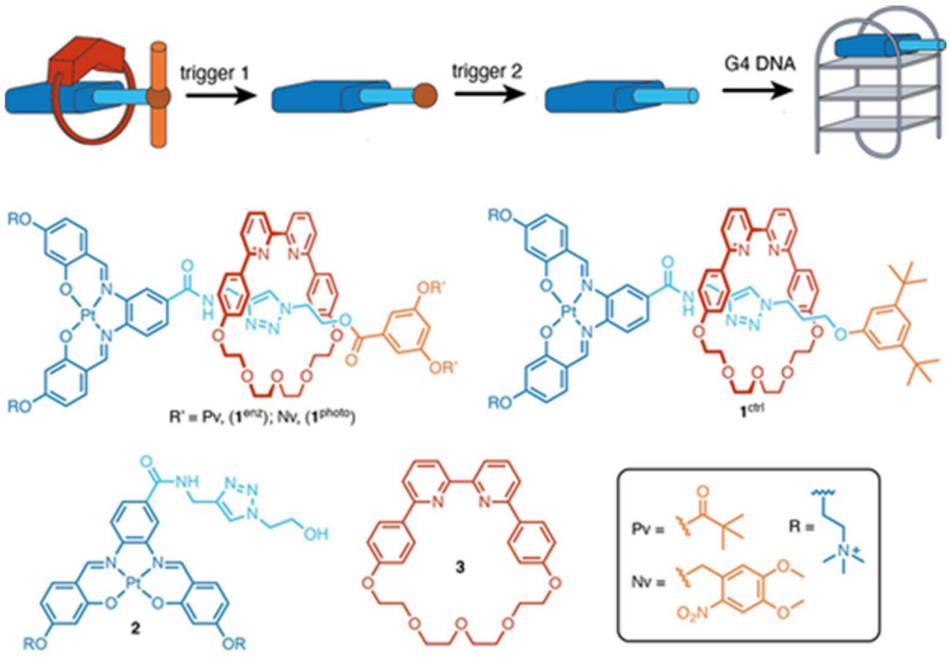


Figure 1.41: Show the structures and schemes of action of the rotaxanated platinum salphen quadruplex binding drug which is capable of enzyme or photo-cleavage and subsequent release. Taken from reference with permission.[210]

1.4: Thesis overview

Our DNA contains all the information required for our growth and continued function. As a result of this, it is extensively manipulated by biological processes to extract information and to ensure its safe storage and repair. During manipulation, unique, non-canonical, DNA structures arise, either intentionally to allow control of processes such as transcription, replication, and repair, or unintentionally in the case of certain diseases. These structures provide unique chemical environments to target which convey additional targeting specificity due to their occurrence during the aforementioned situations. This provides an opportunity to avoid the shortcomings of non-specific biological interactions which previous therapeutics have exhibited, such as cisplatin.

The aim of this thesis is to explore the influence of metallo-supramolecular architectures on nucleic acid binding. To do this, different organic frameworks and metal centres are used and their binding to different key nucleic acid structures is assessed. Due to the effectiveness of the metallo-supramolecular cylinder rotaxane, plans have been set to start studying this complex *in vivo*. To progress this, a method for extraction of these complexes from whole blood was established and subsequent detection of structure and concentration.

Chapter two reports the development of a metallo-supramolecular rotaxane and its ability to control DNA binding. Also reported is a new mechanism of rotaxane formation via a slippage mechanism as opposed to post assembly modification. Studies were also done on a modified rotaxane which was designed to release a metallo-supramolecular cylinder *in vivo*, allowing for targeted release. On top of this, the 3WJ

forming ability of new cylinders were investigated along with a study into the interactions of a parent cylinder with a Holliday junction. Finally, the ability for cylinder to bind to different cucurbituril sizes from a crude sample was assessed with the aim of detecting the presence of new cucurbituril ring sizes and the developing an easy purification method for existing ones.

Chapter three reports a method for the quantification, separation, and detection of metallo-supramolecular cylinders from a whole blood sample. The stability of different cylinders, rotaxanes and *pseudo*-rotaxanes in whole blood is also assessed and provides insight into the design of new complexes and the effective delivery of existing ones.

Chapter four includes a publication on the initial studies into the DNA interactions of the relatively new class of metallo-supramolecular complexes, pillarplexes, as part of an international collaboration. The interactions between pillarplexes and canonical DNA as well as DNA 3WJ's and 4WJ's are reported, providing insight into their potential as nucleic acid binding agents.

Chapter 5 contains a summary of the work carried out In this thesis as well as the conclusions which can be drawn from it and how this affects the field as a whole. Further work to carry on from this thesis is also highlighted along with suggestions on how to do this.

1.5: References

1 *Office for National Statistics*, Past and projected period and cohort life tables: 2020-based, UK, 1981 to 2070, 2022, 2–5, https://www.ons.gov.uk/peoplepopulationandcommunity/birthsdeathsandmarriages/lifeexpectancies/bulletins/pastandprojecteddatafromtheperiodandcohortlifetables/2020baseduk1981to2070, (accessed October 2022).

2 Office for National Statistics, *National Life Tables - Life Expectancy in the UK*, 2020, 1–15, https://www.ons.gov.uk/peoplepopulationandcommunity/birthsdeathsandmarriages/lifeexpectancies/bulletins/nationallifetablesunitedkingdom/2018to2020#:~:text=We%20have%20also%20published%20single,higher%20mortality%20observed%20in%202020, (accessed October 2022).

3 D. R. Goldstein, *Virulence*, 2010, **1**, 295–298.

4 J. Leng and D. R. Goldstein, *Microbes Infect.*, 2010, **12**, 1120–1124.

5 E. Laconi, F. Marongiu and J. DeGregori, *Br. J. Cancer*, 2020, **122**, 943–952.

6 V. C. Chitalia and A. H. Munawar, *J. Transl. Med.*, 2020, **18**, 1–6.

7 J. Appleby, *BMJ*, 2022, **376**, o490.

8 L. Strasfeld and S. Chou, *Infect. Dis. Clin. North Am.*, 2010, **24**, 413–437.

9 D. D. Richman, *Trends Microbiol.*, 1994, **2**, 401–407.

10 L. Strasfeld and S. Chou, *Infect. Dis. Clin. North Am.*, 2010, **24**, 413–437.

11 T. M. Belete, *Hum. Microb. J.*, 2019, **11**, 100052.

12 L. Zhong, Y. Li, L. Xiong, W. Wang, M. Wu, T. Yuan, W. Yang, C. Tian, Z. Miao, T. Wang and S. Yang, *Signal Transduct. Target Ther.*, 2021, **6**, 201.

13 C. S. Adamson, K. Chibale, R. J. M. Goss, M. Jaspars, D. J. Newman and R. A. Dorrington, *Chem. Soc. Rev.*, 2021, **50**, 3647–3655.

14 S. Minchin and J. Lodge, *Essays Biochem.*, 2019, **63**, 433-456.

15 G. Wang and K. M. Vasquez, *DNA Repair (Amst).*, 2014, **19**, 143–151.

16 E. Ivens, M. M. D. Cominetti and M. Searcey, *Bioorg. Med. Chem.*, 2022, **69**, 116897.

17 T. Hermann and D. J. Patel, *Structure*, 2000, **8**, R47–R54.

18 S. A. Mortimer, M. A. Kidwell and J. A. Doudna, *Nat. Rev. Genet.*, 2014, **15**, 469–479.

19 A. Oleksi, A. G. Blanco, R. Boer, I. Usón, J. Aymamí, A. Rodger, M. J. Hannon, and M. Coll, *Angew. Chem. Int. Ed.*, 2006, **45**, 1227–1231.

20 A. C. G. Hotze, N. J. Hodges, R. E. Hayden, C. Sanchez-Cano, C. Paines, N. Male, M.-K. Tse, C. M. Bunce, J. K. Chipman and M. J. Hannon, *Chem. Biol.*, 2008, **15**, 1258–1267.

21 C. A. J. Hooper, L. Cardo, J. S. Craig, L. Melidis, A. Garai, R. T. Egan, V. Sadovnikova, F. Burkert, L. Male, N. J. Hodges, D. F. Browning, R. Rosas, F. Liu, F. v. Rocha, M. A. Lima, S. Liu, D. Bardelang and M. J. Hannon, *J. Am. Chem. Soc.*, 2020, **142**, 20651–20660.

22 P. J. Altmann and A. Pöthig, *J. Am. Chem. Soc.*, 2016, **138**, 13171–13174.

23 R. Dahm, *Hum Genet*, 2008, **122**, 565–581.

24 J. D. Watson, J. D. Smith, L. Hamilton, J. White, G. R. Wyatt, M. H. F Wilkins and H. R. Wilson, *Nature*, 1953, **171**, 737–738.

25 J. D. Watson and F. H. C. Crick, *Nature*, 1953, **171**, 737–738.

26 S. Nurk, S. Koren, A. Rhie, M. Rautiainen, A. v. Bzikadze, A. Mikheenko, M. R. Vollger, N. Altemose, L. Uralsky, A. Gershman, S. Aganezov, S. J. Hoyt, M. Diekhans, G. A. Logsdon, M. Alonge, S. E. Antonarakis, M. Borchers, G. G. Bouffard, S. Y. Brooks, G. v. Caldas, N.-C. Chen, H. Cheng, C.-S. Chin, W. Chow, L. G. de Lima, P. C. Dishuck, R. Durbin, T. Dvorkina, I. T. Fiddes, G. Formenti, R. S. Fulton, A. Fungtammasan, E. Garrison, P. G. S. Grady, T. A. Graves-Lindsay, I. M. Hall, N. F. Hansen, G. A. Hartley, M. Haukness, K. Howe, M. W. Hunkapiller, C. Jain, M. Jain, E. D. Jarvis, P. Kerpedjiev, M. Kirsche, M. Kolmogorov, J. Korlach, M. Kremitzki, H. Li, V. v. Maduro, T. Marschall, A. M. McCartney, J. McDaniel, D. E. Miller, J. C. Mullikin, E. W. Myers, N. D. Olson, B. Paten, P. Peluso, P. A. Pevzner, D. Porubsky, T. Potapova, E. I. Rogaev, J. A. Rosenfeld, S. L. Salzberg, V. A. Schneider, F. J. Sedlazeck, K. Shafin, C. J. Shew, A. Shumate, Y. Sims, A. F. A. Smit, D. C. Soto, I. Sović, J. M. Storer, A. Streets, B. A. Sullivan, F. Thibaud-Nissen, J. Torrance, J. Wagner, B. P. Walenz, A. Wenger, J. M. D. Wood, C. Xiao, S. M. Yan, A. C. Young, S. Zarate, U. Surti, R. C. McCoy, M. Y. Dennis, I. A. Alexandrov, J. L. Gerton, R. J. O'Neill, W. Timp, J. M. Zook, M. C. Schatz, E. E. Eichler, K. H. Miga and A. M. Phillippy, *Science*, 2022, **376**, 44–53.

27 A. Travers and G. Muskhelishvili, *FEBS J.*, 2015, **282**, 2279–2295.

28 M. Taniguchi and T. Kawai, *Physica. E. Low. Dimens. Syst. Nanostruct.*, 2006, **33**, 1–12.

29 R. P. Bowater and A. J. Gates, in *eLS*, Wiley, 2015, 1–9.

30 C. Fonseca Guerra, F. M. Bickelhaupt, J. G. Snijders and E. J. Baerends, *J. Am. Chem. Soc.*, 2000, **122**, 4117–4128.

31 M. Blackburn, M. J. Gait, D. Locks, D. M. Williams, *Nucleic Acids in Chemistry and Biology*, Royal Society of Chemistry, Cambridge, 2007.

32 R. Wing, H. Drew, T. Takano, C. Broka, S. Tanaka, K. Itakura and R. E. Dickerson, *Nature*, 1980, **287**, 755–758.

33 R. Rohs, S. M. West, A. Sosinsky, P. Liu, R. S. Mann and B. Honig, *Nature*, 2009, **461**, 1248-1253.

34 P. L. Privalov, A. I. Dragan, C. Crane-Robinson, K. J. Breslauer, D. P. Remeta and C. A. S. A. Minetti, *J. Mol. Biol.*, 2007, **365**, 1-9.

35 G. S. Khan, A. Shah, Zia-Ur-Rehman and D. Barker, *J. Photochem. Photobiol.*, 2012, **115**, 105–118.

36 D. W. Ussery, DNA Structure: A-, B- and Z-DNA Helix Families, in *eLS*, (Ed.)Wiley, 2002. https://doi.org/10.1038/npg.els.0003122.

37 D. R. Whelan, T. J. Hiscox, J. I. Rood, K. R. Bambery, D. McNaughton and B. R. Wood, *J. R. Soc. Interface*, 2014, **11**, 20140454.

38 G. Palermo, *Chem*, 2019, **5**, 1364–1366.

39 G. Wang and K. M. Vasquez, *Front. Biosci.*, 2007, **12**, 4424–4438.

40 P. R. Marshall, Q. Zhao, X. Li, W. Wei, A. Periyakaruppiah, E. L. Zajaczkowski, L. J. Leighton, S. U. Madugalle, D. Basic, Z. Wang, J. Yin, W.-S. Liau, A. Gupte, C. R. Walkley and T. W. Bredy, *Nat. Neurosci.*, 2020, **23**, 718–729.

41 H. Tateishi-Karimata and N. Sugimoto, *Chem.Commun.*, 2020, **56**, 2379–2390.

42 L. Wiesmüller, J. M. Ford and R. H. Schiestl, *J. Biomed. Biotechnol.*, 2002, **2**, 921363.

43 T. D. Tran and D. T. Pham, *Sci. Rep.,* 2021, **11**, 1–11.

44 J. Zhang, Q. Dai, D. Park and X. Deng, *Genes (Basel)*, 2016, **7**, 51.

45 A. R. Leman and E. Noguchi, *Genes (Basel)*, 2013, **4**, 1-32.

46 J. Malina, M. J. Hannon and V. Brabec, *Sci. Rep.*, 2016, **6**, 29674.

47 L. Melidis, I. B. Styles and M. J. Hannon, *Chem. Sci.*, 2021, **12**, 7174–7184.

48 L. Melidis, H. J. Hill, N. J. Coltman, S. P. Davies, K. Winczura, T. Chauhan, J. S. Craig, A. Garai, C. A. J. Hooper, R. T. Egan, J. A. McKeating, N. J. Hodges, Z. Stamataki, P. Grzechnik and M. J. Hannon, *Angew. Chem. Int. Ed.*, 2021, **60**, 18144–18151.

49 A. Bansal, S. Kaushik and S. Kukreti, *Front. Genet.*, 2022, **13**, 959258.

50 M. Peyrone, *Justus Liebigs Ann. Chem.*, 1844, **51**, 1–29.

51 B. Rosenberg, L. van Camp and T. Krigas, *Nature*, 1965, **205**, 698–699.

52 D. J. Higby, D. J. Higby, H. J. Wallace, D. J. Albert and J. F. Holland, *Cancer*, 1974, **33**, 1219–1225.

53 L. Messori and A. Merlino, *Coord. Chem. Rev.*, 2016, **315**, 67–89.

54 S. Möltgen, E. Piumatti, G. M. Massafra, S. Metzger, U. Jaehde and G. v. Kalayda, *Cells,* 2020, **9**, 1322.

55 I. Russo Krauss, G. Ferraro and A. Merlino, *Inorg. Chem.*, 2016, **55**, 7814–7816.

56 S. Dasari and P. Bernard Tchounwou, *Eur. J. Pharmacol.*, 2014, **740**, 364–378.

57 A. Brown, S. Kumar and P. B. Tchounwou, J. Cancer. Sci. Ther., 2019, **11**, 97.

58 D.-W. Shen, L. M. Pouliot, M. D. Hall and M. M. Gottesman, *Pharmacol Rev*, 2012, **64**, 706–721.

59 S. H. Chen and J. Y. Chang, *Int. J. Mol. Sci.,* 2019, **20**, 4136.

60 B. J. S. Sanderson, L. R. Ferguson and W. A. Denny, *Mutat. Res.*, 1996, **355**, 59–70.

61 R. Oun, Y. E. Moussa and N. J. Wheate, *Dalton Trans.*, 2018, **47**, 6645–6653.

62 R. J. Knox, F. Friedlos, D. A. Lydall and J. J. Roberts, *Cancer Res.*, 1986, **46**, 1972–1979.

63 A. H. Calvert, S. J. Harland, D. R. Newell, Z. H. Siddik, A. C. Jones, T. J. McElwain, S. Raju, E. Wiltshaw, I. E. Smith, J. M. Baker, M. J. Peckham and K. R. Harrap, *Cancer Chemother. Pharmacol.,* 1982, **9**, 140–147.

64 J. Zhou, Y. Kang, L. Chen, H. Wang, J. Liu, S. Zeng and L. Yu, *Front. Pharmacol.*, 2020, **11**, 343.

65 J. Graham, M. Muhsin and P. Kirkpatrick, *Nat. Rev. Drug Discov.*, 2004, **3**, 11–12.

66 L. M. Pasetto, M. R. D'Andrea, E. Rossi and S. Monfardini, *Crit. Rev. Oncol. Hematol.*, 2006, **59**, 159–168.

67 M. Coluccia and G. Natile, *Anticancer Agents Med. Chem.*, 2007, **7**, 111–123.

68 M. B. G. Kloster, J. C. Hannis, D. C. Muddiman and N. Farrell, *Biochemistry*, 1999, **38**, 14731–14737.

69 D. I. Jodrell, T. R. J. Evans, W. Steward, D. Cameron, J. Prendiville, C. Aschele, C. Noberasco, M. Lind, J. Carmichael, N. Dobbs, G. Camboni, B. Gatti and F. de Braud, *Eur. J. Cancer*, 2004, **40**, 1872–1877.

70 J. Malina, K. Čechová, N. P. Farrell and V. Brabec, *Inorg. Chem.*, 2019, **58**, 6804–6810.

71 F. Pelletier, V. Comte, A. Massard, M. Wenzel, S. Toulot, P. Richard, M. Picquet, P. le Gendre, O. Zava, F. Edafe, A. Casini and P. J. Dyson, *J. Med. Chem*, 2010, **53**, 6923-6933.

72 E. Alessio and L. Messori, *Molecules*, 2019, **24**, 1995.

73 A. A. Nazarov, C. G. Hartinger and P. J. Dyson, *J. Organomet. Chem.*, 2014, **751**, 251–260.

74 S. Neidle, *Nat. Prod. Rep.*, 2001, **18**, 291–309.

75 K. K. Woods, T. Lan, L.W. McLaughlin, L. D. Williams, *Nucleic Acids Res.*, 2003, **31**, 1536–1540.

76 R. Rohs, S. M. West, A. Sosinsky, P. Liu, R. S. Mann and B. Honig, *Nature,* 2009, **461**, 1248–1253.

77 P. L. Privalov, A. I. Dragan, C. Crane-Robinson, K. J. Breslauer, D. P. Remeta and C. A. S. A. Minetti, *J. Mol. Biol.*, 2007, **365**, 1–9.

78 C. A. Bewley, A. M. Gronenborn and G. M. Clore, *Annu. Rev. Biophys. Biomol. Struct.*, 1998, **27**, 105–131.

79 S. E. Ades and R. T. Sauer, *Biochemistry*, 1995, **34**, 14601–14608.

80 L. Cardo, I. Nawroth, P. J. Cail, J. A. McKeating and M. J. Hannon, *Sci. Rep.*, 2018, **8**, 13342.

81 M. P. Barrett, C. G. Gemmell and C. J. Suckling, *Pharmacol. Ther.*, 2013, **139**, 12–23.

82 X. Cai, P. J. Gray and D. D. von Hoff, *Cancer Treat. Rev.*, 2009, **35**, 437–450.

83 M. Beran, S. Jeha, S. O'Brien, E. Estey, L. Vitek, M. G. Zurlo, M. B. Rios, M. Keating and H. Kantarjian, *Clin. Cancer Res.*, 1997, **3**, 2377–84.

84 B. S. P. Reddy, S. M. Sondhi and J. W. Lown, *Pharmacol. Ther.*, 1999, **84**, 1–111.

85 G. S. Khan, A. Shah, Zia-Ur-Rehman and D. Barker, *J. Photochem. Photobiol. B.*, 2012, **115**, 105–118.

86 V. R. Machha, C. G. Mikek, S. Wellman and E. A. Lewis, *Biochem. Biophys. Rep.*, 2017, **12**, 158–165.

87 S. Simonsson, T. Samuelsson and P. Elias, *J. Biol. Chem.*, 1998, **273**, 24633–24639.

88 N. N. Singh and A. M. Lambowitz, *J. Mol. Biol.*, 2001, **309**, 361–386.

89 S. Iuchi, in *Zinc Finger Proteins*, Springer US, Boston, MA, 2005.

90 P. L. Hamilton and D. P. Arya, *Nat. Prod. Rep.*, 2012, **29**, 134–143.

91 E. Tuite, U. Sehlstedt, P. Hagmar, B. Nordén and M. Takahashi, *Eur. J. Biochem.*, 1997, **243**, 482–492.

92 S. K. Kim and B. Nordén, *FEBS Lett.*, 1993, **315**, 61–64.

93 M. J. Hannon, V. Moreno, M. J. Prieto, E. Moldrheim, E. Sletten, I. Meistermann, C. J. Isaac, K. J. Sanders and A. Rodger, *Angew. Chem. Int. Ed.*, 2001, **40**, 879–884.

94 A. S. Biebricher, I. Heller, R. F. H. Roijmans, T. P. Hoekstra, E. J. G. Peterman and G. J. L. Wuite, *Nat. Commun.,*2015, **6**, 1–12.

95 S. N. Rao and P. A. Kollman, *Proc. Natl. Acad. Sci., USA,*, 1987, **84**, 5735–5739.

96 Y. Pommier, R. E. Schwartz, L. A. Zwelling and K .W. Kohn, *Biochemistry*, 1985, **24**, 6406-6410

97 A. Mukherjee and W. D. Sasikala, *Adv Protein Chem Struct Biol*, 2013, **92**, 1–62.

98 G. J. Quigley, A. H. J. Wang, G. Ughetto, G. van der Marel, J. H. van Boom and A. Rich, *Proc. Natl. Acad. Sci., USA,*, 1980, **77**, 7204–7208.

99 F. M. Balis, J. S. Holcenberg and W. Archie Bleyer, *Clin. Pharmacokinet.*, 1983, **8**, 202–232.

100 P. Borst, *IUBMB Life*, 2005, **57**, 745–747.

101 P. Stevenson, K. R. Sones, M. M. Gicheru and E. K. Mwangi, *Acta. Trop.*, 1995, **59**, 77–84.

102 K. D. Mjos and C. Orvig, *Chem. Rev.*, 2014, **114**, 4540–4563.

103 A. E. Friedman, J. K. Barton, J. C. Chambron, J. P. Sauvage, N. J. Turro and J. K. Barton, *J. Am. Chem. Soc.*, 1990, **112**, 4960–4962.

104 S. Estalayo-Adrián, S. Blasco, S. A. Bright, G. J. McManus, G. Orellana, D. C. Williams, J. M. Kelly and T. Gunnlaugsson, *ACS Appl. Bio. Mater.*, 2021, **4**, 6664–6681.

105 H. Xu, K. C. Zheng, H. Deng, L. J. Lin, Q.-L. Zhang and L. N. Ji, *New J. Chem.*, 2003, **27**, 1255-1263.

106 G. Li, L. Sun, L. Ji and H. Chao, *Dalton Trans.*, 2016, **45**, 13261–13276.

107 T. Sabir, A. Toulmin, L. Ma, A. C. Jones, P. Mcglynn, ⊥ Gunnar, F. Schrö Der, and S. W. Magennis, *J. Am. Chem. Soc.*, 2012, **134**, 6280-6285.

108 M. R. Singleton, S. Scaife and D. B. Wigley, *Cell*, 2001, **107**, 79–89.

109 D. R. Duckett and D. M. J. Lilley, *EMBO J.*, 1990, **9**, 1–659.

110 C. Altona, J. A. Pikkemaat and F. J. J. Overmars, *Curr. Opin. Struct. Biol.*, 1996, **6**, 305–316.

111 K. C. Woods, S. S. Martin, V. C. Chu and E. P. Baldwin, *J. Mol. Biol.*, 2001, **313**, 49–69.

112 M. M. Slean, K. Reddy, B. Wu, K. Nichol Edamura, M. Kekis, F. H. T. Nelissen, R. L. E. G. Aspers, M. Tessari, O. D. Schärer, S. S. Wijmenga and C. E. Pearson, *Biochemistry*, 2013, **52**, 773–785.

113 G. Wang and K. M. Vasquez, *DNA Repair (Amst).*, 2014, **19**, 143–151.

114 E. V. Mirkin and S. M. Mirkin, *Microbiol. Mol. Biol. Rev.*, 2007, **71**, 13–35.

115 J. Zhao, A. Bacolla, G. Wang and K. M. Vasquez, *Cell. Mol. Life Sci.*, 2010, **67**, 43–62.

116 A. Bowry, R. D. W. Kelly and E. Petermann, *Trends Cancer*, 2021, **7**, 863–877.

117 H. Gaillard, T. García-Muse and A. Aguilera, *Nat. Rev. Cancer*, 2015, **15**, 276–280.

118 M. Dobbelstein and C. S. Sørensen, *Nat. Rev. Drug Discov.*, 2015, **14**, 405–423.

119 A. J. Berdis, *Biochemistry*, 2008, **47**, 8253-8260.

120 J. Magden, L. Kääriäinen and T. Ahola, *Appl. Microbiol. Biotechnol.*, 2005, **66**, 612-621

121 S. Bagga and M. J. Bouchard, in *Methods in Molecular Biology*, Noguchi, E., Gadaleta, M. (eds). Humana Press, New York. 2014, vol. 1170, 165–227.

122 M. J. Hannon, C. L. Painting, A. Jackson, J. Hamblin and W. Errington, *Chem. Commun.*, 1997, 1807–1808.

123 L. Cerasino, M. J. Hannon and E. Sletten, *Inorg. Chem.*, 2007, **46**, 6245–6251.

124 S. Vuong, L. Stefan, P. Lejault, Y. Rousselin, F. Denat and D. Monchaud, *Biochimie*, 2012, **94**, 442–450.

125 J. M. Lehn, E. Sonveaux and A. K. Willard, *J. Am. Chem. Soc.*, 1978, **100**, 4914–4916.

126 J. Novotna, A. Laguerre, A. Granzhan, M. Pirrotta, M. P. Teulade-Fichou and D. Monchaud, *Org. Biomol. Chem.*, 2014, **13**, 215-222.

127 J. Zell, K. Duskova, L. L. Chouh, M. Bossaert, N. Chéron, C. Chéron, A. Granzhan, S. Britton and D. Monchaud, *Nucleic Acids Res.*, 2021, **49**, 10275–10288.

128 K. Duskova, P. Lejault, E. Benchimol, R. Guillot, S. Britton, A. Granzhan and D. Monchaud, *J. Am. Chem. Soc.*, 2020, **142**, 1, 424–435.

129 S. A. Barros and D. M. Chenoweth, *Angew. Chem. Int. Ed.*, 2014, **53**, 13746–13750.

130 S. A. Barros and D. M. Chenoweth, *Chem. Sci.*, 2015, **6**, 4752–4755.

131 R. Holliday, *Genet. Res. (Camb).*, 1964, **5**, 282–304.

132 N. Agmon, M. Yovel, Y. Harari, B. Liefshitz and M. Kupiec, *Nucleic Acids Res.*, 2011, **39**, 7009–7019.

133 P. A. Khuu, A. R. Voth, F. A. Hays and P. S. Ho, *J. Mol. Recognit.*, 2006, **19**, 234–242.

134 J. C. Puigvert, K. Sanjiv and T. Helleday, *FEBS J.*, 2016, **283**, 232–245.

135 S. Haider, P. Li, S. Khiali, D. Munnur, A. Ramanathan and G. N. Parkinson, *J. Am. Chem. Soc.* 2018, **140**, 15366–15374

136 K. V. Kepple, J. L. Boldt and A. M. Segall, PNAS., 2005, **102**, 6867-6872.

137 A. L. Brogden, N. H. Hopcroft, M. Searcey and C. J. Cardin, *Angew. Chem. Int. Ed.*, 2007, **46**, 3850–3854.

138 L. A. Howell, Z. A. E. Waller, R. Bowater, M. O'Connell and M. Searcey, *Chem. Commun.*, 2011, **47**, 8262-8264.

139 V. H. S. van Rixel, A. Busemann, M. F. Wissingh, S. L. Hopkins, B. Siewert, C. van de Griend, M. A. Siegler, T. Marzo, F. Papi, M. Ferraroni, P. Gratteri, C. Bazzicalupi, L. Messori and S. Bonnet, *Angew. Chem. Int. Ed.*, 2019, **58**, 9378–9382.

140 D. M. J. Lilley, *Proc. Natl. Acad. Sci. USA*, 1995, **92**, 7140–7142.

141 S. Roy, U. Delling, C. H. Chen, C. A. Rosen and N. Sonenberg, *Genes Dev.*, 1990, **4**, 1365–1373.

142 M. Chastain and I. Tinoco, *Prog. Nucleic Acid Res. Mol. Biol.*, 1991, **41**, 131-177.

143 D. H. Turner, *Curr. Opin. Struct. Biol.*, 1992, **2**, 334–337.

144 T. Hermann and D. J. Patel, *Structure*, 2000, **8**, R47–R54.

145 J. H. Bae and D. Y. Zhang, *Nucleic Acids Res.*, 2021, **49**, 7901–7908.

146 H. Budworth and C. T. McMurray, *Methods Mol. Biol.*, 2013, **1010**, 3-17.

147 L. S. Kappen, Y. Lin, G. B. Jones and I. H. Goldberg, *Biochemistry*, 2007, **46**, 561–567.

148 B. M. Zeglis, J. A. Boland and J. K. Barton, *J. Am. Chem. Soc.*, 2008, **130**, 7530–7531.

149 J. Spiegel, S. Adhikari and S. Balasubramanian, *Trends Chem.*, 2020, **2**, 123–136.

150 P. Murat and S. Balasubramanian, *Curr. Opin. Genet. Dev.*, 2014, **25**, 22–29.

151 K. wei Zheng, Z. Chen, Y. hua Hao and Z. Tan, *Nucleic Acids Res.*, 2010, **38**, 327–338.

152 N. Kosiol, S. Juranek, P. Brossart, A. Heine and K. Paeschke, *Mol. Cancer,* 2021, **20**, 1–18.

153 K. Paeschke, T. Simonsson, J. Postberg, D. Rhodes and H. J. Lipps, *Nat. Struct. Mol. Biol.,* 2005, **12**, 847–854.

154 T. Endoh, A. B. Rode, S. Takahashi, Y. Kataoka, M. Kuwahara and N. Sugimoto, *Anal. Chem*, 2016, **88**, 899-903.

155 A. K. Mukherjee, S. Sharma and S. Chowdhury, *Trends Genet.*, 2019, **35**, 129-144.

156 C. Reina and V. Cavalieri, *Int. J. Mol. Sci.*, 2020, **21**, 4172.

157 E. Palma, J. Carvalho, C. Cruz and A. Paulo, *Pharmaceuticals*, 2021, **14**, 605.

158 L.-Y. Liu, T.-Z. Ma, Y.-L. Zeng, W. Liu and Z.-W. Mao, *Cite This: J. Am. Chem. Soc.*, **2022**, 11878–11887.

159 F. J. Groelly, M. Porru, J. Zimmer, H. Benainous, Y. de Visser, A. A. Kosova, S. di Vito, V. Serra, A. Ryan, C. Leonetti, A. Bruna, A. Biroccio and M. Tarsounas, *EMBO Mol. Med.*, 2022, **14**, e14501.

160 N. H. Abd Karim, O. Mendoza, A. Shivalingam, A. J. Thompson, S. Ghosh, M. K. Kuimova and R. Vilar, *RSC Adv.*, 2013, **4**, 3355–3363.

161 K. Gehring, J. L. Leroy and M. Guéron, *Nature,* 1993, **363**, 561–565.

162 S. Benabou, A. Aviñó, R. Eritja, C. González and R. Gargallo, *RSC Adv.*, 2014, **4**, 26956–26980.

163 E. P. Wright, J. L. Huppert and Z. A. E. Waller, *Nucleic Acids Res.*, 2017, **45**, 2951–2959.

164 M. Zeraati, D. B. Langley, P. Schofield, A. L. Moye, R. Rouet, W. E. Hughes, T. M. Bryan, M. E. Dinger and D. Christ, *Nat. Chem.*, 2018, **10**, 631–637.

165 J. Choi, S. Kim, T. Tachikawa, M. Fujitsuka and T. Majima, *J. Am. Chem. Soc.*, 2011, **133**, 16146–16153.

166 H. A. Day, P. Pavlou and Z. A. E. Waller, *Bioorg. Med. Chem.*, 2014, **22**, 4407–4418.

167 M. A. S. Abdelhamid, Z. A. E. Waller and T. D. Craggs, *Biophys. J.*, 2022, **121**, 171a.

168 Y. Cui, D. Kong, C. Ghimire, C. Xu and H. Mao, *Biochemistry*, 2016, **55**, 2291–2299.

169 J. J. King, K. L. Irving, C. W. Evans, R. v. Chikhale, R. Becker, C. J. Morris, C. D. Peña Martinez, P. Schofield, D. Christ, L. H. Hurley, Z. A. E. Waller, K. S. Iyer and N. M. Smith, *J. Am. Chem. Soc.*, 2020, **142**, 20600–20604.

170 K. L. Irving, J. J. King, Z. A. E. Waller, C. W. Evans and N. M. Smith, *Biochimie*, 2022, **198**, 33–47.

171 H. A. Assi, M. Garavís, C. González and M. J. Damha, *Nucleic Acids Res.*, 2018, **46**, 8038-8056.

172 R. v. Chikhale, D. Guneri, R. Yuan, C. J. Morris and Z. A. E. Waller, *Bioorg. Med. Chem. Lett.*, 2022, **73**, 128886.

173 A. S. Tikhomirov, M. A. S. Abdelhamid, G. Y. Nadysev, G. v Zatonsky, E. E. Bykov, P. J. Chueh, Z. A. E. Waller and A. E. Shchekotikhin, *J. Nat. Prod.*, 2021, **84**, 1617–1625.

174 O. Y. Fedoroff, A. Rangan, V. v Chemeris and L. H. Hurley, *Biochemistry*, 2000, **39**, 15083–15090.

175 G. Kuang, M. Zhang, S. Kang, D. Hu, X. Li, Z. Wei, X. Gong, L.-K. An, Z.-S. Huang, B. Shu and D. Li, *J. Med. Chem.*, 2020, **63**, 9136–9153.

176 S. Kendrick, H.-J. Kang, M. P. Alam, M. M. Madathil, P. Agrawal, V. Gokhale, D. Yang, S. M. Hecht and L. H. Hurley, *J. Am. Chem. Soc.*, 2014, **136**, 4161–4171.

177 B. J. Pages, S. P. Gurung, K. McQuaid, J. P. Hall, C. J. Cardin and J. A. Brazier, *Front. Chem.*, 2019, **7**, 744.

178 P. Spence, J. Fielden and Z. A. E. Waller, *J. Am. Chem. Soc*, 2020, **15**, 13856-13866.

179 A. C. Jamieson, J. C. Miller and C. O. Pabo, *Nat. Rev. Drug. Discov.,* 2003, **2**, 361–368.

180 A. Klug and D. Rhodes, *Trends Biochem Sci*, 1987, **12**, 464–469.

181 M. J. Hannon, I. Meistermann, C. J. Isaac, C. Blomme, A. Rodger and J. R. Aldrich-Wright, Chem. Commun., 2001, 1078–1079.

182 J. M. C. A. Kerckhoffs, J. C. Peberdy, I. Meistermann, L. J. Childs, C. J. Isaac, C. R. Pearmund, V. Reudegger, S. Khalid, N. W. Alcock, M. J. Hannon and A. Rodger, *Dalton Trans.*, 2007, 734–742.

183 E. Moldrheim, M. J. Hannon, I. Meistermann, A. Rodger and E. Sletten, J. Biol. Inorg. Chem., 2002, **7**, 770–780.

184 I. Meistermann, V. Moreno, M. J. Prieto, E. Moldrheim, E. Sletten, S. Khalid, P. Mark Rodger, J. C. Peberdy, C. J. Isaac, A. Rodger and M. J. Hannon, *Proc. Natl. Acad. Sci. USA*, 2002, **99**, 5069–5074.

185 S. Khalid, M. J. Hannon, A. Rodger and P. Mark Rodger, *Chem. Eur. J.*, 2006, **12**, 3493–3506.

186 J. Malina, M. J. Hannon and V. Brabec, *Chem. Eur. J*, 2007, **13**, 3871–3877.

187 S. Phongtongpasuk, S. Paulus, J. Schnabl, R. K. O. Sigel, B. Spingler, M. J. Hannon and E. Freisinger, *Angew. Chem. Int. Ed.*, 2013, **52**, 11513–11516.

188 C. Ducani, A. Leczkowska, N. J. Hodges and M. J. Hannon, *Angew. Chem. Int. Ed.*, 2010, **49**, 8942–8945.

189 G. I. Pascu, A. C. G. Hotze, C. Sanchez-Cano, B. M. Kariuki and M. J. Hannon, *Angew. Chem. Int. Ed.*, 2007, **46**, 4374–4378.

190 J. Malina, M. J. Hannon and V. Brabec, *Chem. Eur. J.*, 2008, **14**, 10408–10414.

191 L. J. Childs, J. Malina, B. E. Rolfsnes, M. Pascu, M. J. Prieto, M. J. Broome, P. M. Rodger, E. Sletten, V. Moreno, A. Rodger and M. J. Hannon, *Chem. Eur. J*, 2006, **12**, 4919–4927.

192 Y. Parajó, J. Malina, I. Meistermann, G. J. Clarkson, M. Pascu, A. Rodger, M. J. Hannon and P. Lincoln, *Dalton Trans.*, 2009, 4868-4874.

193 L. Cardo, V. Sadovnikova, S. Phongtongpasuk, N. J. Hodges and M. J. Hannon, *Chem. Commun.*, 2011, **47**, 6575–6577.

194 L. Cardo and M. J. Hannon, *Inorg. Chim. Acta*, 2009, **362**, 784–792.

195 P. J. Altmann, C. Jandl and A. Pöthig, *Dalton Trans.*, 2015, **44**, 11278–11281.

196 S. Guan, T. Pickl, C. Jandl, L. Schuchmann, X. Zhou, P. J. Altmann and A. Pöthig, *Org. Chem. Front.*, 2021, **8**, 4061–4070.

197 A. Pöthig, S. Ahmed, H. C. Winther-Larsen, S. Guan, P. J. Altmann, J. Kudermann, A. M. Santos Andresen, T. Gjøen and O. A. Høgmoen Åstrand, *Front. Chem.*, 2018, **6**, 584.

198 P. J. Altmann and A. Pöthig, *Angew. Chem. Int. Ed.*, 2017, **56**, 15733–15736.

199 A. A. Heidecker, M. Bohn and A. Pöthig, *Z. Kristallogr. Cryst. Mater.*, 2022, **237**, 167–177.

200 J. Zhu, Z. Yan, F. Bošković, C. J. E. Haynes, M. Kieffer, J. L. Greenfield, J. Wang, J. R. Nitschke and U. F. Keyser, *Chem. Sci.*, 2021, **12**, 14564–14569.

201 V. Brabec, S. E. Howson, R. A. Kaner, R. M. Lord, J. Malina, R. M. Phillips, Q. M. A. Abdallah, P. C. McGowan, A. Rodger and P. Scott, *Chem. Sci.*, 2013, **4**, 4407-4416.

202 S. E. Howson, L. E. N. Allan, N. P. Chmel, G. J. Clarkson, R. J. Deeth, A. D. Faulkner, D. H. Simpson and P. Scott, *Dalton Trans.*, 2011, **40**, 10416-10433.

203 S. E. Howson, L. E. N. Allan, N. P. Chmel, G. J. Clarkson, R. van Gorkum and P. Scott, *Chem. Commun.*, 2009, 1727–1729.

204 A. Zhao, S. E. Howson, C. Zhao, J. Ren, P. Scott, W. Chunyu and X. Qu, *Nucleic Acids Res.*, 2017, **45**, 5026–5035.

205 C. Zhao, H. Song, P. Scott, A. Zhao, H. Tateishi-Karimata, N. Sugimoto, J. Ren and X. Qu, *Angew. Chem. Int. Ed.*, 2018, **57**, 15723–15727.

206 J. Malina, P. Scott and V. Brabec, *Dalton Trans.*, 2015, **44**, 14656–14665.

207 H. Song, N. J. Rogers, S. J. Allison, V. Brabec, H. Bridgewater, H. Kostrhunova, L. Markova, R. M. Phillips, E. C. Pinder, S. L. Shepherd, L. S. Young, J. Zajac and P. Scott, *Chem. Sci.*, 2019, **10**, 8547–8557.

208 I. Gamba, G. Rama, E. Ortega-Carrasco, J. D. Maréchal, J. Martínez-Costas, M. Eugenio Vázquez and M. V. López, *Chem. Commun.*, 2014, **50**, 11097–11100.

209 J. Gómez-González, Y. Pérez, G. Sciortino, L. Roldan-Martín, J. Martínez-Costas, J. D. Maréchal, I. Alfonso, M. Vázquez López and M. E. Vázquez, *Angew. Chem. Int. Ed.*, 2021, **60**, 8859–8866.

210 T. Kench, P. A. Summers, M. K. Kuimova, J. E. M. Lewis and R. Vilar, *Angew. Chem. Int. Ed.*, 2021, **60**, 10928–10934.

211 M. C. Vega, I. Garcia Saez, J. Aymami, R. Eritja, G. A. van der Marel, J. H. van Boom, A. Rich and M. Coll, *Eur. J. Biochem.*, 1994, **222**, 721–726.

212 J. A. Feng, R. C. Johnson and R. E. Dickerson, *Science,* 1994, **263**, 348–355.

213 J. P. Hall, S. P. Gurung, J. Henle, P. Poidl, J. Andersson, P. Lincoln, G. Winter, T. Sorensen, D. J. Cardin, J. A. Brazier and C. J. Cardin, *Chem. Eur. J*, 2017, **23**, 4981–4985.

214 J. Müller, *Metallomics*, 2010, **2**, 318–327.

Chapter 2: Rotaxanating metallo-supramolecular cylinders - towards controlled release

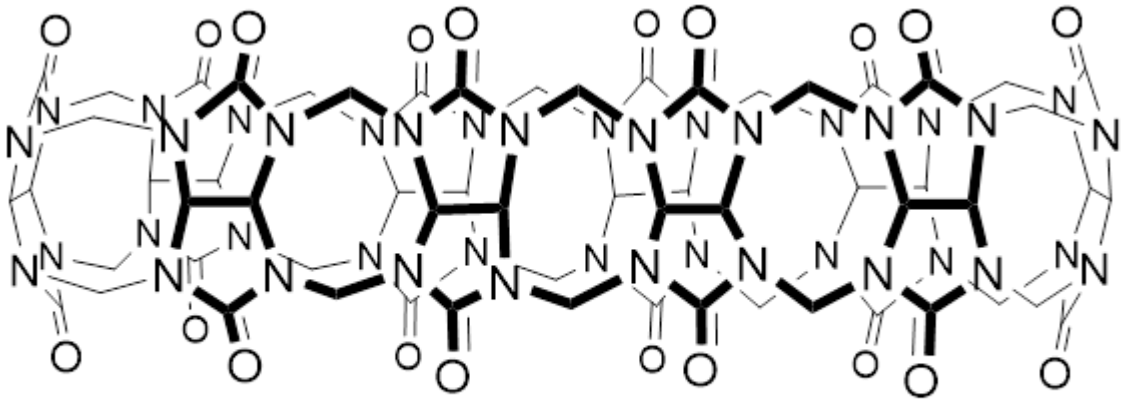
2.1: Introduction

Rotaxanes are supramolecular complexes which are traditionally comprised of a macrocycle threaded by a two-dimensional linear molecule.[1,2] This creates a ring (macrocycle) and axle (linear molecule) structure where the ring cannot leave the axle due to stopper groups at the end of the axle. The macrocycle ring and molecular axle may take many different forms allowing for several different applications. This includes chemical environment sensing, protection of the axle species and specific break down and release of active components in biological environments in response to specific stimuli.[3–9] We aim to bring rotaxanes and their added functionality into our own work by changing the conventional 2D linear axle to one of our metallo-supramolecular cylinders. The rotaxanation of these complexes could provide added functionality on top of what they already possess (discussed in 1.3).

Metallo-supramolecular cylinders have demonstrated the ability to bind to and condense DNA structures as well as producing cytostatic effects and apoptotic cell death in cell lines.[10–16] They have also demonstrated specific binding to DNA three-way junctions (3WJ) which can occur during DNA replication and present a potentially potent therapeutic target.[17–24] More recently these cylinders have also shown binding to unique RNA structures, resulting in inhibition of key biological interactions required for viral replication, showing efficacy against HIV-1 and SARS-CoV-2 viruses.[25–30] It is the aromatic groups that present π-π stacking interactions along the central axis of the

cylinders which allows for this DNA/junction/bulge binding, in combination with their electrostatic forces.[24,31] Interfering with these interactions by trapping a macrocycle, perpendicular to the cylinders central axis, which blocks these interactions, could afford a level of control over the cylinders activity.

Cucurbiturils are a class of supramolecular host-guest complexes which have exhibited applications in a medicinal context.[32] Cucurbit[10]uril (CB[10]) (Figure 2.i) presents itself as a suitable macrocycle host for the cylinder with an appropriate cavity size.[33,34] Cucurbiturils have demonstrated good stability, solubility when occupied and low toxicity, making them a prime candidate for therapeutic applications.[32,35–37] By turning our cylinders into rotaxanes using CB[10] we aim to control the intermolecular chemistry which gives them their biological activity (discussed in section 1.3). By doing this we can improve/change factors such as stability, cellular uptake, and localisation, all of which have an impact on a drug's efficacy and help in reducing unintended/unwanted side effects like those seen with cisplatin.[38–42] After establishing certain levels of control over the cylinders biological interactions by rotaxanation, our next aim was to release the cylinder out of the rotaxane and have it retained its original



CB[10]

Figure 2.i: Chemical structure of Cucurbit[10]uril (CB[10]).

biological functionality. This would be achieved using a glutathione mediated nucleophilic aromatic substitution (SNAr) reaction of di-nitrobenzene capping groups, this would leave the $[Ni_2(L')_3]^{4+}$ *pseudo*-rotaxane as the product where the cylinder can leave the CB[10] macrocycle. This reaction could theoretically occur more readily in environments with greater glutathione levels such as those of a tumour environment, allowing for improved specificity during treatment and therefore overall greater efficacy.[43] Examples of rotaxane based metallo-drug designs exist already and utilise both external stimuli in the form of irradiation and enzyme mediated release to improve uptake, localisation and efficacy.[44] Other rotaxanes with biological sensing functionality are also in development which highlight the sensitivity which can be achieved for specific biological analytes with certain properties like steric bulk.[45]

From here in we show we can make rotaxanes and *pseudo*-rotaxanes using different methods from our metallo-supramolecular cylinders and CB[10]. Rotaxanation inhibits the biological interactions and *pseudo*-rotaxanation does not. Showing that whilst fully capped rotaxanation restricts these interactions, the uncapped species can leave the host and regain its previous biological interactions which have resulted in the previously reported activity.[10-16]

We also discuss the development of another mechanically locked and capped rotaxane with different capping groups. This rotaxane is capable of undergoing SNAr with GSH causing cleavage and formation of the *pseudo*-rotaxane species where the cylinder demonstrates its previously reported functionality of DNA-3WJ formation.

2.2: Effects of full and *pseudo*-Rotaxanation on DNA interactions of metallo-supramolecular cylinders

The work described in this section 2.2 has been published as part of the publication entitled “Rotaxanating Metallo-supramolecular Nano-cylinder Helicates to Switch DNA Junction Binding” J. Am. Chem. Soc. 2020, 142, 49, 20651–20660, https://dx.doi.org/10.1021/jacs.0c07750. The work was carried out in collaboration with colleagues in the group and external collaborators with the co-authors of the paper being Catherine A. J. Hooper, Lucia Cardo, James S. Craig (the author of this thesis), Lazaros Melidis, Aditya Garai, Ross T. Egan, Viktoriia Sadovnikova, Florian Burkert, Louise Male, Nikolas J. Hodges, Douglas F. Browning, Roselyne Rosas, Fengbo Liu, Fillipe V. Rocha, Mauro A. Lima, Simin Liu, David Bardelang,and Michael J. Hannon. This section focuses primarily on my contributions, but to contextualise and rationalise the studies some aspects of the wider studies from others are included. The work that is discussed and supported by Figures represents my contributions (comprising some mass spectrometry, gel, CD and LD experiments).

CB[10] was chosen as the macrocycle due to the biocompatibility of cucurbiturils and the open cavity of CB[10] being of suitable size for the cylinder to occupy.[32,34,42] The binding capability of CB[10] to metallo-supramolecular cylinders first needed to be assessed. This was done by mixing in aqueous solution. CB[10] is a solid white precipitate when mixed with water alone, however upon adding $[Fe_2(L)_3]^{4+}$ important to include charges throughout to this solution this precipitate dissolves immediately. This shows that the CB[10] has been solubilised which is a strong indicator of a host-guest complex being formed because of how other cucurbiturils are solubilized.[46] The

exclusion of water from the central cavity of CB[10] is the driving force for this interaction.[47] The formation of a *pseudo*-rotaxane where the CB[10] rests around the central CH_2 atoms was proved using ESI-MS in conjunction with proton and DOSY Nuclear Magnetic Resonance (NMR). We explored the binding kinetics of the $[Fe_2(L)_3]^{4+}\cdot$(CB[10]) *pseudo*-rotaxane by mixing it with $[Ni_2(L)_3]^{4+}$ and seeing if there was any exchange of the guest cylinder. Upon mixing and immediate injection in the ESI-MS we can see the presence of both iron and nickel *pseudo*-rotaxanes (Figure 2.01 T = 0), the ratio of which remained unchanged during the experiment. This suggests exchange takes place on the millisecond/second timescale and highlight the potential suitability of the *pseudo*-rotaxane as a drug due to its ability to expel cylinder.

To explore the biological interactions of these complexes we performed several biophysical experiments using spectroscopic and electrophoretic mobility shift assay (EMSA) methods. The first experiment was a polyacrylamide gel electrophoresis (PAGE) assay where we use 3 different DNA oligomers which are 14 bases in length. Together in the presence of cylinder, they form a DNA three-way junction (3WJ) which has a discrete band in the EMSA. We use the strength of this band shift to assess the 3WJ binding abilities of the cylinder which is present. Gels were imaged by radiolabeling strand 1 with Phosphorus-32 and detecting the beta radiation emitted with a phosphor imaging screen.

We can see in Figure 2.02 that the DNA 3WJ strands do not form a 3WJ on their own. This is because it is entropically unstable at room temperature and exists as the three separate single strands (SS). We can however see that upon addition of $[Ni_2(L)_3]^{4+}$ there is a dramatic shift to the 3WJ band with all single stranded species being lost

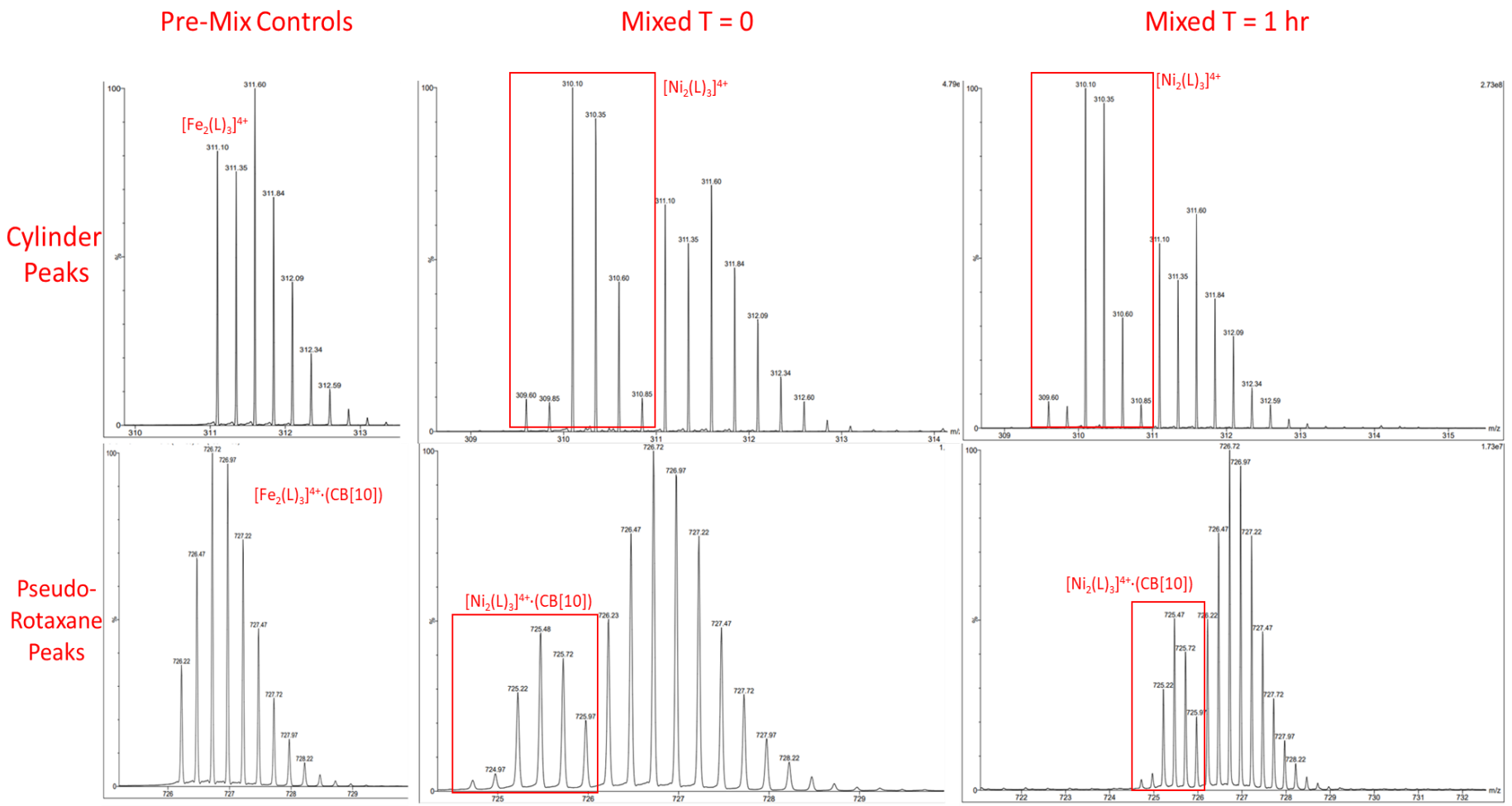


Figure 2.01: Shows the mass spectra of $[Ni_2(L)_3]^{4+}\cdot(CB[10])$ pseudo-rotaxane alone and upon mixing with $[Fe_2(L)_3]$ at time 0 and 1 hr.

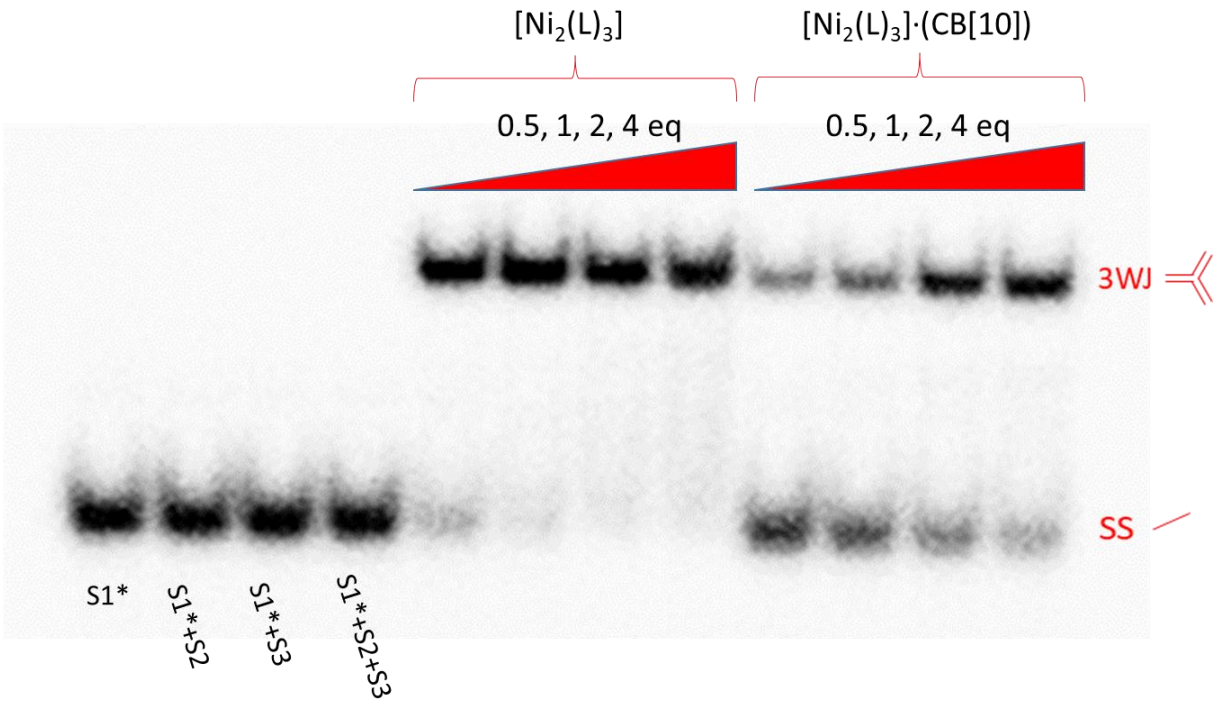


Figure 2.02: Shows the PAGE gel of DNA 3WJ (left to right) alone controls (1-4) with different combinations of component oligos. Then upon incubation with $[Ni_2(L)_3]$ cylinder at 0.5,1,2 and 4 equivalents (5-8) and finally upon incubation with $[Ni_2(L)_3]$·(CB[10]) pseudo-rotaxane at 0.5,1,2 and 4 equivalents (9-12).

upon reaching a 1:1 ratio of 3WJ to $[Ni_2(L)_3]^{4+}$. This interaction behaves as expected and presents itself as a positive control for the following experiments. Upon addition of $[Ni_2(L)_3]^{4+}$·(CB[10]) *pseudo* rotaxane we can see the formation of 3WJ, but the band shift is not as pronounced and not all the SS shifts to 3WJ even by 4 eq. This indicates that the $[Ni_2(L)_3]^{4+}$ cylinder can leave the CB[10] cavity and form and stabilise DNA 3WJ. However, the CB[10] presents itself as a competitor, creating a dynamic equilibrium where the cylinder binds both species. We cannot rule out that the *pseudo*-rotaxane itself binds to the 3WJ, but if this were the case, we would expect the complex to have a larger hydrodynamic radius which would present itself as a band with a different shift in the gel.

We explored this relationship further by presenting $[Ni_2(L)_3]^{4+}$·(CB[10]) *pseudo*-rotaxane with methyl viologen (MV^{2+}) which is an alternative guest for CB[10]. We also

explored $[Ni_2(L)_3]^{4+}$ cylinder binding by offering it CB[10] which has been solubilised with the guest molecule MV^{2+}. In Figure 2.03 with $[Ni_2(L)_3]^{4+}$·CB[10] *pseudo*-rotaxane on addition of MV^{2+} we can look at graph A to see that the overall trend shows an increasing proportion of 3WJ is formed. This indicates that a competitor guest molecule such as MV^{2+} can shift the equilibrium to displace more of the cylinder resulting in more cylinder available for junction binding. We can also see in Figure 2.03 in graph B that the addition of MV^{2+}·CB10 to $[Ni_2(L)_3]^{4+}$ cylinder results in a decreasing proportion of 3WJ being formed. This implies that cylinder can leave a junction and bind to CB[10] whilst displacing a competitor guest, highlighting the strength of the host-guest relationship between cylinder and CB[10].

In the case of the *pseudo*-rotaxane we also must factor in the enthalpy of formation of the DNA 3WJ as when the cylinder leaves the CB[10] there will be no pre-formed 3WJ to bind. This indicates that although the CB[10] seems to offer itself as a competitor to

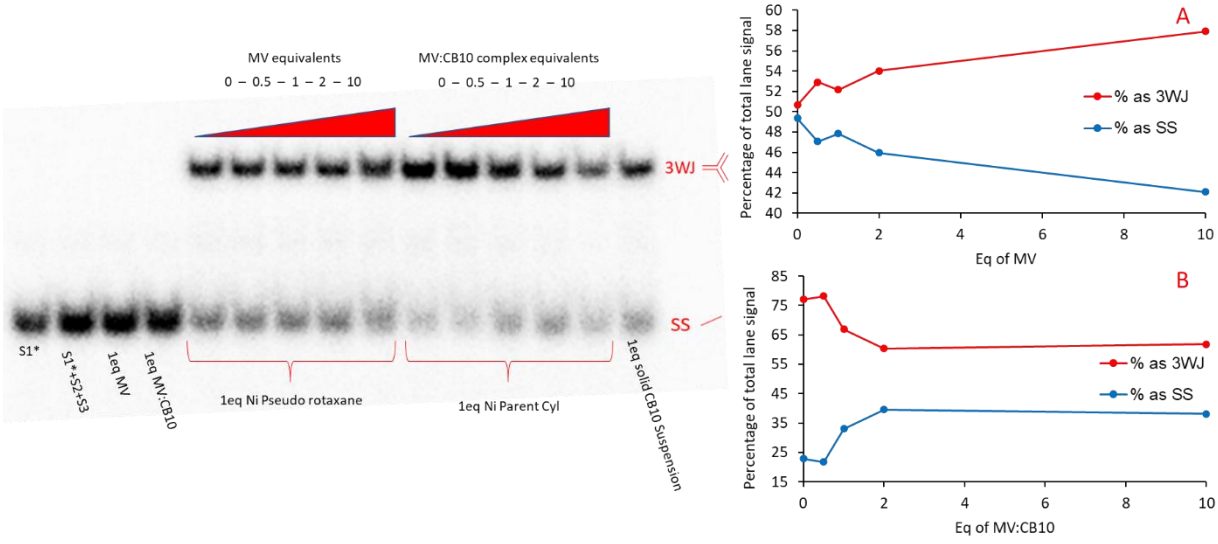


Figure 2.03: Shows the PAGE gel of DNA 3WJ (left to right) of 3WJ controls (1-4), $[Ni_2(L)_3]$·(CB[10]) pseudo-rotaxane and 3WJ (1:1) upon addition of methyl viologen at 0,0.5,1,2 and 10 eq (5-9). $[Ni_2(L)_3]$ cylinder and 3WJ (1:1) upon addition of MV^{2+}·CB[10] at 0,0.5,1,2 and 10 eq (10-14). And finally $[Ni_2(L)_3]$ cylinder and 3WJ (1:1) upon addition of 1 eq of non-solubilised CB[10] (15). Graphs A and B show how the percentages of 3WJ and SS DNA change as a percentage of total lane signal as we add the competitor molecules in increasing amounts across both series. A is for $[Ni_2(L)_3]$·(CB[10]) pseudo-rotaxane on addition of methyl viologen and B is for $[Ni_2(L)_3]$ cylinder on addition of MV^{2+}·CB[10] complex.

3WJ, when factoring in the enthalpy of formation of 3WJ, and entropy, the binding preference for 3WJ must be much greater than that for CB[10].

The next experiments we did were spectroscopic studies of the cylinder's interactions with calf thymus (CT) DNA. We first did a control titration of $[Ni_2(L)_3]^{4+}$ cylinder into CT-DNA and recorded the spectra at different ratios of DNA base pairs to complex. We can see in Figure 2.04 that the circular dichroism (CD) spectra (left) show the retention of the primary B-DNA signal between 200-300 nm and the formation of an induced signal around 300 nm because of the $[Ni_2(L)_3]^{4+}$ cylinder binding. The linear dichroism (LD) spectra in Figure 2.04 (right) shows a drastic reduction in the 260 nm peak which is indicative of a reduction in orientation caused by condensation because of $[Ni_2(L)_3]^{4+}$ cylinder binding which was expected for this complex.[48] We then explored the interactions of the $[Ni_2(L)_3]^{4+}$·(CB[10]) *pseudo*-rotaxane to see the effect of CB[10] *pseudo*-rotaxanation on DNA binding. We can see in Figure 2.05 that the CD spectra (left) shows the same signals between 200-300 nm for the DNA and the same characteristic cylinder ICD above 300 nm as the cylinder alone (Figure 2.04 left). This tells us that the interaction remains almost unchanged except for increased noise and

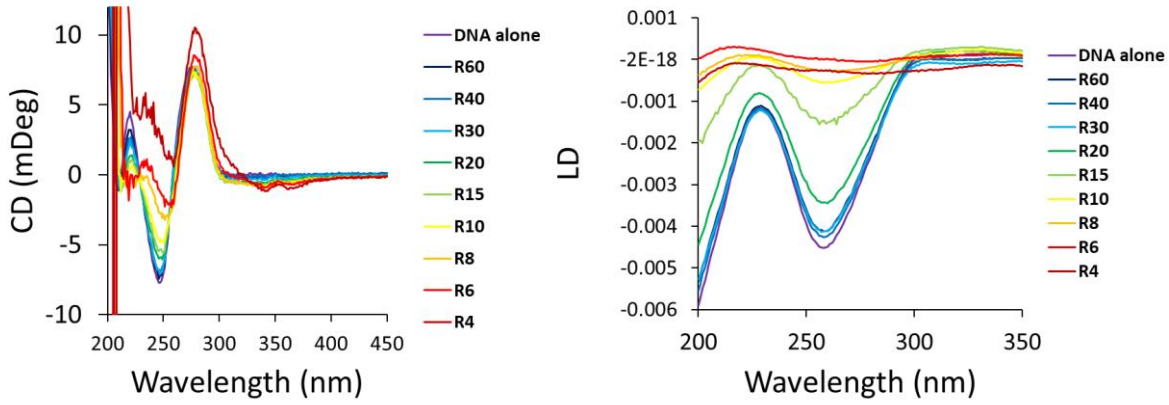


Figure 2.04: Shows the circular dichroism (left) and linear dichroism (right) spectra of titrations of $[Ni_2(L)_3]$ cylinder into calf thymus DNA (100 μM) in 10 mM sodium chloride and 1 mM sodium cacodylate. The R values represent the ratio of DNA base pairs to complex.

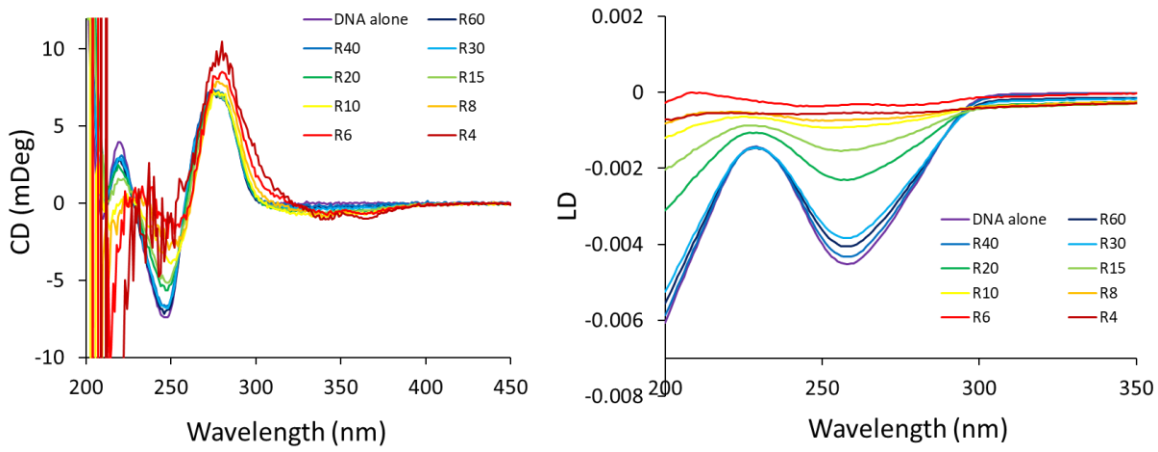


Figure 2.05: Shows the circular dichroism (left) and linear dichroism (right) spectra for titrations of $[Ni_2(L)_3]$·(CB[10]) pseudo-rotaxane into calf thymus DNA (100 µM) in 10 mM sodium chloride and 1 mM sodium cacodylate. R values represent the ratio of DNA base pairs to complex.

scattering at around 260 nm and below, which we have attributed to CB[10] precipitation caused by the cylinder leaving the central cavity of CB[10] rendering it insoluble. We can also see in the LD spectra (right) that the same reduction in the 260 nm peak can be observed. This supports the theory that the cylinder leaves CB[10] and binds to the DNA in a similar manor to that without CB[10]. The driving force for the cylinder leaving the cavity of CB[10] is the forces of electrostatic attraction between the polyanionic DNA and the tetra-cationic cylinder.

Cells (A2780 ovarian and MDA-MB-231 breast cancer lines) were treated with cylinder·CB[10] *pseudo*-rotaxane complexes with varying metal centres. MTT assays showed inhibition of cell proliferation for *pseudo*-rotaxanes which was comparable to that of the cylinders alone. ICP-MS was carried out and revealed that there were minor changes in cell uptake between cylinders and their corresponding *pseudo*-rotaxanes. This suggests the cylinder retains its biological activity *in cellulo* and is supported by PAGE/CD/LD studies showing that the cylinder leaves the CB[10] macrocycle to bind a biological target. This shows that CB[10] makes a suitable macrocycle host for

cylinders as it does not interfere with the biological effects that make cylinders attractive but also contributes by increasing thermal stability.

Having established that *pseudo*-rotaxanation occurs between cylinder and CB[10] and that biological effects remain intact, the next step was to establish full rotaxanation. To do this we needed to add bulky substituents (caps) to the ends of the cylinder which prevent the cylinder from leaving the central cavity of CB[10]. To do this we first modified the ligand L to change the pyridine groups to a 2-imidazole group. This enabled an alkylation reaction on the non-metal coordinated nitrogen, this is the L' ligand. We would then alkylate this nitrogen with a 2-picolyl group which would serve as the bulky cap, this would occur at all six locations on the cylinder, 3 at each end and was named L'' ligand.

Rotaxanation was achieved by synthesising $[Ni_2(L')_3]^{4+}$ cylinder and *pseudo*-rotaxanating it by mixing CB[10] into the solution. The $[Ni_2(L')_3]^{4+}\cdot$CB[10] pseudo rotaxane was then turned into $[Ni_2(L'')_3\cdot CB10]^{4+}$ rotaxane by reacting with the alkylating agent 2-(bromomethyl)pyridine and Hunig's base in aqueous methanol and heating at reflux overnight which produced the hexa-alkylated product. Lesser amounts of penta-alkylated product were also noticed in the MS, while this may be a product of the reaction it could also be formed under MS conditions in situ. The presence of this species was verified by paramagnetically shifted proton NMR, the cylinder peak was broadened which is consistent with rotaxanation. Increased stability via rotaxanation was demonstrated by treating $[Ni_2(L'')_3\cdot CB10]^{4+}$ rotaxane and $[Ni_2(L'')_3]^{4+}$ cylinder with EDTA which can complex the nickel ions from the cylinder resulting in near complete degradation in 24 hrs. We observed that even after 24 hrs, the rotaxane remained

intact which is consistent with the hypothesis of rotaxanation with CB[10] improving stability.

Having developed a rotaxane using our cylinder and CB[10] the next step was to assess the activity of the new cylinder species and the rotaxane itself. To do this, we first looked at the 3WJ binding activity of all new complexes and compared it to the parent (L) cylinder. In Figure 2.06 we can see that the control of $[Fe_2(L)_3]^{4+}$ behaves as expected, causing a characteristic shift to 3WJ. The $[Ni_2(L')_3]^{4+}$ cylinder behaves more poorly, with a reduction in the amount of 3WJ formed, though there is still a shift to 3WJ, it appears around 50% as effective as $[Fe_2(L)_3]^{4+}$. This is likely due to protonation of the imidazole group reducing the cationic charge of the cylinder in solution, thereby reducing the force of electrostatic attraction between the cylinder and polycationic 3WJ resulting in less 3WJ formation. The $[Ni_2(L'')_3]^{4+}$ cylinder appears to be the most effective cylinder, surpassing the 3WJ forming ability of $[Fe_2(L)_3]^{4+}$, this could be because of the aromatic picolyl groups increasing the binding strength to the 3WJ and

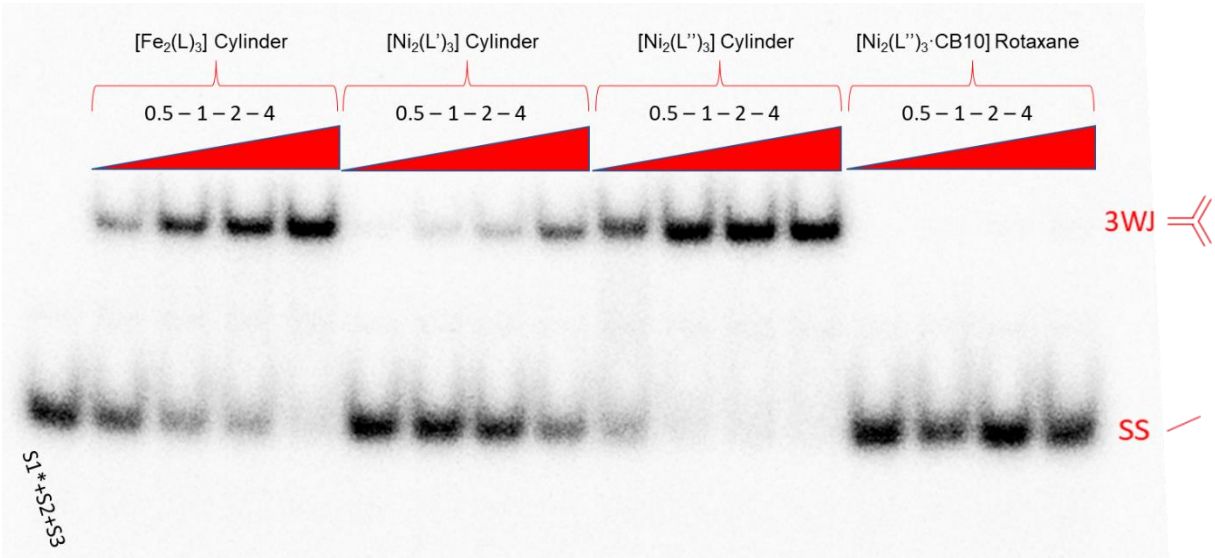


Figure 2.06: Shows the PAGE gel of DNA 3WJ (left to right) alone control (1) with different combinations of component oligos. Then upon incubation with $[Fe_2(L)_3]$ cylinder at 0.5,1,2 and 4 equivalents (2-5), upon incubation with $[Ni_2(L')_3]$ cylinder at 0.5,1,2 and 4 equivalents (6-9), upon incubation with $[Ni_2(L'')_3]$ cylinder at 0.5,1,2 and 4 equivalents (10-13) and finally upon incubation with $[Ni_2(L'')_3CB10]$ ROTAXANE at 0.5,1,2 and 4 equivalents (14-17).

increasing stability by stacking or groove binding. The $[Ni_2(L'')_3 \cdot CB10]^{4+}$ rotaxane shows no formation of 3WJ even at 4eq of rotaxane, this indicates that rotaxanation by CB[10] completely inhibits 3WJ binding, this serves as a highly efficient control of the cylinder's activity.

Following this, we compared the CT-DNA binding of the new cylinders and rotaxane using CD and LD. In Figure 2.07 we can see the spectra of $[Ni_2(L')_3]^{4+}$ cylinder shows a similar interaction with CT-DNA to that of the $[Ni_2(L)_3]^{4+}$ cylinder, showing a retention of the B-DNA structure in the CD between 200-300 nm and an induced cylinder signal above 300 nm. In the LD we can see a dramatic reduction in the signal at 260 nm, this shows $[Ni_2(L')_3]^{4+}$ cylinder is still condensing DNA similarly to that of $[Ni_2(L)_3]^{4+}$ cylinder. A binding curve was made (Figure A4 in appendix) by plotting the CD values at 250 nm against the corresponding concentrations. This allowed fitting with the one-site specific binding model in GraphPad Prism and subsequent determination of a dissociation constant (K_d) of $5x10^{-7}$. These results are positive as they show strong binding which is comparable to that of the $[Ni_2(L)_3]^{4+}$ cylinder and we want to provide

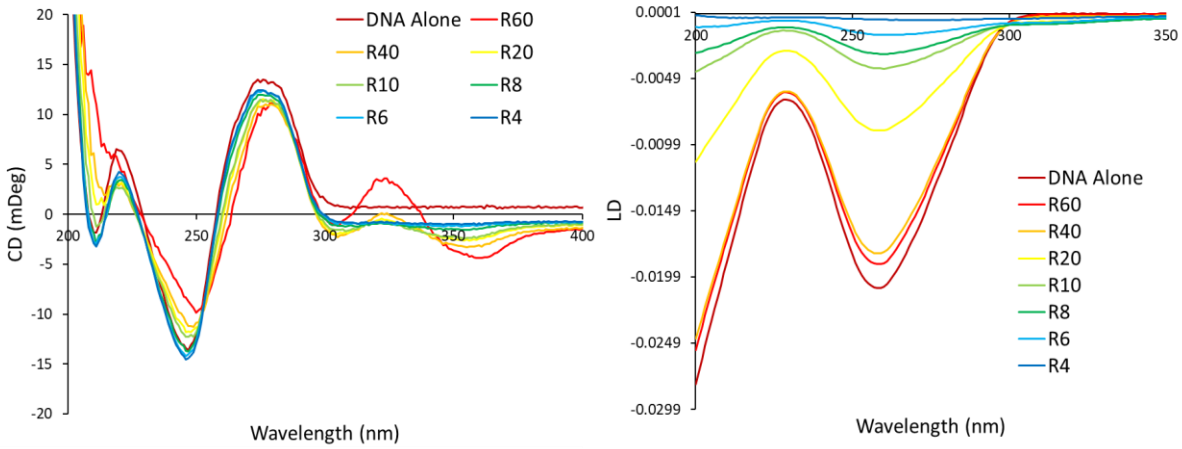


Figure 2.07: Shows the circular dichroism (left) and linear dichroism (right) spectra for titrations of $[Ni_2(L')_3]$ cylinder into calf thymus DNA (100 µM) in 10 mM sodium chloride and 1 mM sodium cacodylate. R values represent the ratio of DNA base pairs to complex.

added functionality without removing any of the biological interactions which have given the cylinders their intrigue.

Next, we looked at the interactions of $[Ni_2(L'')_3]^{4+}$ cylinder in Figure 2.08, the CD spectra also shows a retention of the primary B-DNA signal between 200-300 nm but there is also a large cylinder ICD signal between 300-400 nm which is an indicator of strong DNA binding. The LD spectra also shows potent DNA condensation comparable to that of other cylinders (Figures 2.04/5/7).[11] This cylinder shows stronger DNA binding effects than cylinder with ligand L, which is backed up by its superior 3WJ binding In the PAGE experiment (Figure 2.06). This is likely due to extra groove binding and π-stacking interactions because of the added picolyl capping groups at either end. We can see the same experiment with the $[Ni_2(L'')_3 \cdot CB10]^{4+}$ rotaxane in Figure 2.09 which shows both the CD and LD spectra. The CD spectra shows complete retention of the B-DNA signal with little to no change observed at all. The LD spectra also shows no condensation like the non-rotaxanated cylinder (figure 2.08) and in contrast shows a minor increase in signal which would correspond with an increase in the alignment of the DNA with the flow of the Couette cell. These spectra support the data from PAGE experiments (Figure 2.06) that rotaxanation inhibits DNA interactions. The slight

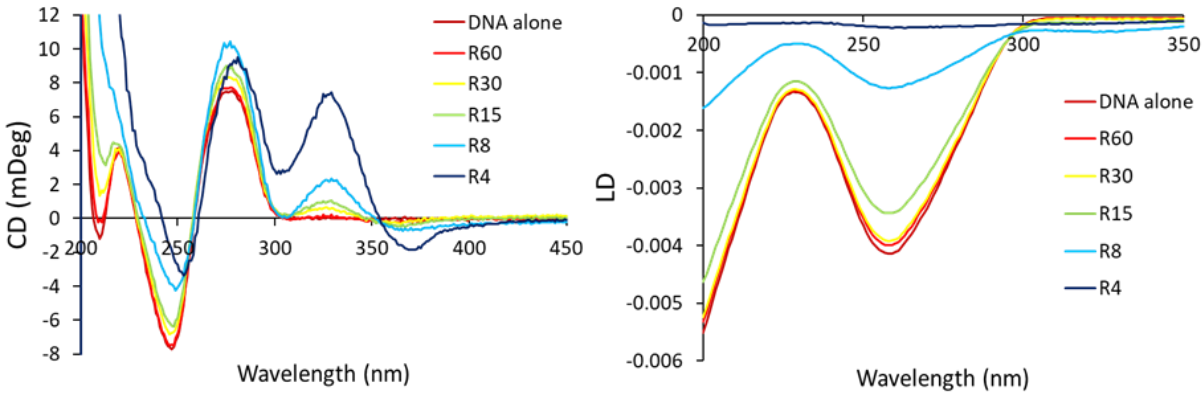


Figure 2.08: Shows the circular dichroism (left) and linear dichroism (right) spectra for titrations of $[Ni_2(L'')_3]$ cylinder into calf thymus DNA (100 μM) in 10 mM sodium chloride and 1 mM sodium cacodylate. R values represent the ratio of DNA base pairs to complex.

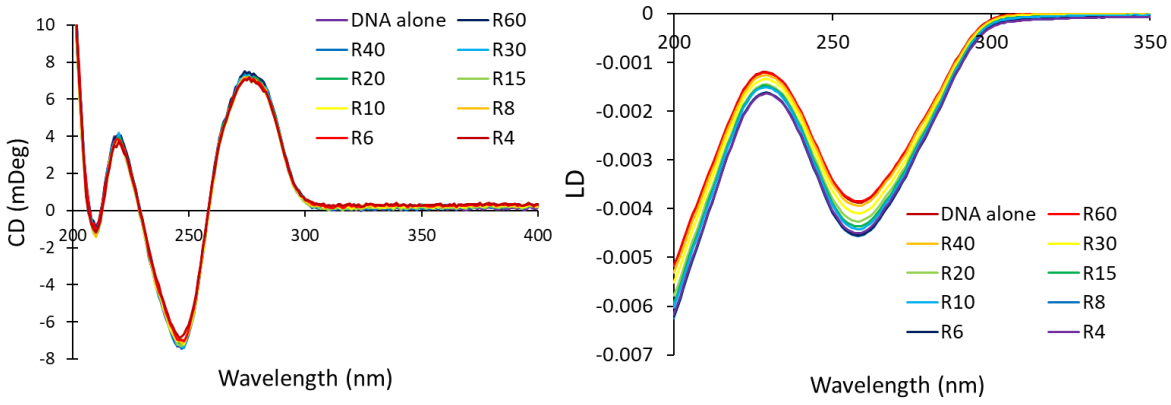


Figure 2.09: Shows the circular dichroism (left) and linear dichroism (right) spectra for titrations of [Ni_2(L'')$_3$·CB10] rotaxane into calf thymus DNA (100 µM) in 10 mM sodium chloride and 1 mM sodium cacodylate. R values represent the ratio of DNA base pairs to complex.

increase in orientation of DNA during the LD experiment could be explained by the rotaxane binding to the DNA's grooves which was shown by MD simulations.[28]

The next step was to establish the effectiveness of these new cylinder and rotaxane *in cellulo* and compare it to that of the L cylinder. Cell proliferation (MTT) assays showed a 72 hr IC_{50} for $[Ni_2(L'')_3]^{4+}$ of 55 ± 10 µM and 52 ± 5 µM in MDA-MB-231 and SKOV3 cells, respectively. This indicated that biological effects were maintained despite the new functionalisation's which allow rotaxanation. The $[Ni_2(L'')_3{\cdot}CB10]^{4+}$ rotaxane showed no cytotoxic effect in cell proliferation (MTT) assays with a 72 hr IC_{50} of greater than 140 µM in MDA-MB-231 cells. This supports the *in vitro* experimental data that rotaxanation inhibits biological interactions and effectively stops the cylinders activity.

Finally, we explored the ability for the partially capped cylinder to de-thread the rotaxane towards the aim of controlled release. We observed upon mixing 3/4/5 capped $[Ni_2(L'')_3{\cdot}CB10]^{4+}$ rotaxane with memantine (a competitor guest molecule for CB[10]) or $[Fe_2(L)_3]^{4+}$ that 3 and 4 capped rotaxane is displaced and after a longer period 5 capped rotaxane is also displaced. Fully (6) capped $[Ni_2(L'')_3{\cdot}CB10]^{4+}$ rotaxane is not displaced even by 28 hrs, further demonstrating the inert nature of the fully capped must have one side with 0 or 1 cap, and 4 capped rotaxane must have

one side with 1 or 2 caps. However, the 5 capped cylinder must have one side with 2 caps, these observations may explain why 3 and 4 capped cylinders are displaced rapidly whereas 5 capped cylinder takes a longer period to be de-threaded. This suggests removal of only 1 cap is required to achieve release, but removal of 2 caps from one side (3 caps minimum to achieve in 100% of the population) is optimal for immediate release. This hypothesis is corroborated by the effect that added steric bulk and alkylation from more caps would present. We mixed $[Ni_2(L'')_3 \cdot CB10]^{4+}$ rotaxane with 3WJ in a PAGE gel (Figure 2.10) which shows that some cylinder is capable of de-threading the rotaxane and forming a small amount of 3WJ. These results highlight the real possibility of controlled release, and therefore controlled activity of cylinders by a mechanism which removes capping groups from the rotaxane.

Overall, we have shown the development of a new rotaxane which used a metallo-supramolecular cylinder as the axle and CB[10] as the macrocycle. We observed that *pseudo*-rotaxanation alone was insufficient in controlling the activity of the cylinders. However, it did little to no impact on the cylinder's biological activity which is highly desirable characteristic when the product of a de-capping reaction to release the cylinder from a full rotaxane, is a *pseudo*-rotaxane.

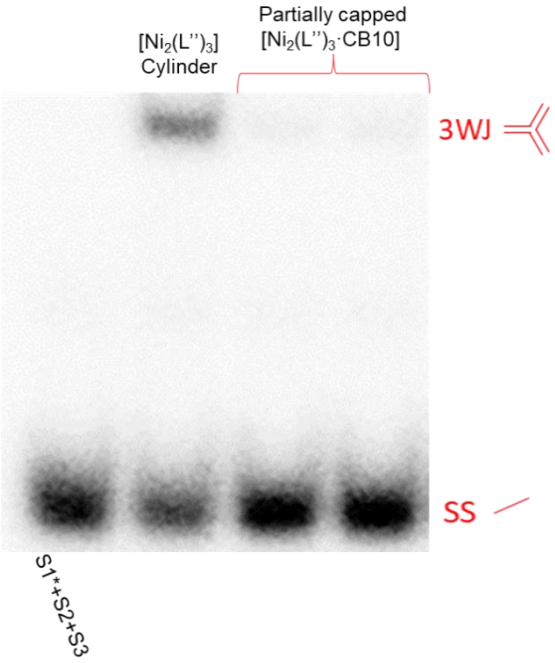


Figure 2.10: Shows the PAGE gel of DNA 3WJ (left to right) alone control (1) with different combinations of component oligos. Then upon incubation with $[Ni_2(L'')_3]$ cylinder at 1 equivalent (2) and upon incubation with partially capped $[Ni_2(L'')_3 \cdot CB10]$ rotaxane at 1 equivalent (3-4).

We found that upon full rotaxanation of the cylinder with CB[10] by using picolyl groups (3 each side) the observed biological activity

was effectively stopped. This indicates that CB[10] (whilst rotaxanated) is capable of interfering with the biological interactions that cylinders have *in vitro*, whilst also increasing their stability. It also shows that the picolyl stopper groups are effective at holding the CB[10] in place and preventing de-threading of the rotaxane whilst the cylinder is fully (6) capped.

Finally, we observed that when rotaxanes are not fully capped (5 or less caps) the cylinder is capable of de-threading. This is likely due to the sufficiently reduced steric bulk because of less caps, which allows the cylinder to leave the CB[10] cavity. When this occurs, we can see that the cylinder can still for DNA 3WJ which indicates it is still biologically active. This opens the prospect of using these rotaxanes as a basis for a controlled release system for metallo-supramolecular cylinders. These are very desirable properties for a drug molecule as they could dramatically increase efficacy and significantly reduce side effects, resulting in a potent therapeutic agent. Controlled release may also be achieved in response to different stimuli such as light, enzymes or chemical environment, all of which are capable of tailoring or completely changing the biological effects of this rotaxane, which highlights the versatility a system such of this may have. Future work which is in development involves the use of glutathione to de-cap a similar rotaxane (see chapter 2.4) which would give the rotaxane preferential release in a tumour environment,[43] thereby increasing efficacy against cancerous cells and reducing side effects.

This work represents the first case where a metallo-supramolecular architecture has been used as the central axle for a rotaxane. Conventionally, a linear thread guest molecule is used as the axle, however this metallo-supramolecular structure offers unique and useful properties. These include charge, photophysics and structural

properties that are difficult to achieve with purely organic structures. Rotaxanating these cylinders also offers control over their activity, with a link between the number of caps and kinetic release. This opens the possibility for controlled release with a suitable cap which is explored in section 2.4. A rotaxanated metal complex discussed in section 1.3.5 is an example of how controlled release may be achieved in response to irradiation and enzyme interactions.

2.3: Slippage - An alternative method for cylinder·CB[10] based Rotaxane formation

The work in this section follows on from the work in section 2.2 and was undertaken by the author in that context.

Forming a rotaxane from metallo-supramolecular cylinder was initially done (chapter 2.2) using a post-synthetic modification method where the *pseudo*-rotaxane was formed followed by an alkylation reaction to form the caps. This can result in incomplete alkylation and produce a rotaxane that is not fully capped which can de-thread as shown previously. To avoid this, we would have to develop a method of rotaxanation which could allow for all 6 caps being present. To do this, fully capped $[Ni_2(L'')_3]^{4+}$ cylinder could first be formed from pre-alkylated L'' ligand (which has been purified) and nickel chloride hexahydrate. This would remove the possibility of only 5 or less alkylation's occurring and allows us to achieve a pure 6 capped cylinder. This, however, presents itself with an issue of being unable to be rotaxanated due to the bulky alkyl groups.

We have hypothesised that rotaxanation may be possible by a "slippage" mechanism, this would involve the CB[10] slipping over the picolyl stopper groups (shown as red in Figure 2.11) of one end. We can see that rotaxanation does not appear to occur upon

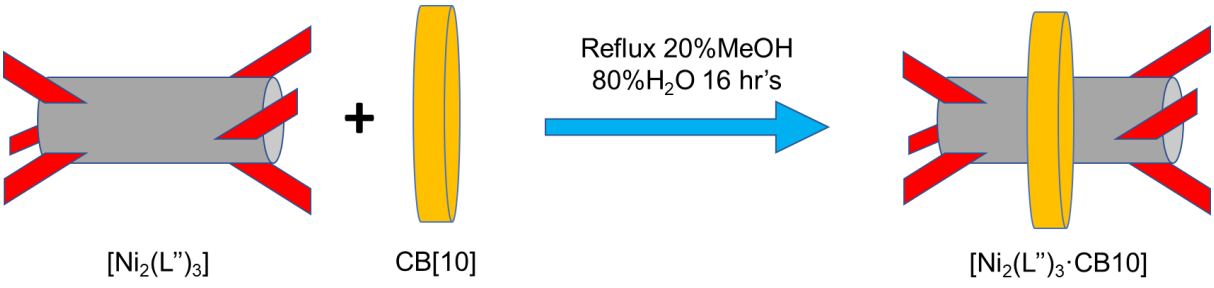


Figure 2.11: Shows the slippage reaction scheme for forming full 6 capped $[Ni_2(L'')_3{\cdot}CB10]$ rotaxane from pre-alkylated $[Ni_2(L'')_3]$ cylinder.

mixing $[Ni_2(L'')_3]^{4+}$ cylinder and CB[10] as the CB[10] does not dissolve even when left stirring overnight. However, when heating to reflux in methanolic water for 16 hrs we can see the amount of CB[10] reduces drastically. This is a strong indicator of host-guest complexation by the CB[10] as the solubility is enhanced when its cavity is occupied. To investigate this, we looked at a sample via mass spectrometry to see if we could find a rotaxane peak. The mass spectra can be seen in Figure 2.12, spectra B shows the spectra for $[Ni_2(L'')_3]^{4+}$ cylinder alone and there is a prominent $[Ni_2(L'')_3]^{4+}$ peak at 431 m/z. There are also peaks present at 408 m/z and 386 m/z which match up with 5 and 4 alkylated $[Ni_2(L'')_3]^{4+}$ cylinder respectively. Spectra A shows $[Ni_2(L'')_3]^{4+}$ cylinder after incubation with 1.34 eq CB[10] in 20% methanol and 80% water at reflux at 60 °C for 16 hrs. The most prominent peak is at 847 m/z which corresponds to the $[Ni_2(L'')_3{\cdot}CB10]^{4+}$ rotaxane. This suggests that the rotaxane is capable of being formed using this method (Figure 2.11). There are also peaks at 824 and 801 m/z which correspond to the 5 and 4 capped rotaxane respectively which were present in the control. This shows that the CB[10] may also slide over an end of the cylinder with 2 picolyl groups. Notably the $[Ni_2(L'')_3]^{4+}$ cylinder peaks corresponding to 5 and fewer caps appear to have all but gone whilst the 6-cap peak remains. This suggests it may be easier to rotaxanate 5 and fewer capped cylinders using this slippage procedure which would agree with the lower steric bulk at either end they would have, lowering the barrier for rotaxanation. The peak at 431 m/z corresponds to the $[Ni_2(L'')_3]^{4+}$ cylinder, this suggests that not all the cylinders could be rotaxanated under these conditions.

This work highlights another method for rotaxanation of metallo-supramolecular cylinders. It could also give rise to a method which reduces unwanted products such

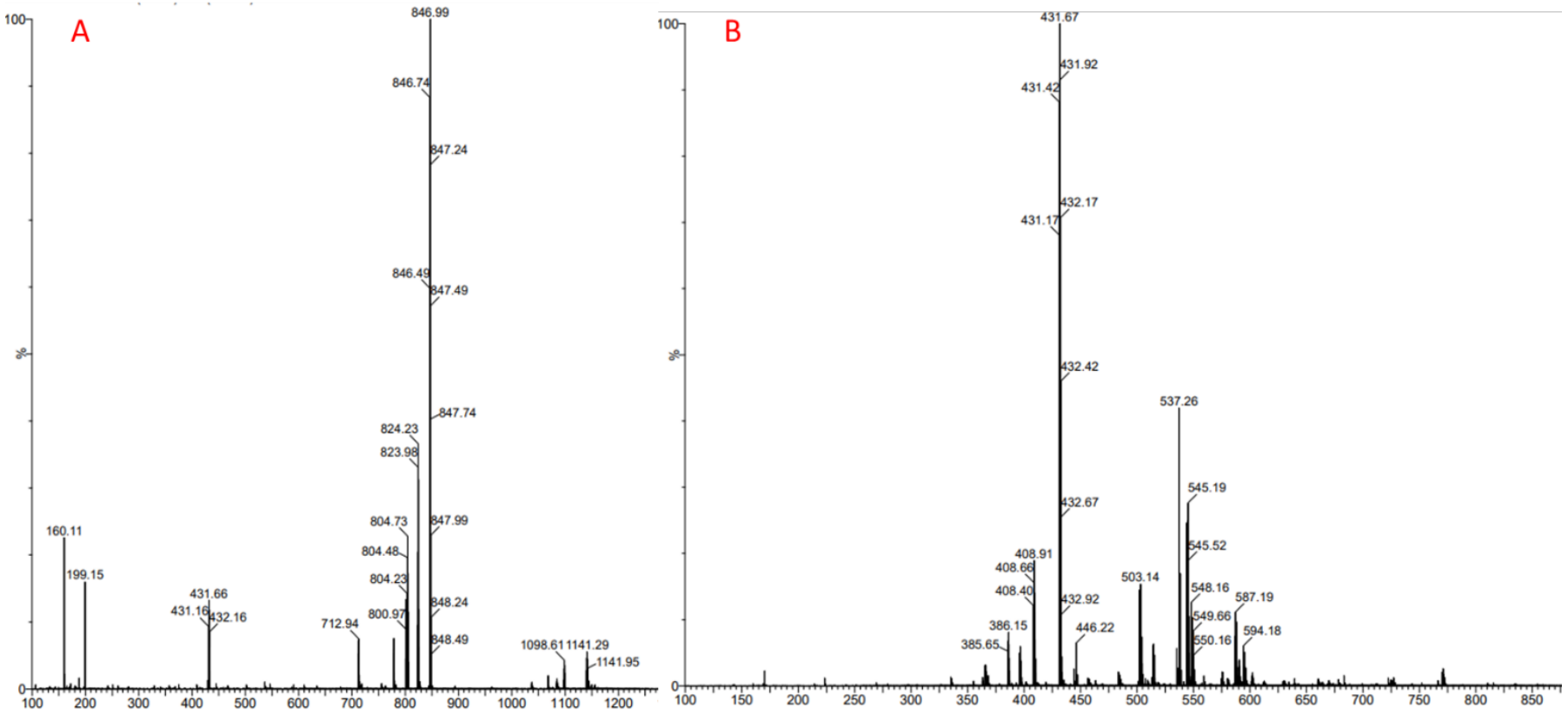


Figure 2.12: Shows 2 mass spectra A and B. Spectra A shows the MS of $[Ni_2(L'')_3]$ cylinder after incubation with 1.34 eq CB[10] in 20% methanol 80% water at reflux for 16 hrs. Spectra B shows the MS of $[Ni_2(L'')_3]$ cylinder alone before CB[10] was added.

as partially alkylated cylinders by pre-forming the cylinder from purified ligand and rotaxanating by this slippage procedure. Conditions such as solvent and temperature could influence this reaction. The correct solvent/mix of solvents is important to solubilise the cylinder for *pseudo*-rotaxanation by the CB[10], whilst water presence is important to drive the CB[10]'s host guest interactions. Temperature is important to optimise as you would like to improve the kinetics of rotaxanation whilst not destabilising the cylinder. Future work would involve modifying these conditions and observing the effect on complete rotaxanation of the samples. The limitations of this work include its application to different rotaxanes, as the stopper group will have a significant impact on whether slippage is possible.

2.4: De-capping Di-Nitrobenzene capped cylinder rotaxanes - towards controlled release

The work described in this section 2.2 comprises part of a manuscript approaching submission entitled “Thiol triggered uncaging of DNA 3-way junction binding nano cylinder from rotaxane”. The work was carried out in collaboration with colleagues in the group and external collaborators with the co-authors of the paper being Aditya Garai, Ross T. Egan, James S. Craig, Lazaros Melidis, Hugo Williams, Christopher M. Williams, Fengbo Liu, Simin Liu, Neil Champness, Sarah Griffin, Alex Pöthig, Nikolas J. Hodges and Michael J. Hannon. This section focuses primarily on my contributions, but to contextualise and rationalise the studies, some aspects of the wider studies from others are included, where this is this case, it is pointed out. The work that is discussed and supported by Figures represents my contributions, comprising optimising *in vitro* function, gel electrophoresis and cell studies.

We have established that we can form a rotaxane (chapter 2.2) using metallo-supramolecular cylinders and the cucurbituril CB[10]. We found that CB[10] enhances the stability of the cylinder and effectively switches off the DNA binding and cellular toxicity of this cylinder. However, we also noted that *pseudo*-rotaxanated (no caps) cylinder can leave the CB[10] to bind a preferred biological target. This was observed by the formation of 3WJ in PAGE experiments, ICD/ILD signals in spectroscopic studies and an IC_{50} comparable to that of the free cylinder in cell studies. We also observed in samples of $[Ni_2(L'')_3 \cdot CB10]^{4+}$ rotaxane where some rotaxane had 5 or fewer caps 3WJ binding and formation still occur which indicates the cylinders capability to de-thread CB[10] and bind DNA targets whilst partially capped. These

properties highlight the suitability of this class of rotaxane to be an active targeting drug.

The next step towards this aim was to change the picolyl capping groups we used on the initial rotaxane to groups which are capable of being removed under desired conditions. The conditions chosen were those of glutathione (GSH) sensitivity with the aim of increasing activity disproportionately. This would occur because cancer cells have increased production of GSH which would result in increased cleavage of capping groups and therefore increases intracellular activity.[43,49]

To achieve this activity, we needed to develop a cap which cleaves in the proximity of glutathione. Figure 2.13 shows the ligand L^{DNB} which was made for this purpose, it is based on L' which was used in the $[Ni_2(L')_3]^{4+}$ cylinder but the non-metal bounding nitrogen is bound to a di-nitrobenzene (DNB) group. This group is similar in terms of steric bulk to the picolyl cap used in L'', which should allow $[Ni_2(L^{DNB})_3 \cdot CB10]^{4+}$ to behave as a rotaxane with a mechanically locked CB[10] around the di-aniline units. This DNB group was chosen as it has been shown to cleave in the presence of GSH to produce a DNB-GSH adduct which should leave behind the $[Ni_2(L')_3] \cdot CB[10]^{4+}$ *pseudo*-rotaxane.[50,51] The proposed mechanism for this reaction can be seen in Figure 2.14.

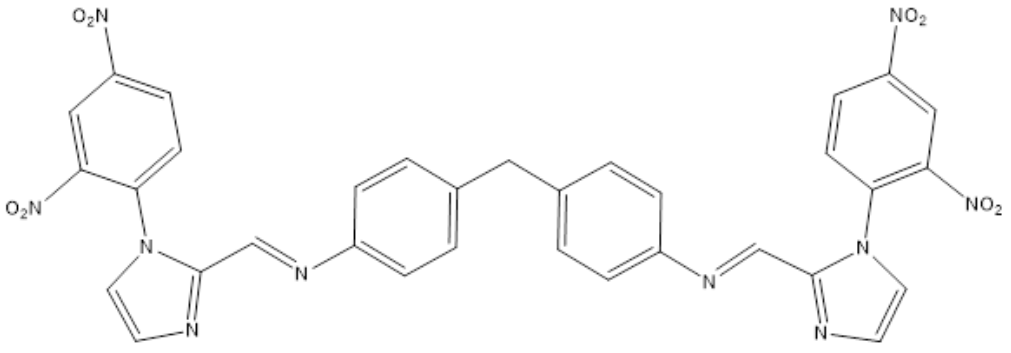


Figure 2.13: Shows the ligand structure of L^{DNB} which is used to form the di-nitrobenzene (DNB) cylinder and rotaxane.

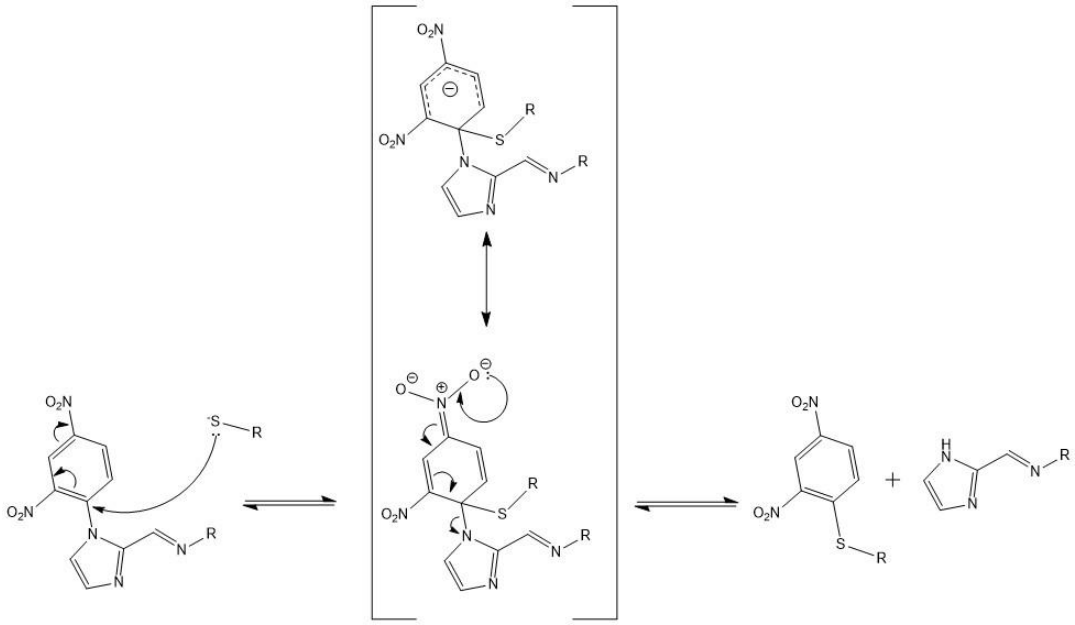


Figure 2.14: Shows the proposed reaction scheme for L^{DNB} reacting with GSH. R at the imine group represents the rest of L^{DNB} and R attached to S^- represents GSH. The Meisenheimer intermediate can be seen in the upper central part of the reaction scheme.

Synthesis, characterization, and establishment of the de-capping process *in vitro* using 2-Mercaptoethanol were done by Dr Aditya Garai and Ross Egan. 2-Mercaptoethanol was used in place of GSH during ESI-MS due to issues with adducts overloading the mass spectra, and initial solubility issues in methanol/water. It was also established that the slippage mechanism reported in chapter 2.3 does not work with the $[Ni_2(L^{DNB})_3]^{4+}$ cylinder, this could be due to the absences of a methyl spacer between the imidazole nitrogen and benzene ring, which would have allowed a greater degree of rotational freedom. Alternatively, the nitro groups could be providing enough added steric bulk to prevent slippage occurring.

Having established the functionality of the $[Ni_2(L^{DNB})_3{\cdot}CB10]^{4+}$ rotaxane, the next step was to explore its functionality with biological substrates. In Figure 2.15 we can see the PAGE gel of 3WJ incubated with $[Ni_2(L^{DNB})_3]^{4+}$ cylinder and $[Ni_2(L^{DNB})_3{\cdot}CB10]^{4+}$ rotaxane with 10 eq of 2-mercaptoethanol. All components of each lane were incubated together for 1 hr at 37.5 °C prior to being ran on the gel. We can observe

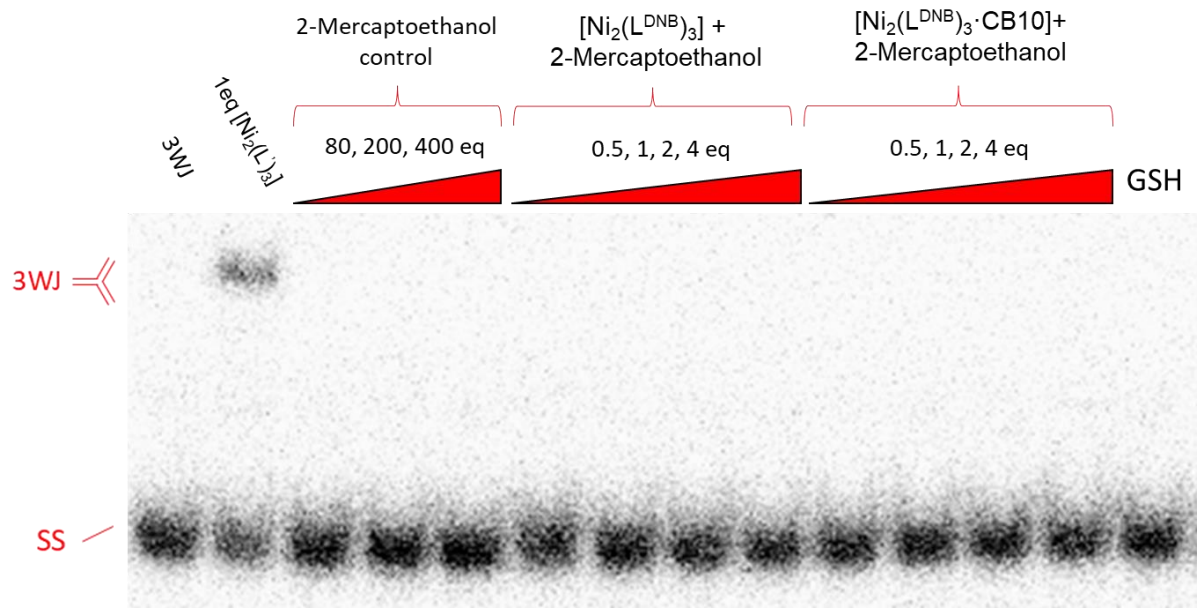


Figure 2.15: Shows the PAGE gel of DNA 3WJ (left to right) of 3WJ control (1), $[Ni_2(L')_3]$ cylinder and 3WJ at 1:1 (2). 2-Mercaptoethanol and 3WJ controls at 80:1, 200:1 and 400:1 (3-5). $[Ni_2(L^{DNB})_3]$ cylinder, 2-Mercaptoethanol (10 eq) and 3WJ at 0.5, 1, 2 and 4 eq (6-9). $[Ni_2(L^{DNB})_3{\cdot}CB10]$ rotaxane, 2-Mercaptoethanol (10eq) and 3WJ at 0.5, 1, 2 and 4 eq (10-13) and lastly a GSH and 3WJ control at 400 eq.

that $[Ni_2(L')_3]^{4+}$ cylinder was used as the control as it serves as the de-capped cylinder product. This $[Ni_2(L')_3]^{4+}$ cylinder forms 3WJ (if weaker than $[Ni_2(L)_3]^{4+}$) however the DNB cylinders and rotaxane show no formation of 3WJ at any point. 2-Mercaptoethanol and GSH also shows no effect on the 3WJ oligos. This gel raises questions about the optimal conditions for cylinder release, given the weak intensity of the positive control which we hypothesise was associated with pH and protonation states, we decided to lower the pH of subsequent experiments from 8.30 to 7.05. We also decided to increase the ratios of complex:3WJ to observe if only a small proportion of rotaxane is being de-capped. Figure 2.16 shows the PAGE gel using these new conditions. We can see the $[Ni_2(L')_3]^{4+}$ cylinder control with a comparably unchanged 3WJ band and a 3WJ band from the $[Ni_2(L)_3]^{4+}$ cylinder for comparison. The $[Ni_2(L^{DNB})_3]^{4+}$ cylinder and $[Ni_2(L^{DNB})_3{\cdot}CB10]^{4+}$ rotaxane alone show no formation of 3WJ. It is not a surprise that $[Ni_2(L^{DNB})_3{\cdot}CB10]^{4+}$ rotaxane does not show 3WJ formation, however its absence with $[Ni_2(L^{DNB})_3]^{4+}$ cylinder is notable when its most

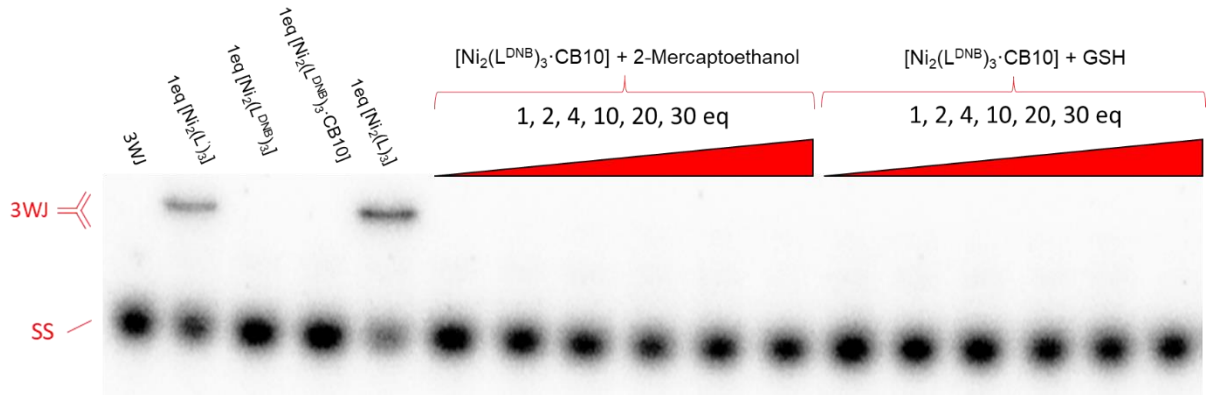


Figure 2.16: Shows the PAGE gel of DNA 3WJ (left to right) of 3WJ control (1), $[Ni_2(L')_3]$ cylinder and 3WJ at 1:1 (2). $[Ni_2(L^{DNB})_3]$ cylinder and 3WJ 1:1 (3). $[Ni_2(L^{DNB})_3{\cdot}CB10]$ rotaxane and 3WJ at 1:1 (4). $[Ni_2(L)_3]$ cylinder and 3WJ at 1:1 (5). $[Ni_2(L^{DNB})_3{\cdot}CB10]$ rotaxane, 2-Mercaptoethanol (10 eq) and 3WJ at 1, 2, 4, 10, 20 and 30 eq (6-11). $[Ni_2(L^{DNB})_3{\cdot}CB10]$ rotaxane, GSH (10 eq) and 3WJ at 1, 2, 4, 10, 20 and 30 eq (12-17).

comparable predecessor, $[Ni_2(L'')_3]^{4+}$ cylinder, showed remarkable 3WJ formation. One possible explanation could be that the rigidity of the DNB groups (which are missing a methyl spacer between themselves and the imidazole ring) prevents optimal base stacking interactions to the DNA bases. Alternatively, this combined with the steric bulk from the NO_2 groups may prevent the formation of 3WJ outright. We can see that neither GSH nor 2-mercaptoethanol produce any active cylinder species when incubated with $[Ni_2(L^{DNB})_3{\cdot}CB10]^{4+}$ rotaxane even at 30 eq. This is surprising as *in vitro* de-capping experiments have shown the presence of partially and fully de-capped rotaxane after incubation with 2-mercaptoethanol. One explanation could be that the reaction is not occurring for an unknown reason, possibly linked to dimethyl sulfoxide (DMSO) which was used to aid solubility.

To address this, we de-capped a sample of the $[Ni_2(L^{DNB})_3{\cdot}CB10]^{4+}$ rotaxane separately in acetonitrile (no DMSO) using 2-mercaptoethanol (3 hrs 37 Type equation here.C), removed the acetonitrile under vacuo and re-dissolved in 50:50 methanol: water. We then used this pre-treated sample in the next 3WJ-PAGE gel to

observe if this resulted in 3WJ formation. For this experiment onwards we also switched from radiolabelled PAGE to fluorescent PAGE due to availability of ^{32}P.

Figure 2.17 shows the results of the PAGE gel with the pre-treated $[Ni_2(L^{DNB})_3{\cdot}CB10]^{4+}$ rotaxane incubated with 3WJ. Notably in the $[Fe_2(L)_3]^{4+}$ cylinder positive control there is no obvious 3WJ band, however when the contrast is adjusted a band became visible with sub-background contrast in the region, we would expect the 3WJ band. This could be explained by Förster resonance energy transfer (FRET) between the DNA dye, SYBR Gold, and the $[Fe_2(L)_3]^{4+}$ cylinder. Curiously, this reverse contrast is only seen when the $[Fe_2(L)_3]^{4+}$ cylinder is bound to the 3WJ and does not occur with any other DNA structure we have looked at so far with this complex. Lanes including the pre-treated $[Ni_2(L^{DNB})_3{\cdot}CB10]^{4+}$ rotaxane show small but increasing amounts of 3WJ formation. At higher equivalents there is prominent smearing of the bands in the lane

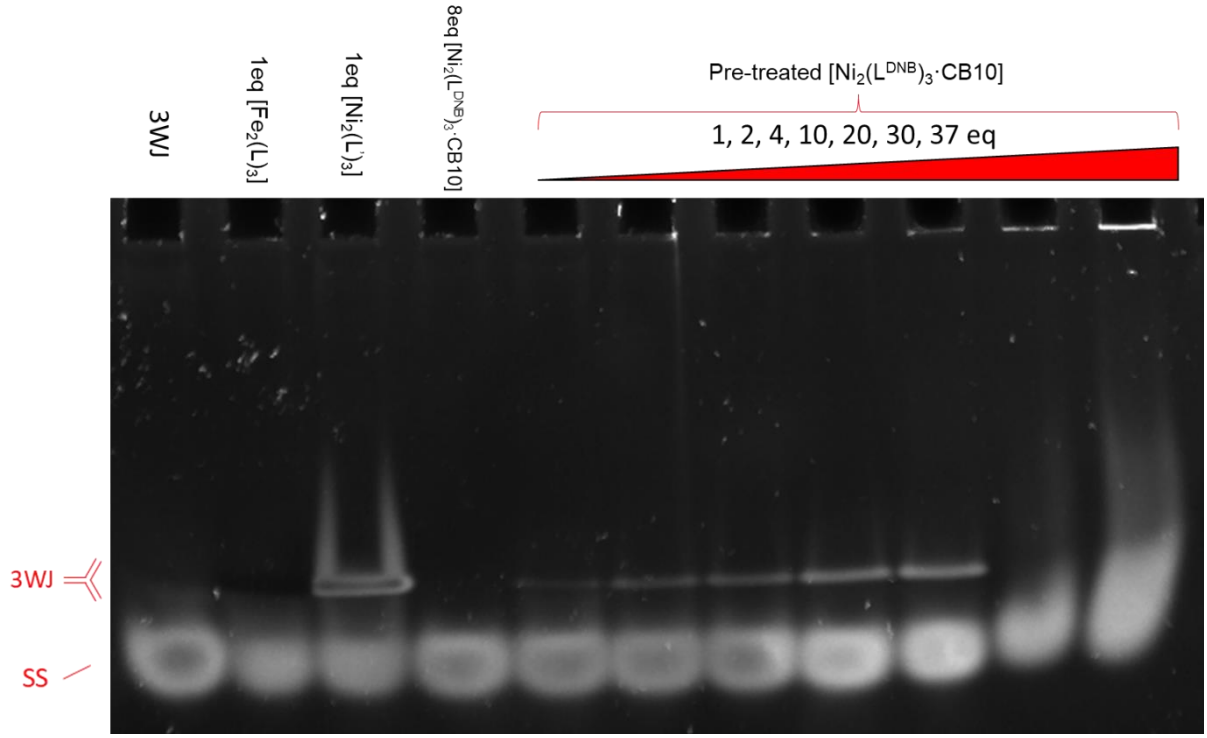


Figure 2.17: Shows the PAGE gel of DNA 3WJ (left to right) of 3WJ control (1), $[Fe_2(L)_3]$ cylinder and 3WJ at 1:1 (2). $[Ni_2(L')_3]$ cylinder and 3WJ 1:1 (3). $[Ni_2(L^{DNB})_3{\cdot}CB10]$ rotaxane and 3WJ at 8:1 (4). $[Ni_2(L^{DNB})_3{\cdot}CB10]$ rotaxane (pre-treated with 2-Mercaptoethanol in acetonitrile for 3 hrs at 37 °C, acetonitrile removed and redissolved in 50:50 MeOH:H_2O) and 3WJ at 1, 2, 4, 10, 20, 30 eq (5-11).

°and some precipitation in the well, this could be due to oversaturation or precipitation of CB[10]. The formation of 3WJ where previously there was none, demonstrates the capability of $[Ni_2(L^{DNB})_3{\cdot}CB10]^{4+}$ rotaxane to release active cylinder species upon de-capping. The previous inability to form active cylinder species is likely due to the ability of DMSO to break down the cylinder, hence excluding this prevents active cylinder species being degraded. Alternatively, there may be steric conflict between the de-cappant and the $[Ni_2(L^{DNB})_3{\cdot}CB10]^{4+}$ rotaxane due to it interacting with nucleic acids. To investigate the de-capping ability further, we explored the effectiveness of other de-cappants using the same sample preparation.

Figure 2.18 Shows the PAGE gel of $[Ni_2(L^{DNB})_3{\cdot}CB10]^{4+}$ rotaxane after pre-treatment with the two different de-cappants NaSH and GSH. We can see that GSH treatment results in a small amount of DNA 3WJ which becomes more evident as greater equivalents of rotaxane is added. NaSH treatment by comparison shows considerable

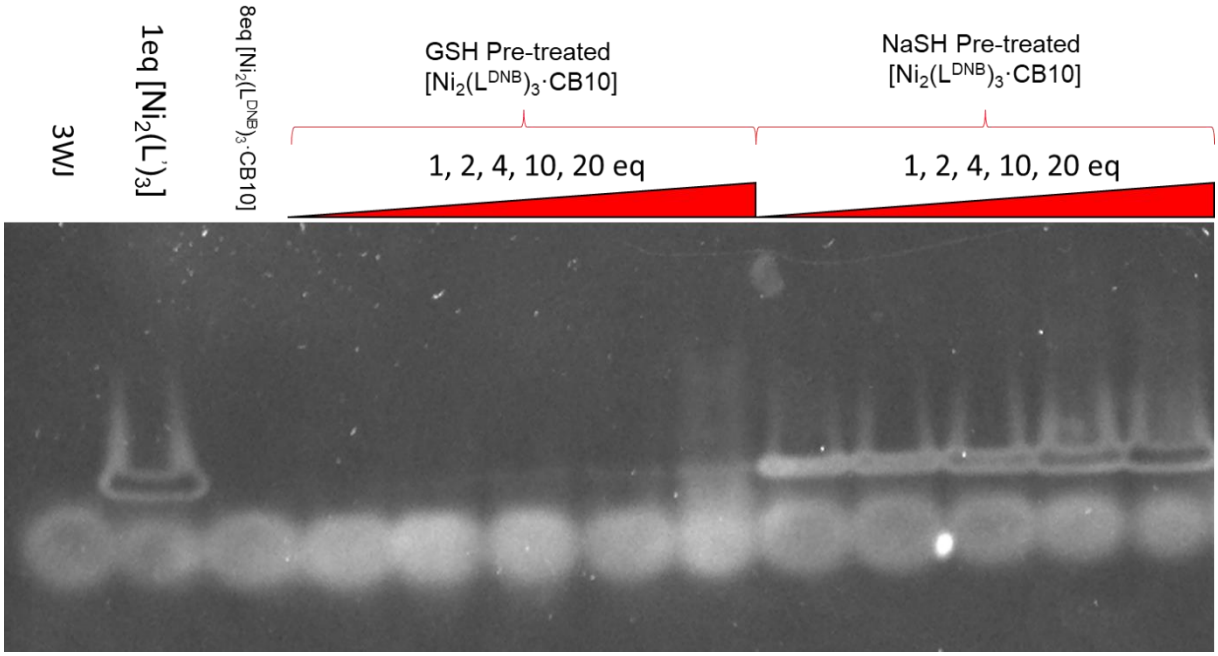


Figure 2.18: Shows the PAGE gel of DNA 3WJ (left to right) of 3WJ control (1), $[Ni_2(L')_3]$ cylinder and 3WJ at 1:1 (2). $[Ni_2(L^{DNB})_3{\cdot}CB10]$ rotaxane and 3WJ at 8:1 (3). $[Ni_2(L^{DNB})_3{\cdot}CB10]$ rotaxane (pre-treated with GSH (4-8) and NaSH (9-13) in acetonitrile for 3 hrs at 37 °C, acetonitrile removed and redissolved in 50:50 MeOH:H_2O) and 3WJ at 1, 2, 4, 10, 20, 30 eq (4-13).

3WJ formation, though is still weaker than the control of $[Ni_2(L')_3]^{4+}$. These results could be due to the poor solubility of GSH in acetonitrile compared to the much greater solubility of NaSH. Given GSH is the desired de-cappant and will be the available de-cappant *in vivo*, we changed the pre-treatment process to better reflect the *in vivo* environment. We changed the solvent to 10% acetonitrile 90% water and included the tris-boric acid buffer and sodium chloride. This also removed the need to remove the solvent and resuspend in a different solvent mixture, therefore no methanol was included in these samples.

Figure 2.19 shows the PAGE gel where the $[Ni_2(L^{DNB})_3{\cdot}CB10]^{4+}$ rotaxane was incubated with 10 mM of de-cappant in aqueous TB buffer at pH 7.05 as opposed to acetonitrile. The rotaxane control shows some smearing which is likely because of the higher concentration and electrostatic interactions. Overall, 3WJ band shifts are more pronounced with 2-mercaptoethanol and GSH. NaSH shows a much weaker 3WJ band than the previous gel, this is likely due to decreasing solubility in the aqueous buffer. The significant increase in the proportion of 3WJ with GSH treatment is of foremost

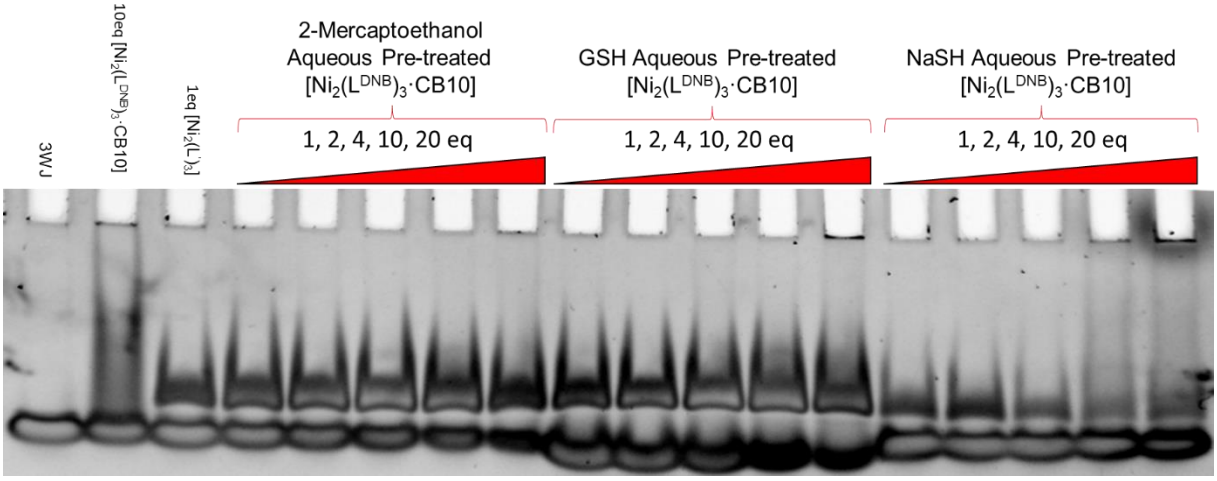


Figure 2.19: Shows the PAGE gel of DNA 3WJ (left to right) of 3WJ control (1), $[Ni_2(L^{DNB})_3{\cdot}CB10]$ rotaxane and 3WJ at 10:1 (2). $[Ni_2(L')_3]$ cylinder and 3WJ at 1:1 (3). $[Ni_2(L^{DNB})_3{\cdot}CB10]$ rotaxane (pre-treated with 10 mM 2-Mercaptoethanol (4-8), GSH (9-13) and NaSH (14-18) in 10% acetonitrile 90% water with tris boric acid buffer and NaCl 10 mM at pH 7.05 for 3 hrs at 37 °C, this was directly added to the DNA samples) and 3WJ at 1, 2, 4, 10, 20, 30 eq (4-18).

importance as these conditions are also the most reflective of *in vivo* conditions so far. This gel shows the proof of concept that the $[Ni_2(L^{DNB})_3 \cdot CB10]^{4+}$ rotaxane can release active cylinder species upon removal of the caps by treatment with GSH *in vitro* under biologically relevant conditions. We also observed that 10 eq compared to 10 mM of GSH showed considerably less 3WJ formation, however the trend remains the same (Figure 2.20). This could indicate that de-capping and release of active cylinder may be dependent on the concentration of GSH as theoretically only 1 eq of GSH (or any de-cappant) is required to remove a capping group. This could further support the aim of achieving greater release in the presence of higher GSH level like those associated with the cancer cell environment.

In the final PAGE gel, we used memantine which is a competitor guest for the CB10 so assess whether it influenced increased release of active cylinder species. We can see this PAGE gel in Figure 2.21, the trends in 3WJ formation between de-cappants appear the same as those in Figure 2.20 without Memantine. However, at 20 eq there

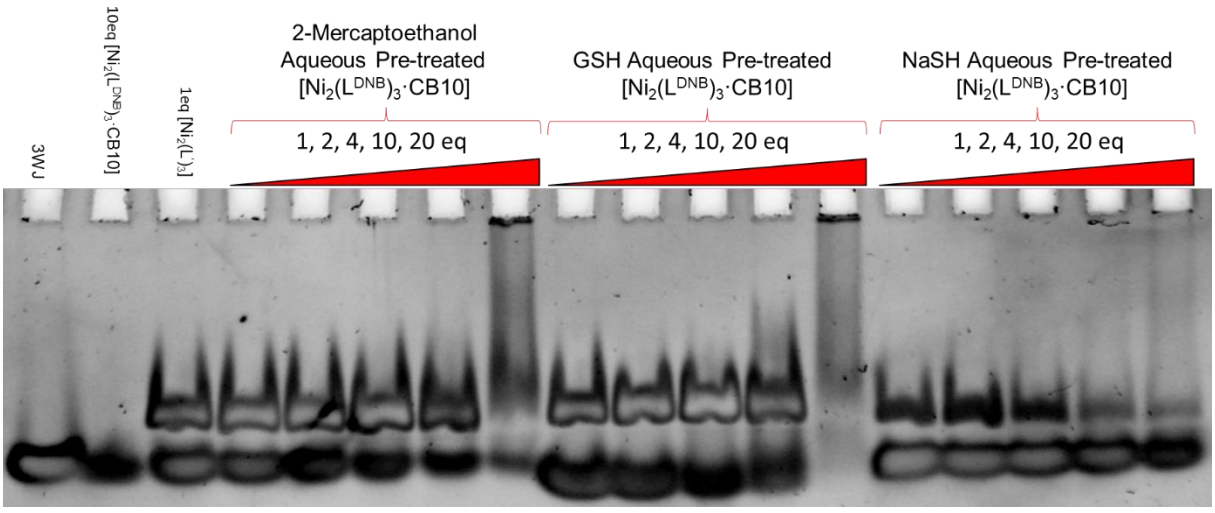


Figure 2.21: Shows the PAGE gel of DNA 3WJ with 10 mM memantine in all lanes (left to right) of 3WJ control (1), $[Ni_2(L^{DNB})_3 \cdot CB10]$ rotaxane and 3WJ at 10:1 (2). $[Ni_2(L')_3]$ cylinder and 3WJ at 1:1 (3). $[Ni_2(L^{DNB})_3 \cdot CB10]$ rotaxane (pre-treated with 10 eq to complex of 2-Mercaptoethanol (4-8), GSH (9-13) and NaSH (14-18) in 10% acetonitrile 90% water with tris boric acid buffer and NaCl 10 mM at pH 7.05 for 3 hrs at 37 °C, this was directly added to the DNA samples) and 3WJ at 1, 2, 4, 10, 20, 30 eq (4-18).

is a noticeable difference as smearing and precipitation occur with both 2-mercaptoethanol and GSH. This is a strong indicator that there is greater release of active cylinder species due to being displaced from the CB[10] ring by memantine. The smearing and precipitation are likely due to greater quantities of cylinder binding to the DNA and causing aggregation and precipitation. This interaction between memantine and $[Ni_2(L^{DNB})_3 \cdot CB10]^{4+}$ rotaxane suggests the active species is the cylinder but also that the presence of a competitor guest for CB[10] could improve release and therefore increase biological effects.

Having explored the interactions of the $[Ni_2(L^{DNB})_3 \cdot CB10]^{4+}$ rotaxane *in vitro* we moved onto cell studies to explore its biological effects. To do this we did MTT assays using the MDA-MB-231 cell line which we dosed with 50 μM of complexes which were pre-treated both with and without GSH. This MTT assay was carried out by my co-supervisor Dr Nikolas Hodges with samples preparation and experimental design was done by myself. This was due to restricted access to cell culture hoods because of Covid-19 social distancing restrictions. We can see in Figure 2.22 that with and without GSH treatment, both $[Ni_2(L^{DNB})_3 \cdot CB10]^{4+}$ rotaxane and $[Ni_2(L^{DNB})_3]^{4+}$ cylinder produce statistically identical absorbances in the MTT assay. This indicates that pre-treatment with GSH does not play an active role in increasing the proportion of active cylinder species which are released from the rotaxane, or the toxicity of the cylinder alone. This appears contradictory to the point of development at first glance; however, cells naturally produce GSH, and MDA-MB-231 cells are a breast cancer cell line and therefore would have greater levels of GSH again. Given both treated and un-treated $[Ni_2(L^{DNB})_3 \cdot CB10]^{4+}$ rotaxane have statistically identical A595 values, we can say there is enough GSH *in cellulo* to achieve the same level of de-capping as that of the GSH

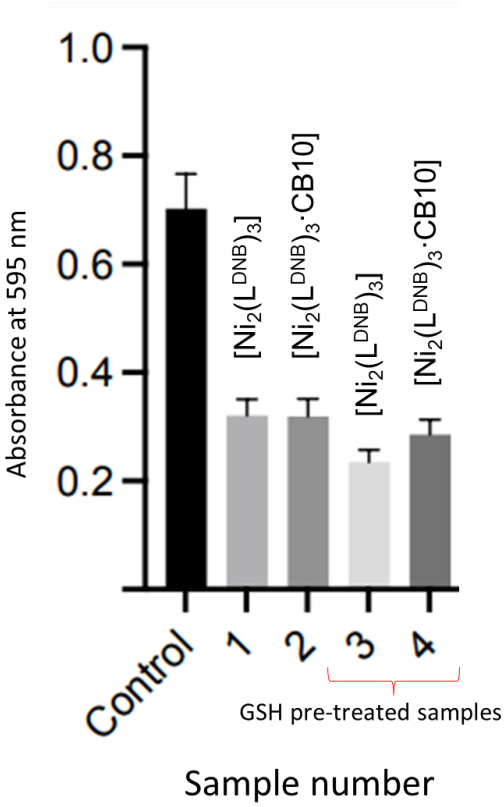


Figure 2.22: Shows the results from the MTT assay of MDA-MB-231 cells treated with 50 μM of the specified complex for 72 hrs. Samples 1-2 were treated with the specified complex which were pre-treated without GSH. Complexes used in samples 3-4 were pre-treated with GSH.

pre-treated $[Ni_2(L^{DNB})_3{\cdot}CB10]^{4+}$ rotaxane. This explains the cytotoxicity of the $[Ni_2(L^{DNB})_3{\cdot}CB10]^{4+}$ rotaxane and shows proof of concept that the complex can de-cap *in cellulo*. Due to the inability to avoid GSH production *in cellulo*, a suitable negative control may be that of the $[Ni_2(L'')_3{\cdot}CB10]^{4+}$ rotaxane. This complex presents a similar structure however it lacks the ability to be cleaved *in cellulo*. This complex as previously mentioned has exhibited a cytotoxicity > 140 μM. This suggests that the $[Ni_2(L^{DNB})_3{\cdot}CB10]^{4+}$ rotaxane must be de-capped as the cytotoxicity corresponds more closely to that of free cylinder than the inert rotaxane.

In summary we have developed a new rotaxane utilising a metallo-supramolecular cylinder and CB[10] with a cleavable capping group. This capping group has been shown to be removed in the presence of GSH (as well as 2-mercaptoethanol and

NaSH) to leave a *pseudo*-rotaxane with 5 or less caps. This *pseudo*-rotaxanes released active cylinder species which have bound and formed 3WJ in PAGE gels, demonstrating their presence and functionality. Cell studies also revealed a toxicity comparable to that of the free cylinder for the $[Ni_2(L^{DNB})_3 \cdot CB10]^{4+}$ rotaxane, further suggesting the presence of an active cylinder species.

This work represents the first instance of a metallo-supramolecular junction binding structure, rotaxanated as a thread by a macrocycle, which has shown controlled release. The release mechanism is biologically relevant as its release is dependent on thiol concentration, where higher concentrations release more cylinder, and higher thiol concentrations have been found in cancer cell lines.[43,49]

Further work includes investigating the effects of this new GSH sensitive rotaxane in other cell lines with differing GSH levels. We also aim to establish what the active species are, using mass spectrometry on a purified sample of cell extract. This will allow us to observe the different cylinder species which are produced from the $[Ni_2(L^{DNB})_3 \cdot CB10]^{4+}$ rotaxane *in cellulo*. We are using the information we have gathered from this new complex to investigate new capping groups to achieve improved and unique functionality/activity for new rotaxanes.

2.5: Nucleic acid interactions of cylinders with modified structures

The work in this section follows on from the work in section 2.2 and was undertaken by the author in that context. Some of the complexes have been prepared previously or were prepared by colleagues in the group and where this is the case, this is explicitly stated.

Metallo-supramolecular cylinders have demonstrated a wide range of biological effects and interactions because of their structure as discussed in section 1.3.1. Whilst these are desirable, we also acknowledge that modifying this structure could result in new, even more beneficial, effects such as increased selectivity, potent toxicity and fluorescence-based effects. Towards this, we have investigated the nucleic acid interaction of several unique cylinders with modified ligand structures with both nickel and iron metal centres.

Figure 2.23 shows the ligand structure of one new cylinder which is based on L' which was used to make the $[Ni_2(L'')_3 \cdot CB10]^{4+}$ rotaxane. Switching the 2-Imidazole to a 4-Imidazole changes the direction and therefore steric effects of any group substituted at the NH position. This could (depending on the group) influence the number of substitutions possible or the ability to either *pseudo* or fully rotaxanate. Towards

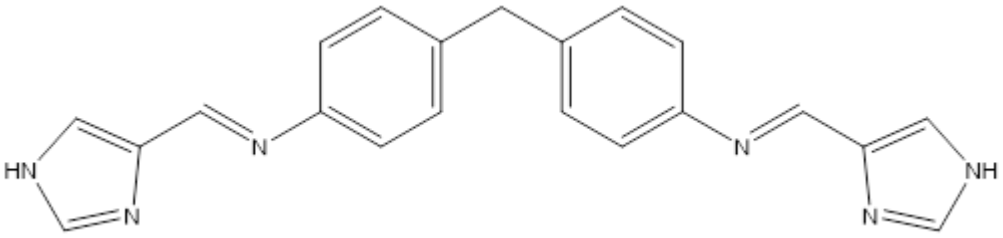


Figure 2.23: Shows the structure of the L'⁴ ligand which has a 4-imidazole group instead of the 2-imidazole that the L' ligand has.

exploring these possibilities, we looked at how the $[Ni_2(L'^4)_3]^{4+}$ and $[Fe_2(L'^4)_3]^{4+}$ interact with DNA 3WJ's. These complexes were synthesised by Catherine A. J. Hooper following approaches established by Dr Floriana Tuna[52] and the 3WJ binding studies were conducted by myself.

In Figure 2.24 we can see the PAGE gels of both the $[Ni_2(L'^4)_3]^{4+}$ and $[Fe_2(L'^4)_3]^{4+}$ cylinders with DNA 3WJ. We can see that the $[Fe_2(L'^4)_3]^{4+}$ cylinder forms a small amount of 3WJ compared to that of the control. Whereas the $[Ni_2(L'^4)_3]^{4+}$ cylinder shows a large amount of 3WJ which is comparable to that of the control. The link between 3WJ formation and the metal centre (Fe or Ni) is likely due to stability as the $[Fe_2(L'^4)_3]^{4+}$ cylinder, which has previously shown poor stability in aqueous systems (alongside its L' counterpart). These results suggest that nickel should be the metal ion of choice going forward for these complexes to maximise stability and therefore biological

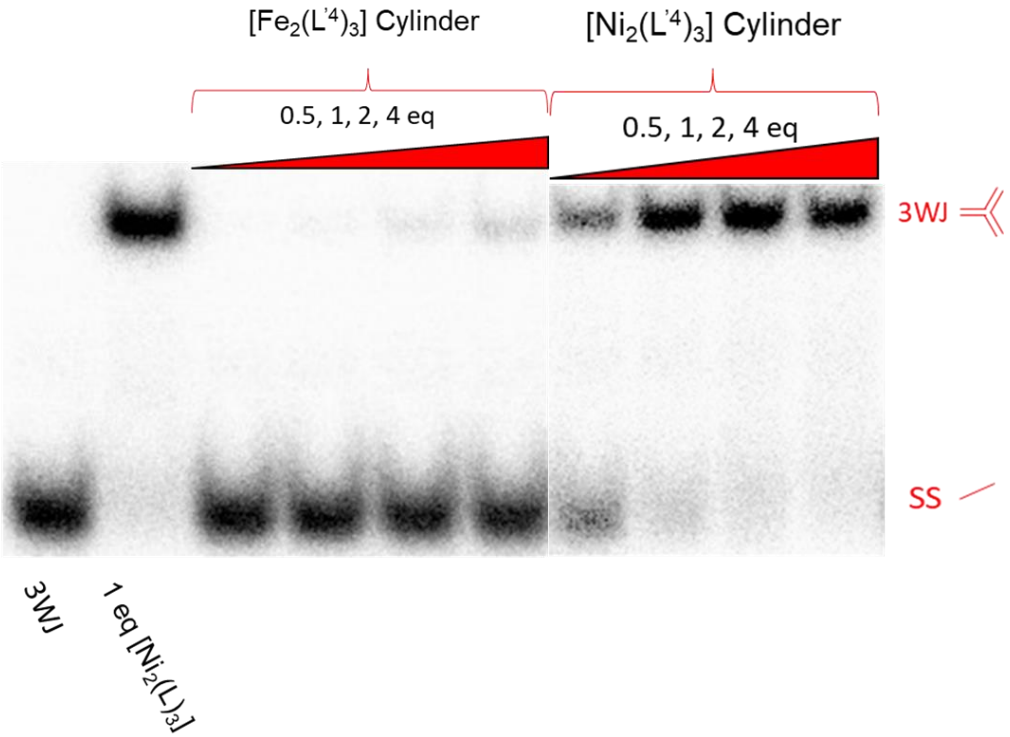


Figure 2.24: Shows the PAGE gel of DNA 3WJ (left to right) of 3WJ control (1), $[Ni_2(L)_3]$ cylinder and 3WJ at 1:1 (2). $[Fe_2(L'^4)_3]$ or $[Ni_2(L'^4)_3]$ cylinder and 3WJ at 0.5,1,2 and 4 eq (3-6 and 7-10 respectively).

interaction (due to greater structure stability *in vivo*). It cannot be ruled out that functionalisation of the N-H on the 4-imidazole may improve the stability considerably. Rotaxanation will likely dramatically improve stability, hence releasing this complex from a rotaxanated system *in cellulo/vivo* may yield drastically different results to that of the non-rotaxanated system. These factors are worth considering when developing iron imidazole cylinders and should be acknowledged through active testing and controls when conducting biological studies of any kind.

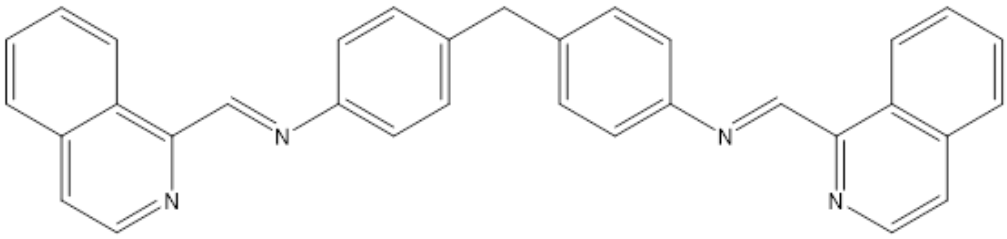


Figure 2.25: Shows the structure of the L^Q ligand which has an isoquinoline unite in place of the pyridine group on the original L ligand.

Another ligand we investigated was the L^Q ligand which replaces the pyridine with an isoquinoline group on the original L ligand (Figure 2.25). This ligand was used to form the $[Ni_2(L^Q)_3]^{4+}$ and $[Fe_2(L^Q)_3]^{4+}$ cylinders which were intended to explore the effects of an extended aromatic system at the ends of the ligand on the 3WJ forming capabilities of cylinders. This quinoline ligand and complexes were first described by Dr Mirela Pascu.[53]

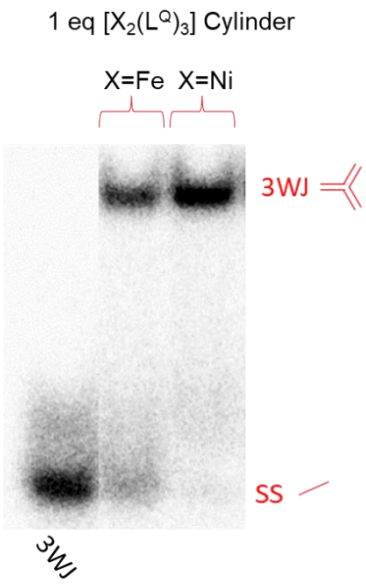


Figure 2.26: Shows the PAGE gel of DNA 3WJ (left to right) of 3WJ control (1). $[Fe_2(L^Q)_3]$ cylinder and 3WJ at 1:1 (2). $Ni_2(L^Q)_3]$ cylinder and 3WJ at 1:1 (3).

Figure 2.26 shows the PAGE gel of the $[Ni_2(L^Q)_3]^{4+}$ and $[Fe_2(L^Q)_3]^{4+}$ cylinders with DNA 3WJ. We can see that both cylinders result in 3WJ formation at 4eq of cylinder to junction though $[Ni_2(L^Q)_3]^{4+}$ cylinder shows reduced quantities of SS species and increased quantity of 3WJ compared to the $[Fe_2(L^Q)_3]^{4+}$ cylinder. The ability for these cylinders to form 3WJ shows that the isoquinoline modifications do not interfere with junction formation. However, these extended aromatic π-surfaces could allow for new biological interactions *in cellulo/vivo*. Further work would involve investigating the cellular effects of these complexes in comparison to that of the original L cylinders.

Figure 2.27 shows the ligand structure of L* which was based on ligand L where the imine bond was replaced by an azo bond. This was done because the imine bond is susceptible to reverse hydrolysis in certain conditions, whereas the azo bond is much more resistant to this. This in turn should increase the stability of the L* cylinders in these conditions which would avoid stability issues and could lead to a differing biological effect. These complexes were synthesised by Dr Aditya Garai following approaches established by Laura Childs[54] and 3WJ binding experiments were

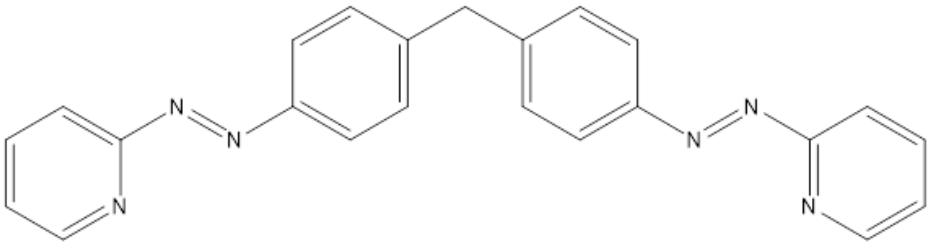


Figure 2.27: Shows the ligand structure of L which is a modified version of L where the imine bond has been replaced with an azo bond.*

conducted by me. In Figure 2.28 we can see the PAGE gel of $[Fe_2(L^*)_3]^{4+}$ cylinder with DNA 3WJ. $[Fe_2(L^*)_3]^{4+}$ cylinder can be seen to form a large quantity of 3WJ starting from 0.5 eq and showing only small quantities of SS DNA at 4 eq. This suggests that switching the imine bond with an azo bond does not interfere with 3WJ formation. Further work would investigate the effects of changing the metal centre and looking at the biological activity of these complexes *in cellulo*.

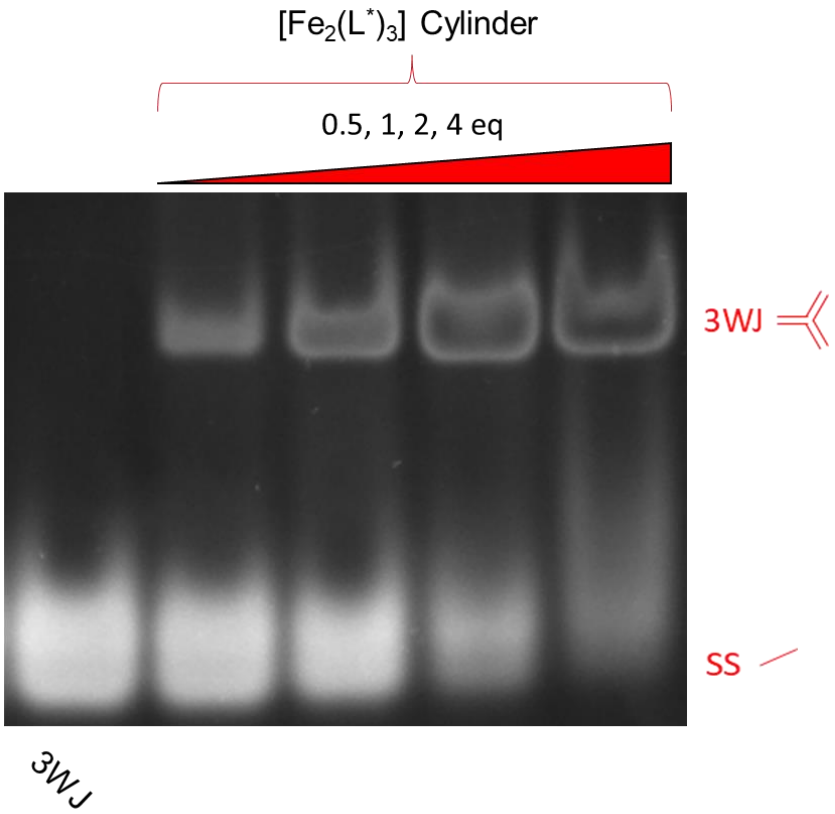


Figure 2.28: Shows the PAGE gel of DNA 3WJ (left to right) of 3WJ control (1). $[Fe_2(L^*)_3]$ cylinder and 3WJ at 0.5,1,2 and 4 eq (2-5).

We also looked at how the base cylinder $[Ni_2(L)_3]^{4+}$ interacted with a Holliday junction (HJ) structure which is a four-way junction (4WJ) comprised of 4 non-palindromic DNA sequences. 4WJ's share some similar structural properties with 3WJ's which could make them a suitable binding target for cylinders. They occur during homologous recombination where genetic information is transferred between two DNA molecules for the purpose of DNA repair or meiosis.[55] Interfering with homologous recombination

presents an opportunity to achieve toxicity against bacteria or cancer cells lines.[56,57] This is achieved by inhibiting the DNA repair process which disproportionately affects these types of cells. In Figure 2.29 we can see the PAGE gel of the four HJ/4WJ oligos with $[Ni_2(L)_3]^{4+}$ cylinder. We can see that 4WJ forms in both the negative control of the oligos alone and in the positive control where it has been incubated with added magnesium and sodium chloride. It is however noticeable that there is an increased proportion of 4WJ in the positive control when the salt cations are included in the sample prep. There is also a reduction in the single stranded species and increased smearing, likely due to increased stability of semi-stable structures. There is also a faint but present band above the 4WJ, it is hypothesised that this is either an open configuration 4WJ or a dimeric structure comprised of 2 4WJ's which arises due to high cation concentrations. Upon addition of $[Ni_2(L)_3]^{4+}$ cylinder we can see the formation of three new bands. The first which is labelled as Y-J is thought to be a Y shaped junction

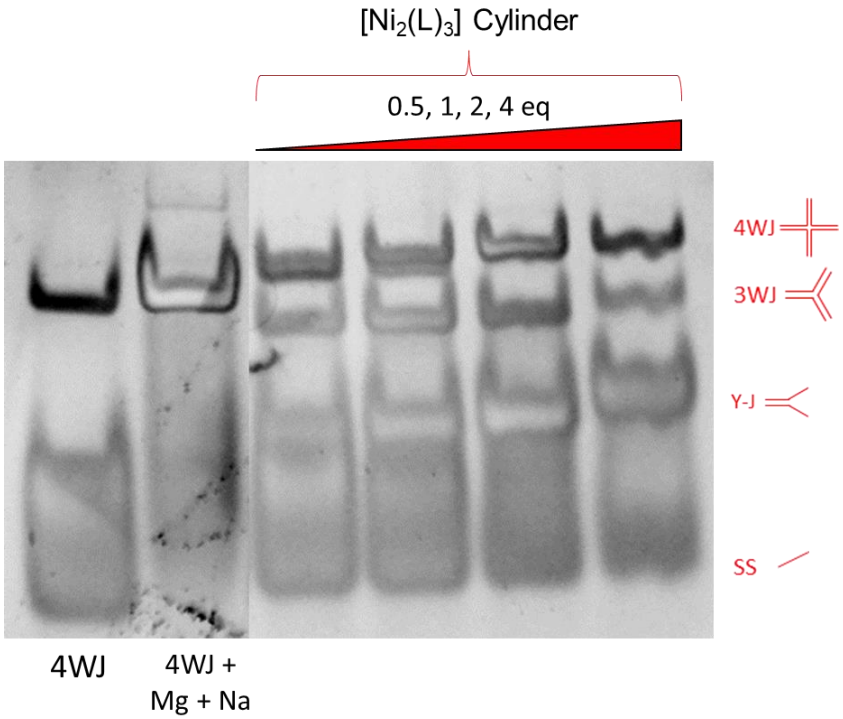


Figure 2.29: Shows the PAGE gel of DNA 3WJ (left to right) of 3WJ alone negative control (1). 3WJ positive control with 2mM $MgCl_2$ and 10 mM NaCl (2) $[Ni_2(L^Q)_3]$ cylinder and 3WJ at 0.5,1,2 and 4 eq (3-6).

which is comprised of any 2 complementary strands present. This would be a duplex structure where complementary and SS segments where they are not. The promotion of this band on increasing equivalents of cylinder is explained by the cylinders ability to bind DS DNA alongside its ability to bind to junction and fork structures such as this. Another band is formed between the Y-J and 4WJ band which is thought to be a 3WJ structure with a mismatched arm, where two of the strands are not complementary. Finally, the 4WJ band Is still formed with comparable intensity to that of the control, however upon addition of cylinder a second 4WJ band is formed which is most visible at 1eq of $[Ni_2(L)_3]^{4+}$ cylinder. As the equivalents of cylinder increases, we shift from the initial band to the new second band which has a reduced shift likely due to an increased hydrodynamic radius. This indicates that this is a unique 4WJ structure which comprises the cylinder in specific and distinct capacity which is backed up by the discreteness of the band and could be different conformations of 4WJ.[58,59] These shifts indicate that cylinder can interact with 4WJ in a discrete manner though it is not binding to them selectively and simultaneously binds DS/Y/3WJ structures. This opens the possibility for cylinders to interact with 4WJ *in vivo*, potentially linking their activity to homologous recombination pathways *in vivo*.

We continued the study of $[Ni_2(L)_3]^{4+}$ cylinder with 4WJ by investigating every combination of the four oligos used, alone and with 1eq of cylinder. The PAGE gel of this study can be seen in Figure 2.30 with labels along the bottom indicating the strand composition of each lane. We can see in the control that the 4WJ forms upon mixing all strands together, with small quantities of 4 oligo species being found in samples where 3 oligos are mixed including S4. Smearing of the SS band to the Y-J band can be seen in lanes combining 2 or more strands, particularly where there is complementarity and S4. This indicates S4 is important for higher order structure formation. When $[Ni_2(L)_3]^{4+}$ cylinder is included in these same samples we can see prominent shifts of the SS species to Y species in most sample, notable S4 alone shows a slightly shifted Y-J structure, despite S4 not being palindromic. This shift is expected due to the cylinders ability to bind to and interact with DS and Y-J structures. Small quantities of 3WJ can be seen to form in several of the strand combinations which include S4. Similarly small quantities of 4WJ can be seen in combinations of 3

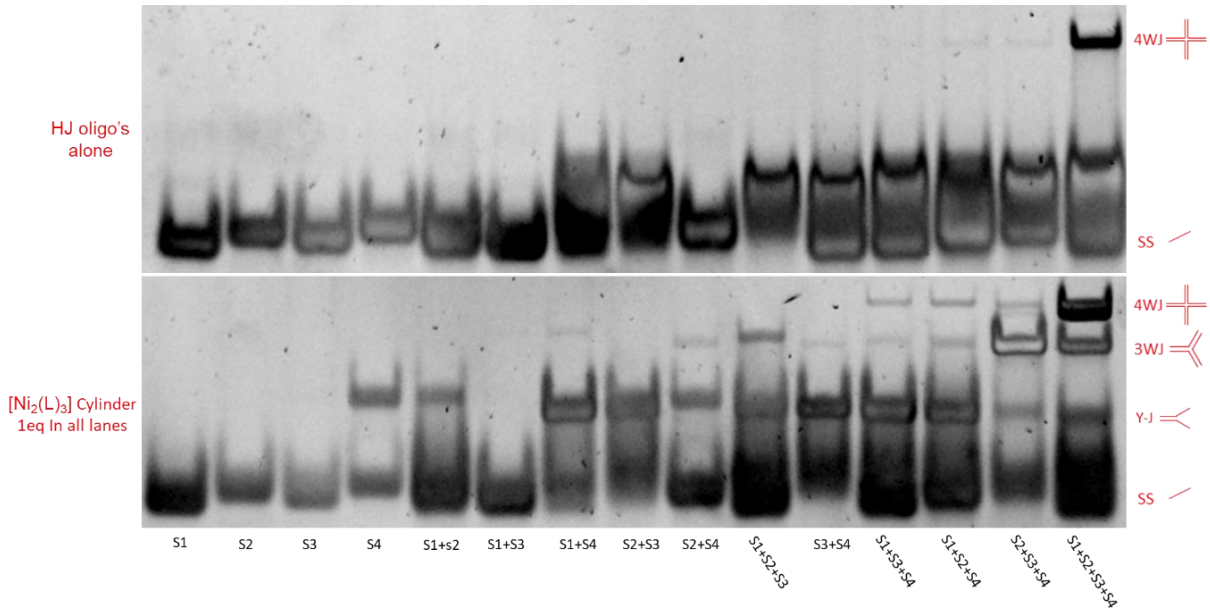


Figure 2.30 Shows the PAGE gel of every different combination of the 4 oligos used to form the 4WJ. The top gel is the negative control of the oligos alone and the bottom gel is the same with 1eq of $[Ni_2(L)_3]^{4+}$ cylinder in each lane.

strands including S4. Interestingly in S2+S3+S4 there is a prominent 3WJ band suggesting this is the dominant structure in this sample. There are also two faint and discrete 4WJ bands, notable this only occurs when the lower half of S4 lacks a complementary strand (5′-TCATGCTAGGC-3′) which is situated on S1. Upon mixing all strands, 4WJ becomes more prominent and displays a broader band suggesting both species are present, 3WJ intensity also decreases but remains prominent. This shift in band intensities is like due to the relative thermodynamic stabilities of the structures and the binding interactions are the sites where the cylinder interacts with them. This gel highlights the importance of S4 in higher order structure formation and warrants further study. It is also clear that the cylinder promotes the formation of these higher order structures in a manner beyond that of purely electrostatic interactions. This is evidenced by the presence of the 3WJ band in most of the samples which is absent when these oligos interact with other supramolecular metal complexes (see chapter 4 on Pillarplexes). Whilst the $[Ni_2(L)_3]^{4+}$ cylinder has showed the ability to bind to 4WJ's in a discrete manner and promote their formation, it seems clear that 3WJ's are still the prominent binding target.

This work shows that modifying the original cylinder (L) structure with azo ligands, isoquinoline ligands, and Ni centres maintains the cylinders 3WJ binding capability. This has implications for *in vivo* studies where these modifications can make a substantial difference due to increased stability, resistance to degradation pathways, and alternative binding targets. Through comparison to other cylinders this can provide information on the biological mechanism of action of these complexes. This is possible due to their isostructural nature and may provide a great amount of insight into the optimal design of such drugs in wider field.

Interestingly these cylinders show interaction with 4WJ's, promoting their formation, possibly due to electrostatic interactions. More surprisingly, they support the formation of 3WJ's out of the 4WJ oligonucleotide mix. This not only highlights the cylinders extreme preference for 3WJ's but also shows a novel mode of interaction with biological systems. Highlighting a complexes activity can be linked not just to the promotion of one structure but also to the simultaneous breakdown of another.

2.6: Investigation of crude CB[n] reaction mixture

Cucurbiturils were first synthesised in 1905 but were not characterised until 1981.[60,61] They take the generic formulae CB[n] where n may be different numbers of glycoluril units.[62,63] The synthesis produces a mixture of different CB ring sizes with CB[5], CB[6], CB[7], CB[8] and CB[10] being already established.[64] CB[10] has been uniquely isolated whilst complexed with a CB[5] ring in its cavity.[34] More recently CB[14] has been identified with a twisted conformation, giving rise to an overall more complex structure.[65] The presence of other CB rings has not been confirmed, however there has been some evidence which hints at their existence through the presence of unassigned NMR signals.[65]

We have worked in collaboration with Dr Simin Liu to investigate if our complexes have the potential to interact (MD modelling by colleague Lazaros Melidis has suggested it is possible) with presently unidentified CB species, namely CB[9] and CB[11] and allow them to be detected via mass spectrometry. As well as this, the cylinders may prove to be a suitable way of purifying the different CB rings from the mix that the synthesis produces, which is normally a challenging feat. This would be achieved via differences in solubility between complexed and un-complexed states, combined with other solvents and guest species.

We were provided with a crude CB[n] reaction mixture by Simin Liu's team which we have incubated with $[Fe_2(L)_3]^{4+}$ cylinder and investigated the resulting solution using MS. Investigating this sample was challenging as it is a crude reaction mixture and un-purified. We are also unaware of the ratios of unidentified CB's which are produced in

this reaction; however, it is expected that it is low, making detection more challenging if they are present.

We incubated the $[Fe_2(L)_3]^{4+}$ cylinder (500 µM) with 3.46 mg of CB[n] mixture in 1.5 mL of ultra-pure water (18.0 MΩ). This sample was incubated for 1 and 72 hrs at 37 °C with periodic vortexing to ensure the CB[n] solid can mix with the solution. We also incubated $[Fe_2(L)_3]^{4+}$ cylinder for 1 hr at 37 °C with a CB[n] sample that was washed with ultra-pure water (18.0 MΩ) 4 times with vortexing. This was to observe if this process removed water soluble CB's and other reaction materials/products and enhanced visualisation of the desired peaks.

In Figure 2.31 we can see the m/z range where we expect to observe the complex $[Fe_2L_3]^{4+}\cdot$(CB9). At t=1 and t=72 hrs. we can see the presence of a 4+ species with the m/z peaks 683.72, 683.97 and 683.47 which could correspond with this complex. We

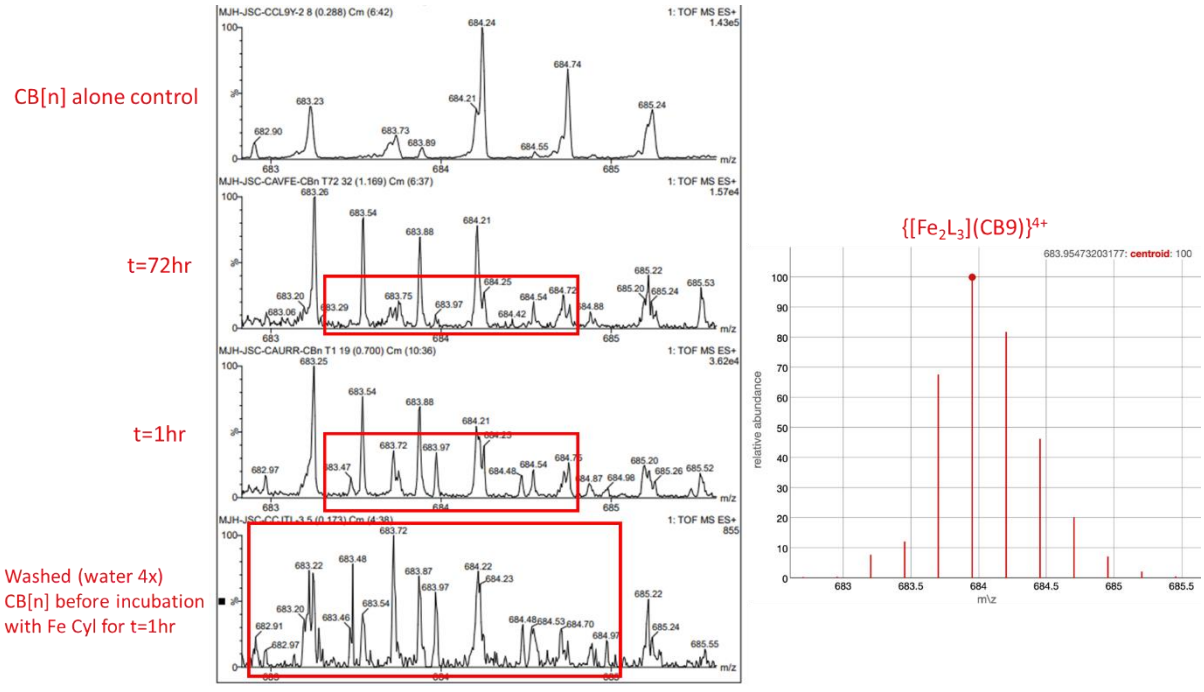


Figure 2.31: CB[9] m/z range. Shows MS spectra of crude CB[n] reaction mixture incubated with $[Fe_2(L)_3]^{4+}$ cylinder and alone, with and without pre-washing for the allocated length of time at 37 °C. The red boxes highlight the regions where we can see the expected peaks and to the right of the spectra is the isotope pattern expected for this complex generated by enviPat.

do however lack a complete isotope pattern and high-resolution peaks which is impeded by substantial overlap with other peaks. There may also only be small quantities of CB[9] produced by the synthesis, making it more challenging to detect. With washing we can see a more discernable isotope pattern with potential peaks at 682.97, 683.22, 684.22, 684.48, 684.73 and 684.97 m/z. This is a more clearly defined isotope pattern, due to the removal of overlapping peaks by the washing process. These peaks more clearly suggest the presence of the $\{[Fe_2L_3](CB9)\}^{4+}$ structure though they are not themselves conclusive.

Figure 2.32 shows the m/z range where we would expect to see $\{[Fe_2L_3](CB10)\}^{4+}$. There are prominent peaks with a clear isotope pattern for this complex at t=1 and t=72 hrs. Given the abundance of the peaks, it is likely there is a significant amount of CB[10] in the crude reaction mixture that the $[Fe_2L_3]$ cylinder can react with. This also shows that the cylinder can dislodge the CB[5] which is present inside CB[10] because

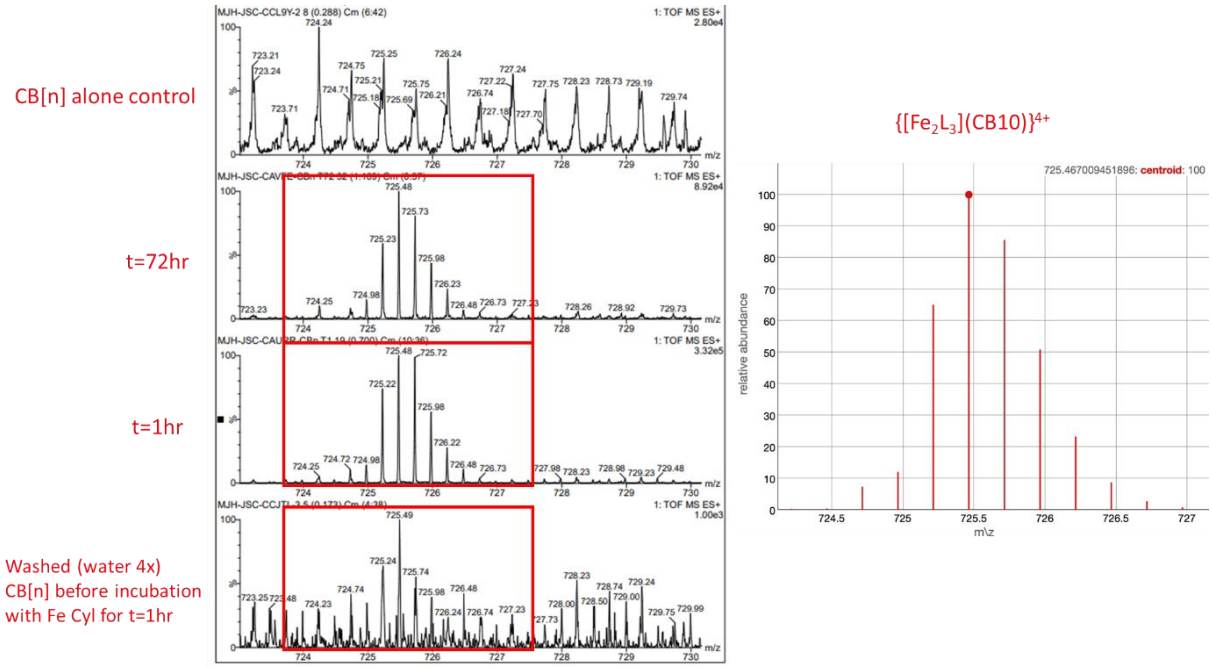


Figure 2.32: CB[10] m/z range. Shows MS spectra of crude CB[n] reaction mixture incubated with $[Fe_2(L)_3]$ cylinder and alone, with and without pre-washing for the allocated length of time at 37 °C. The red boxes highlight the regions where we can see the expected peaks and to the right of the spectra is the isotope pattern expected for this complex generated by enviPat.

of the synthesis. CB[10] could be isolated by removing the cylinder from the central cavity by providing an alternative guest, or by destroying the cylinder with DMSO/EDTA and collecting the precipitated CB[10].

Figure 2.33 shows the m/z range where we would expect to see $\{[Fe_2L_3](CB11)\}^{4+}$. There appears to be a 4+ species present at t=1 and t=72 hrs which could be this complex at 766.49, 766.73, 766.99, 767.24, 767.49, 767.74 and 767.99. These peaks do not appear withing the washed sample or control and have a definable isotope pattern at t=1. The isotope pattern is not perfectly clear due to surrounding signals however it does appear to be different from the calculated version. This highlights the possible presence of CB[11] however further investigation would be required with different metal centres to confirm it shifts.

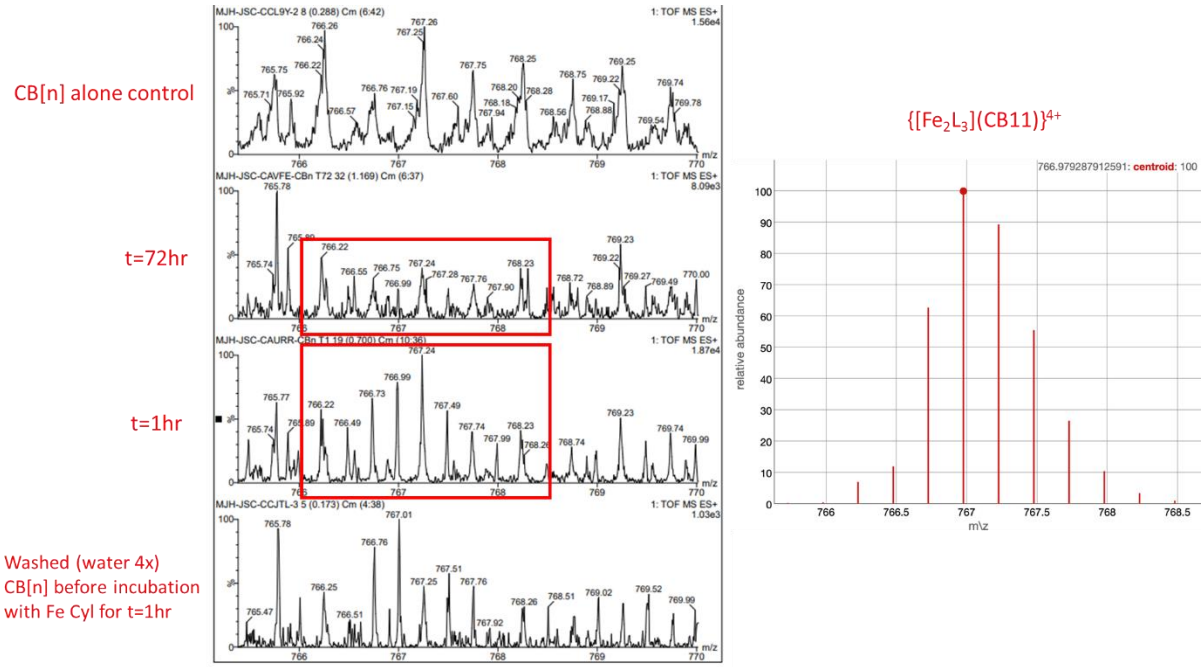


Figure 2.33: CB[11] m/z range. Shows MS spectra of crude CB[n] reaction mixture incubated with $[Fe_2(L)_3]$ cylinder and alone, with and without pre-washing for the allocated length of time at 37 °C. The red boxes highlight the regions where we can see the expected peaks and to the right of the spectra is the isotope pattern expected for this complex generated by enviPat.

Overall, we have identified that CB[10] can be bound by [Fe_2L_3] cylinder from the crude CB[n] synthesis mixture. This could prove to be a useful method of CB[10] purification, to establish this, further work would have to be conducted including the removal of the cylinder via solubility, degradation, or alternative binding target. We also identified the potential presence of CB[9] and CB[11] macrocycles which were complexes with [Fe_2L_3] cylinder. Their abundance was low and overlapped with the presence of other signals making accurate quantification challenging. This presents an issue as their yield is likely very low from the synthesis making signal to noise ratio a problem. To improve this and to acquire better quantification, other purification methods should be tried to remove background signal. Also, looking for how these peaks shift, and their isotope patterns differ with the metal in the cylinder (switching to [Ni_2L_3] cylinder for example) may provide another way to assess the presence of these species.

2.7: Conclusions

We have demonstrated that rotaxanes and *pseudo*-rotaxanes can be formed using metallo-supramolecular cylinders and CB[10] using either a post-synthetic modification or slippage mechanism. This effectively controls the DNA 3WJ binding of these complexes which has been linked to their biological effects. We also highlighted that upon removal of 1 or more of the 6 capping groups which form the rotaxane the cylinder can leave the CB[10] cavity and showing activity again. This has highlighted the therapeutic potential of these complexes.

We then expanded on this class of rotaxane by developing a functional capping group which was cleaved in the presence of a thiol leaving a partially capped *pseudo*-rotaxane in its place. The release of the cylinder was shown by the cleaving of the groups with GSH in a PAGE 3WJ gel which revealed activity once de-capped. Cell studies also showed this L^{DNB} rotaxane showing cellular toxicity comparable to that of its corresponding cylinder with an IC_{50} µM. This is markedly higher than that of the original L'' unreactive rotaxane which has an IC_{50} of >140 µM. This highlights the functionality of these rotaxanes *in cellulo* and demonstrates their potential going forward.

We showed the 3WJ binding of several cylinders with modified ligands which highlights the variety of modifications which are possible to provide added functionality with these complexes. Cylinders have also demonstrated 4WJ binding which opens new opportunities for biological activity via homologous recombination pathways among others.

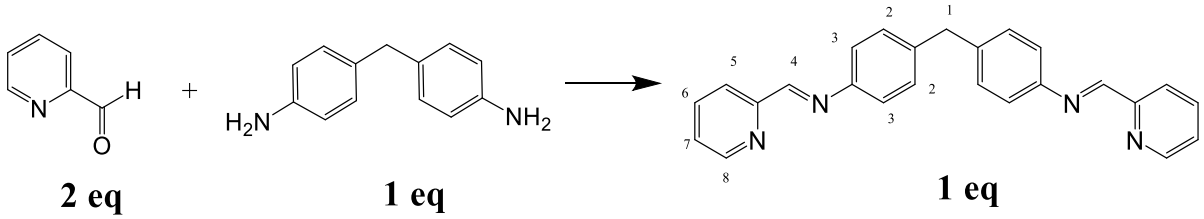
Lastly, we showed CB[10] could be bound by $[Fe(L)_3]^{4+}$ from the crude synthesis product of CB[n], potentially offering a new method for CB[10] purification. We also highlighted the potential presence of CB[9] and CB[11] by mixing $[Fe(L)_3]^{4+}$ cylinder with the CB[n] reaction mixture and observing the mass spectra. Further work is required to establish this; however, this offers the opportunity for exciting now CB complexes should their existence be proved.

Overall, these complexes have shown tremendous potential for therapeutic activity whilst providing novelty in the form of a 3D rotaxane containing metal centres. Their unique structures provide numerous structural permutations allowing for the growth of this class of compound and room for study for the foreseeable future. Going forward, work is currently being undertaken to develop new ligand structures which provide sensitivity to external stimuli and alternative chemical environments with the aim of changing/improving their biological activity.

2.8: Experimental

Unless otherwise stated, starting materials, chemicals and organic solvents were purchased from Merck, VWR, or Thermo Fisher Scientific and were used without further purification. Water was acquired from a MiliQ (resistance 18 MΩ) water supply. Oligonucleotides were purchased from Eurofins and purified by HPLC-MS.

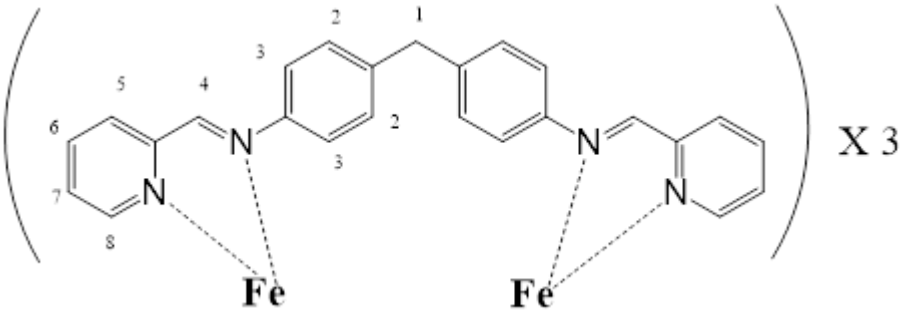
2.8.1: Synthesis and Characterization of complexes



Synthesis of parent ligand $C_{25}H_{20}N_4$ (L): 4,4'-methylenedianiline (1.90 g, 0.01 mol) was dissolved in 10 mL of ethanol. Pyridine-2-carboaldehyde (1.90 mL, 0.02 mol) was added dropwise to the solution which immediately caused precipitation, this solution as left stirring overnight at room temperature. The product was purified by recrystallization from ethanol and dried using vacuum filtration. The product was a pale-yellow crystalline solid (2.39 g, 66% yield).[66]

Mass spectrum (TOF MS ES+): m/z = 377 [M+H]

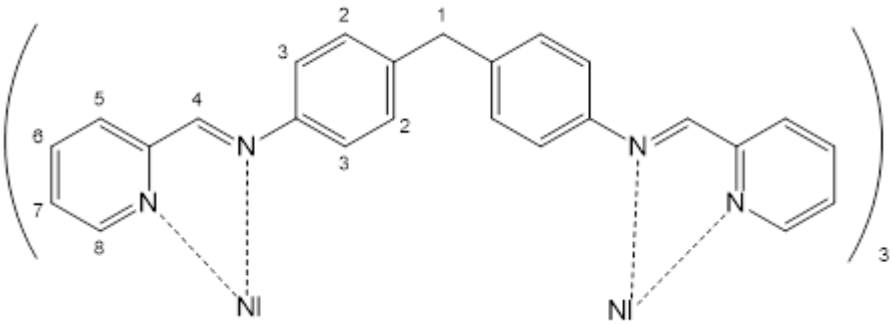
^{1}H NMR (300 MHz, Methylene Chloride-d_2) δ = 8.68 (ddd, *J*=4.8, 1.8, 1.0 Hz, 1H, P8), 8.61 (s, 1H, P4), 8.21 (dt, *J*=8.0, 1.1 Hz, 1H, P5), 7.88 – 7.76 (m, 1H, P6), 7.37 (ddd, *J*=7.5, 4.9, 1.2 Hz, 1H, P7), 7.33 – 7.20 (m, 4H, P2/3), 4.04 (s, 1H,P1).



Synthesis of Iron parent cylinder $[Fe_2(L)_3]^{4+}\cdot(Cl^-)_4$: L (1.5 g, 3.98 mmol) was dissolved in 200 mL of methanol, to which iron(II)chloride tetrahydrate (0.53 g, 4.18 mmol) was added and heated to reflux (70 °C) with stirring for 3 hours leaving a purple solid. When cooled, the solvent was removed under vacuum and the solid was re-dissolved in the minimum amount of methanol. To this, a saturated solution of ammonium hexafluorophosphate was added (approximately 30 molar equivalents) and was stirred for 30 minutes. The precipitate was collected by vacuum filtration and washed 2 x 10 mL of water and 5 x 25 mL of di-ethyl ether. The precipitate was then suspended in methanol and excess dowex™ 1X8 200-400 (Cl) was added and stirred for 30 minutes. The dowex was filtered off under vacuum filtration and washed with methanol. Methanol was removed under vacuum to leave a purple solid. This was then dissolved in the minimum amount of methanol and pipetted dropwise into a conical flask with 200 mL of di-ethyl ether in, the product precipitated out of solution and was filtered off under vacuum and dried under vacuum in a desiccator. Product was a purple solid $[Fe_2(L)_3]^{4+}\cdot(Cl^-)_4$ (1.8 g, 97 % yield).

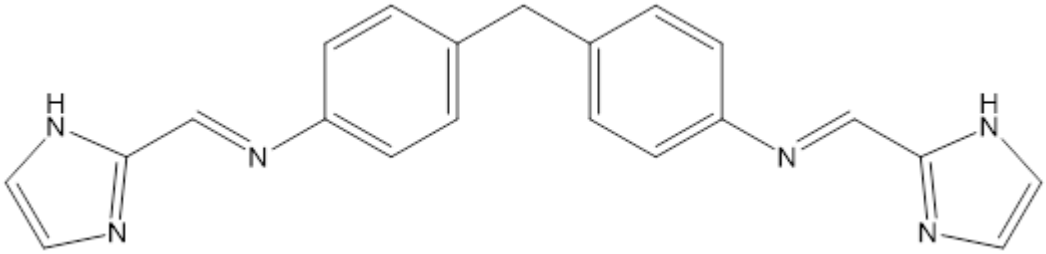
Mass spectrum (TOF MS ES+): m/z = 425.1 $[Fe_2L_3]Cl^{3+}$, 310 $[Fe_2(L)_3]^{4+}$

^{1}H NMR (300 MHz, Methanol-d_4) δ = 9.11 (s, 6H, P4), 8.65 (dd, *J*=7.5, 1.3 Hz, 6H, P5), 8.45 (td, *J*=7.7, 1.3 Hz, 6H, p6), 7.81 (ddd, *J*=7.5, 5.7, 1.5 Hz, 6H, P7), 7.41 (d, *J*=5.5 Hz, 6H, P8), 7.00 (s, 14H, P3), 5.57 (s, 13H, P2), 4.02 (s, 7H, P1).



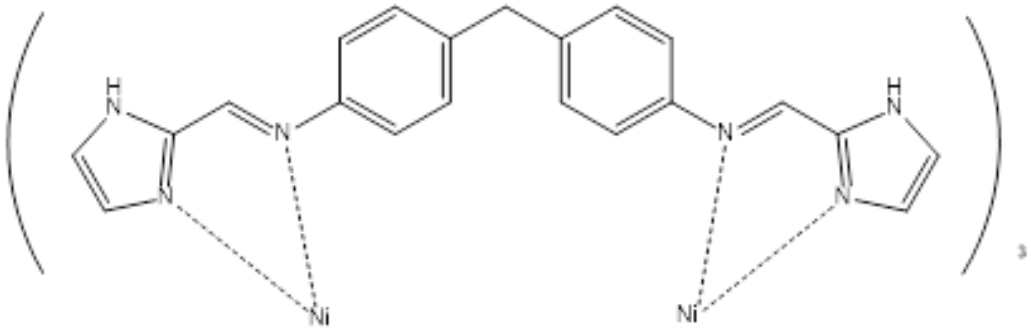
Synthesis of Nickel parent cylinder $[Ni_2(L)_3]^{4+}\cdot(Cl^-)_4$: L (0.5 g, 1.33 mmol) was dissolved in 100 mL of hot methanol, to which nickel (II) acetate tetrahydrate (0.21 g, 0.844 mmol) was added and heated to reflux (70 °C) with stirring for 15.5 hours leaving and orange/brown solid. When cooled, the solvent was removed under vacuum and the solid was re-dissolved in the minimum amount of methanol. To this, a saturated solution of ammonium hexafluorophosphate was added (approximately 30 molar equivalents) and was stirred for 30 minutes. The precipitate was collected by vacuum filtration and washed 2 x 10 mL of water and 5 x 25 mL of di-ethyl ether. The precipitate was then suspended in methanol and excess dowex™ 1X8 200-400 (Cl) was added and stirred for 30 minutes. The dowex was filtered off under vacuum filtration and washed with methanol. Methanol was removed under vacuum to leave $[Ni_2(L)_3]^{4+}\cdot(Cl^-)_4$. This was then dissolved in the minimum amount of methanol and pipetted dropwise into a conical flask with 200 mL of di-ethyl ether in, the product precipitated out of solution as a yellow/orange precipitate and was filtered off under vacuum and dried under vacuum in a desiccator. 0.541 g 88% yield

Mass spectrum (TOF MS ES+): m/z = 430.46 $[Ni_2L_3]Cl^{3+}$, 311.59 $[Ni_2L_3]^{4+}$



Synthesis of Imidazole ligand $C_{21}H_{18}N_6$ (L'): This complex was synthesised by Catherine A.J. Hooper and is published as a part of the co-authored paper. 4,4'-methylenedianiline (0.790 g, 4.00 mmol) dissolved in methanol (15 mL) was added to 2-imidazolecarboxaldehdye (0.770 g, 8.00 mmol) in methanol (15 mL) giving a cloudy white solution which was stirred for 10 minutes under a nitrogen atmosphere. Glacial acetic acid (3 drops) was added, and the solution heated under reflux for 2 hours. The solution was cooled to room S33 temperature, and the white precipitate isolated by filtration. The yellow precipitate was washed with methanol (2 x 10 mL) and dried in vacuo (1.25 g, 3.53 mmol, 88%).[67]

^{1}H NMR: (400 MHz, DMSO-d_6) δ 13.02 (NH, s, 1H), 8.40 (Him, s, 1H), 7.32 (H4/5, s,



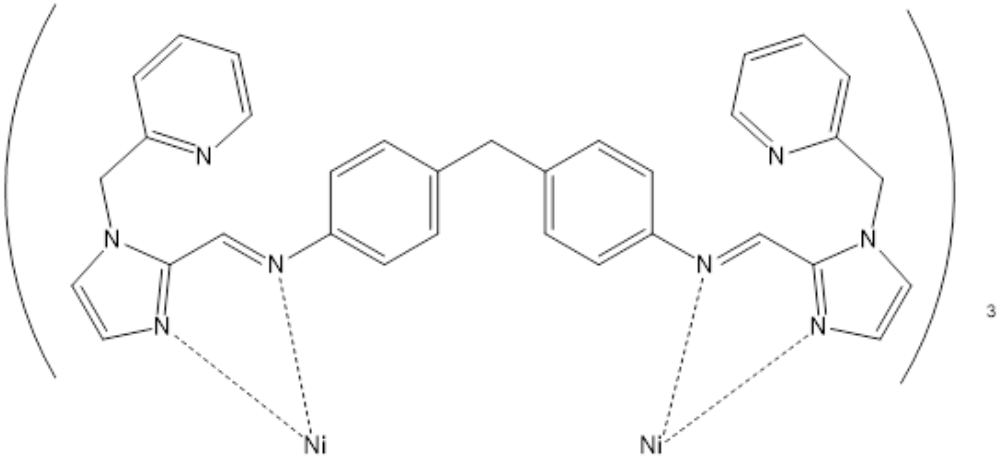
1H), 7.30 (HPha/b, dt, J=8.6, 2.1 Hz, 2H), 7.25 (HPha/b, dt, J=8.6, 2.1 Hz, 2H), 7.18 (H4/5, s, 1H), 3.98 (CH_2, s, 1H).

Mass spectrum (TOF MS EI+): m/z = 355 [C21H18N6 + H] +.

Synthesis of Nickel 2-imidazole cylinder $[Ni_2(L')_3]^{4+}\cdot(Cl^-)_4$: This complex was synthesised by Catherine A.J. Hooper and is published as a part of the co-authored paper. L' (0.425 g, 1.2 mmol) was suspended in 20 mL of methanol under nitrogen

gas. Nickel (II) Chloride hexahydrate (0.19g, 0.8 mmol) dissolved in 10 ml of methanol was added and washed in with 10 mL of extra methanol to the ligand suspension. This caused a colour change to a clear orange solution. After stirring for 30 minutes the solution was filtered through celite, washed with methanol and ammonium hexafluorophosphate (770 mg) was added. The product was then allowed to precipitate at 4 °C. The precipitate was then collected by vacuum filtration (620 mg, orange semi crystalline powder). Product (400 mg) was then stirred with dowex for 30 mins in 10 mL methanol. The dowex was filtered off, methanol evaporated under vacuo and 332.9mg (63% yield) of product was collected which was an orange powder.[67]

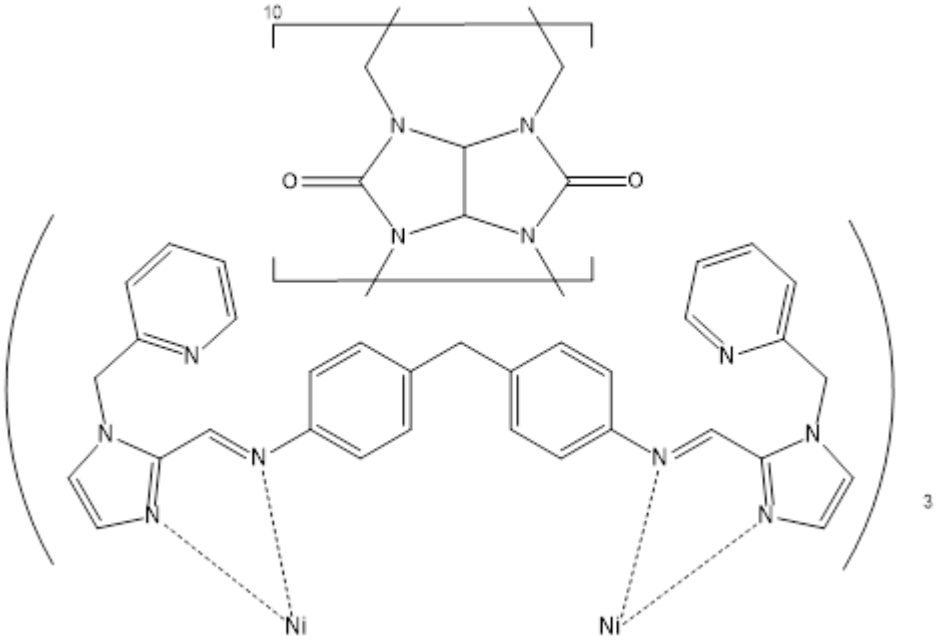
Mass spectrum (TOF MS ES+): M/Z = 589.16 $([Ni_2(L')_3]\text{-}2H)^{2+}$



Synthesis of Nickel picolyl capped imidazole cylinder $[Ni_2(L'')_3]^{4+}\cdot(Cl^-)_4$: This complex was synthesised by Catherine A. J. Hooper and is published as a part of the co-authored paper.[67] Synthesis of $[Ni_2(L'')_3][PF_6]_4$ by post-assembly modification of $[Ni_2(L')_3][PF_6]_4$. $[Ni_2(L')_3][PF_6]_4$ (0.10 g, 0.06 mmol) and 2-(bromomethyl)pyridine hydrobromide (0.09 g, 0.34 mmol) were dissolved in acetonitrile (20 mL) under argon atmosphere. After 10 minutes, Hunig's base (0.18 mL, 1.02 mmol) was added, and the solution was heated overnight under reflux. The solution was cooled to room

temperature before being vacuum filtered and washed with acetonitrile (2 mL). The solvent was removed from the filtrate to give an orange, waxy crude product. The crude product was washed with chloroform (10 mL), the precipitate collected by vacuum filtration and washed with chloroform (2x5 mL) to yield an orange powder (0.05 g, 0.02 mmol, 35%). This was converted to chloride by a dowex chloride anion exchange by stirring with dowex for 30 minutes, dowex was removed by vacuum filtration. Complex was dissolved in the minimum amount of ethanol and precipitated out of di-ethyl ether. Orange powder, 0.05 g, 35% yield.

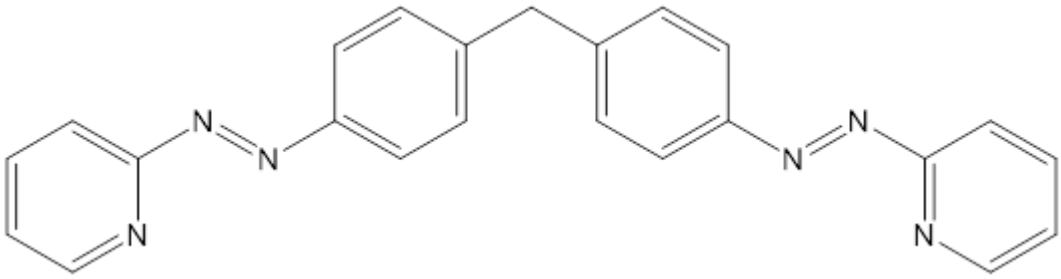
Mass spectrum (TOF MS ES+): m/z = 587.6 $[Ni_2(L'')_3]Cl^{3+}$, 431.8 $[Ni_2(L'')_3]^{4+}$



Synthesis of Nickel picolyl capped imidazole rotaxane $[Ni_2(L'')_3{\cdot}(CB10)]^{4+}{\cdot}(Cl^-)_4$: This complex was synthesised by Aditya Garai and is published as a part of the co-authored paper https://dx.doi.org/10.1021/jacs.0c07750 J. Am. Chem. Soc. 2020, 142, 20651−20660. $[Ni_2L'_3]^{4+}[Cl^-]_4$ (0.025 g, 0.02 mmol) and CB[10] (0.031 g, 0.02 mmol) were dissolved in deionised water (15 mL) and allowed to stir under argon for 30 minutes to make a solution of *pseudo*-rotaxane. 2-(Bromomethyl)pyridine

hydrobromide (0.030 g, 0.12 mmol) was separately dissolved in deionised water (10 mL) under argon and cooled in an ice bath. Hunig's base (0.04 mL, 0.23 mmol) was added slowly to the 2- (bromomethyl)pyridine solution to give a bright pink solution. This solution was added dropwise to the *pseudo*-rotaxane solution and water (5 mL) was used to ensure all the basic solution had been transferred. The reaction mixture was heated under reflux under argon for 16 hours at 100^{o}C. The solution was cooled to room temperature, water (30 mL) was added, and the solution filtered under vacuo. The crude solution was reduced to dryness and the solid washed with chloroform (2 x 5mL) before being allowed to dry. The remaining precipitate was dissolved in water (10 mL), filtered and then freeze dried overnight to yield a pale orange solid (0.042 g, 0.012 mmol, 63% yield).

Mass spectrum (ESI): m/z = 847.3 $[Ni_2(L'')_3{\cdot}(CB10)]^{4+}$, 1141.1$[Ni_2(L'')_3{\cdot}(CB10)]^{4+}Cl^-$

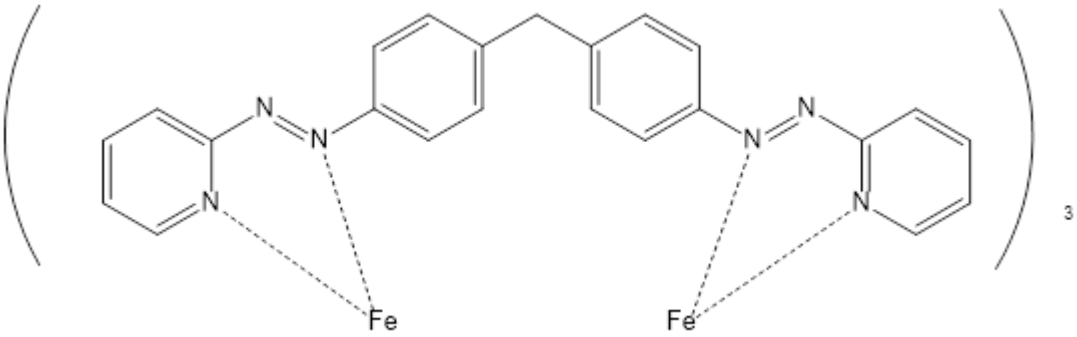


Synthesis of Azo ligand $C_{23}H_{18}N_6$ (L*): This complex was synthesised by Ross T. Egan. 4-4'-methylenedianiline (0.00727 moles, 1.439 g, 2-nitrosopyridine (1.57g,0.0145 mmol) and acetic acids (dropwise until colour change to orange) were stirred in DCM (100 ml) at room temperature for 24 hours. The solvent was then removed under vacuo to yield and orange solid which was purified using column

chromatography on silica with DCM:MeOH (97:3) as the eluent. The compound was collected at Rf = 0.4 (2.754 g) 99% yield orange powder.

Mass spectrum (ESI): m/z = 379.17 L*H+

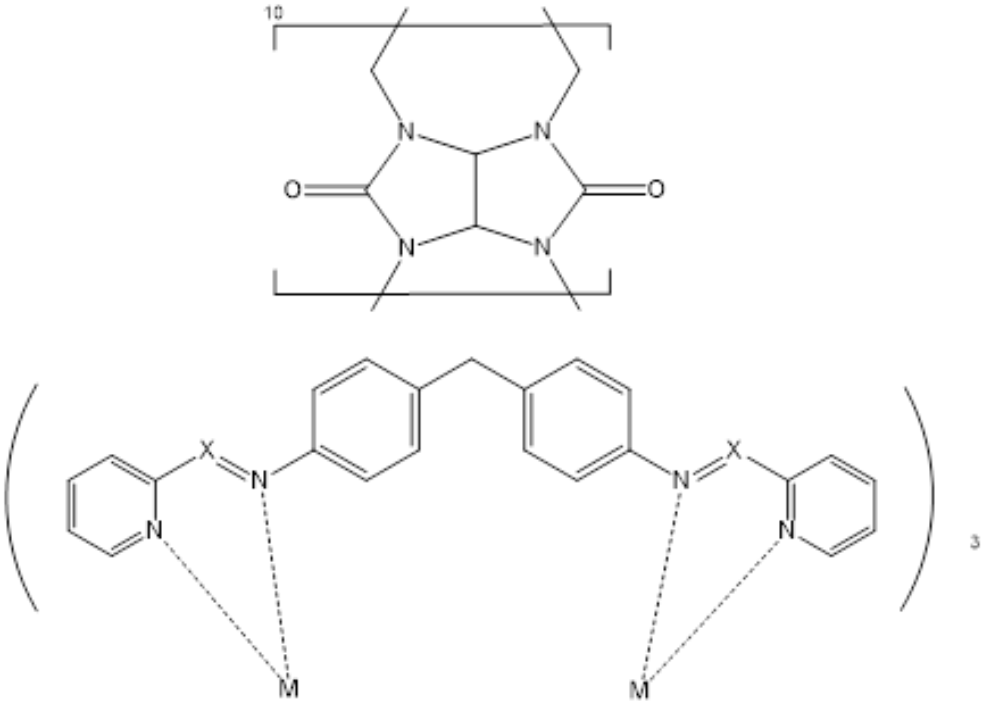
^{1}H NMR (300 MHz, Chloroform-*d*) δ = 8.76 – 8.72 (m, 1H), 8.02 (d, *J*=8.4, 2H), 7.95 – 7.86 (m, 1H), 7.87 – 7.79 (m, 1H), 7.44 – 7.36 (m, 3H), 4.17 (s, 1H).



Synthesis of the Iron azo cylinder $[Fe_2(L^*)_3]^{4+}\cdot(Cl^-)_4$: This complex was synthesised by Dr Aditya Garai. L* (0.04 g, 0.106 mmol) was dissolved in methanol whilst stirring under an inert atmosphere of N_2. Iron(II) chloride tetrahydrate (0.014 g, 0.071 mmol) was added, this resulted in a dark green solution. The solution is then heated under reflux for 3 days then cooled to room temperature. Ammonium hexafluorophosphate was added in excess to precipitate a dark green solid. This was filtered and dried with di-ethyl ether. This was converted to a chloride salt by stirring in methanol with excess dowex™ 1X8 200-400 (Cl) for 30 mins. The dowex was then filtered off and the filtrate was collected under vacuum. The methanol was removed under vacuo and the solid was re-dissolved in the minimum amount of methanol. This was then precipitated out of di-ethyl ether. Left a dark green solid 0.032 g, 25.7 µmol 73% yield.

^{1}H NMR (300 MHz,D_2O) δ 9.06 (dd, *J* = 8.1, 1.3 Hz, 2H), 8.60 (td, *J* = 7.9, 1.4 Hz, 2H), 7.82 – 7.69 (m, 2H), 7.04 (dd, *J* = 5.7, 1.4 Hz, 2H), 6.96 (d, *J* = 1.7 Hz, 2H), 6.94 (s, 2H), 6.19 (s, 2H), 6.16 (s, 2H), 4.00 (s, 2H).

MS = Unable to obtain cylinder peak, ligand is the predominant peak at 379.17 m/z stability in the mass spectrometer was thought to be the issue. See chapter 4 for the MS of this complex in blood.



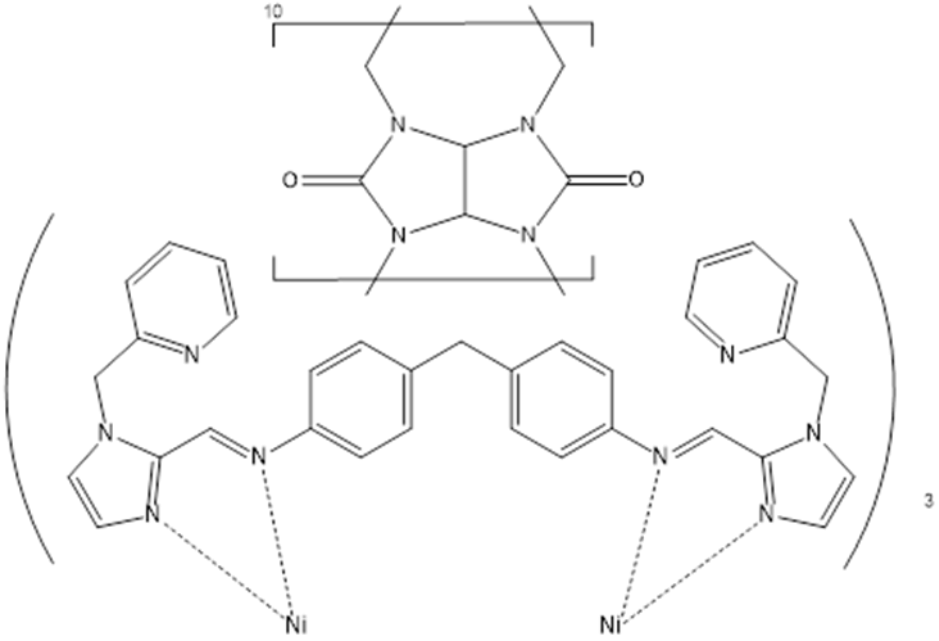
Preparation of *pseudo*-rotaxanes: All *pseudo*-rotaxanes were prepared using the same method, 1eq of cylinder was dissolved in water and 1.1 eq of CB[10] was added. This leaves a near clear solution of *pseudo*-rotaxane, the excess CB[10] is a white powder and is separated by centrifugation and filtration. The above schematic shows the product *pseudo*-rotaxane, where CB[10] surrounds the central axis of the cylinder. Where X is carbon in L.

CB10-$[Fe_2L_3]^{4+}[Cl^-]_4$:

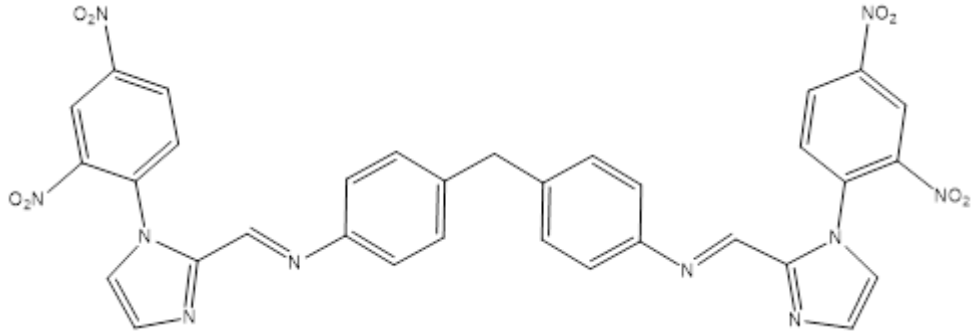
Mass spectrum (TOF MS ES+): m/z = 310.1 $[Fe_2L_3]^{4+}$, 725.5 CB10-$[Fe_2L_3]^{4+}$

CB10-$[Ni_2L_3]^{4+}[Cl^-]_4$:

Mass spectrum (TOF MS ES+): m/z = 311.6 $[Ni_2L_3]^{4+}$, 726.7 CB10-$[Ni_2L_3]^{4+}$



Preparation of $[Ni_2(L'')_3{\cdot}(CB10)]^{4+}{\cdot}(Cl^-)_4$ via slippage mechanism: $[Ni_2(L'')_3]^{4+}$ cylinder (1.12 mg) was dissolved in 1mL methanolic water (20:80) with CB[10] (1.334 mg, 1.34 eq) and heated to reflux for 16 hrs. the solution changed from cloudy to clear after 10 minutes at reflux. The solution was centrifuged, filtered and the solvent was removed under vacuo to leave the product, a light yellow powder (0.962g, 45.4% yield). Mass spectrum (ESI): m/z = 846.99 $[Ni_2(L'')_3{\cdot}(CB10)]^{4+}$, 1141.29 $[Ni_2(L'')_3{\cdot}(CB10)]^{3+}Cl^-$

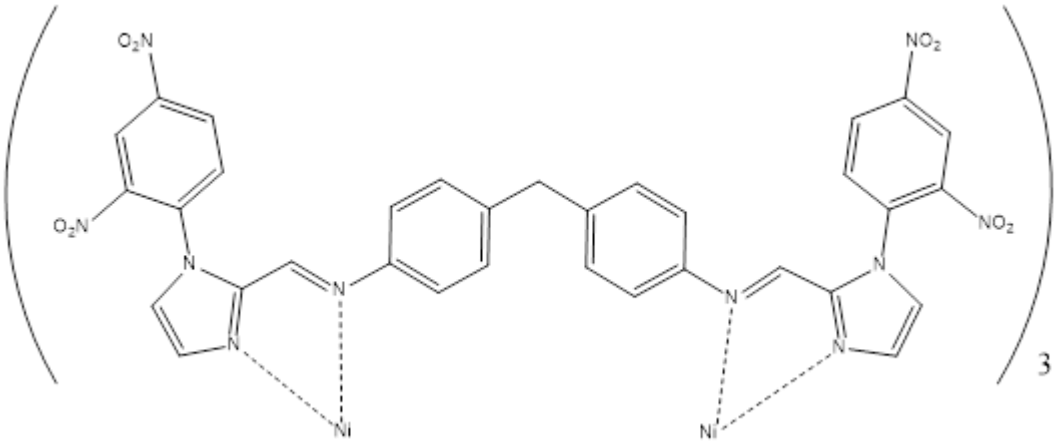


Synthesis of DNB capped ligand (L^{DNB}): This compound was synthesis by Dr Aditya Garai as part of a paper which is approaching submission (paper 5 in publication section). DNB aldehyde (50 mg, 0.19 mmol, 2.1 equivalents) and 4,4'-Methylenedianiline(18 mg, 0.09 mmol, 1 equivalent) were taken in a 25 ml round bottom flask in 15 ml ethanol and stirred at room temperature over night to obtain the ligand as a yellow precipitate. The precipitate was filtered and washed with cold ethanol and dried over vacuum to leave a bright yellow powder. Yield (50 mg) 80%

^{1}H NMR (400 MHz, DMSO-d_6) δ 8.92 (d, J = 2.6 Hz, 1H, DNB-Ha), 8.67 (dd, J = 8.7, 2.6 Hz, 1H, DNB-Hb), 8.47 (d, J = 0.6 Hz, 1H, Imine-H), 7.98 (d, J = 8.6 Hz, 1H, DNB-Hc), 7.75 (dd, J = 1.2, 0.6 Hz, 1H, Imidazole-H), 7.47 (d, J = 1.2 Hz, 1H, Imidazole-H), 7.14 (d, J = 8.4 Hz, 2H, Ph-2H), 6.93 (d, J = 8.4 Hz, 2H, Ph-2H), 3.86(s, 2H, CH_2).

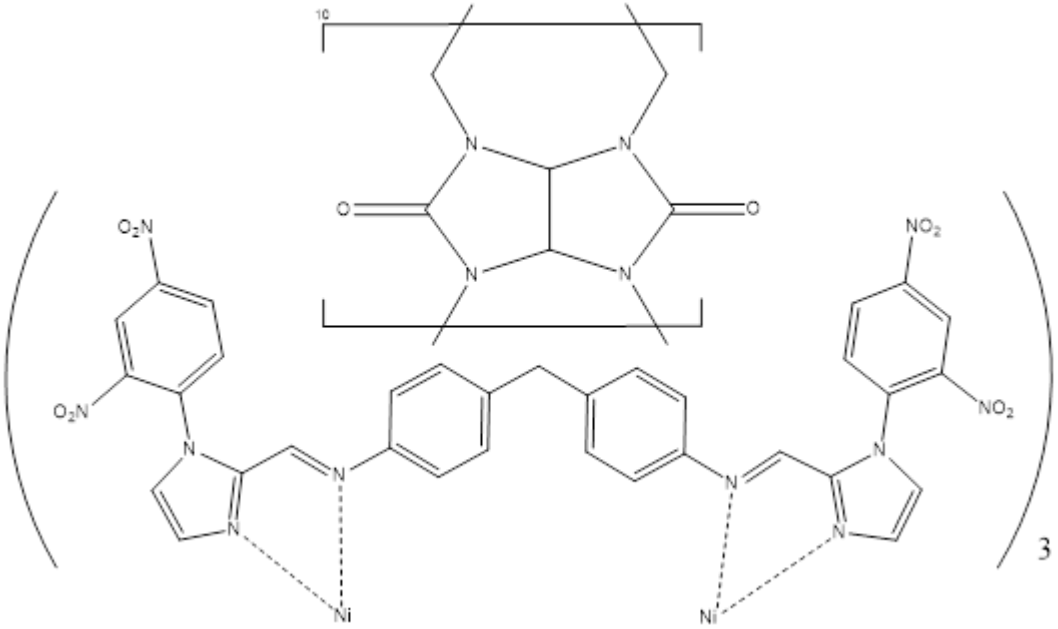
Mass spectrum (ESI): m/z =686.4

CHN: C 57.87 %, H 3.34 %, N 20.67 % (Predicted C 57.73 %, H 3.23 %, N 20.40 %).



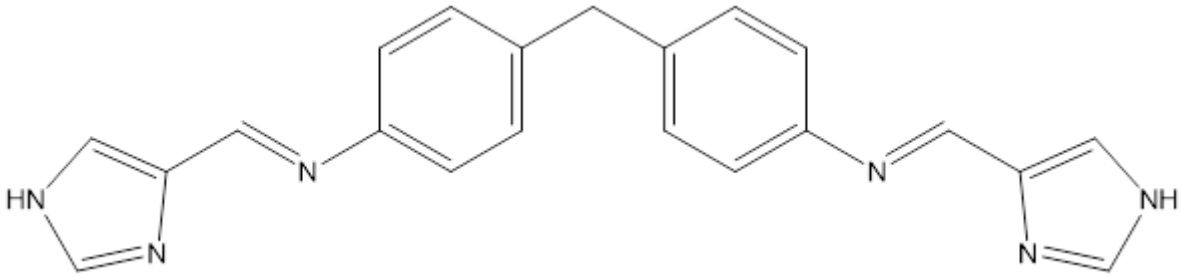
Synthesis of $[Ni_2L^{DNB}{}_3]$ 4Cl: This compound was synthesis by Dr Aditya Garai as part of a paper which is approaching submission (paper 5 in publication section). DNB ligand (20 mg, 0.029 mmol, 3 equivalents) suspended in 5 mL dry methanol under argon. $NiCl_2.6H_2O$ (4.62 mg, 0.019 mmol) in 5 mL ethanol was slowly added to the above suspension slowly. The reaction mixture was heated at 50 °C for 1h. The solution became transparent yellow. The reaction mixture was filtered and to the filtrate excess of methanolic NH_4PF_6 was added. The precipitate was filtered and washed with methanol. The residue was dried in vacuum to obtain the product, a yellow/orange powder. Yield (18 mg) 80%.

Mass spectrum (ESI): m/z = 544.0949 ($[M-4Cl]^{4+}$)



Synthesis of [$Ni_2(L^{DNB})_3$·CB10] rotaxane: This compound was synthesis by Dr Aditya Garai as part of a paper which is approaching submission (paper 5 in publication section). A suspension of CB [10] (10 mg, 6.0 μmol, 1.1 equivalent) was added to a degassed aqueous (10 mL) solution of $[Ni_2(L')_3]Cl_4$ (7.2 mg, 5.5 μmol, 1 equivalent). The mixture was stirred under argon for 10 minutes. To the mixture was added aqueous (5 mL) potassium carbonate (9.2 mg, 66.8 μmol, 12 equivalent) followed by aqueous (5 mL) 1-fluoro-2,4-dinitrobenzene (18.6 mg, 100 μmol, 18.3 equivalent), and the mixture was heated to 80 °C for 60 minutes. The yellow/orange precipitate was collected by filtration and washed with water, methanol, ether, and chloroform and dried under high vacuum to yield 16.5 mg (76 % yield).

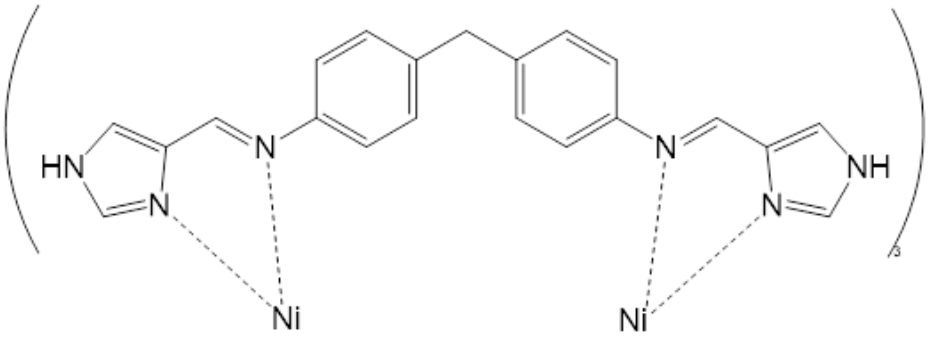
Mass spectrum (ESI): m/z =959.4637 ($[Ni_2(L^{DNB})_3 \bullet CB10]^{4+}$).



Synthesis of L'4: This compound was synthesised by Catherine A. J. Hooper. 4,4'-methylendianiline (0.793 g, 4 mmol) and 4-imidazolecarboxaldehyde (0.768 g, 8 mmol) are stirred in methanol (30 mL) for 10 min; two drops of glacial acetic acid are then added, and the mixture is refluxed for 2 hrs. An off-white solid precipitated and was collected by filtration, washed with methanol, and dried in vacuo. 1.204 g 85% yield.

Mass spectrum (TOF MS ES+): m/z = 355.17 [M+]

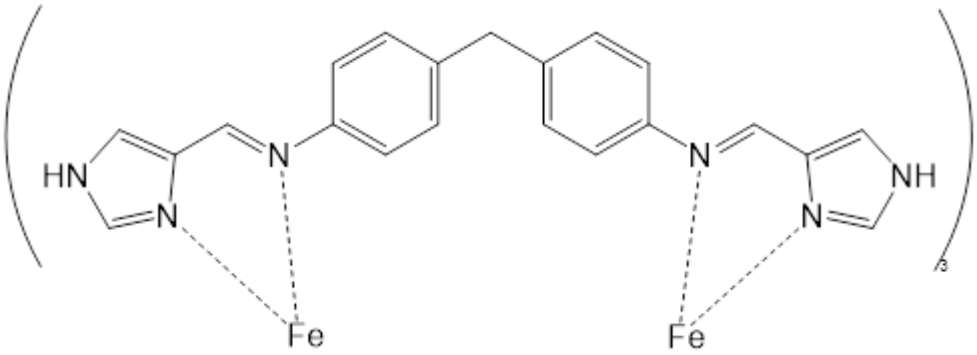
^{1}H NMR (400 MHz, DMSO-d_6): δ 12.99 (s, 1H), 12.52 (s, 1H), 8.43 (d, J = 14.9 Hz, 2H), 7.82 (s, 2H), 7.77 (s, 1H), 7.51 (s, 1H), 7.26 (d, J = 7.8 Hz, 4H), 7.20 – 7.07 (m, 4H), 3.95 (s, 2H).



Synthesis of $[Ni_2(L'^4)_3]Cl_4$ cylinder: This compound was synthesised by Catherine A. J. Hooper. Ligand L (0.053 g, 0.15 mmol) and nickel(II) chloride hexahydrate (0.024 g,

0.10 mmol) were stirred in methanol (10 mL) for 30 min. The resulting green solution was treated with methanolic ammonium hexafluorophosphate (excess) and filtered through Celite, and the filtrate allowed to stand for 48 h at 4 ^{o}C. Green crystals formed and were collected by filtration, washed several times with small amount of cold methanol and finally dried in vacuo over P_4O_{10}. A yellow powder was collected, 0.449 g, Yield: 68%.

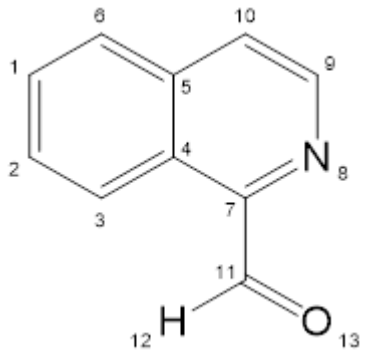
Mass spectrum (TOF MS ES+): m/z = 589.3 $[Ni_2(L'^4)_3]^{2+}$



Synthesis of $[Fe_2(L'^4)_3]Cl_4$ cylinder: This compound was synthesised by Catherine A. J. Hooper. L'^{4} ligand (0.127 g, 0.36 mmol) and iron (II) chloride tetrahydrate (0.048 g, 0.24 mmol) were stirred in methanol (15 mL) for 40 minutes. The resulting orange solution was filtered through celite and treated with methanolic ammonium tetrafluoroborate (excess) to yield an orange product, which was isolated by filtration, washed with methanol, and dried in vacuo. The product was then dissolved in acetonitrile (10 mL). The solution was filtered through celite, concentrated in vacuo, diluted with methanol (15 mL) and allowed to stay at room temperature for 24 hrs. An orange polycrystalline powered resulted, which was collected by filtration, washed with

cold methanol, and finally dried in vacuo under P_4O_{10}. The product was an orange powder, 0.1011 g, yield 64%.

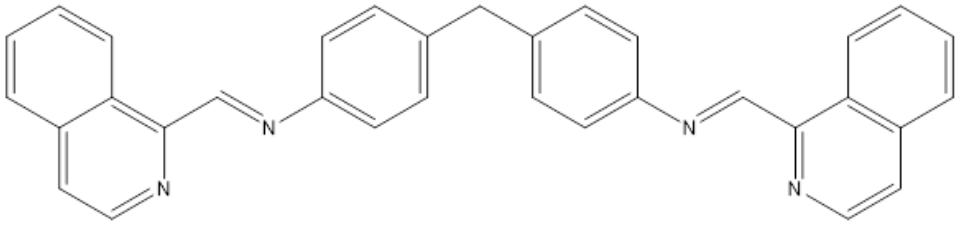
Mass spectrum (TOF MS ES+): m/z = 586.17 $[Fe_2(L'^4)_3]^{2+}$



Synthesis of isoquinoline-1-aldehyde: 1-methylisoquinoline (1g, $6.98*10^{-3}$ mol) was dissolved in 50 ml of dioxane and selenium dioxide (0.89 g, $8.02*10^{-3}$) was added to this which turned the solution a dark brown colour. This was refluxed for 3 hours and then filtered under vacuum to remove selenium dioxide. This was purified by column chromatography with silica as the stationary phase and a mixture of 1:4 ethyl-acetate: hexane (by volume) as the eluent. Column packing was carried out with hexane as the solvent. Product fractions were determined by TLC. The product was a pale orange/pink crystalline solid (0.78g, 71% yield).

Mass spectrum (TOF MS ES+): m/z = 157.1 [M+]

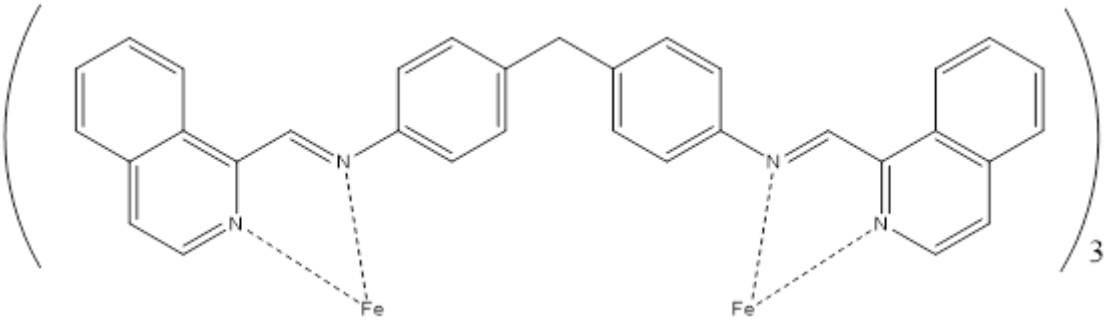
^{1}H NMR (300 MHz, Chloroform-*d*) δ = 10.35 (s, 1H, P12), 9.17 (d, *J*=8.8, 1H, p6), 8.67 (t, *J*=5.6, 1H, P9), 7.82 – 7.74 (m, 2H, P10/2), 7.65 (tt, *J*=6.9, 5.0, 2H, p6/1).



Synthesis of L^Q: Isoquinoline-1-aldehyde (0.403 g, $2.57*10^{-3}$ mol) and 4,4-methylenedianiline (0.254 g, $1.28*10^{-3}$ mol) were stirred in ethanol overnight at room temperature. The solution yielded a solid yellow precipitate which was filtered and washed with cold ethanol under vacuo. This left the product 0.486 g, 79.5% yield.

Mass spectrum (TOF MS ES+): m/z = 477.2 [M+]

^{1}H NMR (300 MHz, Chloroform-*d*) δ = 9.73 – 9.61 (m, 1H), 9.09 (s, 1H), 8.68 (d, *J*=5.6 Hz, 1H), 7.91 (ddd, *J*=6.7, 4.8, 2.2 Hz, 1H), 7.81 – 7.66 (m, 3H), 7.45 – 7.28 (m, 4H), 4.10 (s, 1H).

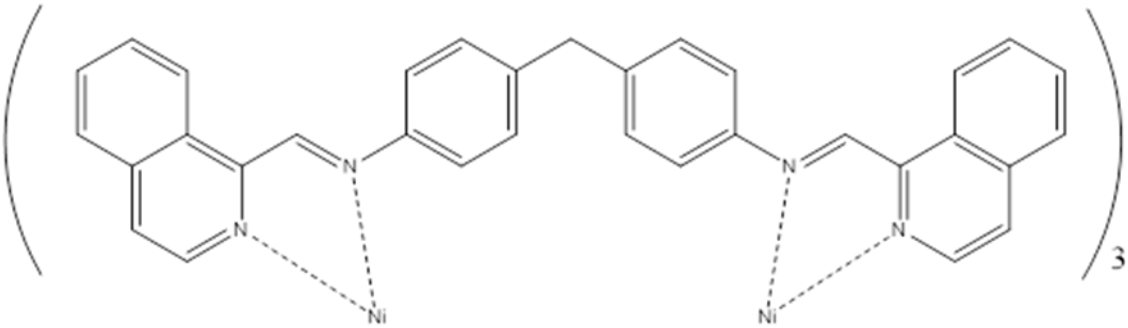


Synthesis of $[Fe_2(L^Q)_3]Cl_4$ cylinder: L^Q (0.2g, $4.19x10^{-4}$m) was mixed with Iron (II) chloride tetrahydrate (0.0556 g, $2.8x10^{-4}$ mol) in methanol for 3 hrs. The solvent was then removed under vacuo and the solid was redissolved in the minimum amount of methanol. A methanol solution saturated with ammonium hexafluorophosphate was added (30 eq) and the solution was stirred for 20 mins. The precipitate was collected via vacuum filtration and washed with water (10 mL) then di-ethyl ether (25 mL).This

was suspended in the minimum amount of methanol and dowex™ 1X8 200-400 (Cl) was added (30 eq) and stirred for 30 minutes. The dowex was filtered off under vacuo and the solvent removed under vacuo. The solid was resuspended in the minimum amount of methanol, this was added dropwise to excess di-ethyl ether and the product precipitated as a deep blue powder and was filtered, 0.2077g, 88% yield.

Mass spectrum (TOF MS ES+): m/z = 385.3 $[Fe_2L^Q_3]^{4+}$, 525.7 $([Fe_2L^Q_3]Cl)^{3+}$.

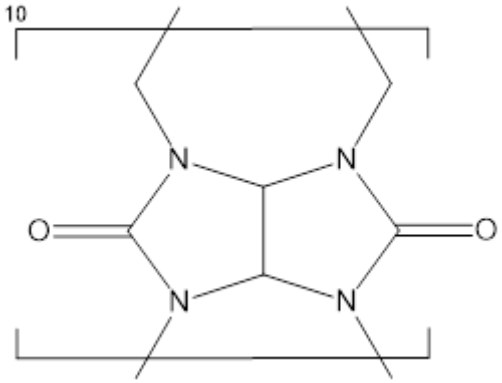
^{1}H NMR (400 MHz, Methanol-*d*$_4$) δ = 10.09 (s, 1H), 8.98 (s, 1H), 8.35 (d, *J*=7.6 Hz, 1H), 8.25 (d, *J*=5.8 Hz, 1H), 8.13 (d, *J*=7.1 Hz, 2H), 7.38 – 7.22 (m, 1H), 7.14 (dd, *J*=15.1, 6.8 Hz, 1H), 6.88 (s, 1H), 5.79 (s, 1H), 5.55 (s, 1H), 4.06 (s, 1H).



Synthesis of $[Ni_2(L^Q)_3]Cl_4$ cylinder: L^Q (0.09 g, 1.89x10^{-4} m) was mixed with nickel (II) chloride hexahydrate (0.02g, 8.41x10^{-5} m) in methanol for 16 hrs. The solvent was then removed under vacuo and the solid was redissolved in the minimum amount of methanol. A methanol solution saturated with ammonium hexafluorophosphate was added (30 eq) and the solution was stirred for 30 mins. The precipitate was collected via vacuum filtration and washed with water (10 mL) then di-ethyl ether (25 mL).This was suspended in the minimum amount of methanol and dowex™ 1X8 200-400 (Cl) was added (30 eq) and stirred for 30 minutes. The dowex was filtered off under vacuo and the solvent removed under vacuo. The solid was resuspended in the minimum

amount of methanol, this was added dropwise to excess di-ethyl ether and the product precipitated as an orange powder (0.0481g, 67.7% yield).

Mass spectrum (TOF MS ES+): m/z = 386.8 $[Ni_2L^{Q}_3]^{4+}$, 527.7 $([Ni_2L^{Q}_3]Cl)^{3+}$.



CB[10] synthesis: CB[10] was synthesised by Fengbo Liu from the group of Dr Simin Liu at the Wuhan University of Science and Technology by previously reported methods.[34]

2.8.2: Experiments

Biophysics experimental: Ultrapure water was used throughout all biophysical work. For Circular and Linear dichroism, DNA samples were made up from Calf thymus DNA sodium salt (Sigma Aldrich) by dissolving in milli-Q water (MΩ cm^{-1}) and washed using a 10 kda MWCO centrifuge tube (ThermoFisher scientific). The solution was then quantified by UV-Vis spectroscopy (Cary 5000 NIR spectrometer) by ε 258 = 13200 M^{-1} cm^{-1} to give a concentration in DNA base pairs. This stock solution was kept frozen with fresh aliquots being taken out for each experiment. Fresh buffer was made up before each experiment (see experimental for specifics). Complexes were dissolved in ultrapure H_2O only with fresh solutions being used for each batch of experiments.

Circular dichroism (CD): Spectra were recorded on a Chirascan-plus spectrometer (Applied Photophysics limited). The samples were scanned in a 1 cm path length cuvette between 800 nm and 200 nm with 3 repeats at 1 nm step size and 0.5 s dwell time per point. Titrations were carried out at a constant concentration of CT-DNA, sodium chloride (10 mM) and sodium cacodylate buffer (1 mM, pH 7.3) by adding compensating solutions of 2x DNA/Buffer of equal volume to the titre of the complex solution. The concentration of complex in the cuvette was increased step wise by adding set volumes of a stock complex solution. The R value refers to the ratio of DNA base pairs to complex, i.e. R60 = 60 bp for every 1 complex, R4 = 4 bp per complex.

Flow Linear Dichroism (LD): was carried out on the same Chirascan+ spectrometer (Applied Photophysics limited) using the LD accessory (Applied Photophysics limited). The LD cell has an angular gap of 0.25 mm giving an overall path length of 0.5 mm. Samples volumes began at 175 µL and stopped at 250 µL. The cell was rotated at 40

revolutions per second to optimise DNA signal. The titration series was carried out using the same method as in the CD studies, with a 3-minute incubation time prior to recording spectra. Binding curves were generated using GraphPad Prism and fitted using the Binding saturation – one site specific binding model. K_d was determined from this fitting by finding the corresponding concentrations at half of B_{max}.

Polyacrylamide gel electrophoresis (PAGE): Studies were performed using following oligonucleotide sequences (from Eurofins Germany).

3WJ:

S1 = 5′-CGGAACGGCACTCG-3′

S2 = 5′- CGAGTGCAGCGTGG-3′

S3 = 5′-CCACGCTCGTTCCG-3′

4WJ:

S1 = 5′-GCCTAGCATGATACTGCTACCG-3′

S2 = 5′-CGGTAGCAGTACCGTTGGTGGC-3′

S3 = 5′-GCCACCAACGGCGTCAACTGCC-3′

S4 = 5′-GGCAGTTGACGTCATGCTAGGC-3′

3WJ radiolabelled PAGE: 1.2 µL of S1 was radiolabelled using 1 µL of adenosine triphosphate γ 32P (Perkin Elmer) at the 5’ end using 2 µl of T4 bacteriophage polynucleotide kinase (New England Biolabs) by incubating them at 37 °C for 1 hr in 2 µL of 10x PNK buffer (New England Biolabs) made up to 20 µl with nuclease free water (ThermoFisher Scientific). This solution was heated to 80 °C for 3 minutes to inactivate the enzyme and before being purified using a QAIquick nucleotide removal column (Qiagen), this was washed twice after binding to the column, and then eluted with 60

µL of nuclease free water to leave a 4 µM solution of radiolabelled S1*. PAGE Polyacrylamide gels were prepared by mixing 25 mL of 29:1 acrylamide/bis-acrylamide (National Diagnostic, protogel) with 5 mL of 10x Tris-Boric acid buffer (890 mM each, pH 8.30 or pH 7.05 adjusted with HCl) and 20 mL of Milli-Q water. To this 400 µL of a 10% w/v ammonium persulfate/water solution and 40 µL of TEMED were added to initialise polymerisation. This is then immediately poured between 2 glass plates and a comb inserted at the top this is then left to set for 1 hr. Samples were made up to 10 µl containing 0.4 µM of DNA per strand, of each strand (S1*, S2 and S3 unless stated otherwise), 1xTBN buffer (89 mM Tris, 89 mM Boric acid, 10 mM NaCl) and the indicated ratio of Complex or competitor. DNA, water, and buffer were mixed in solution before addition of the stated ratios of complex and competitor. Samples were then incubated at 37 °C for 1 hr. 5 µL of 30% w/v glycerol was then added to each sample and the sample was then centrifuged, mixed, and pipetted into the wells on the gel. The Gel was run at 140 V for 2 hrs in 1x TB buffer. The gel was then removed from the plates and placed into a phosphor imaging box with a screen and left for 2 hrs, the screen was then removed and imaged on a BIO-RAD FarosFX Plus molecular imager.

Fluorescent PAGE experiments:

PAGE Polyacrylamide gels were prepared by mixing 25 mL of 29:1 acrylamide/bis-acrylamide (National Diagnostic, protogel) with 5 mL of 10x Tris-Boric acid buffer (890 mM each, pH 8.30, or pH 7.05 adjusted with HCl) and 20 ml of Milli-Q water. To this 400 µL of a 10% w/v ammonium persulfate/water solution and 40 µL of TEMED were added to initialise polymerisation. This is then immediately poured between 2 glass plates and a comb inserted at the top this is then left to set for 1 hr. Samples were made up to 10 µL containing 1 µM of each strand 1x TBN buffer (89 mM Tris, 89 mM

Boric acid, 10 mM NaCl, either pH 8.30 or 7.05) and the indicated ratio of Complex or competitor. DNA, water, and buffer were mixed in solution before addition of the stated ratios of complex and additional components. Samples were then incubated at 37 °C for 1 hr. 5 µL of 30% w/v glycerol was then added to each sample and the sample was then centrifuged, mixed, and pipetted into the wells on the gel. The Gel was run at 140 V for 2 hours in 1x TB buffer. The gel was then removed from the plates and stained using SYBR™ Gold Nucleic Acid Gel Stain in 1xTB buffer for 45 minutes before imaging on a bio-rad ChemiDoc fluorescent imager at 305 nm excitation.

Cell toxicity studies using MDA-MB-231: The MDA-MB-231 cell line was purchased from the European Collection of Authenticated Cell Cultures. All cell culture media and supplements were purchased from Gibco (Thermo Scientific), all plasticware was purchased from Greiner Bio-One. Cells were grown in T_{75} tissue culture flasks as monolayers cultured in DMEM, supplemented with 10% (v/v) foetal bovine serum, 100 U/mL penicillin, 100 mg/mL streptomycin, and 2 mM L-glutamine. Cells were maintained at 37 °C in a 5% CO_2 humidified incubator and sub-cultured twice weekly before confluency. All cell cultures were confirmed free from Mycoplasma sp. contamination using the EZ-PCR mycoplasma detection kit according to the manufacturer's instructions. Cells were not passaged beyond passage 20.

MTT assay: The MTT (3-(4,5-dimethylthiazol-2-yl)-2,5-diphenyltetrazolium bromide) assay was used to assess cytotoxicity. Cells were seeded at a density of 6500 cells per well in a 96-well plate, exposed to different concentrations of test compound and incubated for 72 hours. MTT was added to a final concentration 0.5 mg/ml followed by a 3-hour incubation. DMSO was added to solubilise formazan and absorbance was read at 490 nm in Tecan Infinite F200 Pro (Tecan, Männedorf, Switzerland). Samples

were analysed in triplicate technical replicate and each experiment was repeated three times independently.[68]

Mass Spectrometry: Samples were then run on a Waters SYNAPT G2S MS, with the TriVersa NanoMate LESA and chip attachment, using the time-of-flight MS ES+ method in sensitivity mode. Samples were run using direct injection to eliminate cross contamination between samples. Spectra were analyzed using MassLynx software v4.2.

2.9: References

1 C. J. Bruns and J. F. Stoddart, *The Nature of the Mechanical Bond: From Molecules to Machines*, Wiley, 2016, 1–761.

2 J. F. Stoddart, *Angew. Chem. Int. Ed.*, 2017, **56**, 11094–11125.

3 M. J. Langton and P. D. Beer, *Acc. Chem. Res.*, 2014, **47**, 1935–1949.

4 S. L. Woltering, P. Gawel, K. E. Christensen, A. L. Thompson and H. L. Anderson, *J. Am. Chem. Soc*, 2020, **142**, 13523–13532.

5 N. Pairault, R. Barat, I. Tranoy-Opalinski, B. Renoux, M. Thomas and S. Papot, *C. R. Chim.*, 2016, **19**, 103–112.

6 R. Barat, T. Legigan, I. Tranoy-Opalinski, B. Renoux, E. Péraudeau, J. Clarhaut, P. Poinot, A. E. Fernandes, V. Aucagne, D. A. Leigh and S. Papot, *Chem. Sci.*, 2015, **6**, 2608–2613.

7 A. Fernandes, A. Viterisi, F. Coutrot, S. Potok, D. A. Leigh, V. Aucagne and S. Papot, *Angew. Chem. Int. Ed.*, 2009, **48**, 6443–6447.

8 P. J. Altmann and A. Pöthig, *Angew. Chem. Int. Ed.*, 2017, **56**, 15733–15736.

9 H.-Y. Zhou, Q.-S. Zong, Y. Han and C.-F. Chen, *Chem. Commun.*, 2020, **56**, 9916-9936.

10 J. Malina, M. J. Hannon and V. Brabec, *Nucleic Acids Res.*, 2008, **36**, 3630–3638.

11 M. J. Hannon, V. Moreno, M. J. Prieto, E. Moldrheim, E. Sletten, I. Meistermann, C. J. Isaac, K. J. Sanders and A. Rodger, *Angew. Chem. Int. Ed.*, 2001, **40**, 879–884.

12 A. C. G. Hotze, N. J. Hodges, R. E. Hayden, C. Sanchez-Cano, C. Paines, N. Male, M.-K. Tse, C. M. Bunce, J. K. Chipman and M. J. Hannon, *Chem. Biol.*, 2008, **15**, 1258–1267.

13 J. Malina, M. J. Hannon and V. Brabec, *Chem. Eur. J.*, 2008, **14**, 10408–10414.

14 I. Meistermann, V. Moreno, M. J. Prieto, E. Moldrheim, E. Sletten, S. Khalid, P. Mark Rodger, J. C. Peberdy, C. J. Isaac, A. Rodger and M. J. Hannon, *Proc. Natl. Acad. Sci. USA*, 2002, **99**, 5069–5074.

15 C. Ducani, A. Leczkowska, N. J. Hodges, M. J. Hannon, C. Ducani, A. Leczkowska, M. J. Hannon and N. J. Hodges, *Angew. Chem. Int. Ed.*, 2010, **49**, 8942–8945.

16 G. I. Pascu, A. C. G. Hotze, C. Sanchez-Cano, B. M. Kariuki and M. J. Hannon, *Angew. Chem. Int. Ed.*, 2007, **46**, 4374–4378.

17 S. Vuong, L. Stefan, P. Lejault, Y. Rousselin, F. Denat and D. Monchaud, *Biochimie*, 2012, **94**, 442–450.

18 J. Malina, M. J. Hannon and V. Brabec, *Chem. Eur. J.*, 2007, **13**, 3871–3877.

19 L. S. Shlyakhtenko, V. N. Potaman, R. R. Sinden, A. A. Gall and Y. L. Lyubchenko, *Nucleic Acids Res.*, 2000, **28**, 3472–3477.

20 L. Cardo and M. J. Hannon, in *Metallo-Drugs: Development and Action of Anticancer Agents*, ed. A. Sigel, H. Sigel, E. Freisinger and R. K. O. Sigel, Walter de Gruyter GmbH, Berlin, 2018, vol. 18, ch. 11, 303–324.

21 A. Oleksi, A. G. Blanco, R. Boer, I. Usón, J. Aymamí, A. Rodger, M. J. Hannon and M. Coll, *Angew. Chem. Int. Ed.*, 2006, **45**, 1227–1231.

22 K. Duskova, P. Lejault, É. Benchimol, R. Guillot, S. Britton, A. Granzhan and D. Monchaud, *J Am Chem. Soc.*, 2020, **142**, 424–435.

23 L. Cardo, V. Sadovnikova, S. Phongtongpasuk, N. J. Hodges and M. J. Hannon, *Chem. Commun.*, 2011, **47**, 6575–6577.

24 L. Cerasino, M. J. Hannon and E. Sletten, *Inorg. Chem.*, 2007, **46**, 6245–6251.

25 T. Hermann and D. J. Patel, *Structure*, 2000, **8**, 47–54.

26 J. Malina, M. J. Hannon and V. Brabec, *Sci. Rep.*, 2016, **6**, 29674.

27 S. Phongtongpasuk, S. Paulus, J. Schnabl, R. K. O. Sigel, B. Spingler, M. J. Hannon and E. Freisinger , *Angew. Chem. Int. Ed.,* 2013, **52**, 11513–11516.

28 L. Melidis, H. J. Hill, N. J. Coltman, S. P. Davies, K. Winczura, T. Chauhan, J. S. Craig, A. Garai, C. A. J. Hooper, R. T. Egan, J. A. McKeating, N. J. Hodges, Z. Stamataki, P. Grzechnik and M. J. Hannon, *Angew. Chem. Int. Ed.*, 2021, **60**, 18144–18151.

29 J. Malina, M. J. Hannon and V. Brabec, *FEBS J.*, 2014, **281**, 987–997.

30 L. Cardo, I. Nawroth, P. J. Cail, J. A. McKeating and M. J. Hannon, *Sci. Rep.*, 2018, **8**, 13342.

31 C. R. Martinez and B. L. Iverson, *Chem. Sci.*, 2012, **3**, 2191-2201.

32 D. Das, K. I. Assaf and W. M. Nau, *Front. Chem.*, 2019, **7**, 619.

33 Y. Yu, Y. Li, X. Wang, H. Nian, L. Wang, J. Li, Y. Zhao, X. Yang, S. Liu and L. Cao, *J. Org. Chem.*, 2017, **82**, 540–541.

34 S. Liu, P. Y. Zavalij and L. Isaacs, *J. Am. Chem. Soc.,* 2005, **127**, 15959–15967.

35 J. Murray, K. Kim, T. Ogoshi, W. Yao and B. C. Gibb, *Chem. Soc. Rev.*, 2017, **46**, 2479–2496.

36 S. J. Barrow, S. Kasera, M. J. Rowland, J. del Barrio and O. A. Scherman, *Chem. Rev.*, 2015, **115**, 12320–12406.

37 S. Liu, C. Ruspic, P. Mukhopadhyay, S. Chakrabarti, P. Y. Zavalij and L. Isaacs, *J. Am. Chem. Soc.*, 2005, **127**, 15959–15967.

38 Y. H. Chu, M. Sibrian-Vazquez, J. O. Escobedo, A. R. Phillips, D. T. Dickey, Q. Wang, M. Ralle, P. S. Steyger and R. M. Strongin, *Mol. Pharm.*, 2016, **13**, 2677–2682.

39 S. Dasari and P. Bernard Tchounwou, *Eur. J. Pharmacol.*, 2014, **740**, 364–378.

40 B. J. S. Sanderson, L. R. Ferguson and W. A. Denny, *Mutat. Res.*, 1996, **355**, 59–70.

41 R. Oun, Y. E. Moussa and N. J. Wheate, *Dalton Trans.*, 2018, **47**, 6645–6653.

42 X. Yang, F. Liu, Z. Zhao, F. Liang, H. Zhang and S. Liu, C*hin. Chem. Lett.*, 2018, **29**, 1560–1566.

43 M. P. Gamcsik, M. S. Kasibhatla, S. D. Teeter and O. M. Colvin, *Biomarkers*, 2012, **17**, 671-691.

44 T. Kench, P. A. Summers, M. K. Kuimova, J. E. M. Lewis and R. Vilar, *Angew. Chem. Int. Ed.*, 2021, **60**, 10928–10934.

45 C. E. Otteson, C. M. Levinn, J. M. van Raden, M. D. Pluth and R. Jasti, *Org. Lett.*, 2021, **23**, 4608–4612.

46 J. Murray, K. Kim, T. Ogoshi, W. Yao and B. C. Gibb, *Chem. Soc. Rev.*, 2017, **46**, 2479-2496.

47 F. Biedermann, V. D. Uzunova, O. A. Scherman, W. M. Nau and A. de Simone, *J. Am. Chem. Soc.*, 2012, **134**, 15318–15323.

48 J. Malina, M. J. Hannon and V. Brabec, *Chem. Eur. J.*, 2015, **21**, 11189–11195.

49 G. K. Balendiran, R. Dabur and D. Fraser, *Cell Biochem. Funct.*, 2004, **22**, 343–352.

50 D. W. Boerth and A. C. Arvanites, *J. Phys. Org. Chem.*, 2017, **30**, e3640.

51 Y. J. Zheng and R. L. Ornstein, *J. Am. Chem. Soc.*, 1997, **119**, 648–655.

52 F. Tuna, M. R. Lees, G. J. Clarkson and M. J. Hannon, *Chem. Eur. J.*, 2004, **10**, 5737–5750.

53 M. Pascu, G. J. Clarkson, B. M. Kariuki and M. J. Hannon, *Dalton Trans.*, 2006, 2635–2642.

54 L. Childs, PhD thesis, University of Warwick, 2002.

55 R. Holliday, *Genet. Res. (Camb).*, 1964, **5**, 282–304.

56 S. B. Chernikova, J. C. Game and J. M. Brown, *Cancer Biol. Ther.*, 2012, **13**, 61–68.

57 J. C. Puigvert, K. Sanjiv and T. Helleday, *FEBS J.*, 2016, **283**, 232–245.

58 C. I. Vitoc and I. Mukerji, *Biochemistry*, 2011, **50**, 1432-1441.

59 M. R. Adendorff, G. Q. Tang, D. P. Millar, M. Bathe and W. P. Bricker, *Nucleic Acids Res.*, 2022, **50**, 717–730.

60 R. Behrend, E. Meyer and F. Rusche, *Liebigs Ann.*, 1905, **339**, 1–37.

61 W. A. Freeman, W. L. Mock and N. Y. Shih, *J. Am. Chem. Soc.*, 1981, **103**, 7367–7368.

62 S. Liu, C. Ruspic, P. Mukhopadhyay, S. Chakrabarti, P. Y. Zavalij and L. Isaacs, *J. Am. Chem. Soc.*, 2005, **127**, 15959–15967.

63 J. Lagona, P. Mukhopadhyay, S. Chakrabarti and L. Isaacs, *Angew. Chem. Int. Ed.*, 2005, **44**, 4844–4870.

64 J. Kim, I. S. Jung, S. Y. Kim, E. Lee, J. K. Kang, S. Sakamoto, K. Yamaguchi and K. Kim, *J. Am. Chem. Soc.*, 2000, **122**, 540–541.

65 X.-J. Cheng, L.-L. Liang, K. Chen, N.-N. Ji, X. Xiao, J.-X. Zhang, Y.-Q. Zhang, S.-F. Xue, Q.-J. Zhu, X.-L. Ni and Z. Tao, *Angew. Chem.*, 2013, **125**, 7393–7396.

66 M. J. Hannon, C. L. Painting, A. Jackson, J. Hamblin and W. Errington, *Chem. Commun.*, 1997, 1807–1808.

67 C. A. J. Hooper, L. Cardo, J. S. Craig, L. Melidis, A. Garai, R. T. Egan, V. Sadovnikova, F. Burkert, L. Male, N. J. Hodges, D. F. Browning, R. Rosas, F. Liu, F. v. Rocha, M. A. Lima, S. Liu, D. Bardelang and M. J. Hannon, *J. Am. Chem. Soc.*, 2020, **142**, 20651–20660.

68 J. C. Stockert, R. W. Horobin, L. L. Colombo and A. Blázquez-Castro, *Acta Histochem*, 2018, **120**, 159–167.

Chapter 3: Stability in and extraction of cylinders and rotaxanes from rat whole blood, *in vitro*

3.1: Introduction

Supramolecular cylinders have had their biological activity investigated since their discovery 25 years ago.[1] This has led to many discoveries including their interactions with biologically relevant DNA[2–9] and RNA[10,11] structures, 3WJ's,[12] cytostatic cellular effects,[13] cellular cytotoxicity,[14,15] and their ability to interfere with viral replication.[16–18] With the recent development of rotaxanes[19] based on this supramolecular architecture, and the work done in this thesis on cleaving the blocking groups on modified versions of this rotaxane, these complexes have demonstrated their potential as a therapeutic drug, making *in vivo* studies a suitable next step. To this end, animal studies were planned using Sprague Dawley rats as the live species, with the first tests to be carried out using [Ni_2(L'')3·(CB10)] rotaxane with the anticipation that activity and toxicity should be low due to the high stability and unreactive nature of this complex.[19] We also look at different variations of the base cylinder and rotaxane structures to explore a structure/activity relationship, with the aim of linking those to modes of action. This would improve molecular design for us but could also provide useful information for the wider field. However, these structures present analytical challenges that must first be overcome. Usually, HPLC[20] and ICP-MS[21] are used to separate complexes from biological substrates and then to detect the metal and determine concentration and its related effects such as toxicity. Our supramolecular complexes are not compatible with HPLC due to degradation occurring. On top of this, the metal ion concentration

generated by ICP-MS is not necessarily an exact indicator of structure presence as they may be with other, more inert complexes (such as ruthenium(II) complexes). This is because our structures are capable of degradation, to an extent, in physiological conditions. So even detecting concentrations of nickel ions does not mean we have the equivalent concentration of complex. So, to assess intact supramolecular structure presence *in vivo*, we wanted to explore the use of electrospray ionization mass spectrometry (ESI-MS). Whilst not perfect, as it is not quantitative, it can tell us what supramolecular structures are present (if any) after incubation with blood at 37 °C. This will also allow us to look at the complex's *in vitro* stability in blood, which can be linked up with data from rat trials to explain mode of action. Both ICPMS and ESI+MS will give us more detailed understanding of the complex's stability in whole blood. However, there is an additional challenge, as our complexes are tetra-cationic and aryl rich, they could potentially have a large range of biomolecular interactions meaning they are capable of binding larger nucleic acids structures, and other biological substrates. Therefore, separation of any intact supramolecular structures from this true whole biological substrate (blood) is very challenging. To attempt this, we must develop a separation/purification technique which does not destroy the cylinder, separates it from the complex biological environment of blood, and is capable of being run in MS without causing detection issues because of solutes from the blood/cylinder/extraction process. This *in vitro* work is necessary on ethical grounds, before pursuing *in vivo* studies, as it minimizes animal suffering by providing controls for the *in vivo* experiments, reducing the number of rat tests needed for future studies.

In this chapter we discuss how we developed controls and a method for extraction and purification of supramolecular cylinders and rotaxanes from rat's whole blood. We also

find out the stability of these structures in blood and how varying the organometallic/supramolecular structure affects this.

3.2: Using ICP-MS for quantitative detection of nickel ions from rats' whole blood

Despite nickel ion concentration via ICP-MS not being an reliable measure of cylinder concentration, it remains our most practical quantitative way to assess cylinder/rotaxane concentration from a complex sample. With this in mind, we needed to establish the detection limits of nickel from rat's whole blood. To do this we prepared a nickel calibration standard for the instrument we would be using, which included nickel ions in nitric acid at concentrations between 0.195 and 100 ppb. Figure 4.01 shows that we can detect Ni ion concentrations from as low as 0.195 ppb up to 100 ppb with a linear response. This means we can detect concentrations of cylinder and rotaxane as low as 0.83 µM, and likely even lower than that with the instrument's detection limit dropping into the parts per trillion (ppt) range. To find out the background concentration of Ni in blood, we did a control ICP-MS of rat whole blood alone. To prep

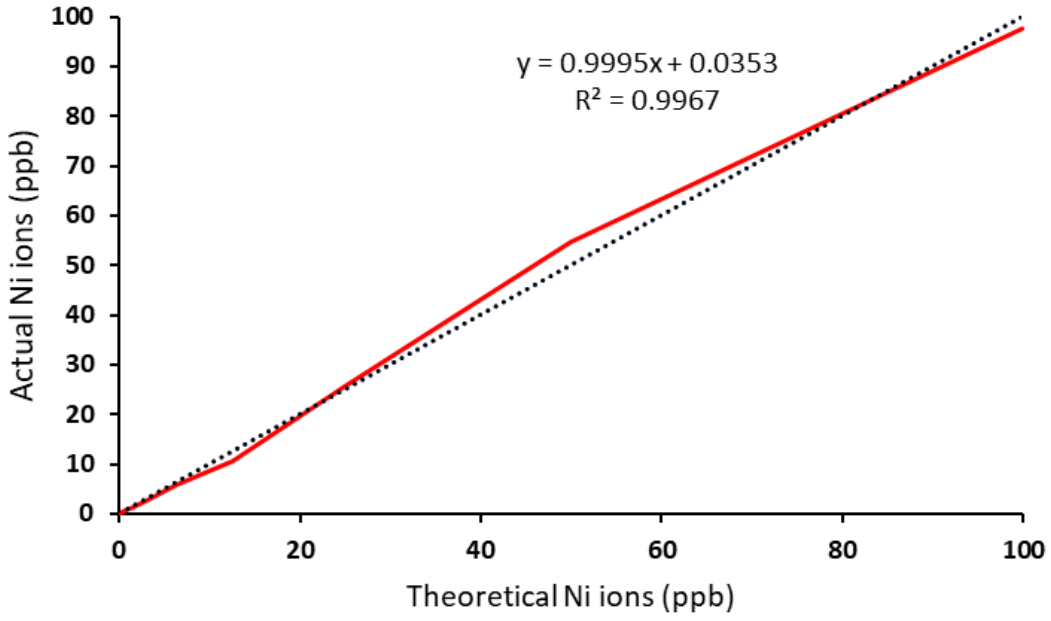


Figure 4.01: Shows the ICPMS nickel calibration graph with concentrations of nickel between 0.195 and 100 ppb.

this blood sample, we used a previously reported protocol by Nico Laur et al.,[22] where nitric acid, hydrogen peroxide and heating were used to break down all biological components. This yielded a nickel concentration of 0.048 ppb, this corresponds to a cylinder concentration of 0.41 µM which is 0.95% of the intended dose (43 µM in the total blood volume of a typical Sprague Dawley rat). We are comfortable this background signal is low enough to not affect our experiments.

3.3: Separation and detection of supramolecular cylinders and rotaxanes from rats' whole blood and their stability

After establishing detection limits, we then sought to confirm the presence of the intact cylinder after incubation with rat's whole blood to show the effects are linked to the intact structure. This poses three main challenges: breakdown of our complexes, separation of them from biological substrates and detecting signal from background. These challenges were addressed by looking at different time points and by developing a separation procedure starting from an established purification procedure of cellulose TLC.[23]

3.3.1: Developing a separation and detection method

Cylinders and enantiomers have been purified by chiral cellulose chromatography previously, using varying concentrations of sodium chloride in water as the eluent.[23] This purification system has separated out not only the cylinder enantiomers but also reaction impurities from more challenging cylinder syntheses. For these reasons it was our starting point for separation of the cylinder from blood.

Initially we used Whatman grade 1 filter paper as the stationary phase, as it provided a quick TLC test to see if separation occurred. We used 0.2 M NaCl in ultrapure water as the eluent and mixed 50 µL of blood with 50 µL of 1 mM $[Fe_2(L)_3]$. This left our blood sample with 500 µM $[Fe_2(L)_3]^{4+}$ from which we then spotted 1 µL onto the filter paper stationary phase and eluted. This yielded no observable separation, with the blood smearing up the filter paper. To reduce blood mobility on the stationary phase we decided to change our eluent to 20% water 80% methanol saturated with NaCl, the

aim being to reduce biological substrate solubility but maintain high solubility of $[Fe_2(L)_3]^{4+}$ which is very soluble in MeOH. This yielded substantially better results with separation of $[Fe_2(L)_3]^{4+}$ from blood occurring nearly immediately evidenced by a visible purple band. $[Fe_2(L)_3]^{4+}$ had an Rf value of 0.69 whereas blood has an Rf value of 0.34. We then switched from sodium chloride to ammonium chloride. This allowed for a greater ionic strength of solution due to greater solubility. Ammonium chloride also forms less adducts in MS, which would make subsequent analysis of results easier. We also switched to 100% methanol for sample dilution and for the eluent with the aim to increase separation further. This yielded similar Rf values. We then cut out the bands of the TLC and incubated them in a vial containing methanol saturated with ammonium chloride for 1 hr at room temperature. Upon MS of this sample on the LCQ fleet MS there was no detection of $[Fe_2(L)_3]^{4+}$ however the background was high which was likely interfering. We later investigated the same samples on the Waters SYNAPT G2S MS using the time-of-flight MS ES+ method in sensitivity mode which yielded a clear $[Fe_2(L)_3]^{4+}$ peak in the MS at 310 m/z (Figure 4.02) with and without incubation and separation from rat's whole blood using this filter paper TLC method.

Due to lack of initial detection and the crude nature of the TLC technique, we moved onto developing a similar method utilizing Polyethersulphone (PES) molecular weight cut off (MWCO) centrifuge tubes, the aim being to improve upon the separation seen in the filter paper TLC method which in turn should improve detection. Samples were prepared similarly with 50 µL of rat's whole blood and 50 µL of 1 mM $[Fe_2(L)_3]^{4+}$. These samples were then incubated for a defined period. 300 µL of methanol saturated with ammonium chloride was added, the sample vortexed and transferred to a 10 kDa PES-

Iron Parent Cylinder alone

Iron Parent Cylinder in blood

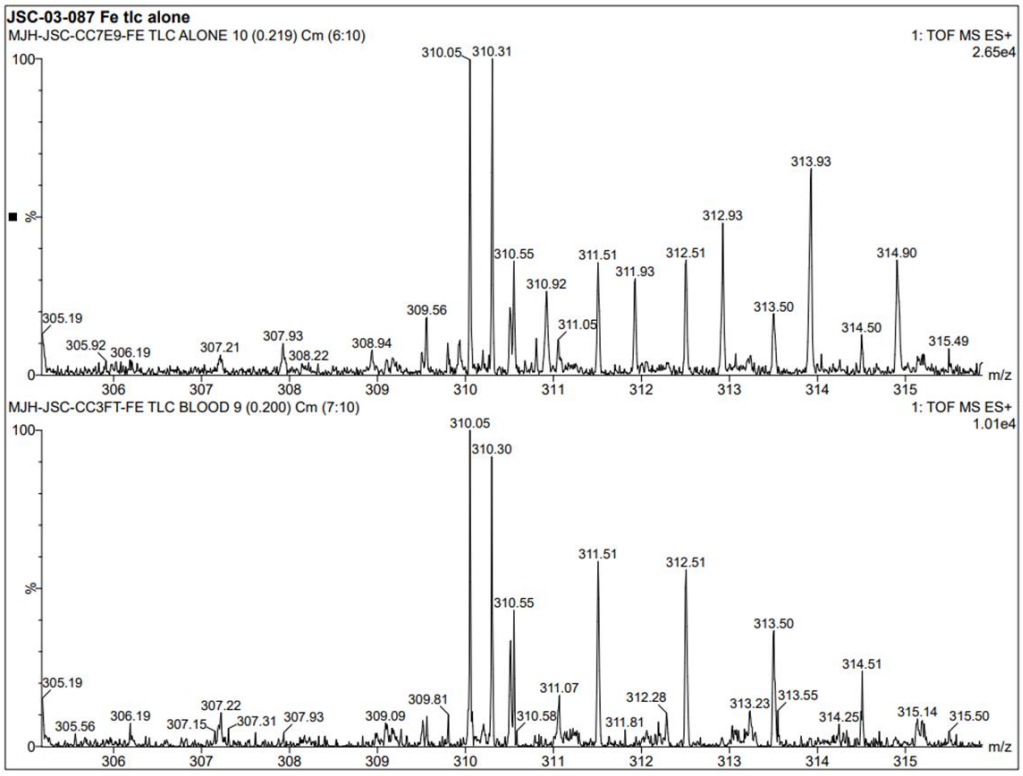


Figure 4.02: Shows the MS spectra of $[Fe_2(L)_3]$ samples after filter paper TLC separation and extraction. The top image is an $[Fe_2(L)_3]$ alone control, and the bottom image is after incubation with rat's whole blood.

MWCO tube and then centrifuged. The filtrate was collected, kept at -20 °C overnight, centrifuged again, then analyzed by MS. The PES-MWCO tubes were used as they provide a standardized form of sample treatment with a small filter which minimizes loss of compound as the cylinder has little to no interaction with PES.[24]

Figure 4.03 shows the MS spectra of the iron parent cylinder after PES-MWCO separation from rats' whole blood and d etected by TOF-ESI+MS. Peaks can be clearly seen at 310 and 425 m/z corresponding to the $[Fe_2(L)_3]^{4+}$ and $\{[Fe_2(L)_3]Cl\}^{3+}$ respectively. These peaks are more pronounced from the background and have better isotope patterns than the same peaks in the MS spectra produced using the initial TLC separation technique. This highlights the main advantage of this technique over TLC.

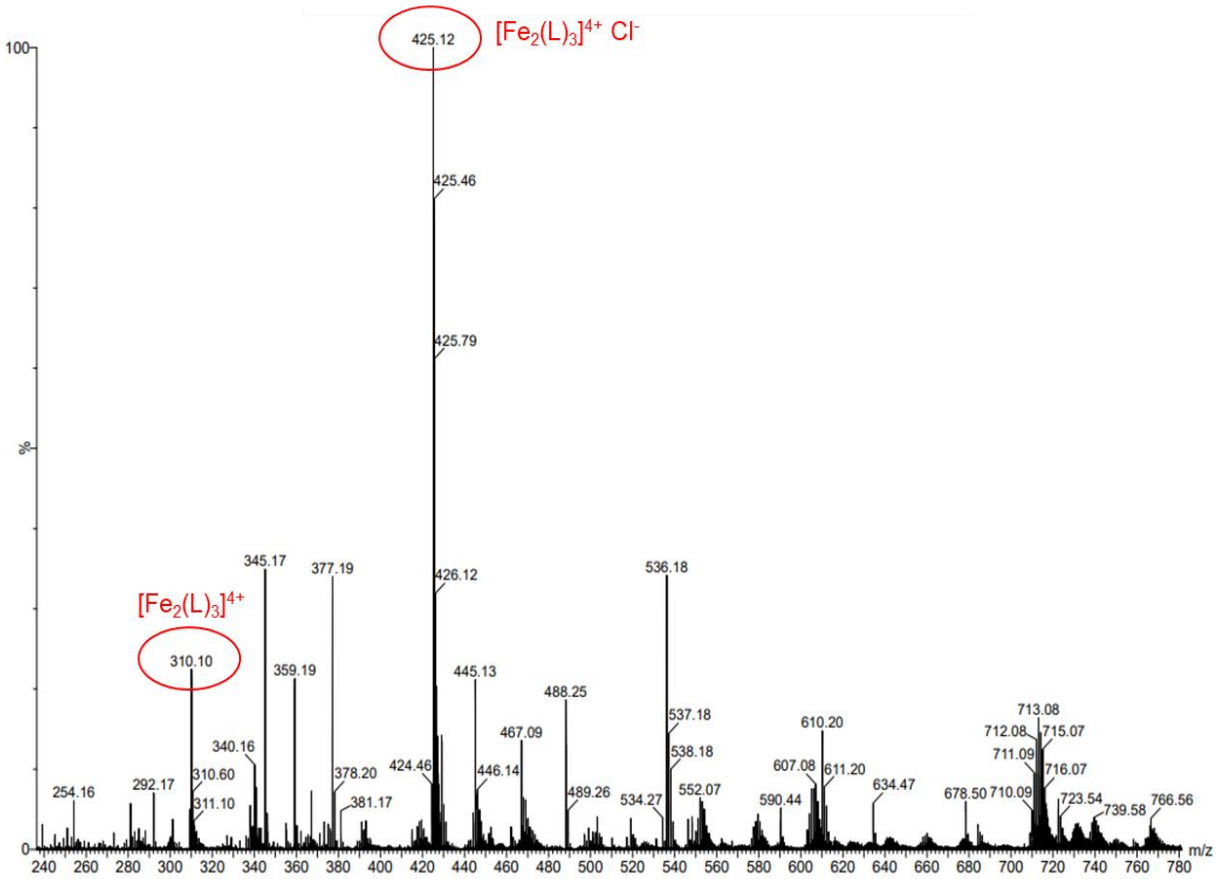


Figure 4.03: Shows the MS spectra of $[Fe_2(L)_3]^{4+}$ samples after PES-MWCO separation from rat's whole blood. 310 and 425 are the 4+ and 3+ peaks of iron parent cylinder.

This effect is likely seen due to the change of materials from cellulose in the TLC to PES in the filter, allowing for increased recovery percentage of the cylinder.

We investigated the effect of solvent on recovery of cylinder from rats' whole blood. We used water and methanol saturated with ammonium chloride as the extraction solvent. We compared the UV-Vis absorption value at 574 nm which corresponds to the MLCT band of the iron parent cylinder. Figure 4.04 shows we obtain a 9.2% recovery of cylinder from blood when water saturated with ammonium chloride was used as the extraction solution. However, when water was replaced with methanol, we achieved 15.5% recovery which is an increase of 6.3%. This clearly marks methanol as the preferred solvent for extraction. This increase in recovery is likely due to reduced solubility of biological substrates in methanol whilst maintaining high solubility of the

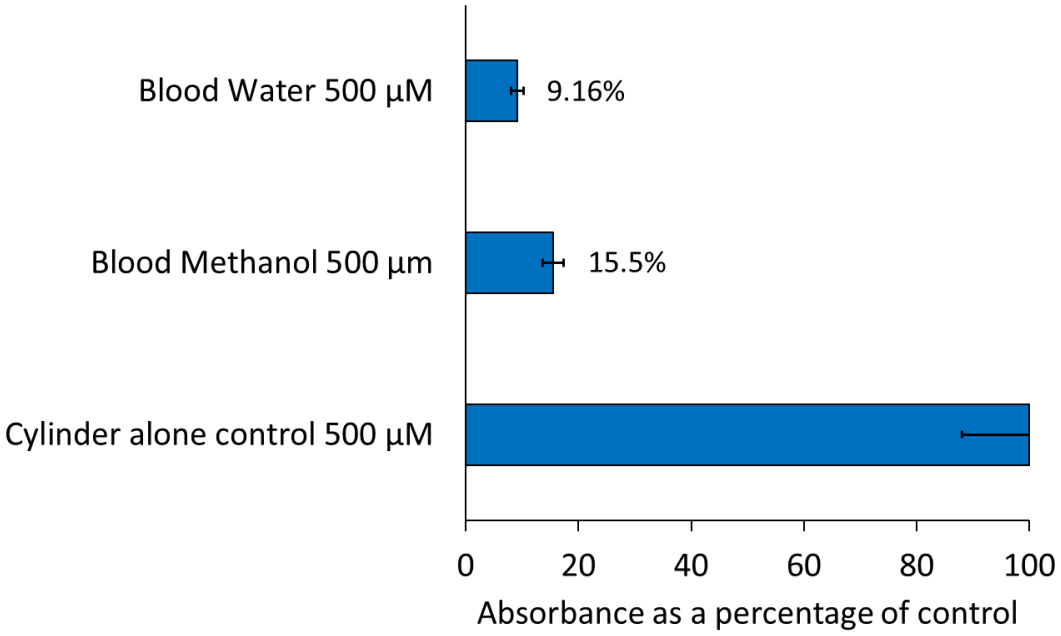


Figure 4.04: The absorption values at 574 nm as a percentage of the control of $[Fe_2(L)_3]$ separated from blood using water or methanol at 574 nm after purification through PES-MWCO tubes. 500 µM was the initial concentration of $[Fe_2(L)_3]$.

cylinder. On top of this, the increased solubility of ammonium chloride in water creates an issue during MS detection. The larger amount of total dissolved solid left large crystalline residues on the chip of the detection plate of the MS NanoMate, this resulted in sample overlap during spray. If water is to be used for alternative purposes going forward, it is suggested that a significantly lower concentration of ammonium chloride is used, comparable to its solubility in methanol (3.3%).[25]

Supramolecular cylinders have optical enantiomers which have previously been shown to have different interactions with DNA.[9] Because of this, we decided to investigate if there were any enantiomer specific interactions with rat's whole blood. To investigate this, we incubated 500 µM iron parent cylinder with rat's whole blood for 1 hr at 37.5 °C before PES-MWCO separation. These samples were then diluted 10 times and had their circular dichroism spectra recorded. The spectra of blood plus cylinder (Figure 4.05 yellow trace) suggests the presence of an optically active species in solution

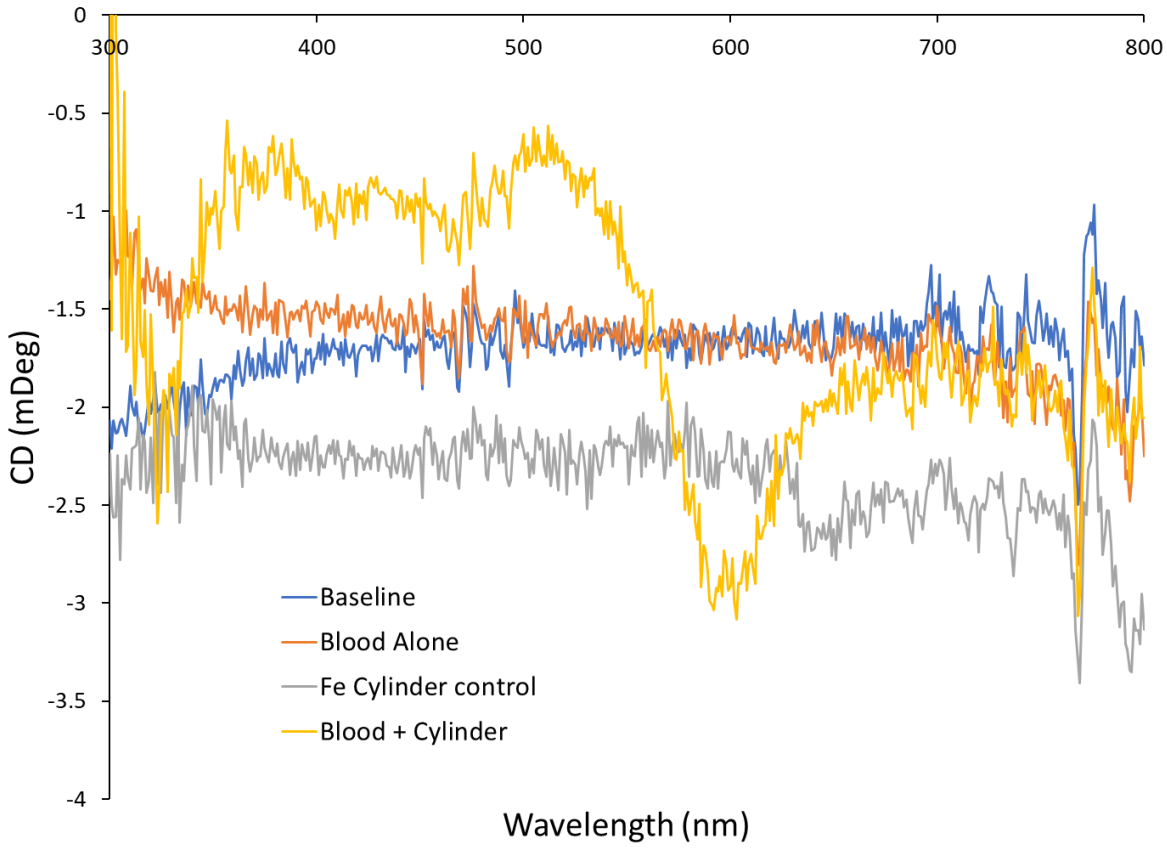


Figure 4.05: Shows the Circular Dichroism spectra for combinations of $[Fe_2(L)_3]$ and blood. There are two control spectra of blood alone and $[Fe_2(L)_3]$ alone, followed by a spectrum of $[Fe_2(L)_3]$ after mixing and separation from blood. All samples underwent the methanol saturated with ammonium chloride PES-MWCO separation method.

which is not present in the controls. Although this signal is weak and contains noise, it is comparable to the CD spectra of the iron parent cylinder's M enantiomer (Figure A2 in appendix). This would indicate there is a preference for one enantiomer over the other. Because the iron parent cylinder is capable of interconversion between M and P enantiomers, it isn't clear whether the preference is M or P. This is because we could be observing slow conversions of P into M due to improved stability upon binding a biological substrate with preference for M. Alternatively, we could be observing M because the binding preference is for P, resulting in proportionally more M being left in solution which is separated and produces the CD spectra we observe. To assess the enantiopurity, we would have to establish CD proportional to absorbance and compare to a known sample. Because the aim of this experiment is not to establish this blood's

preference for enantiomers, we did not pursue this further. However, this is very important for determining biological mode of action and is something which should be investigated at a later stage. To investigate this further we would need to establish controls and carry out more testing regarding the iron parent cylinders enantiomer interconversion rate.

3.3.2: Stability of supramolecular cylinders in rats' whole blood

Having developed a method for separation and detection, we moved onto investigating the stability of these supramolecular cylinders in rat's whole blood. Blood is a complex substrate for these supramolecular cylinders, as it contains many potential binding targets. Cylinders have demonstrated binding to DNA[15] and RNA,[10] both of which will be present in this blood sample. This blood sample has also been freeze-thawed multiple times during its use which has likely led to cell lysis, releasing intracellular components into the blood. This will homogenize the solution, to an extent, and expose the supramolecular cylinder to this plethora of binding targets. The interactions between the cylinders and the biological substrates in this blood will heavily impact the cylinders stability. We know that supramolecular cylinders can break down in water alone at 37 °C, however when bound to a biological substrate, stability could enhance dramatically. This may in turn affect its efficacy *in vivo* and biological mode of action. Because of this we need to establish stability in blood by monitoring presence of the structure in a blood sample over time. We will also be attempting to detect supramolecular cylinders from rats' whole blood during *in vivo* tests at different time points. This will provide information on the cylinder's pharmacokinetics, understanding of which is required to reach clinical testing. To this end, we need to establish how low a concentration we can detect intact structure at, as well as use the stability tests to

estimate how long cylinders will be intact to better plan the rat studies, draw more meaningful conclusions and improve the ethics. We acknowledge ESI-MS is not quantitative in the manner we have used it, and should not be interpreted as such, however, we draw information from these data by examining sequential trends in peak relative abundance. This is made reliable through these experiments being run in parallel, on the same instrument, in the same conditions and at the same time.

Our initial stability tests were carried out with $[Ni_2(L'')_3{\cdot}(CB10)]^{4+}$, which is the rotaxanated supramolecular cylinder the group has recently published.[19] This complex was the initial test as it will be the first to be investigated in rat studies. We can see in spectra A of Figure 4.06 that the $[Ni_2(L'')_3{\cdot}(CB10)]^{4+}$ peak 846 m/z is maintained even after 168 hrs. This indicates that this species is stable and extractable from blood after 1 week at 37 °C. We can also see in spectra B that the control of $[Ni_2(L'')_3{\cdot}(CB10)]^{4+}$ in water shows little to no change over 1 week, further confirming that this complex is stable at this temperature for biologically relevant periods of time. We can see that between t=0 to t=24 hrs the signal to background ratio is poor and the rotaxane peak is poorly defined from the background signal. This improves as time progresses towards 168 hrs, resulting in greater counts and a more defined isotope pattern. This is likely because there is greater separation of the complex from blood over time, resulting in more complex in the solution at the detection time. This is the opposite trend one might expect when investigating the stability of a complex, when degradation is a possible outcome. However, one possible explanation is that the rotaxane is bound to a biological substrate and the rotaxanes stability is greater than that of its substrate. This breakdown could be caused by the experiment conditions or induced by the

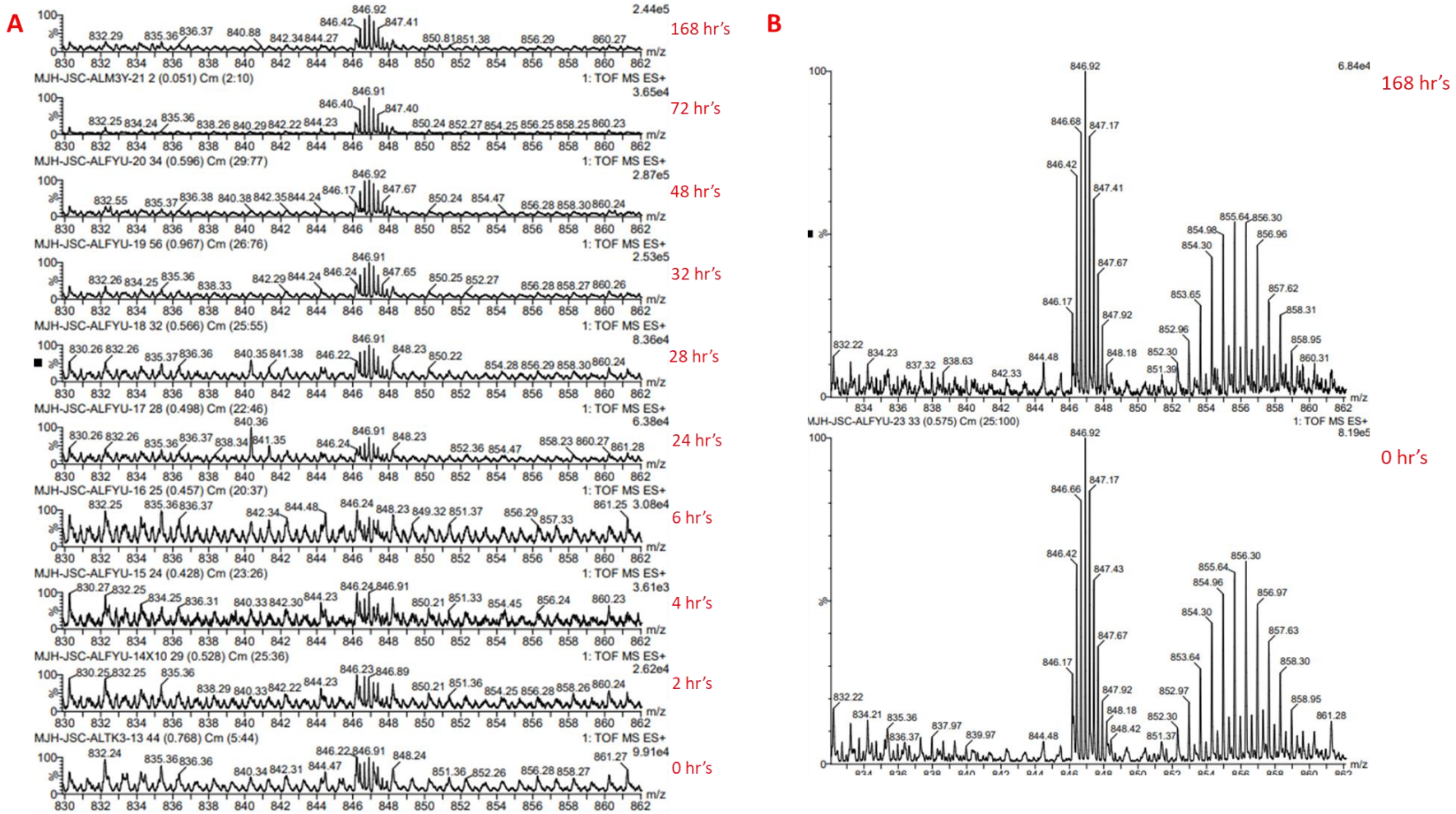


Figure 4.06: Spectra A shows the mass spectra of the $[Ni_2(L'')_3.(CB10)]^{4+}$ after extraction from rat's whole blood using the PES-MWCO separation technique after incubation at 37°C for time points between 0 and 168 hrs. Spectra B shows the MS spectra of $[Ni_2(L'')_3.(CB10)]^{4+}$ after incubation in water at 37°C for 0 and 168 hrs.

rotaxane itself. This result should be considered when carrying out rat studies as it could help explain any observed biological effects.

The next compound to be tested was the $[Fe_2(L)_3]^{4+}$ which is one of the most studied supramolecular cylinders. This makes it useful for understanding the cylinders mode of action inside rat's whole blood, as we understand it the most and can rationalise effect with other results. We can see in spectra A of Figure 4.07 that the 4+ peak at 310 m/z can be seen prominently at t=0 hrs with the expected isotope pattern. However, there is a drastic reduction in the intensity of this peak over the first 6 hours and the peaks have reduced by close to 100% by 24 hrs onwards. This was a strong indicator that the iron cylinder has broken down. The control (Figure 4.07 B) shows much greater stability, however there is still a reduction in signal of approximately 50%. This does not however account for the drop in signal seen when the iron cylinder is mixed with blood. This suggests there is something in blood which causes this rapid breakdown of the cylinder. A main route for cylinder degradation can be the hydrolysis of the imine bond, a bond which is protected whilst rotaxanated, accounting for the rotaxanes stability. A product of this degradation is one of the cylinders starting materials, 4,4-methylenedianiline, potentially making this a suitable MS marker for degradation. However, upon looking for this peak (see Figure SI.4.1) we can see a small proportion is present at t=0 and is not present at all at t=168 whereas in the controls, we can see its presence at both time points, this suggests 4,4-methylenedianiline is sequestered by the blood in some capacity, making it an unsuitable marker for degradation. 4,4-methylenedianiline does pose health risks as a potential carcinogen (see MSDS), with blood showing the ability to sequester this compound, it should be considered when assessing toxicity among other factors during

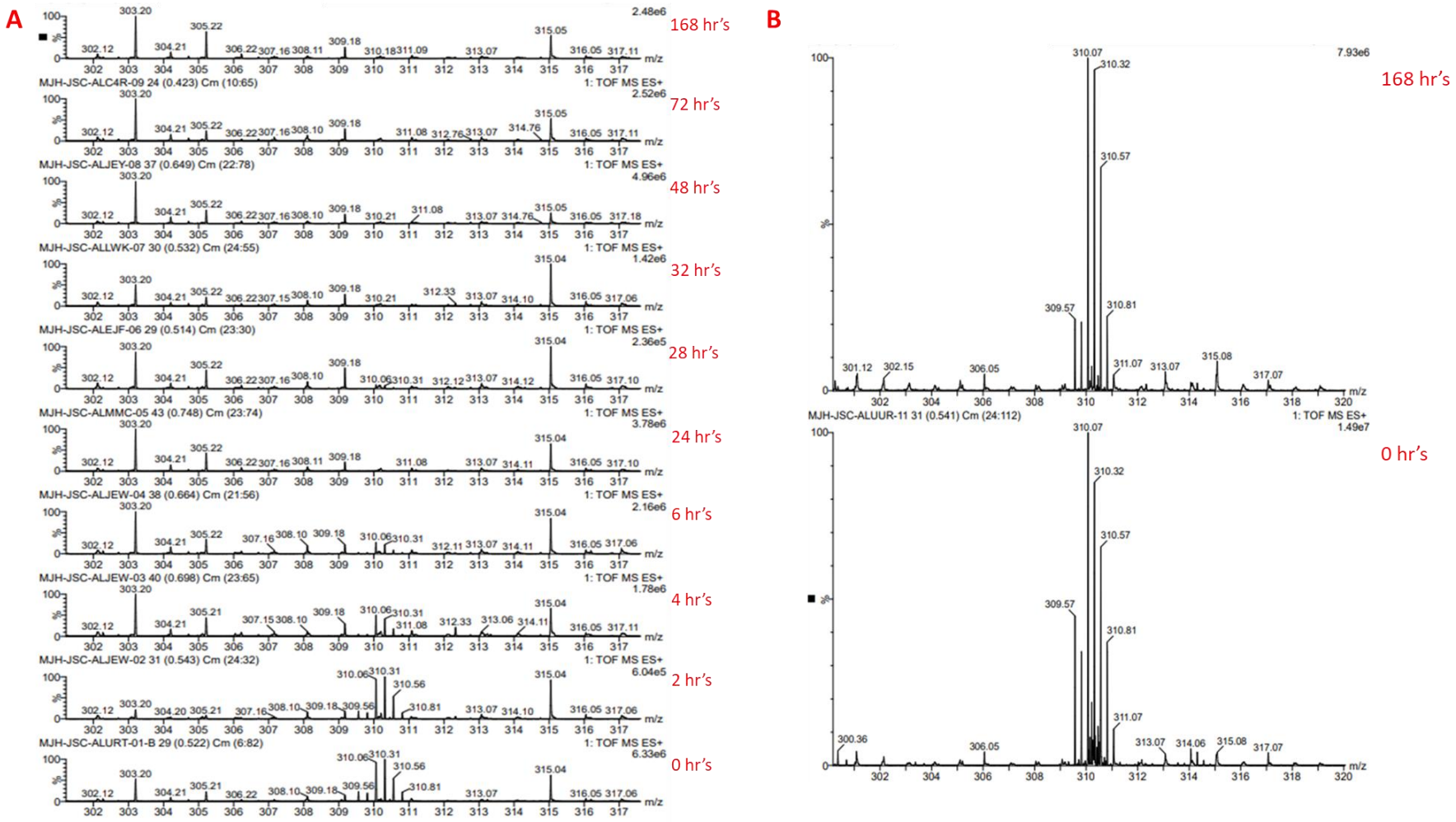


Figure 4.07: Spectra A shows the mass spectra of the $[Fe_2(L)_3]^{4+}$ after extraction from rat's whole blood using the PES-MWCO separation technique after incubation at 37°C for time points between 0 and 168 hrs. Spectra B shows the MS spectra of $[Fe_2(L)_3]^{4+}$ after incubation in water at 37°C for 0 and 168 hrs.

live animal studies. Whilst degradation is likely what is happening, we also cannot completely rule out the cylinder being increasingly sequestered away by the blood in a more stable and inaccessible way, because of incubation at 37 °C over time, resulting in the decrease we see.

We next looked at the stability of $[Ni_2(L)_3]^{4+}$ in rats' whole blood between 0 and 48 hrs. This is the same complex as $[Fe_2(L)_3]^{4+}$, with the same ligand structure, but the iron metal centres have been replaced with nickel. This complex typically exhibits increased stability and lower IC_{50} values than its iron counterpart.[26] In Figure 4.08 we can see from the 4+ peak at 311 and 3+ peak at 426 that the nickel cylinder is present at t=0. These peaks are maintained throughout the 48-hour experiment, showing some fluctuation, but mostly being maintained. This also occurs in the control experiment of

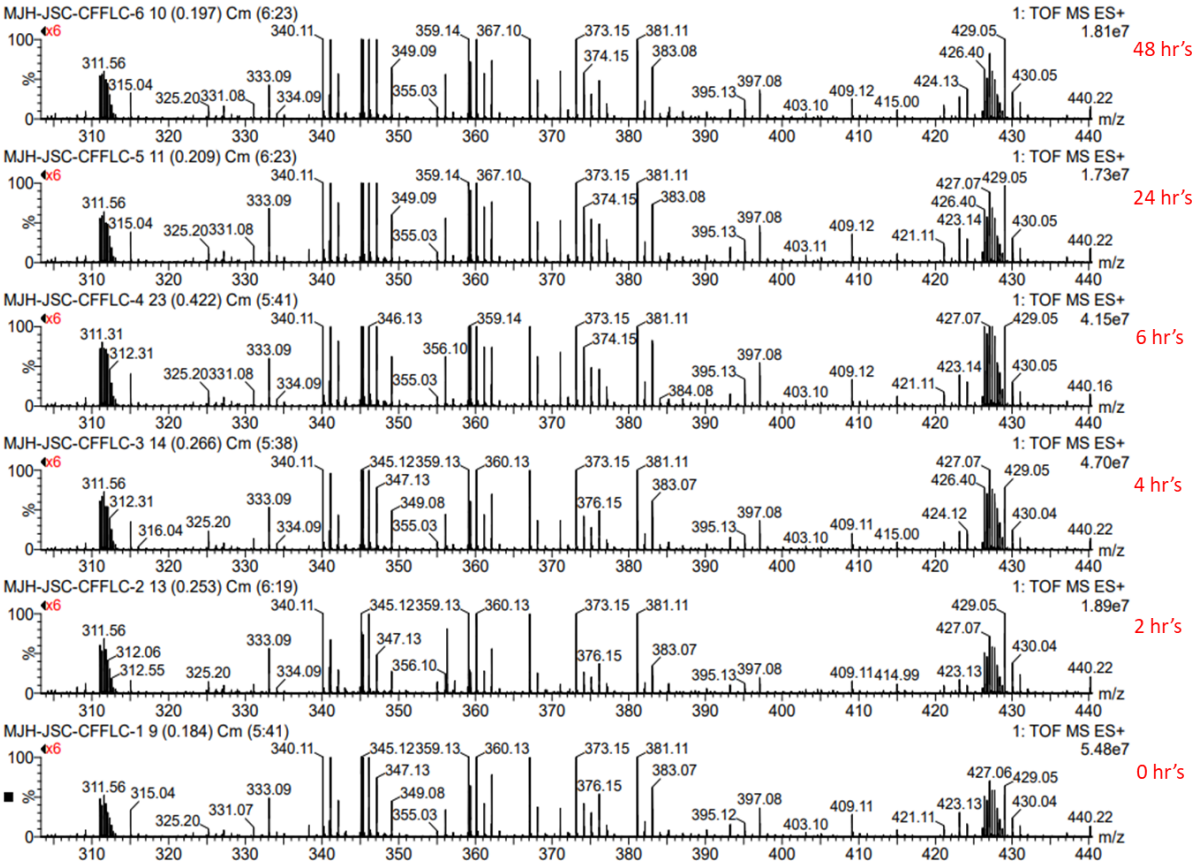


Figure 4.08: Shows the mass spectra of the $[Ni_2(L)_3]^{4+}$ after extraction from rat's whole blood using the PES-MWCO separation technique after incubation at 37°C for time points between 0 and 48 hrs.

nickel cylinder in water, showing little to no change in peak intensities. Whilst MS is not inherently quantitative, little to no change in peak intensity is still a good indicator relative compound presence. It is noteworthy that compared to the iron cylinder where the peaks diminish after 6 hours, nickel cylinder maintains its peaks to 48 hrs, showing little indication of instability. This suggests the nickel cylinder has significantly better stability in blood. It is also important to note that nickel and iron cylinders are isostructural with equal charges. This highlights the importance of the metal for cylinder stability, but also suggests that the iron cylinder does in fact degrade and is not sequestered in the blood. This is because the binding of cylinder is due to their supramolecular architecture and not their metals, as they are locked away in the cylinder's organic framework. So, if the nickel cylinder does not exhibit the same behaviour, it is likely due to stability differences between the two species, which we are already aware of. This could mean nickel cylinders make better therapeutic agents, as they are more likely to remain intact *in vivo* and reach their target. This is unless cylinders' activity is achieved via a degradation pathway.

The next cylinder we looked at was $[Ni_2(L')_3]^{4+}$, where the pyridine ring is replaced by an imidazole ring at the ends of the cylinder. This allows for modification of the ends of the cylinder, which is how rotaxanation was initially achieved, using picolyl stopper groups with CB[10]. The stability of this cylinder is significant, as it represents what a future cylinder drug may look like after the stopper groups are removed, making this the potentially active drug molecule, or an intermediate stage for another drug molecule. We can see the 2+ 588 m/z peak is present at t=0 through to t=48 (Figure 4.09), however there is a significant reduction in intensity of approximately 50%. This is greater degradation than that of the $[Ni_2(L)_3]^{4+}$ cylinder (figure 4.08 – unchanged),

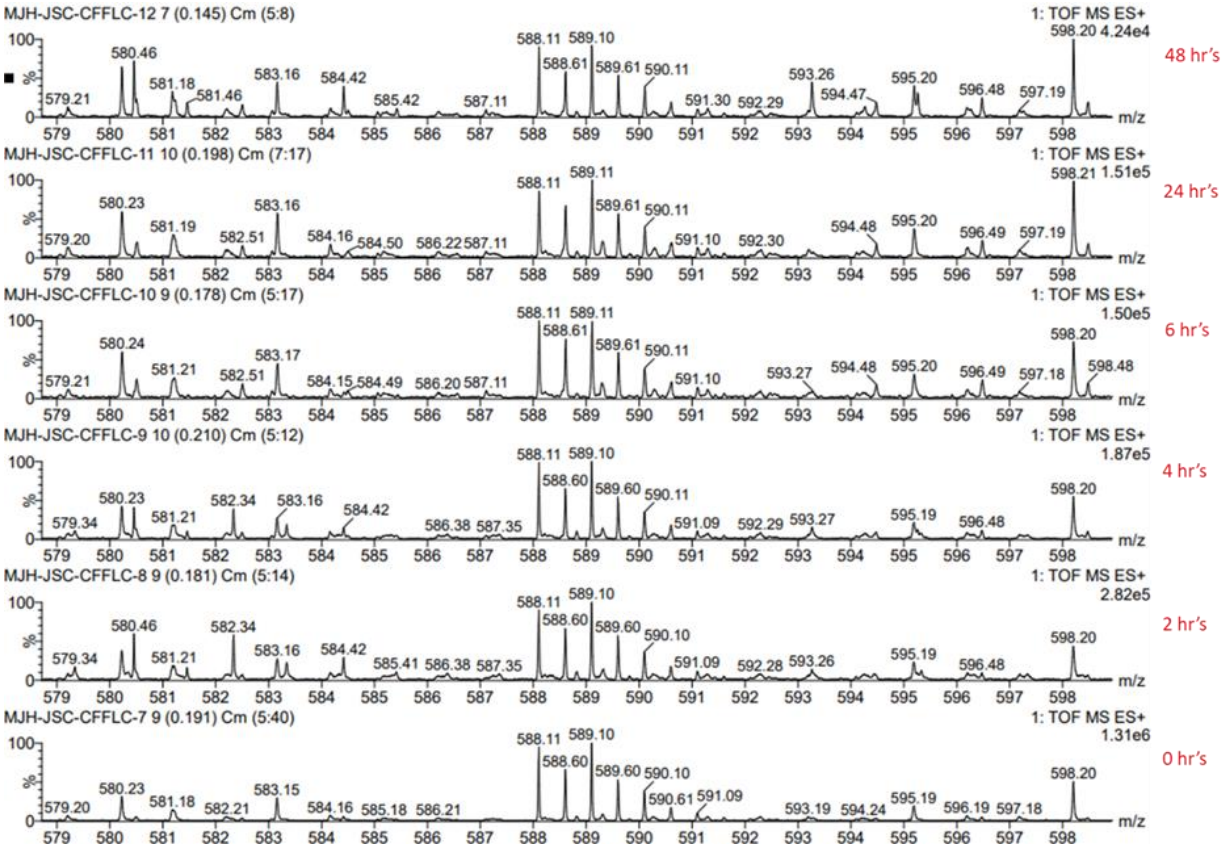


Figure 4.09: Shows the mass spectra of the $[Ni_2(L')_3]^{4+}$ after extraction from rat's whole blood using the PES-MWCO separation technique after incubation at 37°C for time points between 0 and 48 hrs.

but considerably less than that of the $[Fe_2(L)_3]^{4+}$ cylinder (Figure 4.07 - near 100% by 24 hrs). This suggests that it is much more stable than $[Fe_2(L)_3]^{4+}$, but less stable than the nickel parent cylinder. This is likely because the imidazole ligand makes the cylinder less thermodynamically stable than the parent. This is backed up by the control which exhibits a similar level of degradation over the same time points, indicating the degradation is linked to its structure and not a result of its interaction with blood. These results should be considered when developing a drug release system and linked/rationalised to its IC_{50} values.

We next investigated the $[Ni_2(L'')_3]^{4+}$ cylinder, which is the same cylinder as the rotaxane but without the CB[10] around the central axis which makes it a rotaxane. The stability of this cylinder is significant because it highlights the effect of rotaxanation

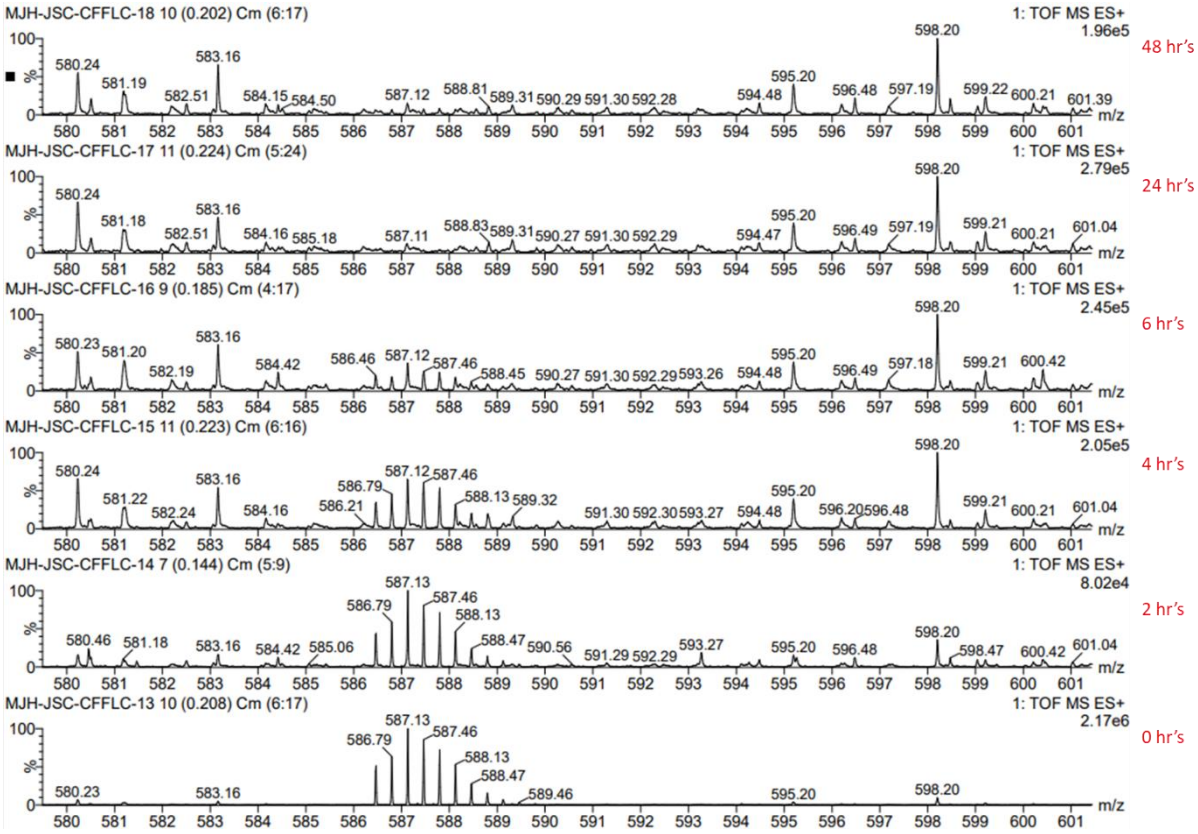


Figure 4.10: Shows the mass spectra of the $[Ni_2(L'')_3]^{4+}$ after extraction from rat's whole blood using the PES-MWCO separation technique after incubation at 37°C for time points between 0 and 48 hrs.

on this cylinder's stability. We can see in Figure 4.10; the MS has a peak at 587 m/z corresponding to the 3+ peak. This peak diminishes substantially by 6 hrs and appears to of reduced by nearly 100% by 24 and 48 hrs. The control experiment of $[Ni_2(L'')_3]^{4+}$ in water shows considerably greater stability than in blood, with a reduction of only approximately 30%. This is comparable stability to that of the iron parent cylinder, though we would expect stability closer to that of $[Ni_2(L')_3]^{4+}$, given the core supramolecular structure is the same. This suggests the picolyl stopper groups cause a significant interaction with blood resulting in its degradation. The picolyl stopper groups do offer a flexible aromatic binding target for a blood component which could help explain this reduction in signal. It could enable interactions with biomolecules which the base cylinder does not interact with, causing them to break down via a

different degradation pathway. Or alternatively they could enable strong binding resulting in this cylinder being sequestered in blood to a greater extent and with stronger binding than the other cylinders. This cylinders relatively poor stability in blood compared to that rotaxane highlights the extent of the stabilising nature of rotaxanation by CB[10]. This is a good indicator that if a cylinder complex is developed using this rotaxanation method and is tested *in vivo*, it is likely to be very thermodynamically and biologically stable in blood until it is exposed to its chosen release system. This could be a desirable trait as it results in increased control of activity and decreased unintended side effects via unintended release outside the chosen location/situation. It also aids in understanding its biological mode of action by eliminating pathways linked to early/unintended degradation.

Finally, we looked at $[Fe_2(L^*)_3]^{4+}$ which is an iron cylinder where the imine bond has been replaced by an azo bond. This changes the fundamental chemistry of the ligand species, as the imine bond is capable of reversible hydrolysis whereas the azo is more stable under physiological conditions. This removes a potential degradation route, which could result in complexes with improved stability in physiological conditions. We can see in Figure 4.11 that $[Fe_2(L^*)_3]^{4+}$ has a 4+ peak at 311 m/z at t=0 hrs, this peak diminishes substantially by t=2 hrs and is not present at t=6 or beyond. This indicates that the $[Fe_2(L^*)_3]^{4+}$ cylinders stability is the poorest of all cylinders studied so far, which is in direct contradiction to our hypothesis. The control experiment shows little to no (~0%) change in the peak intensity over the same time. This would suggest that the cylinders stability in blood may not be linked to hydrolysis of the ligand but be because of another interaction. The azo bond presents an extra lone pair of electrons which could be involved in dative bonding. This could enable binding to an unknown substrate

which is present in blood, resulting in breakdown of the cylinder, or covalently binding the cylinder, preventing its extraction.

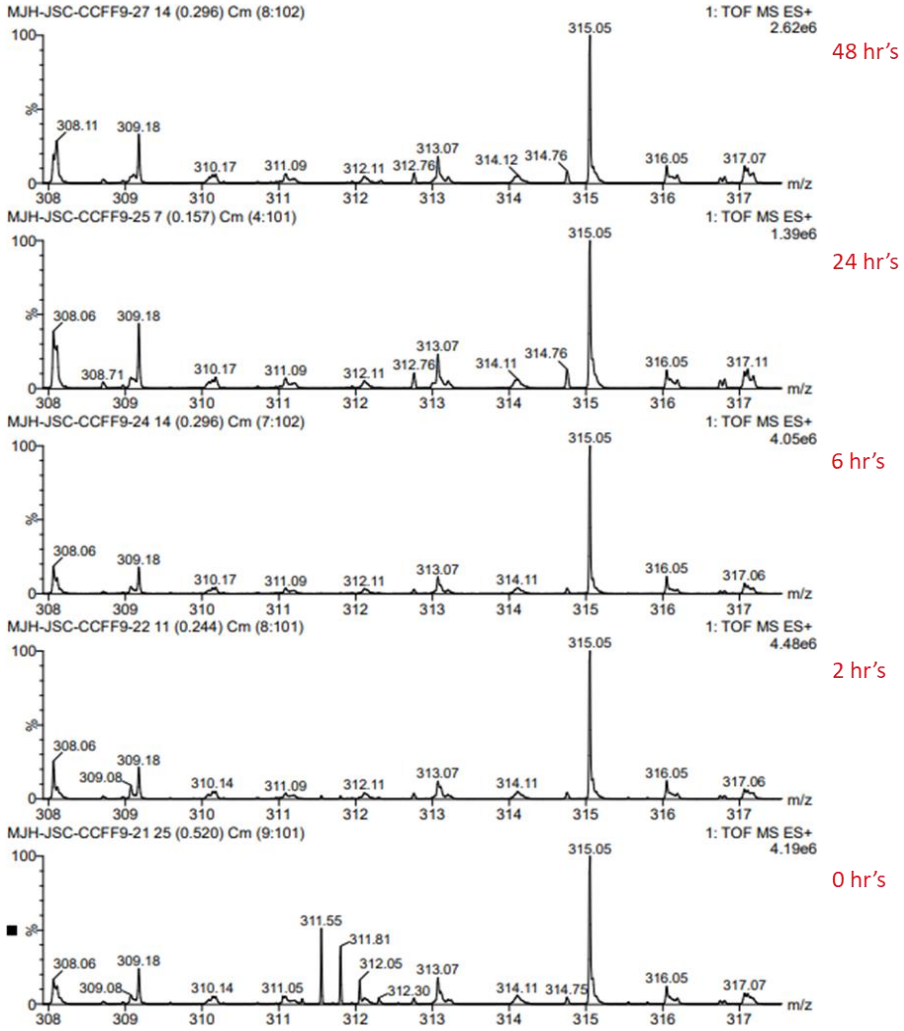


Figure 4.11: The mass spectra of the $[Fe_2(L^*)_3]^{4+}$ after extraction from rat's whole blood using the PES-MWCO separation technique after incubation at 37°C for time points between 0 and 48 hrs.

3.3.3: *Pseudo*-rotaxanation effect on the stability of cylinders in rats' whole blood

The previous blood stability studies of cylinders highlighted the effects that changing the organic ligand and metal had on their stability. This showed that cylinders likely degraded as a result their interactions with substrates in blood. This degradation was eliminated by rotaxanation with CB[10], presumably by removing substrate interactions. This does however mean we have to have a means of removing CB[10] to reinstate these interactions, which is challenging as it introduces chemistry that can be challenging to control due to the complexity of a biological system. With the aim of getting the best of both, we explored *pseudo*- rotaxanation where CB[10] is slid over the cylinder but there are no stopper groups.[19] This means the cylinder can leave the CB[10] ring as there is no mechanical lock. This could influence several characteristics, including stability, release kinetics and substrate binding.[19] We aim to achieve improved stability, which can have a significant impact on the complex's mode of action, potentially allowing it to reach its desired target before degradation or interaction with it, resulting in different and/or more pronounced effects. It should be noted that when performing these MS experiments, we detected no *pseudo*-rotaxane in the MS, only cylinder itself (see figure A3 in appendix). Controls showed this was a result of the extraction process, likely linked to poor solubility of CB10 without a guest and having methanol as the solvent (no H_2O to drive host/guest interaction). This was backed up by poor CB10 and *pseudo*-rotaxane soluble in methanol where cylinder alone is greatly soluble.[19]

The first complex we explored was $[Fe_2(L)_3 \cdot (CB10)]^{4+}$ which is the CB[10] *pseudo*-rotaxanated version of the iron parent cylinder. The primary aim is to assess if this impacts on stability, under the hypothesis the CB[10] ring offers a stabilizing/protecting effect. We can see from the MS in Figure 4.12 that iron parent cylinder appears at 310 m/z at t=0 hrs there is a prominent peak which is present through to t=48 hrs and exhibits a decrease of approximately 30%. This in direct contrast to what occurs with $[Fe_2(L)_3]^{4+}$ on its own in Figure 4.07 where the 310 peak almost completely disappears

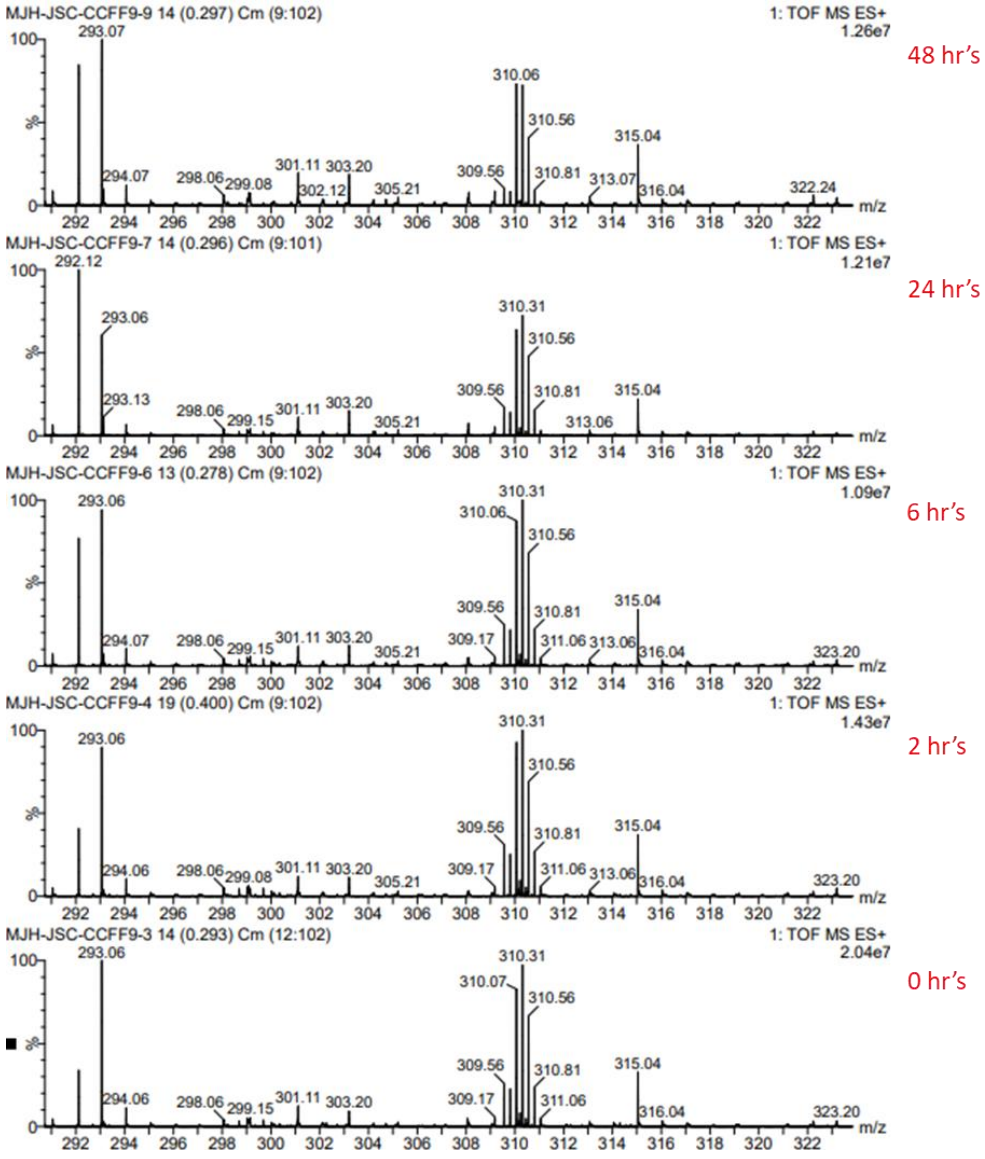


Figure 4.12 Shows the mass spectra of the $[Fe_2(L)_3 \cdot (CB10)]^{4+}$ after extraction from rat's whole blood using the PES-MWCO separation technique after incubation at 37°C for time points between 0 and 48 hrs.

by 6 hrs and is gone by 24 hrs. The control experiment shows an increase in signal intensity, which could be explained by more cylinder being dislodged from the CB[10] ring. Both show that the iron parent cylinder has much greater stability in and out of blood whilst *pseudo*-rotaxanated. The 30% reduction in signal is an important observation, as it indicates the cylinder is still capable of interacting with blood in some capacity. Indicating it can interact from inside the CB[10] ring or can be displaced, allowing it to interact. The considerably slower rate of degradation could be linked to the rate/degree at which this can happen, which could suggest slow and specific interactions. In theory, this should be beneficial as it would allow the cylinder to reach its desired target intact and allow it to achieve a more specific mode of interaction. When considering biological mode of action this should be considered and compared with previous *in cellulo* work.[2,14]

We next looked at $[Ni_2(L)_3 \cdot (CB10)]^{4+}$ which is the most stable of the cylinders is blood. This *pseudo*-rotaxanated cylinder would act as a control to observe any negative effects on cylinder stability. We can see in Figure 4.13 that peaks at 311 and 427 m/z correspond to the 4+ and 3+ peaks for Nickel parent *pseudo*-rotaxane respectively. They can be seen prominently and t=0 and are maintained throughout till t=48 hrs, the control shows the same trend over the same time. This is the same result as the nickel parent cylinder on its own, indicating that the CB[10] has no negative effects on the cylinders stability or detection from blood in the same conditions. This further highlights the option of *pseudo*-rotaxanation for delivery of cylinders.

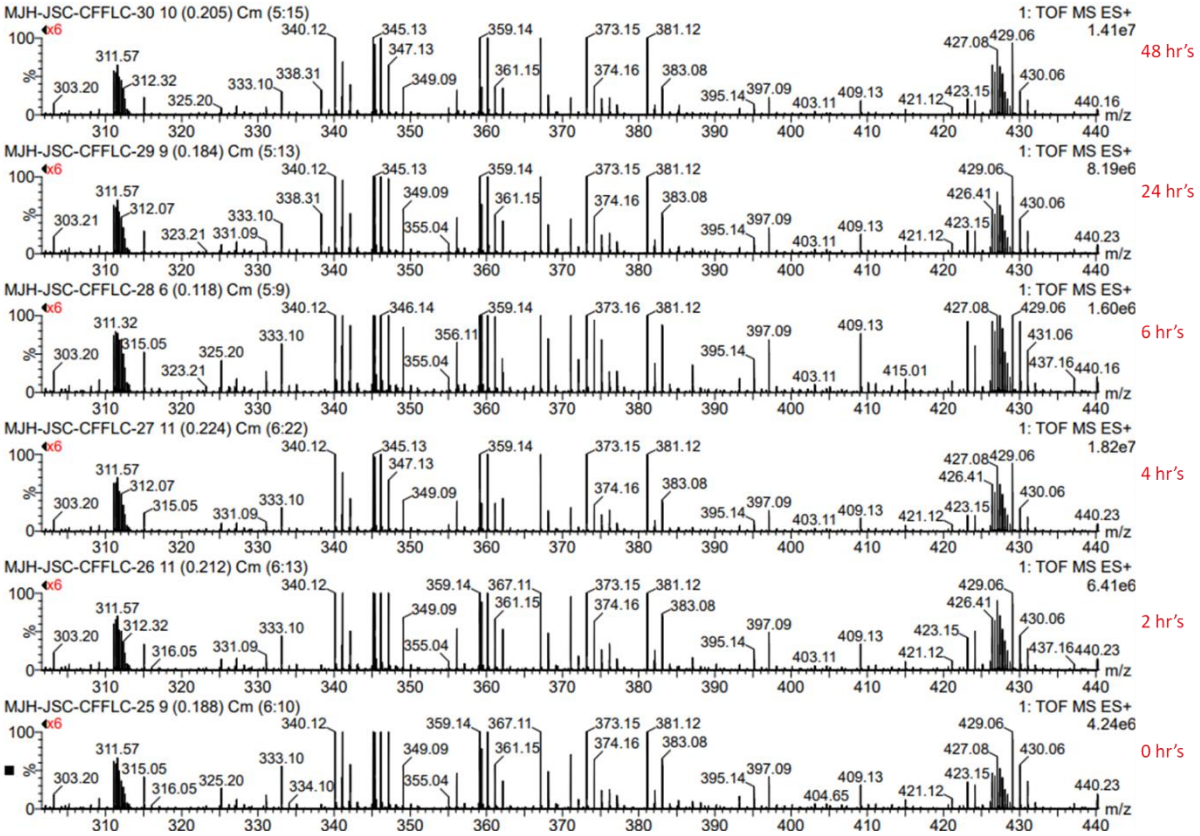


Figure 4.13 Shows the mass spectra of the $[Ni_2(L)_3{\cdot}(CB10)]^{4+}$ after extraction from rat's whole blood using the PES-MWCO separation technique after incubation at 37°C for time points between 0 and 48 hrs.

The final complex we investigated was the *pseudo*-rotaxane of $[Fe_2(L^*)_3{\cdot}(CB10)]^{4+}$ where the imine bond of the parent ligand has been replaced by an azo bond. The non-*pseudo*-rotaxanated version of this cylinder proved unstable in water over as little as 2 hrs, showing rapid degradation whilst mixed with blood. The control of the *pseudo*-rotaxanated version behaved the same as non-*pseudo*-rotaxanated, showing little change whilst is water alone. However, when the *pseudo*-rotaxanated version was mixed with blood we observed increased stability from 2 hrs (figure 4.11) to between 6-24 hrs for full degradation. In Figure 4.14 we can see the 311 m/z peak corresponding to the 4+ peak of the iron azo cylinder, we observe it decrease

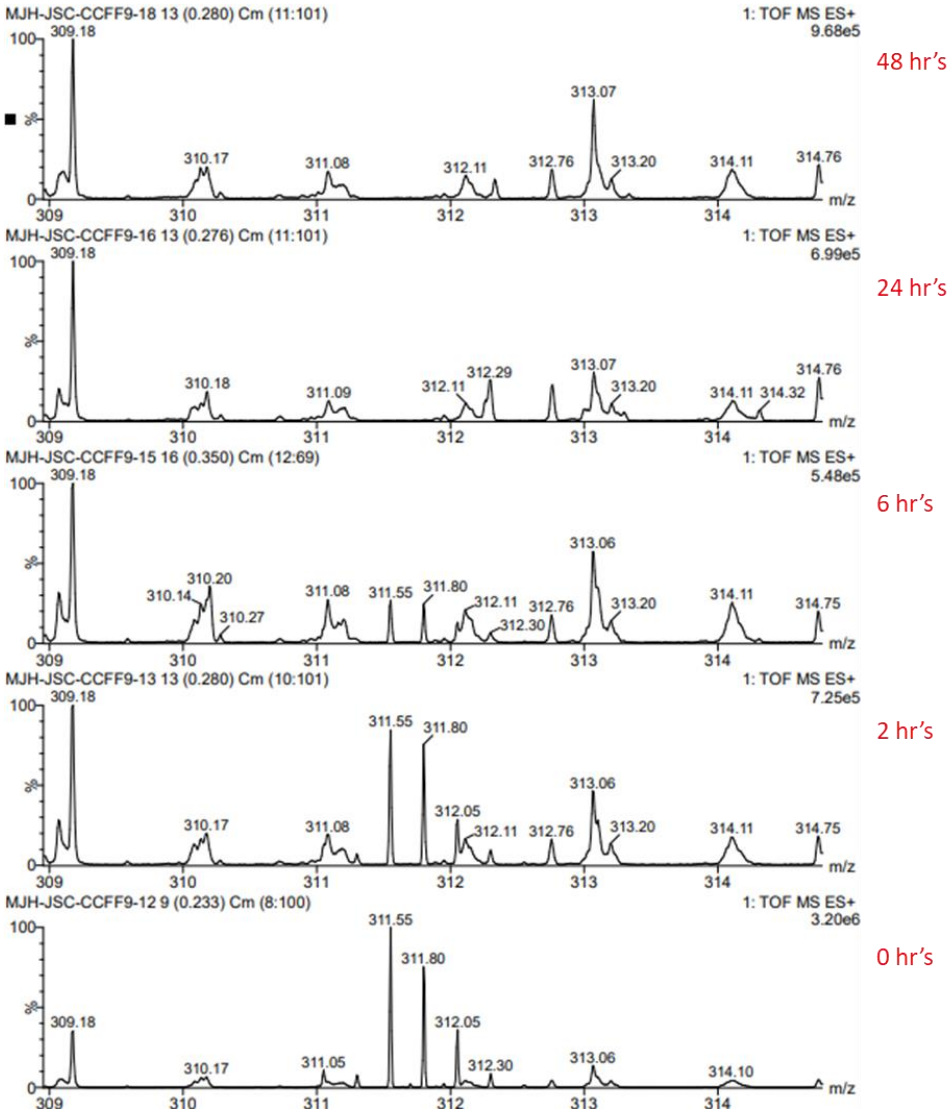


Figure 4.14 Shows the mass spectra of the $[Fe_2(L^*)_3{\cdot}(CB10)]^{4+}$ after extraction from rat's whole blood using the PES-MWCO separation technique after incubation at 37°C for time points between 0 and 48 hrs.

substantially by 6 hrs and is no longer visible by 24 hrs and beyond. This, whilst still showing substantial degradation, represents a substantial stability increase from its non-*pseudo*-rotaxanated counterpart, which had almost entirely degraded by t = 2 hrs. This is consistent with the increase in stability of the iron parent cylinder *pseudo*-rotaxane compared to its non-*pseudo*-rotaxanated variant. This further supports the stabilizing nature of CB[10] even with just *pseudo*-rotaxanation and suggests other cylinders could also be stabilized which could have knock on effects on their *in vivo* mode of action. Figure 4.14 also highlights that even when *pseudo*-rotaxanated the

cylinders are not rendered inert and are still capable of interacting with their environment, but likely do so on a slower timescale which may improve specificity.

3.4: Conclusion

With this work we have been able to establish conditions and procedures that have allowed us to successfully detect intact cylinders and rotaxanes, quantitatively, from rat's whole blood such that *in vivo* studies may proceed. ICPMS was used to quantitatively measure the detection of nickel from a standard and blood at appropriate concentrations for *In vivo* studies This identified that $[Ni_2(L'')_3{\cdot}(CB10)]$ could be detected at concentrations as low as 0.83 µM, and likely even lower than that with the detection limit of the instrument entering the ppt range. The background nickel ion concentration in blood was found to be sub 1% of the initial complex dose, meaning it should not interfere with the detection of cylinder or rotaxane. These studies show quantitative detection of nickel ions at the appropriate concentrations is possible, allowing rat studies to proceed.

We also developed an extraction procedure to remove cylinders and rotaxanes from blood to detect whether their supramolecular structure remains intact. The ability to separate and detect intact cylinder from rats' whole blood gives a powerful analytical tool to assess biological activity and mode of action *in vivo* during the rat trials. This method used a 10 kD PES filter in combination with a methanol solution, saturated with ammonium chloride. This allowed cylinder and rotaxanes to separate from the blood substrate substantially enough to enable supramolecular structure detection by MS. This has confirmed that the rotaxane and cylinder can remain intact whilst interacting with blood, though the length of time varies depending on the identity of the metal centres, organic ligands and if CB10 is either *pseudo* or fully rotaxanating them. These processes (separation, purification and subsequent ICP-MS, ESI-MS) provide the field

with new means to study such complex metallo-supramolecular species *in vitro*. This is valuable as it can produce vast quantities of data that allows for detailed quantitative analysis and understanding of their complex biological interactions without the need for live animal studies.

We further investigated the stability of different variations of these cylinders and rotaxanes to understand their impacts on stability in blood. $[Ni_2(L'')_3{\cdot}(CB10)]^{4+}$, showed no signs of instability over 7 days, this was substantially better than its non-rotaxanated counterpart which deteriorated by 24 hrs. This highlights the stabilising nature of CB[10] rotaxanation and its potential for drug delivery *in vivo*, adding to the list of compounds able to be released from CB's.[27] Iron cylinder showed poorer stability, with the parent L complex degrading within 6-24 hrs and the azo L* complex degraded significantly faster still, in just 2 hrs (close to 100% degradation). L* ligand should be much more resistant to hydrolysis, which is a hypothesised pathway for cylinder degradation, however the speed of degradation for the L* complex is greater than the parent L complex. This suggests there could be an alternative mechanism for cylinder breakdown in blood. As well as this, it could suggest a potent interaction between the free lone pair on the non-metal bound nitrogen atom of the ligand and a biological substrate, resulting in degradation. Nickel complexes have shown improved stability overall, over their iron counterparts and relatives with the Ni L and L' complexes showing approximately 100% and 50% stability respectively. This agrees with our hypothesis and previous studies and suggests nickel should be considered as the metal of choice for cylinder design if high stability is desired.[28] These results provide the field with insight into how a therapeutic or diagnostic agent may be best developed to achieve its intended function *in vivo.*

Finally, we explored the effect of *pseudo*-rotaxanation on the stability of cylinders in blood. This revealed substantially improved stability for the iron parent cylinder, showing approximately 30% reduction in signal over 48 hrs compared to 100% reduction in signal over 24 hrs. Similarly, the iron azo *pseudo*-rotaxane showed complete degradation by 6-24 hrs instead of the 2-6 hrs seen with its non-*pseudo*-rotaxanated counterpart. These data suggest *pseudo*-rotaxanation has a beneficial effect on cylinder stability in blood, despite the cylinders ability to leave and interact with other substrates. For this reason, it should be considered as a simpler delivery mechanism if stability is of importance, possibly offering it own mechanism of interaction in a biological system.

This work, whilst still *in vitro*, represents the first step of *in vivo* studies and offers information for tailoring molecular design towards a therapeutic function. To build on this work, analysis could be done to examine degradation products and patterns for different cylinders and rotaxanes with respect to time. As well as this, examination for biological conjugates could provide valuable information of mechanisms of action, for instance, protein adducts. Cylinders lend themselves well to this due to bi-metalic nature which gives unique isotope patterns which provides a handle for analysis. The next major step for this work would be to use these complexes in rat models and analyze the blood samples produced via ICPMS and MS to assess their pharmacokinetics. The results of that experiment should be compared to the results reported here to help understand the mode of action and rationalize the effects and observations that these complexes produce *in vivo*. The enantiomer preference of blood for cylinders/rotaxanes can also be investigated further with respect to time and will build on the pharmacokinetics information that the *in vivo* studies provide.

Examination of blood samples for biomarkers may also shed light on the mechanism of action of these complexes.

3.5: Experimental

Rats blood was acquired from BioIVT and was used without further treatment and stored frozen at -20 °C. See chapter 2.8 for additional experimental information.

3.5.1: ICP-MS of rat's whole blood:

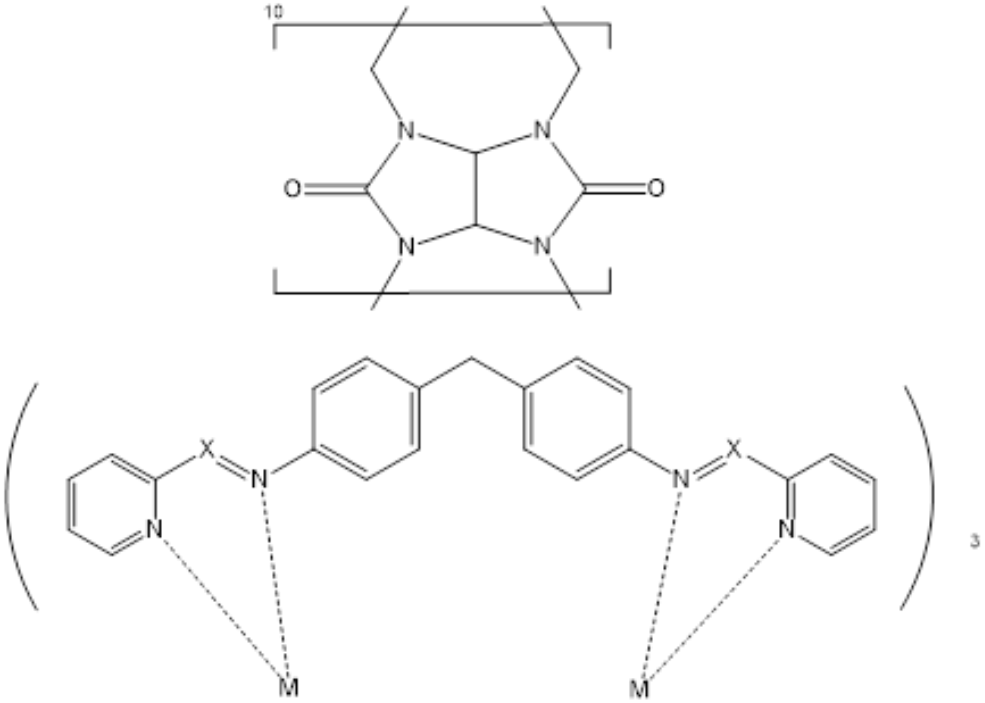
10 mL glass vials were cleaned in aqua regia (1:3 NO_3:HCl) for 4 hours. They were then washed with Milli-Q ultrapure 18 MΩ cm^{-1} water, washed with ethanol and dried in an oven at 80 °C for 2 hours. 25 µl of blood (as this would be the volume, we would be working with during rat studies) (Rats blood was acquired from BioIVT and was used without further treatment and stored frozen at -20 °C) was added to each vial, to which 200 µl of HNO_3 and 100 µl of H_2O_2 were added to digest the blood samples. This was then vortexed gently to ensure the sample was thoroughly mixed. The samples were then incubated at 60 °C for 2 hours before 3.6 ml of ultrapure 18 MΩ cm^{-1} water was added. The samples were then vortexed, centrifuged and filtered with a 0.45 µm syringe filter before being transferred to a 15 ml polypropylene tube. Samples were then run by Dr Lijiang Song at the University of Warwick on an Agilent 7900 ICP-MS instrument. Nickel calibration standards were made by serial dilution of a stock nickel ICP standard, 1000 mg/L dissolved in nitric acid in ultrapure 18 MΩ cm^{-1} water (MERCK).

3.5.2: Blood Incubation and MS detection experiment

For the blood stability tests of cylinder, 50 µl of rat's whole blood was placed in a microcentrifuge tube followed by 4 µl of 1 mM complex and 46 µl of ultrapure water. These samples were then incubated for the specified length of time before being

removed, where 300 µl of methanol saturated with ammonium chloride was added and the sample was vortexed. The samples were then pipetted into a 10 ml, 10 kDa PES centrifuge tube (ThermoFisher scientific) where they were centrifuged until all the filtrate was collected. These samples were then run on a Waters SYNAPT G2S MS, with the TriVersa NanoMate LESA and chip attachment, using the time-of-flight MS ES+ method in sensitivity mode. Samples were run using direct injection to eliminate cross contamination between samples. Spectra were analyzed using MassLynx software v4.2.

3.5.3: Synthesis and Characterization of cylinders



Preparation of *pseudo*-rotaxanes: All *pseudo*-rotaxanes were prepared using the same method, 1eq of cylinder was dissolved in water and 1.1eq of CB[10] was added. This leaves a near clear solution of *pseudo*-rotaxane, the excess CB[10] is a white powder and is separated by centrifugation and filtration. The above schematic shows

the product *pseudo*-rotaxane, where CB[10] surrounds the central axis of the cylinder. Where X is carbon in L and N in L*.

CB10-$[Fe_2L_3]^{4+}[Cl^-]_4$:

Mass spectrum (TOF MS ES+): m/z = 310.1 $[Fe_2L_3]^{4+}$, 725.5 CB10-$[Fe_2L_3]^{4+}$

CB10-$[Ni_2L_3]^{4+}[Cl^-]_4$:

Mass spectrum (TOF MS ES+): m/z = 311.6 $[Ni_2L_3]^{4+}$, 726.7 CB10-$[Ni_2L_3]^{4+}$

CB10-$[Fe_2L^*_3]^{4+}[Cl^-]_4$:

Mass spectrum (ESI): m/z = 726.96 CB10-$[Fe_2L^*_3]^{4+}$

3.6: References

1 M. J. Hannon, C. L. Painting, A. Jackson, J. Hamblin and W. Errington, *Chem. Commun.*, 1997, 1807–1808.

2 C. Ducani, A. Leczkowska, N. J. Hodges, M. J. Hannon, C. Ducani, A. Leczkowska, M. J. Hannon and N. J. Hodges, *Angew. Chem. Int. Ed.*, 2010, **49**, 8942–8945.

3 J. Malina, M. J. Hannon and V. Brabec, *Chem. Eur. J.*, 2015, **21**, 11189–11195.

4 J. Malina, M. J. Hannon and V. Brabec, *Chem. Eur. J.*, 2008, **14**, 10408–10414.

5 J. Malina, M. J. Hannon and V. Brabec, *Nucleic Acids Res.*, 2008, **36**, 3630–3638.

6 J. Malina, M. J. Hannon and V. Brabec, *FEBS J.*, 2014, **281**, 987–997.

7 M. J. Hannon, V. Moreno, M. J. Prieto, E. Moldrheim, E. Sletten, I. Meistermann, C. J. Isaac, K. J. Sanders and A. Rodger, *Angew. Chem. Int. Ed.*, 2001, **40**, 879–884.

8 J. Malina, M. J. Hannon and V. Brabec, *Chem. Eur. J*, 2007, **13**, 3871–3877.

9 I. Meistermann, V. Moreno, M. J. Prieto, E. Moldrheim, E. Sletten, S. Khalid, P. Mark Rodger, J. C. Peberdy, C. J. Isaac, A. Rodger and M. J. Hannon, *Proc. Natl. Acad. Sci. USA*, 2002, **99**, 5069–5074.

10 J. Malina, M. J. Hannon and V. Brabec, *Sci. Rep.*, 2016, **6**, 29674.

11 S. Phongtongpasuk, S Paulus, J Schnabl, R. K. O. Sigel, Priv.-D. B. Spingler, E. Freisinger and M. J. Hannon, *Angew. Chem. Int. Ed.*, 2013, **52**, 11513–11516.

12 A. Oleksi, A. G. Blanco, R. Boer, I. Usón, J. Aymamí, A. Rodger, M. J. Hannon and M. Coll, *Angew. Chem. Int. Ed.*, 2006, **45**, 1227–1231.

13 A. C. G. Hotze, N. J. Hodges, R. E. Hayden, C. Sanchez-Cano, C. Paines, N. Male, M.-K. Tse, C. M. Bunce, J. K. Chipman and M. J. Hannon, *Chem. Biol.*, 2008, **15**, 1258–1267.

14 L. Cardo, V. Sadovnikova, S. Phongtongpasuk, N. J. Hodges and M. J. Hannon, *Chem. Commun.*, 2011, **47**, 6575–6577.

15 G. I. Pascu, A. C. G. Hotze, C. Sanchez-Cano, B. M. Kariuki and M. J. Hannon, *Angew. Chem. Int. Ed.*, 2007, **46**, 4374–4378.

16 L. Cardo, I. Nawroth, P. J. Cail, J. A. McKeating and M. J. Hannon, *Sci. Rep.*, 2018, **8**, 13342.

17 L. Melidis, I. B. Styles and M. J. Hannon, *Chem. Sci.*, 2021, **12**, 7174–7184.

18 L. Melidis, H. J. Hill, N. J. Coltman, S. P. Davies, K. Winczura, T. Chauhan, J. S. Craig, A. Garai, C. A. J. Hooper, R. T. Egan, J. A. McKeating, N. J. Hodges, Z. Stamataki, P. Grzechnik and M. J. Hannon, *Angew. Chem. Int. Ed.*, 2021, **60**, 18144–18151.

19 C. A. J. Hooper, L. Cardo, J. S. Craig, L. Melidis, A. Garai, R. T. Egan, V. Sadovnikova, F. Burkert, L. Male, N. J. Hodges, D. F. Browning, R. Rosas, F. Liu, F. v. Rocha, M. A. Lima, S. Liu, D. Bardelang and M. J. Hannon, *J. Am. Chem. Soc.*, 2020, **142**, 20651–20660.

20 Y. H. Chu, M. Sibrian-Vazquez, J. O. Escobedo, A. R. Phillips, D. T. Dickey, Q. Wang, M. Ralle, P. S. Steyger and R. M. Strongin, *Mol. Pharm.*, 2016, **13**, 2677–2682.

21 B. Woods, R. D. M. Silva, C. Schmidt, D. Wragg, M. Cavaco, V. Neves, V. F. C. Ferreira, L. Gano, T. S. Morais, F. Mendes, J. D. G. Correia and A. Casini, *Bioconjug. Chem.*, 2021, **32**, 1399–1408.

22 N. Laur, R. Kinscherf, K. Pomytkin, L. Kaiser, O. Knes and H. P. Deigner, *PLoS One*, 2020, **15**, e0233357.

23 J. M. C. A. Kerckhoffs, J. C. Peberdy, I. Meistermann, L. J. Childs, C. J. Isaac, C. R. Pearmund, V. Reudegger, S. Khalid, N. W. Alcock, M. J. Hannon and A. Rodger, *Dalton Trans.*, 2007, 734–742.

24 R. Pedrido and M. Hannon, University of Birmingham, Unpublished work.

25 M. I. Pownceby, D. H. Jenkins, R. Ruzbacky and S. Saunders, *J. Chem. Eng. Data.*, 2012, **57**, 1449–1455.

26 G. Mercer, Master of Research Thesis, University of Birmingham, 2018.

27 D. Das, K. I. Assaf and W. M. Nau, *Front. Chem.*, 2019, **7**, 619.

28 Y. Parajo, J. Malina, I. Meisterman, G. J. Clarkson, M. Pascu, A. Rodger, M.J. Hannon and P. Lincoln, *Dalton Trans.*, 2009, **25**, 4868-4874.

Chapter 4: Metallo-supramolecular pillarplexes as DNA Junction and Fork binders

4.1: Introduction

DNA presents itself as an attractive therapeutic target due to its importance, and roles in many biological functions and disease.[1–4] DNA primarily exists as the canonical B-DNA structure, targeting the features in B-DNA therefore does not offer a great deal of specificity, due to its abundance.[5,6] However, the structures that DNA adopts whilst undergoing vital processes such as transcription, replication, and repair allow for process specific targeting.[4,6–9] In this case, junctions, specifically 3WJ's such as those occurring in replication forks, and 4WJ's which occur during homologous recombination are attractive targets to reduce replication rates in disease and prevent repair of DNA damage.[10–12] Targeting these structures with tailored therapeutics could enable increased specificity, reduced side effects, and greater efficacy.[6]

Many metal complexes have been developed which utilize supramolecular interactions to target specific nucleic acid structures. There include small organic molecules such as derivatives of bis-acridine and triptycene, which have been shown to bind to 4WJ's and 3WJ's respectively.[13,14] They utilize their smaller size, cationic charge, and planar aromatic moieties to interact with these structures at their branch points. Other metallo-supramolecular complexes have also demonstrated potent DNA binding, specifically platinum salphen complexes which demonstrate binding to and stabilization of G-quadruplex structures.[15] Similarly, metallo-supramolecular cylinders as discussed in chapters 2 and 3, exploit their tetra-cationic charge and helical aromatic groups to fit

near perfectly in the branch point of 3WJ's.[16,17] This binding is owed to their special distribution of supramolecular interactions, allowing for excellent π-stacking interactions between the cylinders di-aniline unit on the ligand, and the exposed base pairs in the branch point of the DNA 3WJ. These complexes demonstrate the potential of applying supramolecular interactions in drug design to achieve specific nucleic acid binding.

In search of new structures with promise of unique DNA structures, we investigated metallo-supramolecular pillarplexes (Figure 4.01).[18] They are a new class of metallo-supramolecular structure which exhibit many of the supramolecular interactions other complexes have utilized successfully in non-canonical DNA binding. They share resemblance to the metallo-supramolecular cylinders with a cylindrical design, though they are a little wider and shorter in length. They are comprised of two cyclophane ligands which linearly coordinate eight metal centers between one another where the metal can be silver (I) or gold (I). They exhibit π-interactions on the pyrazole rings and have a tetra-cationic charge. Their ligand structures are modifiable, and they can hold a linear guest molecule in their central cavity such as 1,8-diaminooctane.[19–21]

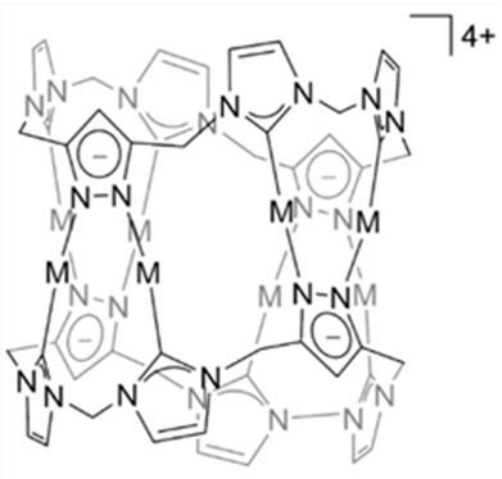


Figure 4.01: Shows the structure of a pillarplex where M may be silver(I) or gold(I).

Within this chapter, the interactions of metallo-supramolecular pillarplexes with different DNA structures are explored. To do this we have utilized gel electrophoresis, spectroscopy, and atomic force microscopy. We also explore the potential of the pillarplex to form a higher order rotaxane by external rotaxanation with CB[10] and simultaneous internal threading with a linear guest.

4.2: Nucleic acid interactions of supramolecular pillarplexes

The work described in this section 4.2.1 and 4.2.2 has been submitted for publication as part of the publication entitled “Organometallic Pillarplexes that bind DNA 4-way Holliday Junctions and forks”.[22] The work was carried out in collaboration with colleagues in the group and external collaborators. This section focuses primarily on my contributions, but to contextualise and rationalise the studies, some aspects of the wider studies from others are included. The work that is discussed and supported by Figures represents my contributions (comprising gel electrophoresis, CD and LD experiments).

4.2.1: Electrophoresis studies

Our initial experiment was to understand how this new structure behaves with DNA three-way junctions (3WJ) compared to the previously studied metallo-supramolecular cylinders. We carried out PAGE experiments comparing the binding to 4 different DNA structures: a ‘perfect’ 3WJ structure, a ‘mismatched’ three-way junction (mm-3WJ) that contains a mismatched T-T base pair at the junction to expand the junction cavity, a double stranded 21-base duplex (DS-21) and a palindromic 24-base strand (PAL24) that can form duplexes but could potentially also form higher order structures. The structures of the different DNA sequences used can be seen in Figure 4.02. Gels were

ran at room temperature, post stained with SYBR Gold and imaged using a UV transilluminator at 305nm.

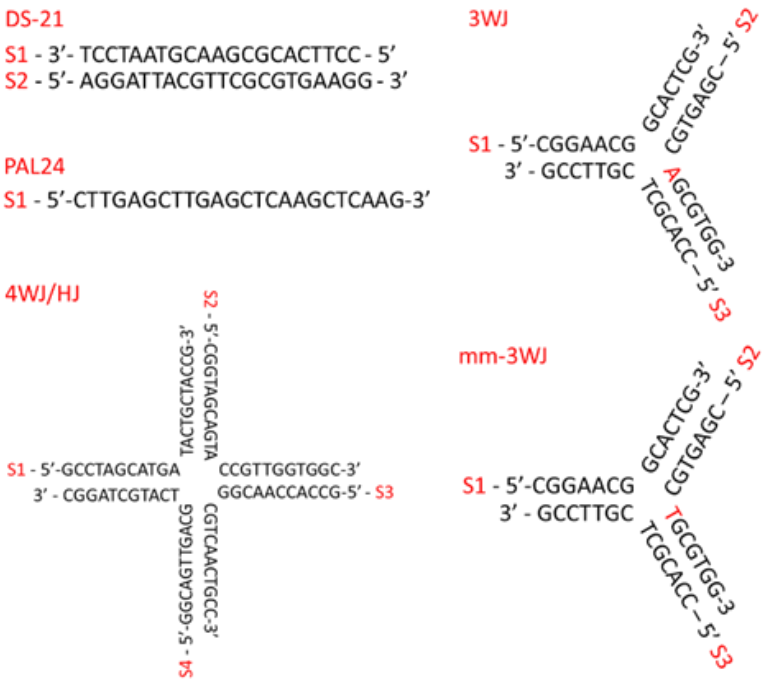


Figure 4.02: Shows the different DNA sequences and their structures used in these studies with appropriate labels.

The first structure (3WJ) is a 3WJ formed from 3 different strands which we have used previously.[16] The structure is not formed at room temperature in absence of cylinder and only single stranded DNA is observed (Figure 4.03 A lane 1), but when $[Ni_2(L)_3]^{4+}$ cylinder binds in the 3WJ, the structure is stabilised and the 3WJ band observed in the gel (Figure 4.03 A lanes 11-14) with an increase in 3WJ observed with increasing cylinder concentration. Similarly, on addition of 0.5, 1 and 2 eq of the gold Pillarplex (Figure 4.03 A lanes 3-5), 3WJ is formed, however, at 4 eq (lane 6) we see the 3WJ structure is replaced by a large, smeared band corresponding to a 2-stranded Y-shaped fork junction. This suggests a preference for Y-shaped or partially double stranded structures, at higher loadings. The broad nature of the Y-shaped band likely reflects the 3 different Y-structures that can be formed by the 3 strands and the

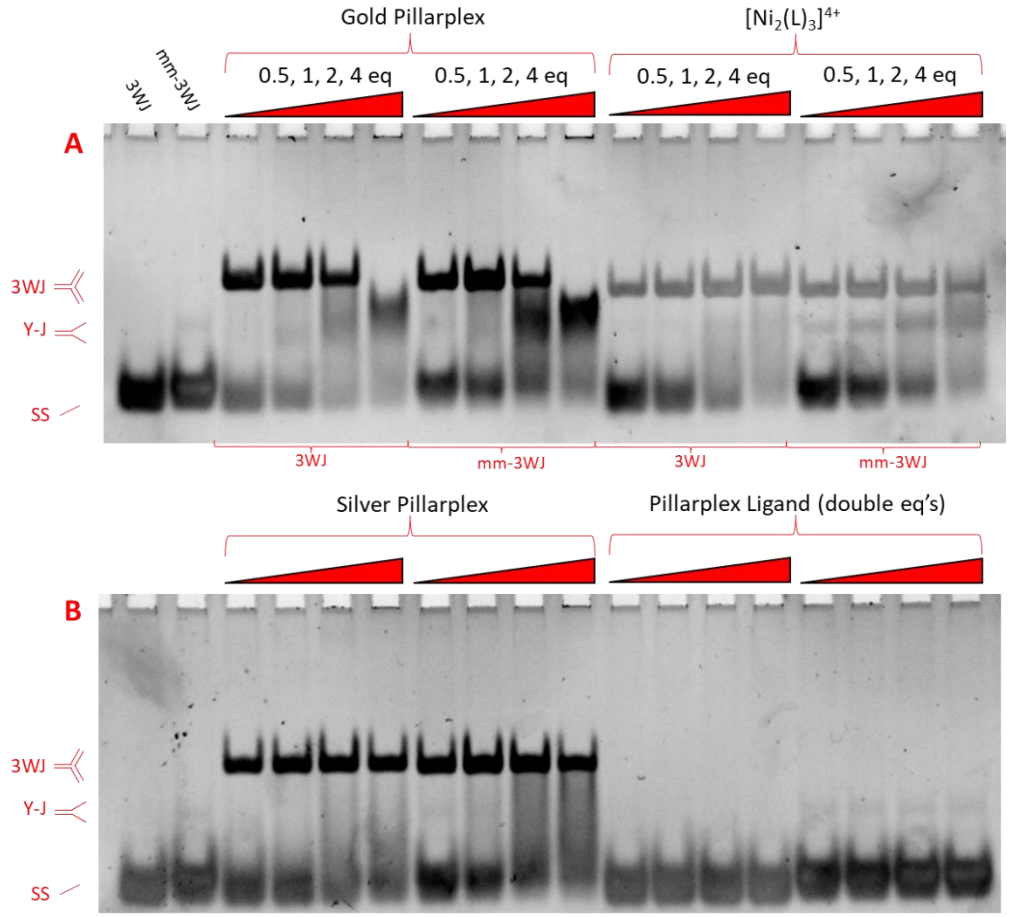


Figure 4.03: Shows 2 PAGE gels (A and B) of different DNA structures incubated with different complexes at varying ratios, all gels read from left to right. Gels A and B both include 3WJ and mm-3WJ DNA strands incubated with gold pillarplex and $[Ni_2(L)_3]^{4+}$ cylinder (gel A) as well as silver pillarplex and pillarplex ligands (gel B). Both these gels include controls in lanes 1-2, then 3WJ is mixed with a complex at 0.5,1, 2 and 4 eq (lanes 3-6 and 11-14), then b-3WJ mixed with a complex at 0.5,1,2,4 eq lanes 7-10 and 15-18).

flexibility of the single stranded branches. Interestingly the 3WJ band also has a small gel-shift (slower gel mobility) compared to our previously studied supramolecular cylinders. This would suggest that the 3WJ structure formed has a larger hydrodynamic radius. Considering the smaller length of the pillarplex, we hypothesise that this may be due to the larger width of the Pillarplex forcing the central cavity of the 3WJ to expand. Implicit in this would be a weakening (perhaps breaking) of at least one set of base-pair hydrogen bonds at the junction, decreasing the stability of the 3WJ.

We also investigated a 'mismatched' 3WJ structure where the central cavity has a mismatched T-T base pair. While this structure might promote 3WJ junction cavity

expansion and allow the gold pillarplex to have a more comfortable fit, it will also reduce the underlying stability of the 3WJ structure. This is reflected in the binding of the cylinder (Figure 4.03 A lanes 15-18) where binding to both mm-3WJ and 2-stranded Y-shaped fork is observed (in contrast to the perfect 3WJ). By contrast, the gold pillarplex binding to mm-3WJ is much more like its 3WJ binding with initial mm-3WJ binding observed and then a similar shift to a Y-fork binding at higher loading (Figure 4.03 A lanes 7-10).

The data confirm that the gold Pillarplex can bind and stabilise both 3WJ and Y-fork structures. At high loading the option is to bind one pillarplex at the junction and others in or at the ends of the 3WJ duplex arms, or to lower the number of strands and bind to Y-shaped forks, where it appears to do the second. The binding to 3WJ is stronger than to Y-fork (as expected on electrostatic grounds) but both Y-junctions (3WJ or fork) are much preferred over binding to duplexes or single-stranded DNA. The similarity between the gold Pillarplex binding to both 3WJ and mm-3WJ is consistent with the hypothesis that the Pillarplex is expanding the 3WJ cavity (breaking some base-pairing at the junction) though it does not completely exclude binding outside the junction.

We then investigated the corresponding silver pillarplex with 3WJ (Figure 4.03 B, lanes 3-6) and mm-3WJ (lanes 7-10). In both cases a shifted 3WJ band is observed which is very similar to that with gold pillarplex. However, we do not see a pronounced Y-shaped band at higher loading. Instead at 2 and 4 equivalents we see a smearing effect below the 3WJ which remains present even at 4 equivalents. The silver Pillarplex has poorer solution stability than the gold, and therefore there is potential for release of silver cations from pillarplexes which may then bind to the DNA. Controls with the

organic ligand from which the Pillarplexes are constructed show no binding of the free ligand to DNA (Figure 4.03 B 11-18).

To probe further into the interactions of the complexes, we looked at a double stranded sequence (DS21) and a palindromic sequence (Pal24). DS21 consists of two non-palindromic complementary strands which form a stable double stranded DNA at room temperature (Fig 4.04 C, lanes 1-3). Pal24 is a palindromic sequence potentially capable of forming duplexes and higher order structures, such as 3WJ and beyond. At room temperature it is principally single stranded with a small amount of double stranded duplex (Fig 4.04 C, lane 4).

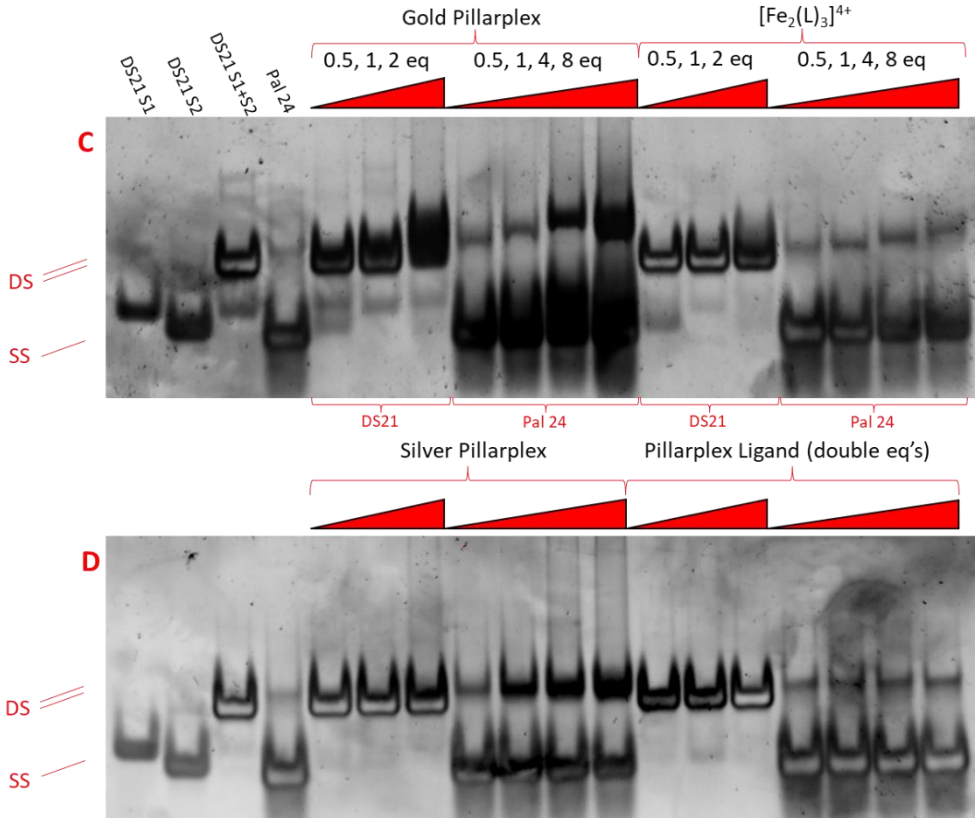


Figure 4.04: Shows 2 PAGE gels (C and D) of different DNA structures incubated with different complexes at varying ratios, all gels read from left to right. Gels C and D both include DS21, and Pal24 DNA strands incubated with gold pillarplex and $[Fe_2(L)_3]^{4+}$ cylinder (gel C) and silver pillarplex and pillarplex ligand (gel D). Both these gels include controls in lanes 1-4, then DS21 mixed with a complex at 0.5,1 and 2 eq (lanes 5-7 and 12-14), then Pal24 mixed with a complex at 0.5,1,2,4 eq lanes 8-11 and 15-18).

With the duplex DS21, gold pillarplex shows an increasingly broader and more smeared band, with a shift to lower mobility, indicating binding to the duplex and an increase in its hydrodynamic radius. The cylinder shows a similar (though less marked effect) while the silver pillarplex shows a gradually increasing proportion of DS-DNA which would be comparable to cationic stabilization. The pillarplex ligand shows little if any effect on either DNA structure which is corroborated with the lack of interaction with 3WJ DNA. When Pal24 is treated with gold pillarplex, the pillarplex increases the proportion of the double-stranded structure and causes a small reduction in shift and large broadening of the band (Figure 4.04 C lanes 8-11). There is also a large broadening and smearing of the SS band, indicative of stochastic binding. This implies that the gold pillarplex promotes and binds to the duplex structure. The DS band remains discrete (though broadened) even at higher loadings (in contrast to the SS band), suggesting a specific structure is being formed instead of a stochastic one. The cylinder causes similar shifts in the ds band but does not seem to increase its proportion, while the silver pillarplex increases the amount of duplex but does not cause a gel shift. The change in hydrodynamic radius of the duplex with gold pillarplex and cylinder would be consistent with a (fluxional) transition towards an open Y-shaped fork structure. Again, there is no evidence of binding by the Pillarplex ligand, corroborated by the previous electrophoresis results (Figure 4.03 B).

Given this tetragonal arrangement of the π-surfaces and the indication that the pillarplex is a little too wide for the perfect 3WJ, we were intrigued to see whether it might also bind a four-way junction structure (4WJ) as it would have a larger central cavity than the 3WJ. To investigate this relationship, we looked at a 4WJ assembled

from 4 complementary strands which have been used in a previous study by Searcy et.al.[24]

The 4WJ can be seen with increasing concentrations of different complexes (Figure 4.05 E). At room temperature the strands form a mixture of 4WJ and individual single strands, with the 4WJ stabilised by high concentrations of $MgCl_2$ and NaCl. A small proportion of a higher order structure is also observed with these cations, potentially formed due to the high cationic strength of solution.

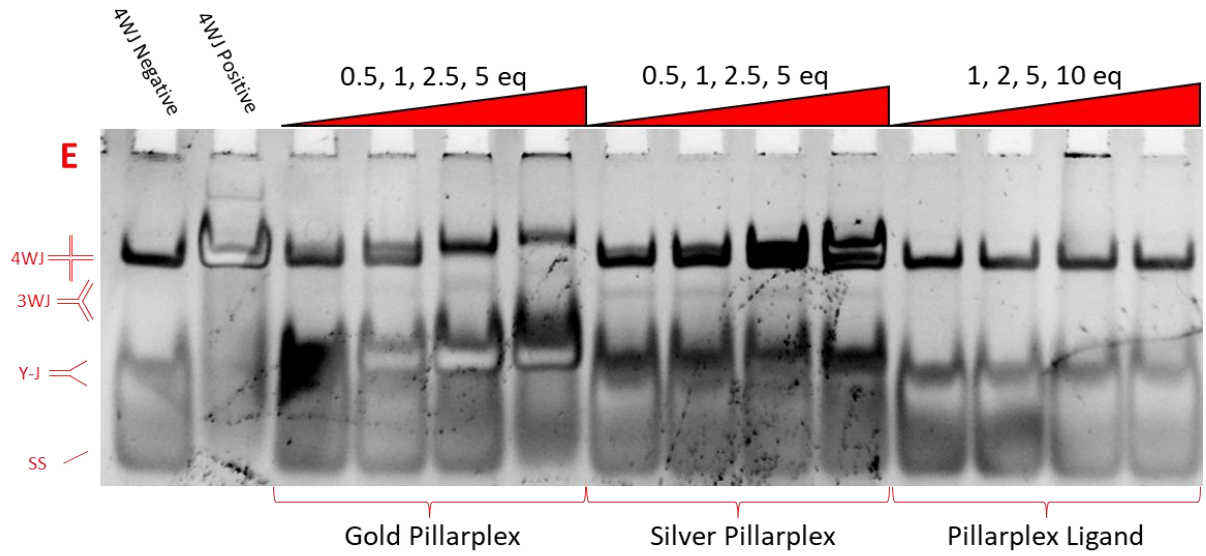


Figure 4.05: Shows PAGE gel E, which contains different DNA structures incubated with different complexes at varying ratios, gel E reads right to left and gels F and G read left to right. Gel E includes S1,S2,S3 and S4 in all lanes, controls in lanes 1-2, 4WJ positive containing 2 mM Mg^{2+} and 450 mM Na^{+}, and complexes added in at 0.5,1,2.5 and 5 eq. Lanes 2-6 gold pillarplex, lanes 7-10 silver pillarplex and lanes 11-14 pillarplex ligand.

The gold pillarplex interacts with 4WJ, causing the appearance of bound and unbound species at 1:1. This is shown by the splitting of the 4WJ band into a broader double band (Figure 4.05 E lane 4). However, as the ratio of gold pillarplex to 4WJ increases, the population of the bands shifts to favour the bound species. A smaller X-stacked arrangement is expected in absence of pillarplex, where the open arrangement is expected when bound by a pillarplex, exhibiting a larger hydrodynamic radius and hence reduced gel shift, which is what we can visualise. This further shift at high

loading (5:1) is likely a result of multiple pillarplexes bound to the same structure. This decrease in 4WJ intensity coincides with the increase in intensity of a Y-fork double stranded band, just as seen in the 3WJ gel. However, at high loading the 4WJ is still present, whereas at the same loading, the 3WJ band had disappeared (Figure 4.03 A lane 6). This suggests that 4WJ is a better binding target than 3WJ, likely due to the increased size of the central cavity. A small proportion of discrete three-strand structure (presumably a forked version of the 4WJ, missing a strand) also starts to appear, likely a thermodynamically unstable forked 4WJ structure (3WJ like), stabilised by bound pillarplex.

The silver Pillarplex also seems to promote the 4WJ band, showing a larger and broader band, indicating binding, with a faint band also observed for the discrete three-strand structure and a larger band for the Y-fork duplex DNA (Figure 4.05). It is interesting that there is comparatively less shift at high loading though this may reflect a lower pillarplex concentration given the lower stability of the silver complex. Once again controls with the ligand do not indicate free-ligand binding (Figure 4.05).

Given the complexity of the samples, we decided to investigate the individual strands in this 4WJ to understand the system better. We looked at all the strands, and combinations of them (Figure 4.06 F) and observed the structures formed. The single strands were pure and combinations of 2+ strands often led to a partially DS structure being formed. Combinations of 3 strands forms small quantities of 4WJ when S4 is included in the mixture. It is hypothesised that S4 could form partially self-paired structures, allowing for the bands we can see when S4 is included. When all strands are combined, we can see a prominent 4WJ band form along with some partial DS structures smearing.

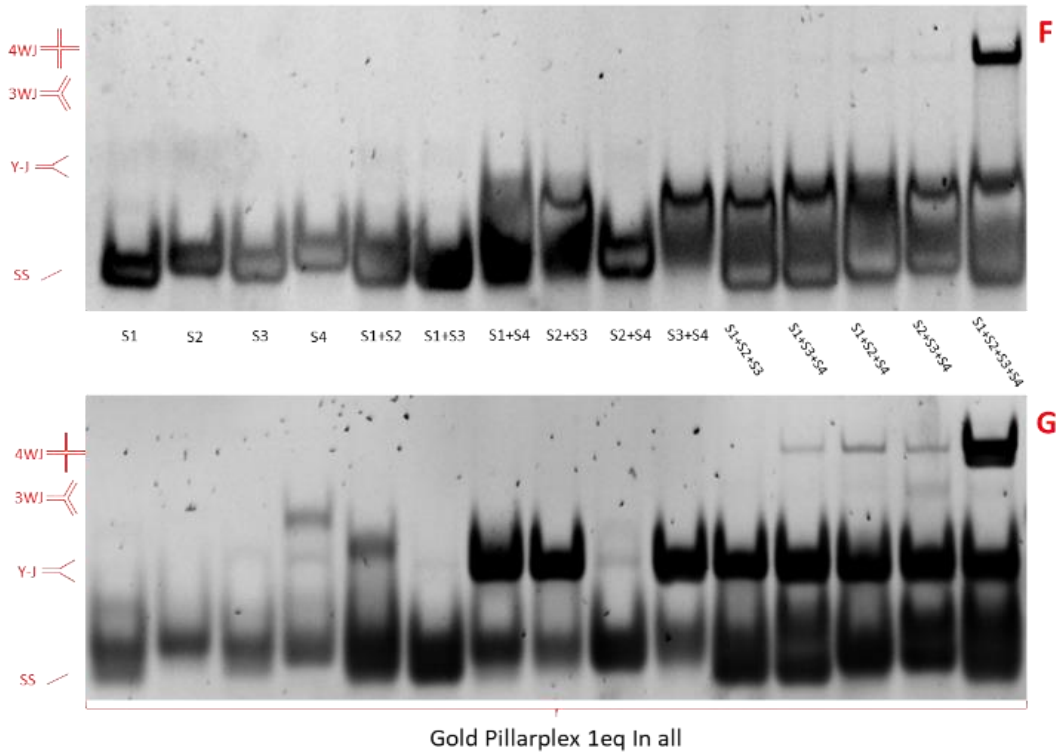


Figure 4.06: Shows PAGE gels F and G, which contain all combinations of S1/S2/S3 and S4 from the 4WJ. Gel F contains lanes with the different combinations of strands on their own. Gel G is the same as gel F but with 1 eq of gold Pillarplex in every lane.

When we incorporate 1 eq of gold pillarplex into each of these lanes (Figure 4.06 G), we can see several distinct changes. Smearing and broadening occurs with the single strands, as well as multiple secondary structures occurring with S4. We can also see across other lanes that most of the SS DNA shifts to form DS/Y structures where possible, except between 1+3 and 2+4 where there is no complementarity. We can also see that a 4WJ structure is promoted with mixtures of 3 strands that include S4. This is enhanced further in the presence of gold Pillarplex, as well as a small proportion of forked 4WJ structure with s2+s3+s4. In the presence of all four strands, we can see the favoured species is DS/Y junction and 4WJ over the possible 3WJ. This is likely due to the size and symmetry of the pillarplex allowing stronger binding to these structures, and their resulting thermodynamic stability.

Agarose gel electrophoresis was used to investigate changes in DS DNA's structure on interaction with these complexes. pBR-322 plasmid DNA was used as it is well characterized and provided a suitable length of 4361 base pairs for agarose band shifts. Samples were prepared and incubated at 37 °C for 1hr before loading into wells. The band shifts for linearized pBR-322 (Figure 4.07 H) show our positive control of $[Fe_2(L)_3]^{4+}$ cylinder inducing DS-DNA condensation, shown by a reduced band shift on increasing loading. The gold pillarplex shows a similar band shift (Figure 4.07 H and 4.08 J), suggesting condensation, however, it exhibits tighter more distinct bands. This indicates very specific and regimented DNA binding, as well as a stronger band shift than the cylinder, suggesting a structure with a larger hydrodynamic radius is formed from repeated and consistent binding. An amount of precipitation can also be noticed in the wells, supporting this hypothesis further.

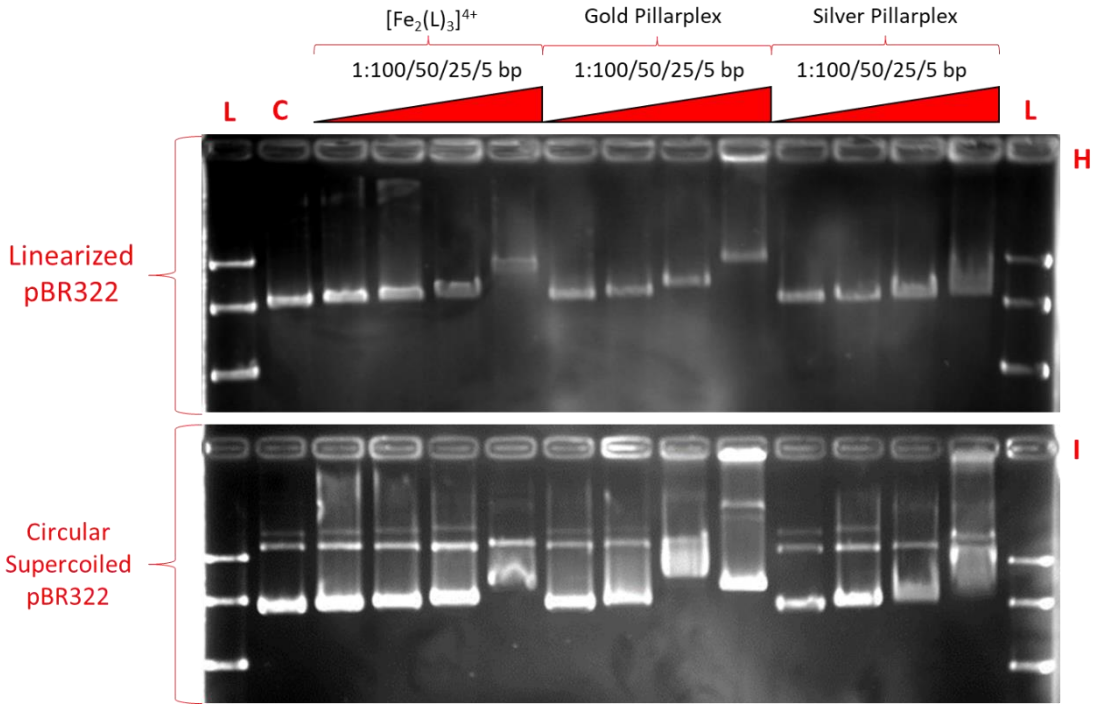


Figure 4.07: Agarose Gel Electrophoresis Studies of Circular supercoiled and linearized pBR-322 plasmid DNA with varying ratios of $[Fe_2(L)_3]^{4+}$ cylinder, gold pillarplex and silver pillarplex. Gel H Shows 15 lanes, 1 and 15 are Ladder, lane 2 DNA alone control, lanes 3-6 $[Fe_2(L)_3]^{4+}$ at 100:1, 50:1, 25:1, and 5:1 DNA base pairs too complex. Lanes 7-10 and 11-14 are the same with gold pillarplex and silver pillarplex respectively. Gel I is identical with Circular supercoiled pBR-322 plasmid DNA.

The silver pillarplex does not induce the same effect on DNA structure, instead causing a “smearing” effect more reminiscent of stochastic DNA binding. This could suggest the silver pillarplex structure is absent, and instead we are seeing stochastic binding of silver cations. This also suggests DS-DNA does not stabilise the silver Pillarplex structure.

The gold pillarplex with circular supercoiled DNA (Fig 4.07 I and 4.08 k) appears to result in the unwinding and re-winding of the supercoiled helix, initially reducing the shift, and then increasing it again. This is because of the DNA is going from a supercoiled helix which moves fastest in the gel, to a non-supercoiled arrangement, which moves slower, and back to a reversely supercoiled helix, now positively supercoiled. With higher binding ratio’s (Figure 4.08 K) this can be seen more clearly,

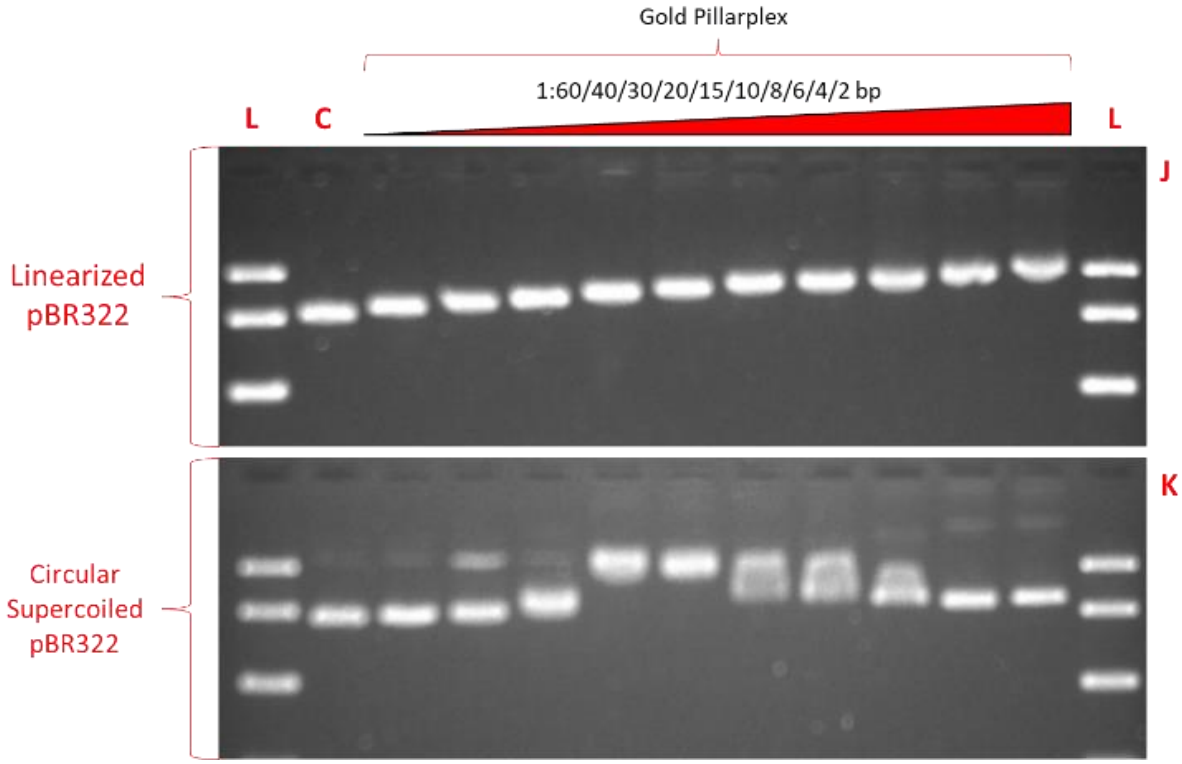


Figure 4.08: Agarose Gel Electrophoresis Studies of Circular supercoiled and linearized pBR-322 plasmid DNA with varying ratios of gold pillarplex. Gel J shows 13 lanes where 1 and 13 are ladder, 2 is linearized pBR-322 alone control and 3-12 are linearized plasmid with gold Pillarplex at ratios of 60:1, 40:1, 30:1, 20:1, 15:1, 10:1, 8:1, 6:1, 4:1 and 2:1 DNA base pairs to Complex. Gel K is identical to J but with circular supercoiled pBR-322 plasmid DNA.

with uncoiling starting at between 1 gold Pillarplex per 20-30bp. Pillarplex ligand alone (see appendix Figure A1) again shows no effect, highlighting the importance of the metal ions.

In summary the strong binding of gold pillarplex is observed by the formation of discrete structures with DNA. In contrast, the addition of silver Pillarplex produces stochastic binding effects, resulting predominantly in smearing with a lack of band shifts, likely due to cationic interactions of silver ions produced by silver pillarplex decomposition.

4.2.2: Spectroscopic studies

For spectroscopic studies, calf thymus (CT) DNA was chosen as a readily available and widely used source of B-DNA which has been used widely in the field, enabling accurate comparisons. Spectra were recorded sequentially starting from a solution of CT-DNA alone, followed by additions of a solution of the complex, and an equal volume of a solution of double concentration DNA and buffer to maintain a constant DNA concentration.

The LD spectra of CT-DNA were studied with increasing loading of gold pillarplex (Figure 4.09 B), from 1 per 60bp to 1 per 8bp. There is a reduction in the DNA signal, indicating DNA condensation, as well as a positive signal formation with peaks at 248 and 260, possibly due to an overlap of pillarplex spectroscopy or DNA bases. This would indicate specific and consistent gold Pillarplex arrangement(s) on the DNA, parallel to the direction of flow, suggesting strong binding to the B-DNA structure. In the CD spectra (Figure 4.09 A), the B-DNA signal appears to be somewhat conserved, however there is a superposition of signal in the same region, likely an induced signal

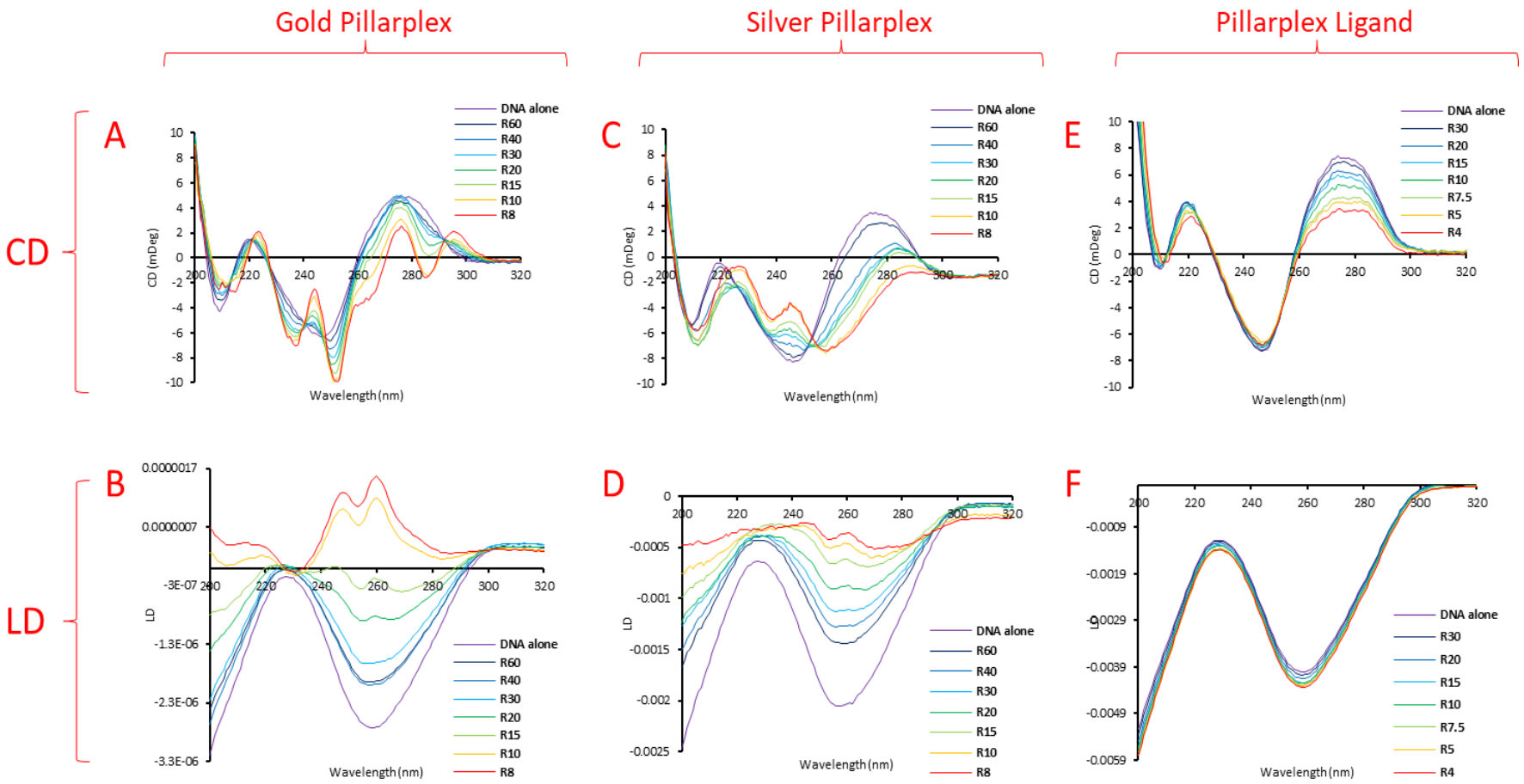


Figure 4.09: Spectroscopic studies of Au and Ag Pillarplexes and Pillarplex ligand with CT-DNA. The R value is the ratio of DNA base pairs too complex. Top row are Circular dichroism spectra; bottom row are linear dichroism spectra. Spectra are acquired by titration of a solution (containing complex of interest) and 2x DNA/buffer solution to an initial solution of 100 µM CT-DNA (bp) with spectra being recorded after each titration addition. Each column refers to a specific complex, left column being gold Pillarplex, middle column being silver Pillarplex and right column being Pillarplex ligand.

from the gold Pillarplex. This makes distinct changes challenging to discern; however, this is strong evidence of binding. A binding curve was plotted with the CD values at 250 nm from Figure 4.09 spectra A against the corresponding concentrations (Figure A5 in appendix). A binding curve was then fitted using the one-site specific binding model in GraphPad Prism. A K_d of $6x10^{-7}$ was then determined from this fitting by finding the concentration at half of B_{max}. The spectra of CT-DNA on addition of silver Pillarplex indicates DNA condensation in a different manner to that of the gold Pillarplex. The LD (Figure 4.09 C) shows a reduction in the DNA signal, consistent with condensation, however no positive signal is seen like in the gold Pillarplex LD, suggesting the silver pillarplex does not bind in the same manner as the gold. The CD signal shows a less convoluted spectrum with a reduction in the magnitude of the B-DNA signal around 280 nm. We suggest this is likely because of silver Pillarplex degradation as demonstrated in stability tests previously, meaning the effect we see is due to cationic degradation products rather than the Pillarplex structure.[24] To test this hypothesis, we carried out a control with the Pillarplex ligand alone to see if decomposition into ligand was inducing the same effect. We can see in the LD (Figure 4.09 F) that no condensation can be observed, indicating that degradation into ligand is not directly responsible for the effect seen with either Pillarplex. This suggests cationic silver ions in solution could be responsible for this condensation - the other data agrees with his hypothesis. The ligand does not induce the same changes seen with either Pillarplex (Figure 4.09 E and F).

In summary, gold pillarplex demonstrates potent binding, and formation of organised discrete structures evidenced by the induced LD signal. B-DNA structure is also mostly intact, although superimposed with Pillarplex signal. Silver Pillarplex induces

condensation, in a different manner to the gold pillarplex as no positive signal is seen. Drastic reduction in signal at 280 nm suggesting stochastic condensation because of excessive cation binding. Pillarplex ligand shows little interaction agreeing with previous experiments on the important of the metal centre. Going forward, spectroscopic data such as this should be utilised to generate binding constants (Kd). This would provide quantitative insight into the binding relationship between these nucleic acid structures and the complex, which can provide information on the mode of interaction.

4.2.3: Atomic force microscopy

To attempt to investigate the structures being formed by pillarplexes with B-DNA we employed atomic force microscopy (AFM) as a technique to probe secondary structure. We used linearized pBR-322 plasmid DNA for these experiments as it provided a mono-disperse DNA length for clearer images and analysis. When looking at linearized plasmid alone (Figure 4.10), we can see the DNA mostly exists as random overlaps of structures, primarily under 1 nm in height. Some larger structures can be seen;

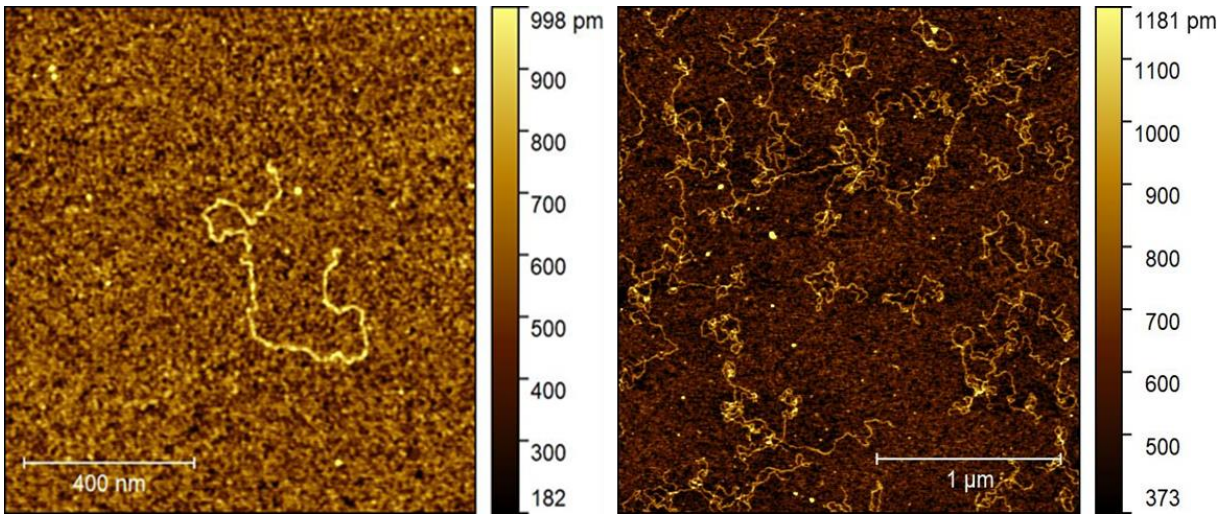


Figure 4.10: Shows 2 AFM images of difference sizes of 1 µM in base pairs of linearised pBR-322 plasmid DNA deposited on mica using a deposition buffer.

however, they are few and do not exhibit a DNA structure. This could mean the larger structures are impurities or contaminants such as salt crystals from the deposition buffer.

We then created samples where linearized pBR-322 plasmid DNA was mixed with each pillarplex at a ratio of 1 per 5 base pairs for 1 hr at 37.5 °C before being deposited on the mica surface for imaging. Whilst imaging the DNA incubated with gold pillarplex (Figure 4.11 left both images) we can see that large structures are found as high as 17 nm. This is a strong indicator of binding, as structures of this size are not found in the samples with DNA alone. Other structures also appear to be composed of 2+ linear

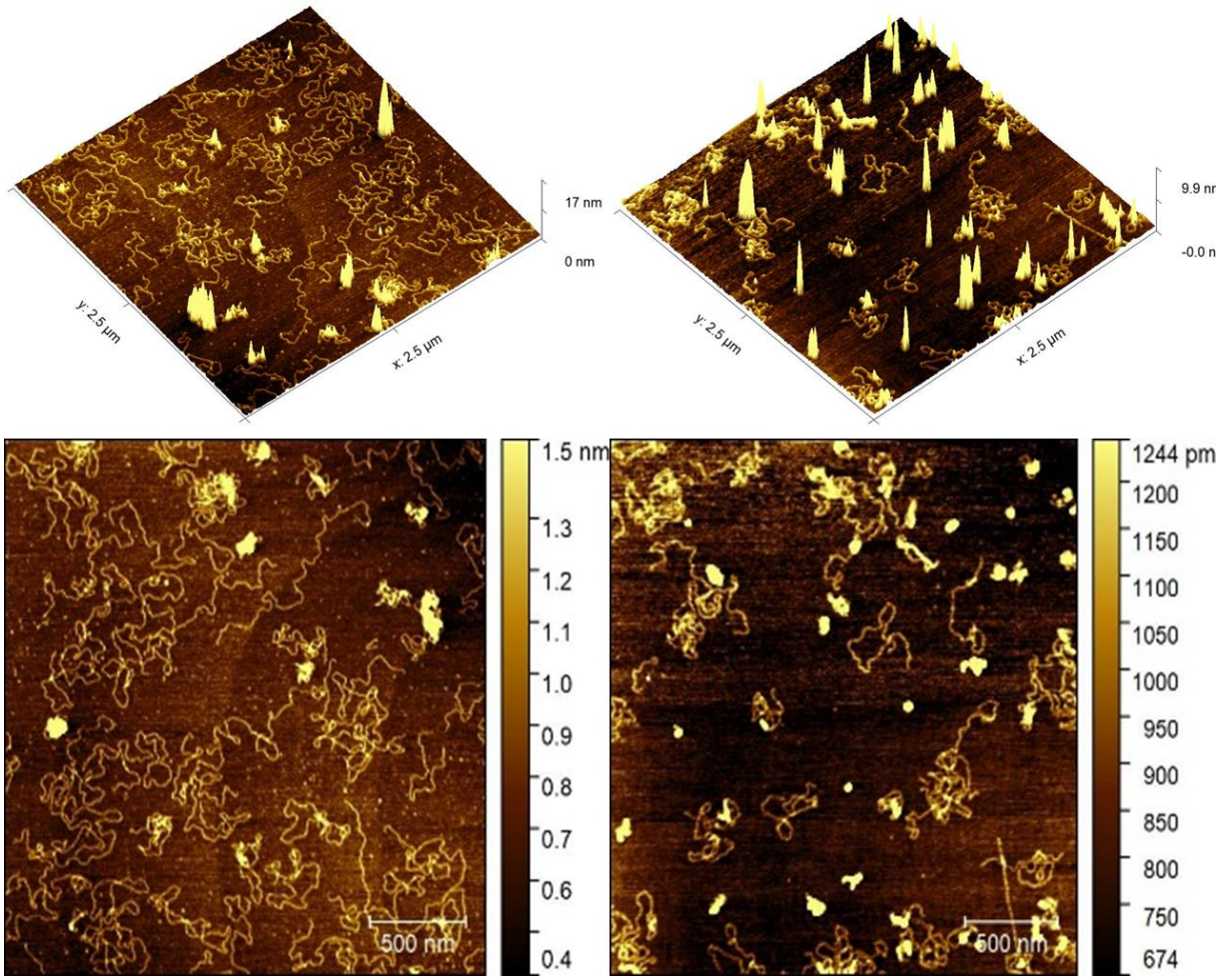


Figure 4.11: Shows 2 AFM images of difference sizes of 1 µM in base pairs of linearised pBR-322 plasmid DNA mixed with gold pillarplex (left) and silver pillarplex (right) before being deposited on mica using a deposition buffer.

plasmid DNA molecules, possibly indicating inter-strand interactions and condensation. In comparison, when the silver pillarplex is incubated with the DNA (Figure 4.11 right both images), we can similarly see lots of larger structure bring formed, around 10 nm and below. These condensed DNA structures appear to be solitary species, possible formed through intra-strand condensation rather than inter-strand. DNA overall appears to be more condensed, possible due to the release of 8 eq of silver ions creation a high cation concentration.

These AFM images appear to support the hypothesis of gel electrophoresis and CD/LD experiments. in that binding and condensation is occurring, and both pillarplexes are causing different interactions. Aside from this, there is no obvious structure being formed as may be anticipated for the gold pillarplex given LD, CD and gel electrophoresis results indicating regimented binding. To acquire more data from these images and those like it, a larger sample size, an AFM instrument with greater resolution, and additional quantitative computational/statistical analysis could provide further insight into the DNA's secondary structure. Alternatively, TEM could be used to visualize DNA interactions, however the preparations conditions are harsher, and a contrast agent is required such as uranyl acetate. Whilst this removes some of the issues associated visualising DNA with AFM, they have their own issues. Perhaps comparison between both methods would provide more reliable and accurate information on the DNA's interactions with these complexes.

4.3: Rotaxanation of Pillarplexes: Towards a 3-tiered Russian doll system

The pillarplex has already demonstrated the ability to be rotaxanated by a small linear guest molecule. We believed, given its similar dimensions, that the pillarplex may also be able to be rotaxanated by an external guest molecule, specifically CB[10], which we had already used to rotaxanated the metallo-supramolecular cylinder. If possible, the aim would then be to form a 3 tier rotaxane where a linear guest molecule would thread a pillarplex, which would in turn be rotaxanated by CB[10] (see Figure 4.12). Through appropriate modification, this would allow multiple tiers of control with numerous potential theragnostic applications.

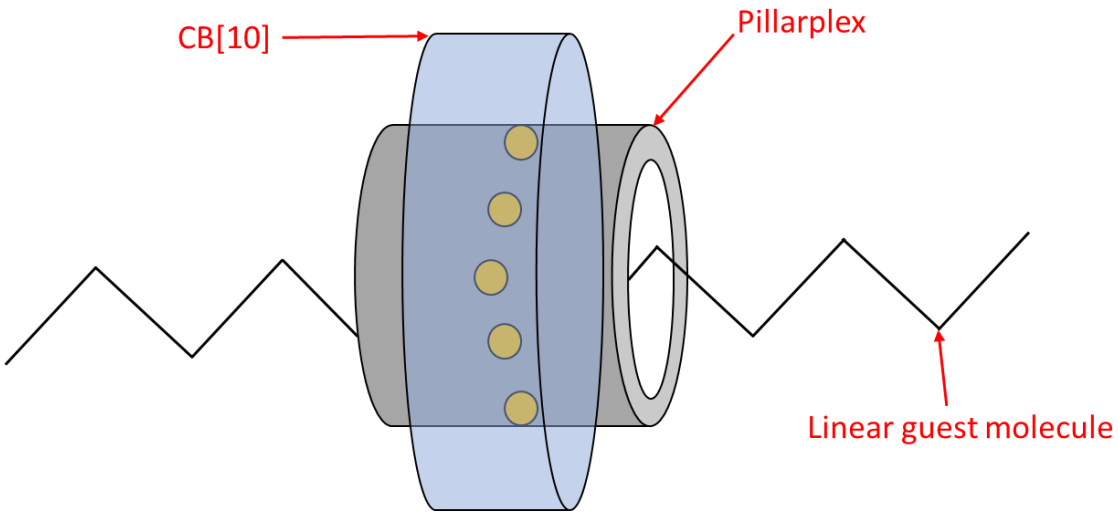


Figure 4.12: Schematic representation of the theorised Russian doll structure containing a linear guest molecule inside a pillarplex, inside a cucurbituril.

Our initial test was to mix CB[10] with each pillarplex and look for the *pseudo*-rotaxane complex in mass spectrometry. The mass spectra of silver pillarplex mixed with 1 eq of CB[10] can be seen in Figure 4.13 after initial mixing (t=0) and after 1 week (t=7 days). On initial mixing we can see silver pillarplex as a tetra-cation at 455 m/z and a peak at 870.4 m/z which corresponds to silver pillarplex + CB[10], also as a tetra-

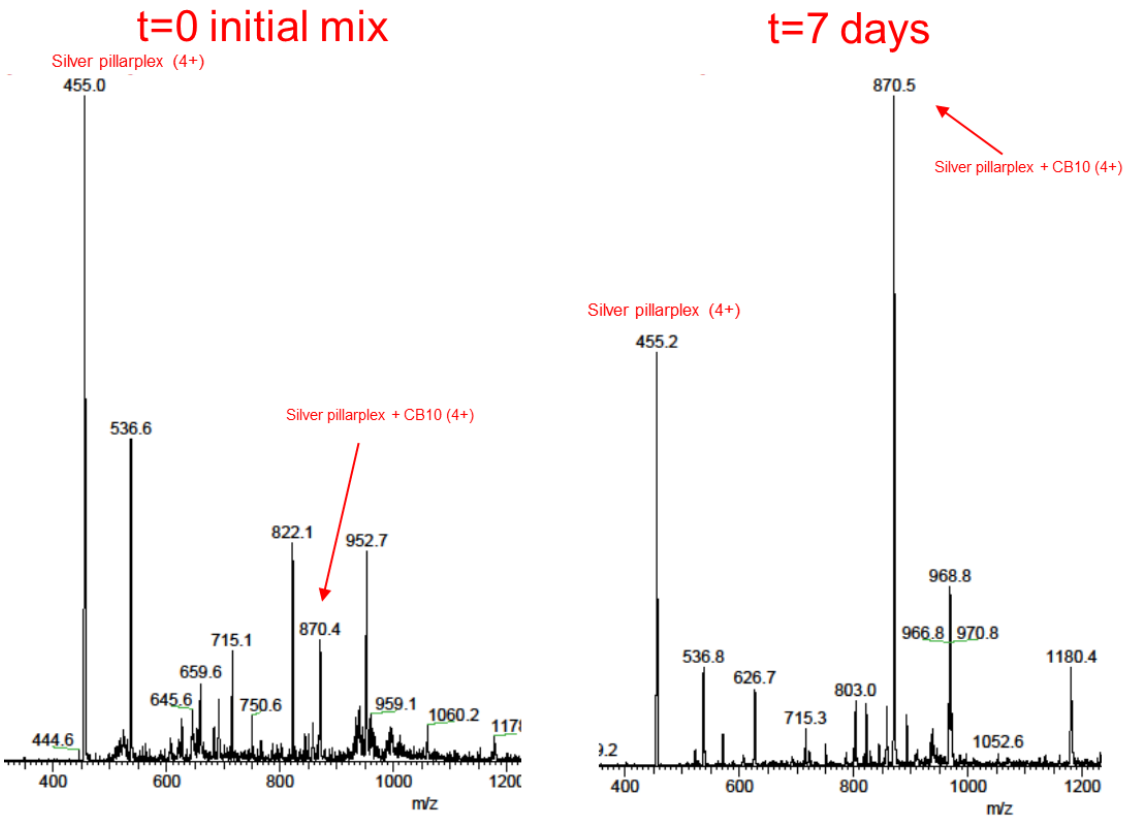


Figure 4.13: Shows the ESI+ mass spectra of silver pillarplex mixed with 1 eq of CB[10] at time t=0 and t=7 days.

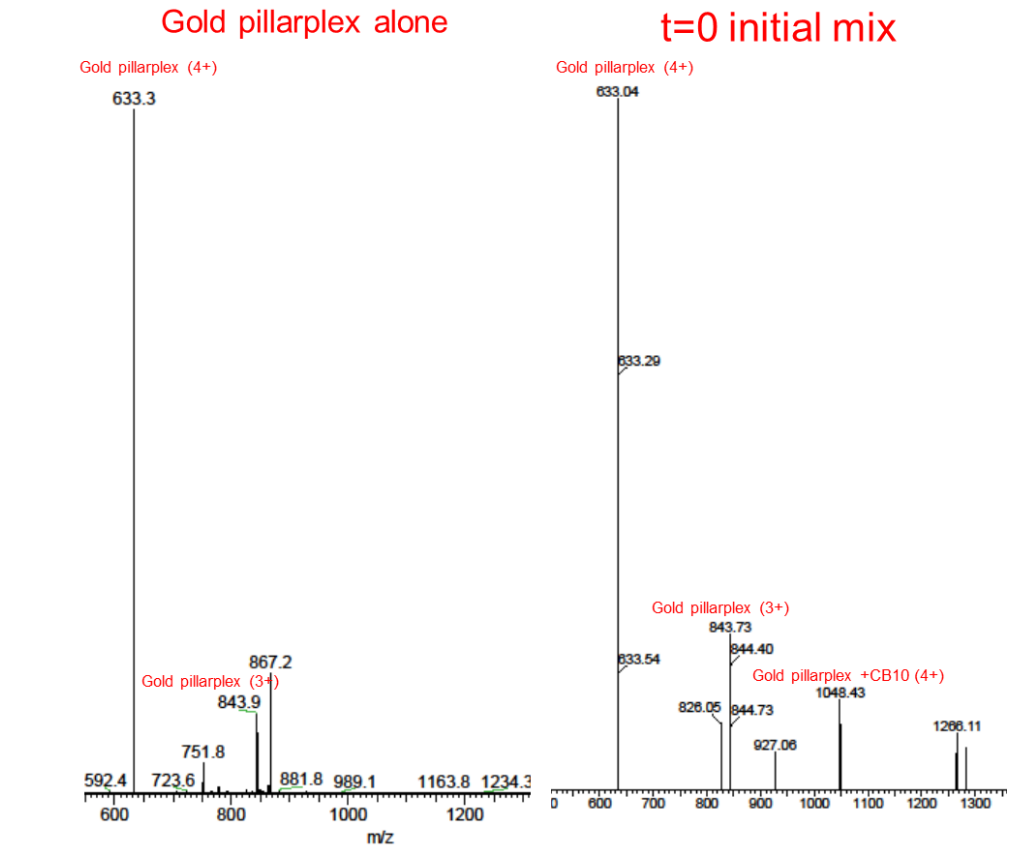


Figure 4.14: Shows the ESI+ mass spectra of gold pillarplex alone (left) and mixed with 1 eq of CB[10] at t=0 (right).

cation. We can see that the ratio of these peaks changes after 7 days, favouring the *pseudo*-rotaxane. The presence of these MS peaks does not confirm a host guest relationship, however, the gradual shift over time could suggest a slower interaction like that of a host-guest complex, supporting the hypothesis.

Next, we incubated gold pillarplex with CB[10] in the same manner (Figure 4.14). We observed the gold pillarplex tetra-cation peak at 633.3 m/z and upon initial mixing with CB[10] we could see a peak at 1048.43 m/z. This peak corresponds with the adduct of gold pillarplex and CB[10] as a tetra-cation, similarly to that of the silver pillarplex.

Having established the appearance of an adduct in MS, we decided to investigate if any binding was occurring via NMR (Firgure 4.15). To do this, we mixed each pillarplex

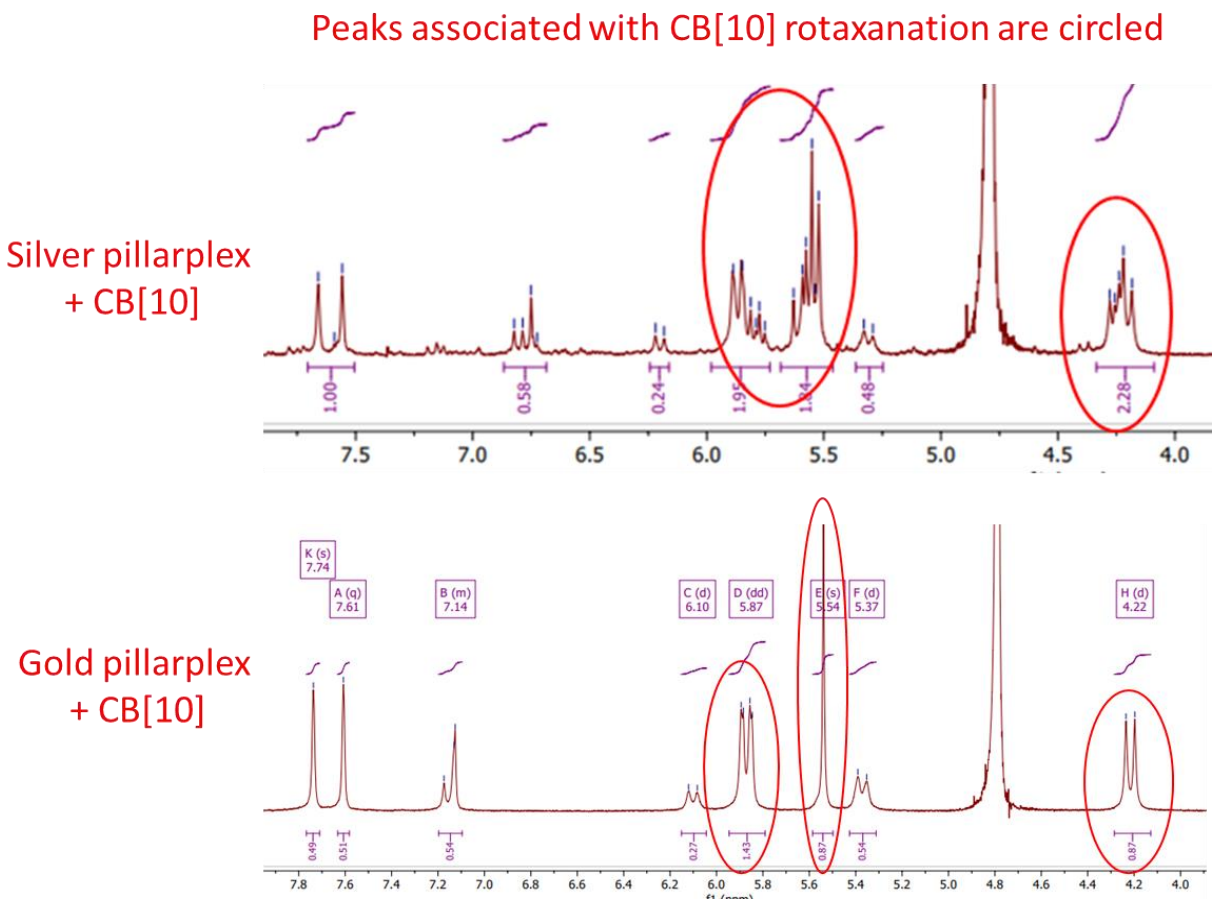


Figure 4.15: NMR spectra of silver pillarplex (top and gold pillarplex (right) on mixing with 1 eq of CB[10] in D_2O.Circled are the signals in each sample associated with CB[10]. Peak lists can be found in the experimental section 4.5.1.

with 1 eq of CB[10] in D_2O and filtered the solution to remove insoluble CB[10]. CB[10] is insoluble without a guest molecule, hence without one, we do not see a signal in NMR.

The NMR spectra reveal peaks associated with solubilised CB[10] when mixed with both pillarplexes in D_2O (Figure 4.15). These peaks are in the same region as those associated with CB[10] in the metallo-supramolecular cylinder *pseudo*-rotaxane NMR.[25] Further investigation with DOSY NMR spectroscopy could separate species of different hydrodynamic radius in solution, identifying if a *pseudo*-rotaxane species is present.

To gauge binding strength between the pillarplex and CB[10], we prepared a sample of 1 eq each of $[Ni_2(L)_3]^{4+}$ cylinder, gold pillarplex and CB[10]. We ran a mass spectra

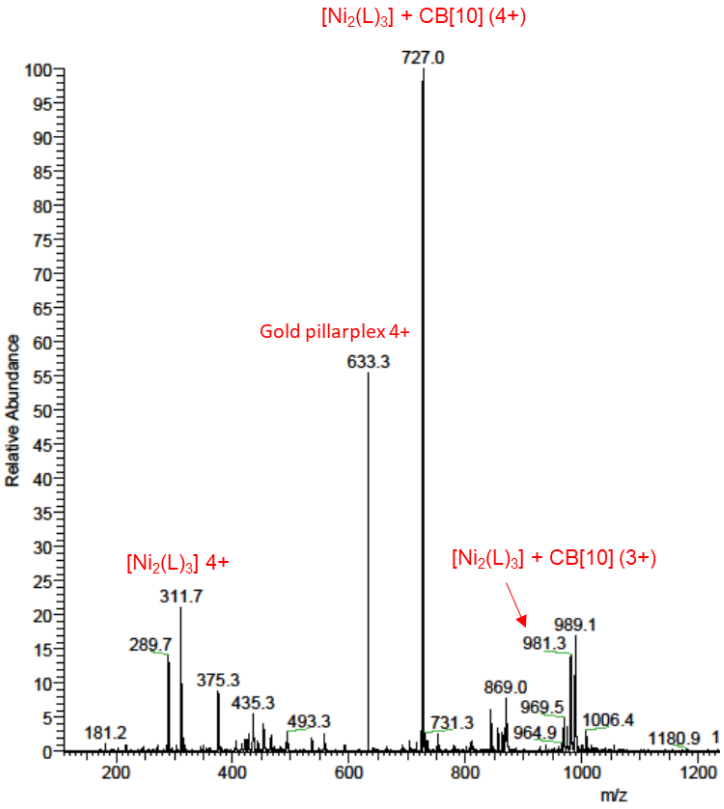


Figure 4.16: Shows the ESI+ MS spectra of a sample of gold pillarplex, $[Ni_2(L)_3]$ cylinder and CB[10] (1 eq each) mixed in 90% water and 10% methanol,

of this sample (Figure 4.16) 96 hrs after initial mixing which revealed no 1048 m/z peak for gold pillarplex + CB[10] *pseudo*-rotaxane 4+ like we have previously seen (Figure 4.13). Instead, $[Ni_2(L)_3]^{4+}$ cylinder *pseudo*-rotaxane at 727 m/z and 3+ at 981 m/z are the dominant *pseudo*-rotaxanated species. This indicates that the $[Ni_2(L)_3]^{4+}$ cylinder is a better fit for the CB[10] cavity than the gold pillarplex. This competition effect also indicates that the pillarplex is likely binding in the cavity of CB[10], as opposed to in another binding side (eg on the exterior).

Finally, we carried out initial studies on the ability for the gold pillarplex + CB[10] *pseudo*-rotaxane to accept a linear 1,12-diaminododecane molecule as a guest, on recommendation by collaborator Dr. Alex Pöthig at TU Munich.[21] The MS spectra before and after initial mixing with 1 eq of 1,12-diaminododecane at room temperature (Figure 4.17) reveal no complex between the linear guest molecule and pillarplex either alone or as part of a *pseudo*-rotaxane with CB[10]. The inability to thread suggests alternative conditions are required, if indeed it is possible.

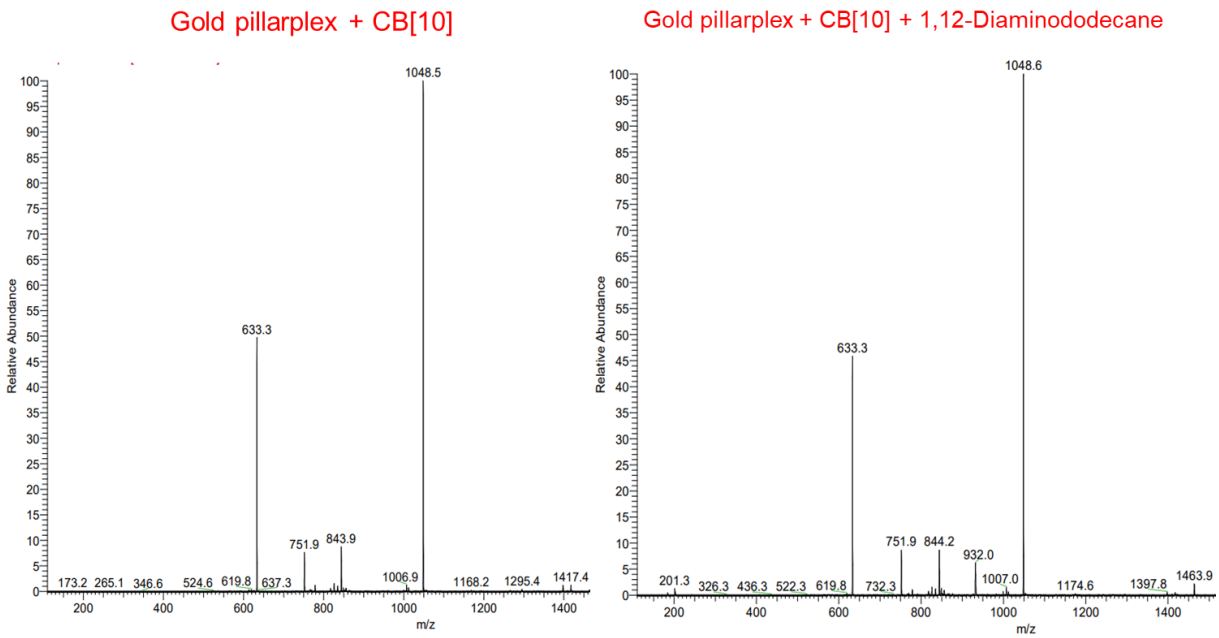


Figure 4.17: MS spectra of gold Pillaplrex and CB[10] with (left) and without (right) the addition of the linear guest molecule 1,12-Diaminododecane.

Further work should establish the formation of the pillarplex rotaxane (*pseudo* and full) with 1,12-diaminododecane prior to mixing with CB[10], as this may impact the host-guest relationship between the pillarplex and CB[10]. This should be done by optimising solvent and temperature, as well as exploring alternative linear guest molecules such as spermidine. Should a 3-tiered rotaxane be formed, the ability to modify the pillarplex and its linear guest should be investigated to provide full rotaxanation for the guest inside the pillarplex and the pillarplex inside CB[10]. A similar [3]rotaxane has been developed which exhibits ring through ring molecular shuttling,[26] setting the premise for this Russian doll like structure. However, this proposed Russian doll structure offers additional unique utility by containing metal atoms with the rings being a complex supramolecular structure. The silver Pillarplex has also already demonstrated potential as a pH sensitive probe,[21] highlighting one application for such a structure. Other chemical groups could also be integrated into the structure to confer activity in response to things such as enzymes, light and specific biomolecules.

4.4: Conclusion

The initial investigation into the DNA interactions of metallo-supramolecular pillarplexes is reported. This reveals their abilities to bind to DNA junction and fork structures, likely through their π-stacking and cationic interactions. Their increased width has demonstrated additional functionality in their junction binding, where at higher loadings, the higher ordered 3WJ and 4WJ structures are broken down into Y junctions. Their larger size also makes them a better match for larger junction cavities, such as those of the 4WJ. This opens up a new theragnostic target in 4WJ's through the tailoring of metallo-supramolecular structures to better occupy this cavity. Pillarplexes also demonstrated potent binding to the canonical B-DNA structures, causing condensation, and in the case of the gold pillarplex, apparent discrete and ordered structures.

Uniquely, the pillarplex has its own host guest interactions, allowing for theoretical formation of a 3-tiered host guest system. We reveal that CB[10] is likely able to form a *pseudo*-rotaxane with the pillarplex, enabling the possibility of developing a higher order system. Further work is required to categorically prove this, namely DOSY NMR to confirm a larger hydrodynamic structure with the pillarplex and CB[10], as well as studies which prove simultaneous internal threading is also possible, though we remain optimistic.

Both silver and gold pillarplex demonstrate differing DNA binding interactions, likely because of the poorer stability of the silver pillarplex, causing it to break down and release 8 eq of silver ions. Despite this, 3WJ binding is still observed, offering potential for targeted release of silver ions, which have been associated with its high toxicity.

The ability to control this release of silver ions could enable the development of a targeted therapeutic agent.

In conclusion, pillarplex DNA binding offer new insights into the development of DNA targeting metallo-supramolecular complexes, with their abilities to bind to higher order DNA structures. They also present strong potential for further studies and development to improve and target their biological properties through the development of higher order rotaxanes.

4.5: Experimental

See chapter 2.8 for additional experimental information.

4.5.1: Synthetic experimental

Synthesis of metallo-supramolecular pillarplexes and ligand:

Silver pillarplex, gold pillarplex and pillarplex ligand were synthesised by Alexandra A. Heidecker from Technische Universität München under the supervision of Dr Alexander Pöthig as part of this collaboration by previously reported methods.[18,28]

Silver pillarplex + 1 eq CB[10] NMR:

^{1}H NMR (400 MHz, Deuterium Oxide) δ = 7.61 (d, *J*=2.11 Hz, 1H), 6.77 (q, *J*=12.5 Hz, 10.2, 1H), 6.20 (d, *J*=14.5 Hz, 0H), 5.83 (dd, *J*=15.1 Hz, 2H), 5.68 – 5.46 (m, 2H), 5.31 (d, *J*=15.3, 0H), 4.23 (dd, *J*=22.7, 15.1, 2H).[18]

Gold pillarplex + 1 eq CB[10] NMR:

^{1}H NMR (400 MHz, Deuterium Oxide) δ = 7.74 (s, *J*=2.03 0H), 7.61 (q, *J*=2.03, 1H), 7.20 – 7.10 (m, 1H), 6.10 (d, *J*=14.9, 0H), 5.87 (dd, *J*=15.1, 4.1, 1H), 5.54 (s, 1H), 5.37 (d, *J*=15.4, 1H), 4.22 (d, *J*=15.1, 1H).[18]

Synthesis of CB[10]:

CB[10] was synthesised by Fengbo Liu from the group of Dr Simin Liu at the Wuhan University of Science and Technology by previously reported methods.[28]

4.5.2: Experiments

Biophysics experimental:

Milli-Q water (18.2 MΩ cm^{-1}) was used throughout all biophysical work. For circular and linear dichroism, DNA samples were made up from calf thymus DNA sodium salt (Sigma Aldrich) by dissolving in milli-Q water (18.2 MΩ cm^{-1}) and washed using a 10 kDa MWCO centrifuge tube (sartorius, Vivaspin, 10 ml). The solution was then quantified by UV-Vis spectroscopy (Cary 5000 NIR spectrometer) by ε258 = 13,200 mol^{-1} dm^3 cm^{-1} to give a concentration in DNA base pairs.[29] This stock solution was kept frozen with fresh aliquots being taken out for each experiment. Fresh buffer was made up before each experiment (see experimental for specifics). Complexes were dissolved in Milli-Q water (18.2 MΩ) only with fresh solutions being used for each batch of experiments.

Circular dichroism (CD):

Spectra were recorded on a Chirascan-plus spectrometer (Applied Photophysics limited). The samples were scanned in a 1 cm path length cuvette between 800 and 200 nm with 3 repeats at 1 nm step size and 0.5s dwell time per point. Titrations were carried out at a constant concentration of CT-DNA, sodium chloride (10 mM) and sodium cacodylate buffer (1 mM, pH 7.3) by adding compensating solutions of 2x DNA/Buffer of equal volume to the titre of the complex solution. The concentration of complex in the cuvette was increased step wise by adding set volumes of a stock complex solution. The R value refers to the ratio of DNA base pairs to complex, i.e. R60 = 60bp for every 1 complex, R4 = 4bp per complex. CT-DNA concentration was 100 µM in DNA base pairs.

Flow Linear Dichroism (LD):

was carried out on the same Chirascan+ spectrometer (Applied Photophysics limited) using the LD accessory (Applied Photophysics limited). The LD cell has an angular gap of 0.25 mm giving an overall path length of 0.5 mm. Samples volumes began at 150 µl and stopped at 250 µl. The cell was rotated at 40 revolutions per second to optimise the DNA signal. The titration series was carried out the same as in the CD studies, with a 3-minute incubation time at a lower revolution speed of 4 revolutions per second. CT-DNA concentration was 100 µM in DNA base pairs.

Polyacrylamide gel electrophoresis (PAGE):

Studies were performed using following oligonucleotide sequences (from Eurofins Germany) which were purified by reverse-phase HPLC.

DS21:

S1 = 5′ - CCTTCACGCGAACGTAATCCT - 3′

S2 = 5′ - AGGATTACGTTCGCGTGAAGG - 3′

PAL24:

S1 = 5′-CTTGAGCTTGAGCTCAAGCTCAAG-3′

mm-3WJ:

S1 = 5′-CGGAACGGCACTCG-3′ (S1),

S2 = 5′- CGAGTGCTGCGTGG-3′ (b-S2),

S3 = 5′-CCACGCTCGTTCCG-3′ (S3).

3WJ:

S1 = 5′-CGGAACGGCACTCG-3′

S2 = 5′- CGAGTGCAGCGTGG-3′

S3 = 5′-CCACGCTCGTTCCG-3′

4WJ:

S1 = 5′-GCCTAGCATGATACTGCTACCG-3′

S2 = 5′-CGGTAGCAGTACCGTTGGTGGC-3′

S3 = 5′-GCCACCAACGGCGTCAACTGCC-3′

S4 = 5′-GGCAGTTGACGTCATGCTAGGC-3′

Fluorescent PAGE experiments:

PAGE Polyacrylamide gels were prepared by mixing 25 ml of 29:1 acrylamide/bis-acrylamide (National Diagnostic, protogel) with 5 ml of 10x Tris-Boric acid buffer (890 mM each, pH 8.3, or pH 7.05 adjusted with HCl) and 20 ml of Milli-Q water. To this 400 µL of a 10% w/v ammonium persulfate/water solution and 40 µl of TEMED were added to initialise polymerisation. This was then immediately poured between 2 glass plates and a comb inserted at the top, this was then left to set for 1 hr. Samples were made up to 10 µl containing 1 µM of each strand 1xTBN buffer (89 mM Tris, 89 mM Boric acid, 10 mM NaCl, either pH 8.3 or 7.05) and the indicated ratio of complex or competitor. DNA, water, and buffer were mixed in solution before addition of the stated ratios of complex and additional components. Samples were then incubated at 37 °C for 1 hr. 5 µL of 30% w/v glycerol was then added to each sample and the sample was then centrifuged, mixed, and pipetted into the wells on the gel. The Gel was run at 140 V for 2 hrs in 1xTB buffer. The gel was then removed from the plates and stained using SYBR™ Gold Nucleic Acid Gel Stain (Thermofisher scientific) in 1xTB buffer for 45 minutes before imaging on a bio-rad ChemiDoc fluorescent imager with 305 nm excitation. DNA structures were at 1 µM in the samples with equal concentrations of each strand needed for their respective structures, complex concentrations are indicated in ratios to this.

Agarose gel electrophoresis:

Agarose gels were prepared by mixing 4 g of agarose (UltraPure™ Agarose, Thermofisher scientific) with 400 ml of Milli-Q water (18.2 MΩ) containing 1x Tris-Boric acid buffer (890 mM each, pH 8.3). This was microwaved till all the solid had dissolved and cast into the agarose gel tray with a 15-lane comb. DNA/complex samples were prepared in 1xTB buffer with 30 µM DNA in base pairs and the labelled ratio of complex to this. Samples were 20 µl in total, to this, 10 µl of 30% w/v glycerol solution was added for sample loading into the gel. A DNA ladder was used in the left and right most lanes with 10, 4 and 0.5 kDa mass, top to bottom. The gel was run at 140 V for 2 hours in 1xTB buffer. . The gel was then removed from the plates and stained using SYBR™ Gold Nucleic Acid Gel Stain (Thermofisher scientific) in 1xTB buffer for 45 minutes before imaging on a Bio-Rad ChemiDoc fluorescent imager with 305 nm excitation.

pBR322 plasmid linearization preparation:

pBR322 plasmid DNA was purchased from MERCK, linearisation was achieved using the pst1-HF restriction endonuclease (new England biolabs). 20 µl of 0.5 µg/µl pBR-322 DNA solution was incubated with 10 µl of pst1-HF (20,000 units/ml), 50 µl of 10x cutsmart buffer and 420 µl Milli-Q water (18.2 MΩ) were incubated together at 37 °C for 1 hr. This reaction mixture was then purified using QAIquick PCR purification columns and eluted with 50 µl Milli-Q water (18.2 MΩ). Concentrations in DNA base pairs was determined using a multichannel nanodrop 8000 spectrophotometers by using the absorbance at 258 nm and ε260 = 13,200 mol^{-1} dm^3 cm^{-1} using the Beer Lambert law.[29] Confirmation of the linearization was confirmed using agarose gel

electrophoresis by observing the characteristic band shift and by comparison to the 4 kDa band in the DNA ladder.

Atomic force microscopy:

Atomic Force Microscopy Atomic Force Microscopy was performed on a Keysight N9418S 9500 Atomic Force Microscope in a tapping mode at room temperature (25 °C and 60 % humidity) using Hi'Res-C15/Cr– Au probes (Apex Probes Ltd; 325 kHz resonance frequency, 40 N/m^{-1} force constant). AFM images had a resolution of 512 x 512 px and were scanned with a speed of 1.5 lines per second.

0.4 µl of 100 µM pillarplex was added to an Eppendorf, followed by 176.2 µl of Milli-Q water. To this, 3.7 µL of 54.2 µM (in base pairs) linearized pBR-322 plasmid DNA was added and mixed before addition of 20 µl of 10x buffer (100 mM NaCl, 10 mM Tris-base). The final ratio was 1 pillarplex per 5 DNA base pairs. Pillarplex/DNA solution (10 µl) was pipetted onto freshly cleaved mica and left for 2 hrs to incubate. This was then washed with 500 mL of Milli-Q water and dried under nitrogen. Images were analysis using the free software Gwyddion.

4.6: References

1 L. Wiesmüller, J. M. Ford and R. H. Schiestl, *J. Biomed. Biotechnol.*, 2002, **2**, 921363.

2 A. Bansal, S. Kaushik and S. Kukreti, *Front. Genet.*, 2022, **13**, 10.3389/fgene.2022.959258

3 L. Strasfeld and S. Chou, *Infect. Dis. Clin. North Am.*, 2010, **24**, 413–437.

4 A. R. Leman and E. Noguchi, *Genes (Basel).*, 2013, **4**, 1-32.

5 D. W. Ussery, DNA Structure: A-, B- and Z-DNA Helix Families, in *eLS*, (Ed.)Wiley, 2002. https://doi.org/10.1038/npg.els.0003122.

6 M. Blackburn, M. J. Gait, D. Loaks, D. M. Williams, *Nucleic Acids in Chemistry and Biology*, Royal Society of Chemistry, Cambridge, 2007.

7 H. Tateishi-Karimata and N. Sugimoto, *Chem. Commun.*, 2020, **56**, 2379–2390.

8 T. Endoh, A. B. Rode, S. Takahashi, Y. Kataoka, M. Kuwahara and N. Sugimoto, *Anal. Chem.*, 2016, **88**, 1984–1989.

9 M. R. Singleton, S. Scaife and D. B. Wigley, *Cell*, 2001, **107**, 79–89.

10 C. Altona, J. A. Pikkemaat and F. J. J. Overmars, *Curr. Opin. Struct. Biol.*, 1996, **6**, 305–316.

11 B. F. Eichman, M. Ortiz-Lombardía, J. Aymamí, M. Coll and P. S. Ho, *J. Mol. Biol.*, 2002, **320**, 1037–1051.

12 D. R. Duckett and D. M. J. Lilley, *EMBO J.*, 1990, **9**, 1659-1664.

13 S. A. Barros and D. M. Chenoweth, *Angew. Chem. Int. Ed.*, 2014, **53**, 13746–13750.

14 A. L. Brogden, N. H. Hopcroft, M. Searcey and C. J. Cardin, *Angew. Chem. Int. Ed.*, 2007, **46**, 3850–3854.

15 N. H. Abd Karim, O. Mendoza, A. Shivalingam, A. J. Thompson, S. Ghosh, M. K. Kuimova and R. Vilar, *RSC Adv.*, 2013, **4**, 3355–3363.

16 J. Malina, M. J. Hannon and V. Brabec, *Chem. Eur. J.*, 2007, **13**, 3871–3877.

17 A. Oleksi, A. G. Blanco, R. Boer, I. Usón, J. Aymamí, A. Rodger, M. J. Hannon and M. Coll, *Angew. Chem. Int. Ed.*, 2006, **45**, 1227–1231.

18 P. J. Altmann and A. Pöthig, *J. Am. Chem. Soc.*, 2016, **138**, 13171–13174.

19 S. Guan, T. Pickl, C. Jandl, L. Schuchmann, X. Zhou, P. J. Altmann and A. Pöthig, *Org. Chem. Front.*, 2021, **8**, 4061–4070.

20 A. A. Heidecker, M. Bohn and A. Pöthig, *Z. Kristallogr. Cryst. Mater.*, 2022, **237**, 167–177.

21 P. J. Altmann and A. Pöthig, *Angew. Chem. Int. Ed.*, 2017, **56**, 15733–15736.

22 J. S. Craig, L. Melidis, H. D. Williams, S. J. Dettmer, A. A. Heidecker, P. J. Altmann, S. Guan, C. Campbell, D. F. Browning, R. K. O. Sigel, S. Johannsen, R. T. Egan, B. Aikman, A. Casini, A. Pöthig, M. J. Hannon *J. Am. Chem. Soc.* 2023, **145**, 13570–13580

23 L. A. Howell, Z. A. E. Waller, R. Bowater, M. O'Connell and M. Searcey, *Chem. Commun.*, 2011, **47**, 8262-8264.

24 A. Pöthig, S. Ahmed, H. C. Winther-Larsen, S. Guan, P. J. Altmann, J. Kudermann, A. M. Santos Andresen, T. Gjøen and O. A. Høgmoen Åstrand, *Front. Chem.*, 2018, **6**, 10.3389/fchem.2018.00584.

25 C. A. J. Hooper, L. Cardo, J. S. Craig, L. Melidis, A. Garai, R. T. Egan, V. Sadovnikova, F. Burkert, L. Male, N. J. Hodges, D. F. Browning, R. Rosas, F. Liu, F. v. Rocha, M. A. Lima, S. Liu, D. Bardelang and M. J. Hannon, *J. Am. Chem. Soc.*, 2020, **142**, 20651–20660.

26 K. Zhu, G. Baggi and S. J. Loeb, Nat. Chem., 2018, **10**, 625-630.

27 P. J. Altmann, C. Jandl and A. Pöthig, *Dalton Trans.*, 2015, **44**, 11278–11281.

28 S. Liu, P. Y. Zavalij and L. Isaacs, *J. Am. Chem. Soc*, 2005, **127**, 15959–15967.

29 M. E. Reichmann, S. A. Rice, C. A. Thomas and P. Doty, *J. Am. Chem. Soc.* 1954, **76**, 3047–3053

Chapter 5: Summary, conclusions, and further work

5.1: Summary

This work has added to the field of supramolecular metallo-drug design by developing and working with new structures to achieve increased functionality. We have further built on this by exploring new biological targets and investigating how slight changes in the supramolecular architecture impact biocompatibility.

To conclude, metallo-supramolecular cylinders were both *pseudo* and fully rotaxanated by the macrocycle CB[10]. This was done in collaboration with colleagues, though modifying the ends of the ligand structure and achieving rotaxanation through a post-assembly modification process. This provided additional functionality to the already bio-active metallo-supramolecular cylinder, by eliminating its cellular toxicity and DNA binding properties. Further studying yielded the ability to achieve rotaxanation by a "slippage" mechanism where CB[10] could pass over the already capped ligands to achieve a full rotaxane. This provides a new method for rotaxane formation and opens the potential for new synthesis routes.

Replacing the rotaxanes capping groups with di-nitrobenzene allowed for removal of the cap in the presence of an appropriate thiol. This allowed us to use the control that CB[10] rotaxanation provides and use it to achieve increased specificity and improved delivery. Studies showed that the cleaved rotaxane maintained biological activity, highlighting the potential of such designs. The effects of tailoring the ligand structure on DNA binding were also investigated. They revealed similar binding properties, with the ability to bind to 4WJ's and even promote 3WJ from non-complimentary oligo's.

Cylinders also showed promise at binding different cucurbituril ring sizes and could allow for extraction of previously undiscovered cucurbiturils.

The next step for metallo-supramolecular cylinders and their associated rotaxanes was to establish a method for extraction from living systems to allow for eventual *in vivo* studies. This would allow for accurate quantitative and qualitative analysis of their biological activity, providing information on the likes of uptake, localisation, stability and biological targets. A method for separation and detection of intact supramolecular structures was established using MWCO centrifuge tubes and high salt conditions. This allowed for *in vitro* blood stability studies to be carried out, revealing most prominently that rotaxanes were stable up to 7 days. *Pseudo* rotaxanation also showed a strong increase of cylinder stability in blood, prompting questions as to whether this alone is enough to improve biological efficacy. Circular dichroism studies revealed there is a difference in enantiomeric activity with rats whole blood *in vitro*. This opens up potential for further control of biological activity by enantiomeric purification.

We investigated a new class of metallo-supramolecular complex called pillarplexes. They also share many of the supramolecular properties that make the cylinder as successful as it has been. These include being tetra-cationic, exhibiting π-stacking interactions and having a cylindrical structure. However, they encapsulate eight gold or silver metal centres, distinguishing themselves from the usual metals used in cylinders. They exhibit potent DNA binding and the ability for form 3WJ's with a slightly different EMSA shift which has been attributed to their slightly larger size. The silver pillarplex also shows reduced stability, which likely accounts for its differing DNA interactions. Most notably, they have also shown binding to 4WJ's and a preferences for 4WJ/YJ over 3WJ, allowing interference with different biological processes to that

of the cylinder. Finally, we explored their rotaxanation potential with CB[10], having already shown their capability to form rotaxanes. They were able to solubilise CB[10], suggesting a host-guest complex is formed between them both. The ability of the pillarplex to also accept a linear guest molecule itself makes this complex especially interesting. Potentially allowing formation of a 3-tiered rotaxanes system with unparalleled control through design.

5.2: Conclusions

This work has explored new methods of rotaxanation which has provided the field with a new class of rotaxane which can be built in different ways. This opens the possibility for development of many new metallo-supramolecular rotaxanes which could contain a variety of hosts and guests, from other metal complexes to peptides. We also hypothesize a Russian doll structure to form a [3]rotaxane with 2 supramolecular rings, one being a Pillarplex and the other being CB[10]. The level of customisation such a structure would have, offers great potential and many new avenues to explore.

The proof of concept of cleaving capping groups to release a functional and active metallo-supramolecular structure sets a new precedent in the field. Many caps may be (and are being) developed which can confer release in the presence of many stimuli, such as light, enzymes, pH and more. This gives the wider field more options and new insight into metallo-supramolecular drug development and will hopefully lead to many new potential metallo-supramolecular drugs in the field.

The discovery of Holliday junctions being a new potential therapeutic target for our metallo-supramolecular cylinders and Pillarplexes draws a great deal of attention to them. They present a unique structure with their own biological processes which may

prove to be a valuable target to achieve therapeutic or diagnostic activity. New variations of our complexes are currently in development with the aim to achieve increased interactivity and specificity for these structures. As this is a lesser explored structure it will be interesting to see if any already developed complexes in the field also show an affinity for this structure.

Lastly, the development of methods and techniques to extract and quantify intact metallo-supramolecular structures from close to in vivo samples such as rats whole blood, is of great benefit to the field. This presents a way to investigate the biological interactions of metallo-supramolecular complexes in a biologically relevant environment. Providing a great deal of insight into binding targets, stability, degradation pathways, enantiomer activity and more. All of these data can be used to build up a picture of how and why a complex works *in vivo*, leading to increased feedback into design and more efficient development.

5.3: Further work

This work also provides many avenues for development and investigation. Regarding the metallo-supramolecular rotaxanes, the development of new capping moieties holds much promise for the development of new therapeutic agents. Photo-activated and enzyme cleavable moieties stand out due to their ability to be controlled externally and through biological specificity respectively. Effective control using these functionalities could allow for highly specific and selective activity, dramatically reducing side effects, increasing efficacy and localising the drug to the desired area of treatment. Changing the metal centre to ruthenium would also provide additional functionality due to its fluorescent properties and increased stability. Adding further functionality and allowing

for seamless microscopy experiments which could yield valuable information on the uptake mechanism for these complexes.

Another step for these complexes would be to complete the *in vivo* rat studies which the separation and detection method was developed to undertake. This would give unparalleled insight into the biological activity of these complexes and would support the development of future designs. Comparison to the *in vitro* studies would also shed light on the impact an active metabolism has on drug stability. Detailed ESI-MS studies could shed light on the *in vivo* biological targets for these complexes as well as their bio-distribution. This would support further *in vitro* studies which in turn could improve biocompatibility. The combinations of ICP-MS and ESI-MS can show degradation patterns and pathways for the removal of these complexes from a living system. This could be done through extraction from localised tissues, cell types and organelles. Further to this, the effect of both enantiomers of the cylinder should be investigated fully alongside these studies. As different enantiomers have shown substantially different biological activity and function previously. Whilst modified rotaxanes show the most potential for a therapeutic drug, the effects of *pseudo* rotaxanating regular cylinders should also be investigated due to their substantially improved stabilities in blood. As a simple system may prove more effective through ease of production, reduced complexity, and interference with fewer biological pathways.

The pillarplex structures have shown potent DNA binding, warranting further investigation. Studies into their biological activity, uptake, localisation and mode of action should be carried out and linked to their structure and associated stabilities. ICP-MS would yield useful information to answer these questions. Pillarplexes with

modified ligand structures have also now been developed, allowing for new studies into how ligand structures affect their DNA binding.

Simultaneous rotaxanation and threading of pillarplexes also offers an opportunity for the design of a unique 3 tiered host guest rotaxane system. This could be tailored to offer multiple levels of control in response to different classes of external stimuli, allowing for high levels of specificity and control.

Chapter 6: Appendix

6.1: Agarose gel electrophoresis of circular supercoiled and linearized pBR-322 plasmid DNA with pillarplex ligand

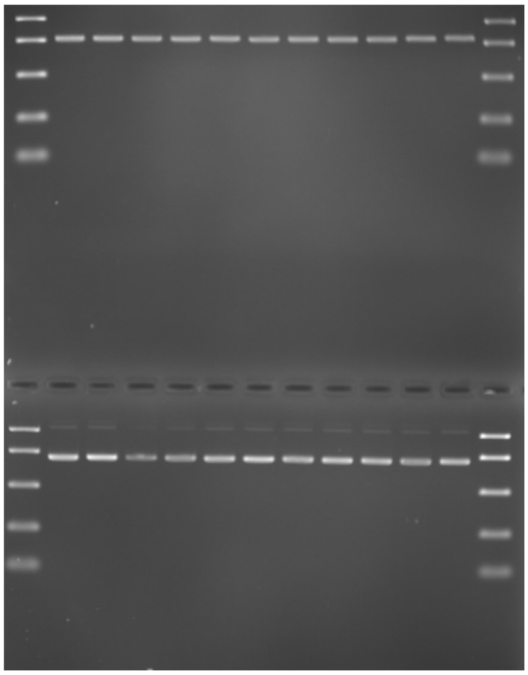


Figure A1: Agarose gel electrophoresis gel of Pillarplex ligand with PBR-322 linearized plasmid DNA (top) and circular plasmid DNA (bottom). 30:1, 20:1, 15:1, 10:1, 7.5:1, 5:1, 4:1, 3:1, 2:1, 1:1 DNA base pairs to ligand. Ratios are 2x the concentration of Pillarplexes in Figure S10, to account for the presence of 2 ligands in each Pillarplex. No evidence of binding is observed.

6.2: CD spectra of both M and P enantiomers of $[Fe_2(L)_3]^{4+}$

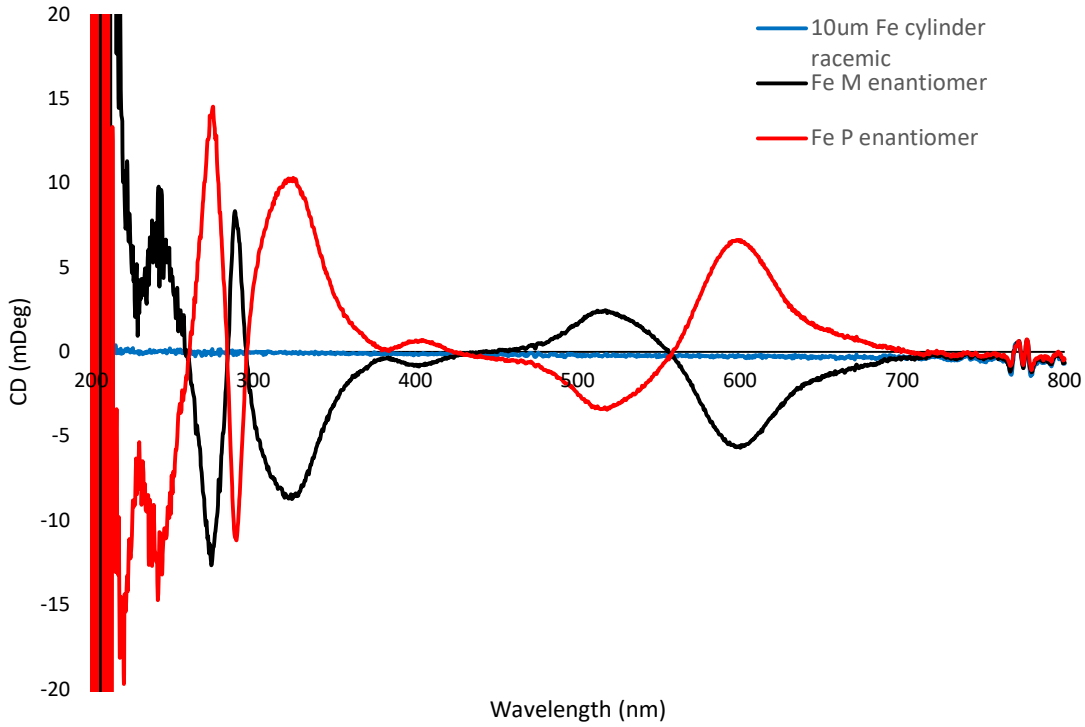


Figure A2: Shows the CD spectra for the racemic iron cylinder (blue) the M enantiomer (black) and the P enantiomer (red). All 3 solutions were in methanol alone, concentration of racemic iron cylinder was 10 µM.

6.3: ESI+ MS spectra of $[Fe_2(L)_3 \cdot (CB10)]^{4+}$ alone after blood purification process at starting and finishing time points

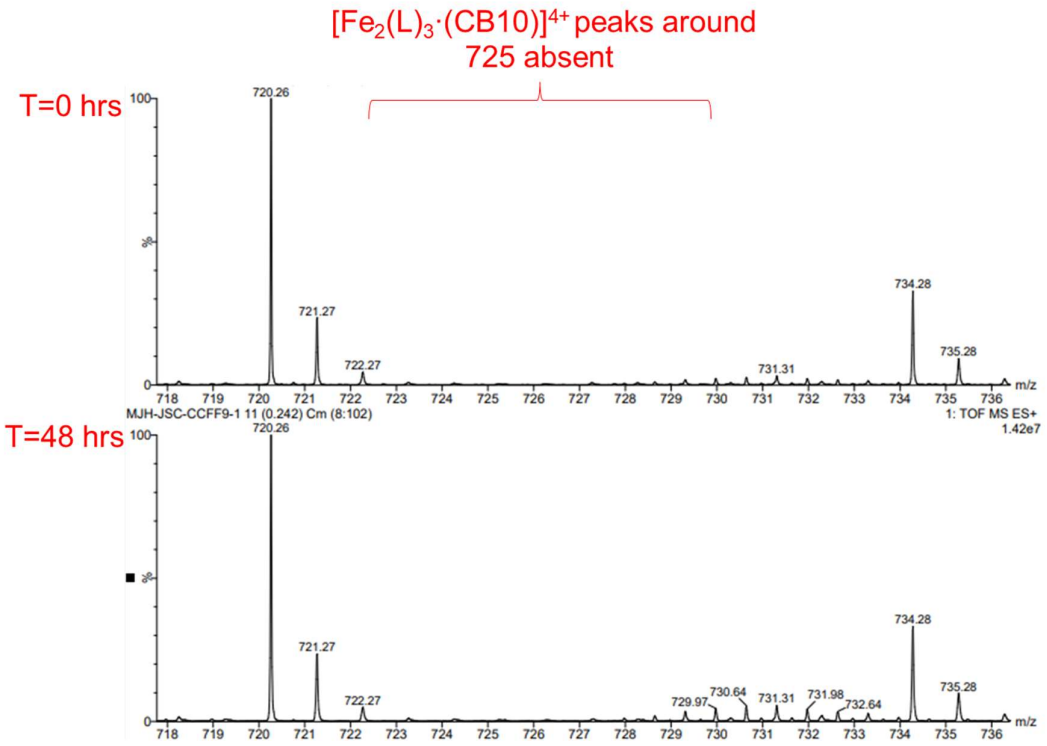


Figure A3: ESI+ MS spectra of $[Fe_2(L)_3 \cdot (CB10)]^{4+}$ after undergoing the purifications from blood process (not mixed with blood). This figure highlights the absence of any $[Fe_2(L)_3 \cdot (CB10)]^{4+}$ complex around 725 m/z, indicating CB10 is removed during this purification process.

6.4: CT-DNA binding curve for $[Ni_2(L')_3]$ from CD values at 250 nm

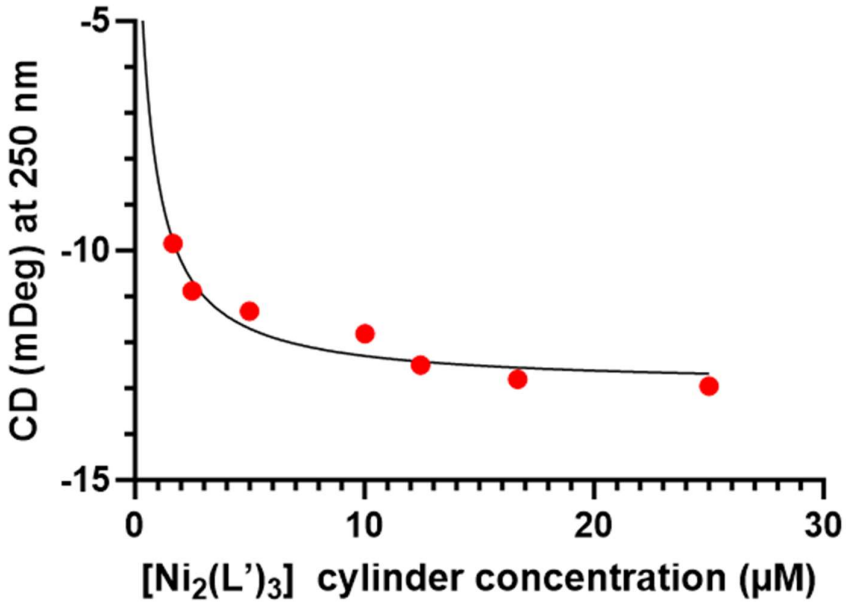


Figure A4: Binding curve generated in GraphPad prism showing the one site specific binding fitting for the binding curve of $[Ni_2(L')_3]$ with CT-DNA. This was used to calculate the K_d for binding. This was done using the CD values at 250 nm from the titration shown in figure 2.07.

6.5: CT-DNA binding curve for gold Pillarplex from CD values at 250 nm

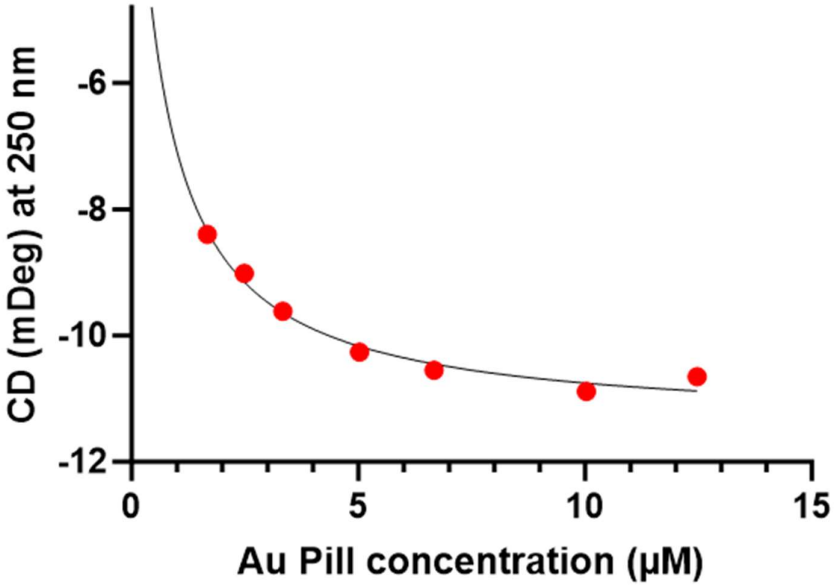


Figure A5: Binding curve generated in GraphPad prism showing the one site specific binding fitting for the binding curve of gold Pillarplex with CT-DNA. This was used to calculate the K_d for binding. This was done using the CD values at 250 nm from the titration shown in figure 4.09 spectra A.